

Nonlocal and Nonlinear Properties of Plasmonic Nanostructures Within the Hydrodynamic Drude Model

Dissertation

zur Erlangung des akademischen Grades

doctor rerum naturalium

(Dr. rer. nat.)

im Fach Physik

Spezialisierung: Theoretische Physik

eingereicht an der

Mathematisch-Naturwissenschaftlichen Fakultät

der Humboldt-Universität zu Berlin

von

Dipl.-Phys. Matthias Moeferd

Präsidentin der Humboldt-Universität zu Berlin

Prof. Dr. Sabine Kunst

Dekan der Mathematisch-Naturwissenschaftlichen Fakultät

Prof. Dr. Elmar Kulke

Gutachter:

1. Professor Dr. Kurt Busch
2. Professor Dr. Oliver Benson
3. Professor Stephen Hughes, Ph.D.

Tag der mündlichen Prüfung: 28. April 2017

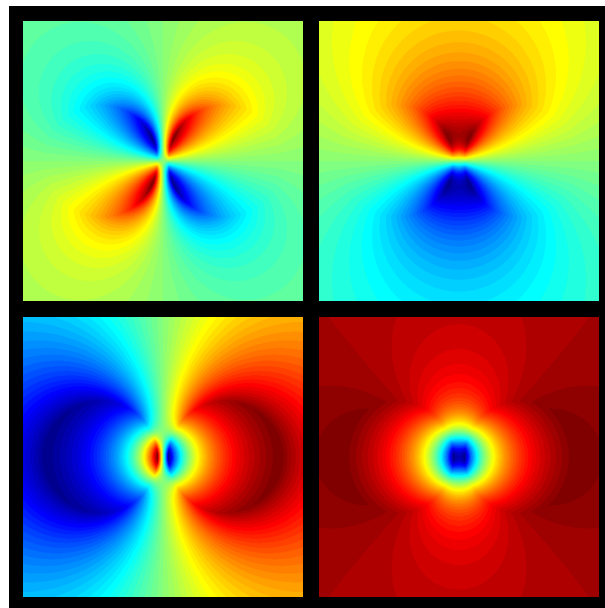
Ich erkläre, dass ich die Dissertation selbständig und nur unter Verwendung der von mir gemäß §7 Abs. 3 der Promotionsordnung der Mathematisch-Naturwissenschaftlichen Fakultät, veröffentlicht im Amtlichen Mitteilungsblatt der Humboldt-Universität zu Berlin Nr. 126/2014 am 18.11.2014 angegebenen Hilfsmittel angefertigt habe.

Weiterhin erkläre ich, dass ich mich nicht bereits anderwärts um einen Doktorgrad im Promotionsfach Physik beworben habe beziehungsweise einen entsprechenden Doktorgrad besitze.

Ich habe Kenntnis der dem Promotionsverfahren zugrunde liegenden Promotionsordnung der Mathematisch-Naturwissenschaftlichen Fakultät, veröffentlicht im Amtlichen Mitteilungsblatt der Humboldt-Universität zu Berlin Nr. 126/2014 am 18.11.2014.

Berlin, den 13. Dezember 2016

Nonlocal and Nonlinear Properties of Plasmonic Nanostructures Within the Hydrodynamic Drude Model



Dissertation

by

Matthias Moefert

Supervisor:

Professor Dr. Kurt Busch

To my parents

*“Die Schwierigkeit bestehe ja nicht
darin, etwas im Kopf zu haben, im
Kopf hätten alle das Ungeheuerlichste
und zwar ununterbrochen bis an ihr
Lebensende, das Ungeheuerlichste,
sondern die Schwierigkeit sei, dieses
Ungeheuerliche aus dem Kopf heraus
auf Papier zu bringen. Im Kopf könne
man alles haben und tatsächlich habe
auch jeder alles im Kopf, aber auf dem
Papier habe fast keiner etwas“*
Thomas Bernhard, Das Kalkwerk [1]

PREFACE

Centuries ago, artists discovered that contaminating glass with very fine metallic dust gave rise to vibrant colors upon illumination [2]. In order to stain church windows, they thus exploited an interesting property of metallic nanoparticles that are smaller than the wavelength of visible light: Namely that they often possess resonances in the visible. Little did they know that the effects they witnessed were due to physical processes at the nanoscale and that it would take scientists until the beginning of the twentieth century to be able to conduct reliable experiments and start developing the corresponding theories [2]. The origin of the resonances lies in the excitation of so-called localized surface plasmon polaritons. Surface plasmon polaritons are mixed excitations, consisting of charge-density oscillations and an electromagnetic field. They occur at metallic surfaces and if they are confined to the geometry of a particle, they are called localized surface plasmons.

From a theoretical point of view, Drude's 1900-paper "*Zur Ionentheorie der Metalle*" [3] can be viewed as a landmark on the way to what is now known as "plasmonics" and its significance to this date will become apparent to the readers of this thesis. Within the model presented by Drude, the electromagnetic properties of a metal are described by a gas of free, non-interacting electrons that move against a positively charged ionic background due to external fields [4]. Based on that theory, Maxwell Garnett was able to explain the colors in metal-doped glasses in 1904 [2, 5]. The corresponding rigorous scattering theory by Gustav Mie followed a few years later, in 1908 [2, 6]. On the experimental side, Wood discovered anomalous reflection from metallic gratings for p-polarized light in 1902 [2, 7]. An effect which could not be explained until half a decade later, when Pines, Fano and Ritchie laid the theoretical foundations for what is nowadays called plasmonics [2]. They were also the ones who coined the terms "plasmons" and "polaritons" [2].

This laid the foundations for a veritable industry built around plasmonics, dealing with the manipulation and confinement of light at the nanoscale. Very prominently, the presence of surface plasmons significantly increases the Raman cross section of molecules placed near a plasmonic nanoparticle. This effect, called *surface enhanced Raman scattering* (SERS), was discovered in the 1970s [8–10] and is today one of the most sensitive spectroscopy methods that exist [11].

In order to achieve good SERS intensities, the size of the nanostructures will usually have to be between 10 nm and 100 nm [12]. At the low end of this range, at around 10 nm, the simpler material descriptions based on the aforementioned model by Drude start to fail as corrections due to quantum mechanical effects have to be accounted for. Most notably, nonlocality plays a role here which can be viewed as a macroscopic manifestation of the Pauli exclusion principle that becomes important as soon as the motion of the electrons with respect to each other is taken into account. This is contained in a more sophisticated material model, called the hydrodynamic Drude model¹, which represents an extension of the Drude model. Investigations of effects contained within this important material model are a central topic of this thesis.

¹I use the terms *hydrodynamic model* and *hydrodynamic Drude model* synonymously.

A second, more recent application of plasmonics are wave-mixing processes from metal nanoparticles, such as second harmonic generation (SHG) or sum-frequency generation. This enables for instance background free imaging at the second harmonic frequency [13, 14]. Since higher harmonic cross-sections from nanoparticles are very small, they need to be enhanced by geometric tuning in very much the same way as the local fields are enhanced in the context of SERS. Additional enhancement is obtained by double-resonant tuning, i.e. having a particle resonance at both the frequency of the incoming light and the frequency of the second harmonic. Higher harmonic generation is completely absent in the Drude model, but it is also included in the aforementioned nonlocal hydrodynamic model. The questions arising in the context of SERS and of SHG are very similar: it is important to know at which frequencies strong fields can be generated, what the corresponding distributions look like, and how they can be excited. This requires a thorough investigation of the modes pertaining to a specific geometric structure. I perform an investigation of the (high order multipole) modes which are present in different nanostructures, i.e. the typical field distributions which are characteristic for a geometrical setup and their corresponding frequency which is determined by the material model. By analyzing the symmetries of the modes, I can draw important conclusions on how to excite them both by linear and nonlinear processes. These studies are done by combining analytical considerations and numerical calculations performed employing the discontinuous Galerkin time domain method (DGTD).

The theoretical findings of this work can be helpful in the design of SERS-active structures or structures featuring strong SHG on the one hand, but I also discuss fundamental effects which are due to nonlocality and could serve to check the validity of the material model.

Outline

Chapter 1 motivates this work by giving a more detailed introduction to the topics and questions addressed. After introducing Maxwell's equations and surface plasmons, I discuss some details of SERS and point out questions that are inspired by this very important application of plasmonics and that I will discuss later on. Furthermore, I give a short introduction to higher harmonic generation.

In Chap. 2, the relevance of the material models is explained by giving a detailed introduction to the Drude and the hydrodynamic model and highlighting the differences and similarities between them. The derivation of both models from the underlying very basic assumptions is carried out. The connection between the hydrodynamic model and Thomas-Fermi theory and density functional theory is also addressed. From the full hydrodynamic model, the linearized hydrodynamic model is derived. In this context, I construct the dielectric function for the linearized hydrodynamic model and discuss bulk plasmons. I comment on nonlinearities in the hydrodynamic model and discuss the importance of the model, as well as possible extensions and modifications.

Chapter 3 deals with analytical considerations that are based on the hydrodynamic Drude model. I start out with some basic considerations for a single cylinder and present an asymptotic description of resonant shifts which are introduced due to nonlocality. This is done both within Mie-theory and within electrostatic theory. The electrostatic treatment of the single cylinder lays the foundation for the second part of the chapter, the electrostatic treatment of a cylindrical dimer which requires a conformal map to bicylindrical coordinates. In the last section of the chapter, I discuss the excitation of modes by linear and nonlinear processes by means of group theory. To do this, the symmetries of the hydrodynamic equations and the Maxwell equations are expressed in terms of the irreducible representations of the

symmetry point group pertaining to the geometry under consideration. This makes it possible to derive selection rules which connect the symmetries of the mode that is excited to the symmetries of the incoming light pulse – both for linear and nonlinear processes.

Chapter 4 is dedicated to the numerical method used here, the discontinuous Galerkin time domain method (DGTD). I start with an introduction to the method in general and then discuss how the hydrodynamic equations are implemented. Furthermore, I introduce the concepts and schemes used here, such as the total field-scattered field formalism and the on-the-fly Fourier transform. Finally, I present convergence checks for the hydrodynamic Drude model within the discontinuous Galerkin method for the test case of a single cylinder, investigating the convergence characteristics of surface plasmons for both linear and nonlinear excitation and the convergence characteristics of bulk plasmons.

In Chap. 5 I present all the results which were obtained numerically, discussing basic features of the hydrodynamic Drude model and presenting studies of field enhancement and SHG. For the example of a single cylinder, I show the influence of nonlocality on surface plasmon resonances and study bulk plasmons and SHG. I discuss the origin of the nonlinear signal and comment on the selection rules for SHG. The second structure which is analyzed is the cylindrical dimer which is treated analytically in Chap. 3. A thorough numerical analysis of the hybridized modes pertaining to this system, using the DGTD method, is backed by further considerations employing a quasinormal mode solver (App. A) and the group theoretical considerations from Sec. 3.4. The selection rules for linear excitation and second harmonic generation are confirmed. Field enhancement is discussed in much detail, especially with regard to the influence of nonlocality. I then discuss second harmonic generation from a double-resonant V-groove, whose selection rules are related to those of the dimer, and study three-wave mixing for a bow tie-antenna.

A summary of the findings of this thesis, conclusions and a short outlook are given in Chapter 6.

CONTENTS

PREFACE	XI
1 INTRODUCTION AND MOTIVATION	1
1.1 Maxwell's Equations	1
1.2 Surface Plasmons	3
1.3 Surface-Enhanced Raman Spectroscopy	4
1.4 Second Harmonic Generation and Sum-Frequency Generation	7
2 MATERIAL MODELS	11
2.1 The Drude Model	11
2.2 The Hydrodynamic Drude Model	14
2.2.1 The Continuity Equation and the Euler Equation	14
2.2.2 Thomas Fermi Theory	16
2.2.3 Perturbative Treatment of the Hydrodynamic Model	21
2.2.4 The Linear Susceptibility, Bulk Plasmons and the Parameter β	25
2.2.5 Nonlinear Susceptibility	28
2.2.6 The Importance of the Hydrodynamic Model: Applicability and Extensions . .	28
3 ANALYTICAL CONSIDERATIONS	33
3.1 The Material Parameters	34
3.2 Analytical Treatment of a Single Cylinder	35
3.2.1 Extended Mie Theory for a Nonlocal Material	35
3.2.2 Asymptotic Behavior	39
3.2.3 Perturbative Treatment of the Parameter β	45
3.2.4 Bulk Plasmons	48
3.2.5 Electrostatics	49
3.3 Electrostatic Treatment of a Cylindrical Dimer	54
3.3.1 Introduction to Bicylindrical Coordinates	54
3.3.2 Conformal Maps	55
3.3.3 Bicylindrical Coordinates as a Conformal Map	58
3.4 Group Theoretical Considerations	62
3.4.1 Cylindrical Dimer	63
3.4.2 SHG from a Single Cylinder	72
3.4.3 SHG from a V-Groove	73

4	THE DISCONTINUOUS GALERKIN TIME DOMAIN METHOD	75
4.1	Numerical Simulations of Plasmonic Nanoparticles	75
4.1.1	Implementation of Maxwell's Equations and the Hydrodynamic Equations . .	77
4.1.2	Dimensionless Units	81
4.2	Aspects of Numerical Simulations with the DGTD Method	82
4.2.1	Total Field-Scattered Field Formalism and On-The-Fly Fourier Transform . . .	82
4.2.2	Material Assignments	85
4.3	Convergence of the Hydrodynamic DGTD Method	87
4.3.1	First Order Quantities	89
4.3.2	Second Harmonics	93
5	NUMERICAL RESULTS	97
5.1	Cylinder	97
5.1.1	Linear Scattering Simulations	97
5.1.2	Second Harmonics	100
5.1.3	Origin and Intensity Dependence of Higher Order Terms	104
5.2	Cylindrical Dimer	106
5.2.1	Local Case	106
5.2.2	Nonlocal Case	112
5.2.3	Nonlinear Scattering	116
5.2.4	Electron Density Fluctuations for the Dimer Modes	118
5.2.5	Field Enhancement in a Dimer for a Local and a Nonlocal Material	120
5.3	Double Resonant SHG from a V-Groove	125
5.4	Sum-Frequency Generation from a Bow-Tie Antenna	128
5.5	Three-Dimensional Structures	132
6	SUMMARY AND CONCLUSIONS	133
A	QUASINORMAL MODE CALCULATIONS	137
	BIBLIOGRAPHY	148
	ACKNOWLEDGMENTS	151

1

INTRODUCTION AND MOTIVATION

In this Chapter, after introducing Maxwell's equations, I start out with a basic introduction of surface plasmons. I then present an important application of surface plasmons, namely surface enhanced Raman spectroscopy (SERS). I discuss some of the challenges and questions which arise in this context and which I am going to address in this work. I motivate why a thorough understanding of the plasmonic modes, i.e., an investigation of which field distributions are found at which frequencies, is of practical importance. Finally, I comment on second harmonic generation from metallic nanoparticles.

1.1 Maxwell's Equations

The equations which are used to describe electromagnetic fields – and therefore light – are Maxwell's Equations. In media, they read [15]

$$\nabla \cdot \mathbf{D}(\mathbf{r}, t) = \rho(\mathbf{r}, t), \quad (1.1)$$

$$\nabla \cdot \mathbf{B}(\mathbf{r}, t) = 0, \quad (1.2)$$

$$\nabla \times \mathbf{E}(\mathbf{r}, t) = -\partial_t \mathbf{B}(\mathbf{r}, t), \quad (1.3)$$

$$\nabla \times \mathbf{H}(\mathbf{r}, t) = \partial_t \mathbf{D}(\mathbf{r}, t) + \mathbf{j}(\mathbf{r}, t). \quad (1.4)$$

Here, $\mathbf{E}(\mathbf{r}, t)$ and $\mathbf{H}(\mathbf{r}, t)$ are the electric and magnetic field, respectively. $\mathbf{D}(\mathbf{r}, t)$ is the magnetic displacement and $\mathbf{B}(\mathbf{r}, t)$ the magnetic induction. The quantities $\rho(\mathbf{r}, t)$ and $\mathbf{j}(\mathbf{r}, t)$ represent the charge density and the current density.

The interaction of electromagnetic fields with matter is thereby described by the charges which constitute the matter and the current densities effected by the movement of these charges. However, in a macroscopic material, it is impossible to describe every single charge, therefore macroscopic quantities

1 Introduction and Motivation

have to be derived. By averaging over the electric and magnetic dipole moments which are induced by the charges in the material, one arrives at macroscopic expressions for the polarization $\mathbf{P}(\mathbf{r}, t)$ and the magnetization $\mathbf{M}(\mathbf{r}, t)$ which connect $\mathbf{E}(\mathbf{r}, t)$ and $\mathbf{D}(\mathbf{r}, t)$, and $\mathbf{H}(\mathbf{r}, t)$ and $\mathbf{B}(\mathbf{r}, t)$

$$\mathbf{D}(\mathbf{r}, t) = \epsilon_0 \mathbf{E}(\mathbf{r}, t) + \mathbf{P}(\mathbf{r}, t), \quad (1.5)$$

$$\mathbf{H}(\mathbf{r}, t) = \mu_0^{-1} \mathbf{B}(\mathbf{r}, t) - \mathbf{M}(\mathbf{r}, t), \quad (1.6)$$

thus completing the set of equations (1.1)-(1.4). The vacuum permittivity ϵ_0 and the vacuum permeability μ_0 are connected to the speed of light:

$$c = \frac{1}{\sqrt{\epsilon_0 \mu_0}}. \quad (1.7)$$

This thesis deals with the optical properties of metallic particles. At optical frequencies, the magnetization is significantly smaller than the polarization and can therefore be neglected [16]. The polarization in a linear, isotropic, local medium in response to an electric field is described by the susceptibility tensor χ :

$$\mathbf{P}(\mathbf{r}, t) = \epsilon_0 \int_{-\infty}^t dt' \chi(\mathbf{r}, t - t') \mathbf{E}(\mathbf{r}, t'). \quad (1.8)$$

Hence, the displacement is given by

$$\mathbf{D}(\mathbf{r}, t) = \epsilon_0 \int_{-\infty}^t dt' \epsilon(\mathbf{r}, t - t') \mathbf{E}(\mathbf{r}, t'), \quad (1.9)$$

where the dielectric function ϵ is given by

$$\epsilon = \epsilon_0(1 + \chi). \quad (1.10)$$

The above consideration were done in time-domain. When interpreting the equations in frequency domain, $\epsilon = \epsilon(\omega)$ depends on the frequency for many materials. This is known as dispersion or temporal nonlocality [15]. To conduct the studies within this thesis, an adequate description for the dielectric function $\epsilon(\omega)$ for metals is needed. The equations for ϵ then have to be solved consistently along with Maxwell's equations. The optical properties of metal nanoparticles are primarily governed by the interaction of the quasi free electrons within the metal structure with the electromagnetic field pertaining to an incoming light pulse [17]. The theoretical models used in this thesis which describe these free electrons – the Drude model and the hydrodynamic Drude model – are introduced and discussed in detail in Chap. 2. The hydrodynamic model exhibits not only dispersion, but also spatial nonlocality, i.e. a dielectric function of the type $\epsilon(\mathbf{r}, \mathbf{r}', t - t')$ (See Sec. 2.2.4). On top of this, metals feature nonlinearities which give rise to light radiated at other frequencies than that of the incoming light which I will comment on later in this Chapter (Sec. 1.4). The discussion of these complicated properties of this material model lie at the heart of this thesis.

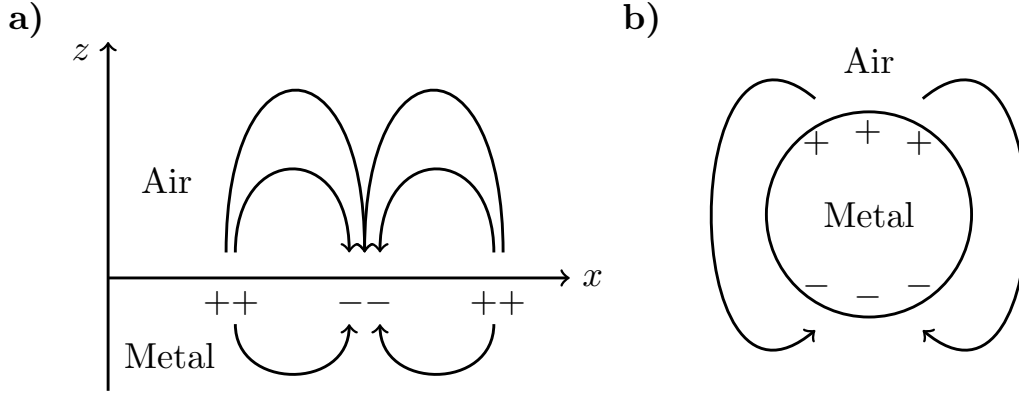


Figure 1.1: **a)** Schematic of the surface charge density wave for a propagating plasmon polariton [18]. **b)** Schematic for a localized surface plasmon for a single cylinder.

1.2 Surface Plasmons

The considerations in the previous section were made for infinitely extended systems. The matter becomes more interesting at interfaces of regions with different dielectric function. An important phenomenon that occurs at the surface of metal nanostructures and that is investigated in this work, are surface plasmon polaritons. In a surface plasmon polariton, the free-moving electrons in a metal, which are displaced by the electromagnetic field, and the electromagnetic field itself, generate mixed (polaritonic) excitations at the boundary between a metal and a dielectric¹ (Fig. 1.1). The fields decay exponentially with the distance from the interface and feature very high fields near the interface. For a flat surface, these excitations propagate along the surface (Fig. 1.1 **a**)), while for other geometries such as cylinders (Fig. 1.1 **b**)) localized modes exist, in principle of arbitrarily high multipole order. They depend highly on the geometry. Such localized surface plasmon polaritons are calculated analytically and numerically for different geometries in Chaps. 3 and 5. For gap structures or for geometries with sharp edges, the field enhancement due to localized surface plasmons can be extremely large, as I will demonstrate. These strong fields are important for applications such as surface enhanced Raman spectroscopy (SERS) and second harmonic generation. The questions inspired by these applications are presented in the following sections.

Theoretically, a condition for surface plasmon polaritons can be derived as follows: As pointed out, the fields are supposed to decay exponentially with increasing distance from the surface. Thus, solutions to electromagnetic wave equation exist, which feature fields that propagate in the plane and exhibit the desired exponential decay. These modes go along with charge density oscillations and strongly confined optical fields. Fields and charges are coupled, hence they form a polariton [2, 4, 17–19].

¹For brevity, I will often refer to the plasmon polaritons simply as plasmons. Since I am only dealing with the mixed type of excitations described here, there is no risk of confusion.

1 Introduction and Motivation

The solutions can be found by solving the wave equation. For transverse waves, it reads

$$\nabla^2 \mathbf{E}_t + \frac{\omega^2}{c^2} \epsilon(\mathbf{r}, \omega) \mathbf{E}_t = 0. \quad (1.11)$$

Having the interface in the xy -plane, with the metal extending to negative z -values, assuming propagation in x -direction, an Ansatz for p-polarized plane-waves decaying exponentially, away from the surface, reads

$$\mathbf{E}_{\pm} = \begin{pmatrix} E_{x,\pm} \\ 0 \\ E_{z,\pm} \end{pmatrix} e^{i(k_x x - \omega t)} e^{ik_{z,\pm} z}, \quad (1.12)$$

where \mathbf{k} can be complex-valued and the index $+$ or $-$ stands for $z > 0$ and $z < 0$ respectively. Using the usual boundary conditions, one arrives at the dispersion relations (for details, see References [4, 17, 18])

$$k_x^2 = \frac{\epsilon_+ \epsilon_-}{\epsilon_+ + \epsilon_-} \frac{\omega^2}{c^2}, \quad (1.13)$$

$$k_{z,\pm}^2 = \frac{\epsilon_{\pm}^2}{\epsilon_+ + \epsilon_-} \frac{\omega^2}{c^2}. \quad (1.14)$$

Since the desired solutions are supposed to be bound to the surface (requiring imaginary k_z) and propagating in x -direction (requiring real k_x), one arrives at the two important conditions

$$\epsilon_+ \epsilon_- < 0 \quad (1.15)$$

and

$$\epsilon_+ + \epsilon_- < 0. \quad (1.16)$$

Hence, for surface plasmons to exist on a planar surface, the dielectric function has to have a change in sign at the surface. This type of behavior is found at metal-dielectric interfaces. Furthermore, the absolute value of the negative permittivity has to be greater than that of the positive permittivity.

In order to study surface plasmon polaritons, it is important to have an adequate description of the materials on both sides of the interface, i.e. to have an expression for ϵ_+ and ϵ_- . The description of the dielectric (lossless and frequency-independent) poses no technical difficulties, while the description of the metal, which is presented in Chap. 2, is very involved. Once the material models for the metal are introduced, surface plasmons can be discussed, based on analytical and numerical studies. This is done in Chaps. 3 and 5.

1.3 Surface-Enhanced Raman Spectroscopy

The high field intensities in the vicinity of the boundaries, due to the presence of localized surface plasmons, give rise to an important effect called surface enhanced Raman scattering (SERS)². Understanding the field distributions, investigating hot-spots of very high field enhancement, depending on

²Additional enhancement due to chemical processes plays a role for certain setups [20] but is not of interest for this thesis.

the geometry and the frequency is an important question inspired by the field of SERS and a motivation for many investigations in this thesis. In Raman scattering, light scatters inelastically from a molecule, thereby exciting (or de-exciting) a vibrational mode [12, 21]. This process is illustrated in Fig. 1.2. The resulting energy shift is a characteristic fingerprint of the molecule. One of the advantages of the method is that it is a non-resonant method, i.e. the excited intermediate state can be a virtual state [22]. The disadvantage of this method is the very small cross section of about $10^{-30} \text{cm}^2/\text{molecule}$ [18, 23]. A resonant excitation yields somewhat larger cross-sections but at the same time induces (usually undesired) photo-induced processes [22].

A significant enhancement of the Raman cross-section is achieved in the presence of a surface: In 1974, Fleischmann et al. [8] subjected a silver electrode to an oxidation-reduction process and showed significant enhancement of the Raman signal. Jeanmaire and Van Duyne [9], as well as Albrecht and Creighton [10] conducted similar experiments and showed that the enhancement could not solely be due to an increase in surface area (and hence an increase in molecules adsorbed at the surface), but that there must be an additional effect. The measured intensities exceeded the expected enhancement by a factor of 10^5 [9, 10, 24]. Albrecht and Creighton already suspected that the interaction with surface plasmons could play a role (Philpott had previously presented a mechanism which led to broadening of the molecular levels due to resonance energy transfer between an excited molecule and the surface plasmon modes [25]).

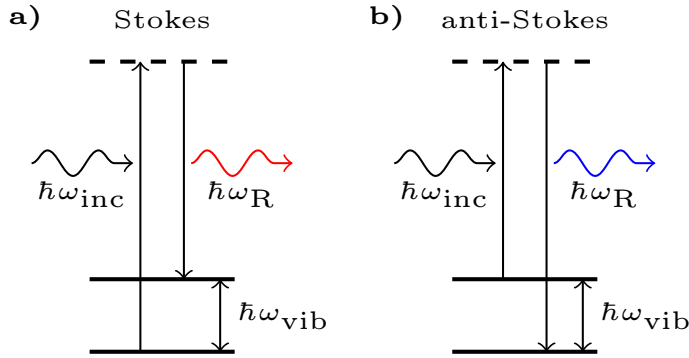


Figure 1.2: Schematics of the a) Stokes Raman process and b) anti-Stokes Raman process. An incoming wave excites the molecule from the ground state to a (virtual) intermediate state from where it is de-excited to a vibrational state (Stokes) or vice versa (anti-Stokes). [18]

Further studies showed that the effect predominantly stems from the interaction with the surface plasmons explained above, and can be described as follows [12, 21]: The average local field near the particle surface $E_s = gE_0$ is enhanced by an enhancement-factor g with respect to the magnitude of the incoming field E_0 due to the excitation of surface plasmons. For light incident at a surface plasmon resonance frequency, the highest enhancement is obtained. The molecule is then excited by the scattered field E_s . Since the shift in frequency is typically very small compared to the frequency of the incoming pulse, it can therefore be neglected and the Raman scattered light

is still on resonance with the surface plasmon and undergoes a second enhancement process with $g' \approx g$. Hence, light is radiated with a field strength

$$E_R \propto \alpha_R E_s \approx \alpha_R g^2 E_0. \quad (1.17)$$

The Raman cross-section is proportional to the intensity, i.e. the square of the field:

$$I_{\text{SERS}} \propto |\alpha_R|^2 |g^2|^2 I_0. \quad (1.18)$$

1 Introduction and Motivation

Therefore, the electromagnetic enhancement of the SERS cross section (known as the SERS-factor) is given by [12, 18, 26]

$$M_{\text{SERS}} \approx |g|^4 \approx \left(\frac{|E_s|}{|E_0|} \right)^4, \quad (1.19)$$

and can be determined from scattering simulations for plasmonic nanoparticles.

An enhancement that scales with the fourth power of the incoming field helps overcome the flaw of small cross-sections, making even detection of single molecules possible [22, 23, 27]. An enhancement of $M_{\text{SERS}} \approx 10^7 - 10^{11}$ is required for single molecule detection, depending on the molecule and whether the excitation is resonant. The measurement of molecular vibrations from a single hemoglobin molecule located in the gap of a spherical silver dimer was for instance reported by Xu et al. [23]. In this work, the authors discuss the influence of particle size and separation while pointing out, that those factors are particularly difficult to control in an experiment. Xu and coworkers aimed at theoretically calculated enhancement factors (at the center point between two spheres) of $M_{\text{SERS}} \approx 6 \cdot 10^6$, but found enhancement factors of up to $M_{\text{SERS}} \approx 10^{10}$ which they calculated to be within reach of the electromagnetic theory for SERS, due to the above-mentioned uncertainties in the experimental setup. The fact that the hemoglobin molecule was placed in the gap of a silver dimer was very important, as SERS-hotspots, i.e. points of very high field intensity, are usually not found in the vicinity of single plasmonic scatterers such as spheres or cylinders, but rather in gaps or near sharp edges. Thus more complicated particle geometries or assemblies of particles are needed [12]. Geometries need to be designed which are experimentally feasible and lead to the best possible results. Dimers are essentially the building blocks of more complicated array-structures and are often used for studies in the context of SERS [28, 29]. They are an important testing platform when it comes to studying plasmonic effects.

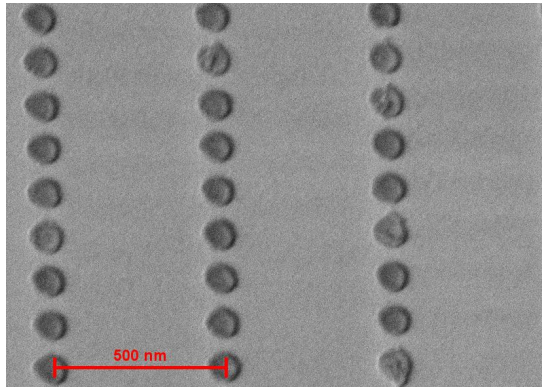


Figure 1.3: Scanning electron microscope image of a periodic nanorod array used for SERS. Photo courtesy of Jörg Schilling.

Many scientists are working towards designing SERS active structures in a well-controlled fashion. The modes of those structures which are associated with specific field distributions for every frequency, have to be well-known in order to effectively exploit their properties for SERS. Those properties can be tuned by using different materials or varying the geometry. For instance, in a dimer one can change the size of the constituents and the distance between the particles. Other popular setups are periodic assemblies such as the nanopillar array depicted in Fig. 1.3 which was designed in the group of Prof. Wehrspohn in Halle. The setup is highly ordered and the distances between the different pillars as well as their thickness can be well-controlled, thus allowing to tune the field distributions and the frequencies of the modes.

Furthermore, for any complicated structure such as a dimer, the field enhancement depends on the type of excitation that is used to illuminate the structure – the polarization of the \mathbf{E} -field or, more generally, the symmetries of the excitation, being the crucial factor. A simple argument goes as follows [12]: If the light is polarized along the dimer axis, the charges

are moved in such a fashion that very strong fields can be obtained in the gap as in Fig. 1.4 **a**), whereas if the polarization is rotated by ninety degrees, there is no charge difference across the gap and hence no large field enhancement (1.4 **b**)). However, a dimer system as depicted in Fig. 1.4 supports more types of different modes than the ones depicted in the figure. Those are only the ones that are excited in the case of a static external field. In Chaps. 3 and 5, I discuss the modes of such a dimer system and their corresponding field enhancements analytically and numerically in full detail and the findings go far beyond the simple picture from Fig. 1.4.

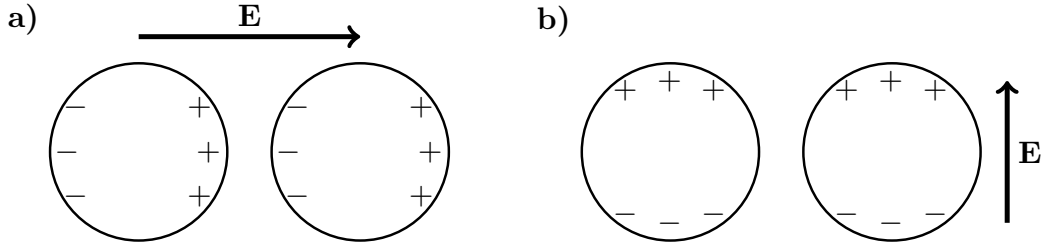


Figure 1.4: The charges in a dimer system are moved under illumination by a static field. **a)** For an electric field polarized along the dimer axis, charge differences across the gap generate a large field enhancement within the gap. **b)** If the electric field polarization is rotated, no strong fields are expected in the gap [12].

In fact, one of the most important topics of this thesis is to perform extensive studies of those modes. The concepts introduced include an analytical investigation of the modes within electrostatic theory, scattering calculations (numerically, and analytically where possible), quasinormal mode calculations as well as group-theoretical symmetry considerations. The tools that I introduce in this thesis and use to discuss a number of geometries provide fundamental insight. They help to gain an intuitive understanding of some important mechanisms and can be adapted to discuss further geometries. The numerical schemes and analytical considerations presented in this thesis can be helpful for experimental design purposes in the context of SERS-experiments. Vice versa, they describe how SERS measurements or other experiments can be used to determine the validity of the material models used here.

1.4 Second Harmonic Generation and Sum-Frequency Generation

Nonlinear processes from metal nanoparticles typically exhibit very small cross sections. However, as in the case of SERS, the process benefits from the strong field enhancement which can be achieved in certain geometrical setups such as for sharp tips or in gap structures [13, 14, 30–34]. Second harmonic generation (SHG) is used for background-free imaging at the second harmonic frequency and has thus important applications. Specifically, metallic tips exhibit a lightning rod effect and can therefore function as efficient point-like light sources with a very sharp emission spectrum [14]. They are stable under illumination with laser beams while other realizations of point-like light sources, such as single molecules or N-V-centers, suffer from blinking or photo-bleaching [14].

Nonlinear optical processes can be described by a generalized susceptibility which describes the polarization as a power series in the field strength [35]. To do this, the tensorial nature of the susceptibility

1 Introduction and Motivation

has to be taken into account. If nonlocality is included, this yields [35–37]

$$P_i(\mathbf{r}, t) = \epsilon_0 \int d\mathbf{r}' \int_{-\infty}^t dt' \chi_{ij}^{(1)}(\mathbf{r}, \mathbf{r}', t - t') E_j(\mathbf{r}', t') + \\ + \epsilon_0 \int d\mathbf{r}' \int d\mathbf{r}'' \int_{-\infty}^t dt' \int_{-\infty}^{t'} dt'' \chi_{ijk}^{(2)}(\mathbf{r}, \mathbf{r}', \mathbf{r}'', t - t', t - t'') E_j(\mathbf{r}', t') E_k(\mathbf{r}'', t''), \quad (1.20)$$

where the indices i, j, k label the cartesian coordinates of the fields and Einstein's sum convention was used. Assuming that the fields can be expressed as a discrete sum of frequency components,

$$\mathbf{E}(\mathbf{r}, t) = \sum_n \mathbf{E}(\mathbf{r}, \omega_n) e^{-i\omega_n t}, \quad (1.21)$$

the polarization in frequency domain is connected to the polarization in time domain via [35]

$$\mathbf{P}(\mathbf{r}, t) = \sum_n \mathbf{P}(\mathbf{r}, \omega_n) e^{-i\omega_n t}, \quad (1.22)$$

where the sum is carried out over all negative and positive frequencies. In this thesis, I consider second harmonic generation, as well as the more general case of sum-frequency generation which requires two distinct incoming pulses. These processes, known as three-wave mixing, are described by the second order susceptibility $\chi_{ijk}^{(2)}$ in frequency space, which is defined as [35]

$$P_i(\mathbf{r}, \omega_n + \omega_m) = \epsilon_0 \int d\mathbf{r}' \int d\mathbf{r}'' \sum_{(nm)} \chi_{ijk}^{(2)}(\mathbf{r}, \mathbf{r}', \mathbf{r}'', \omega_n + \omega_m; \omega_n, \omega_m) E_j(\mathbf{r}', \omega_n) E_k(\mathbf{r}'', \omega_m), \quad (1.23)$$

where the brackets in the sum over (nm) indicate that the sum $\omega_n + \omega_m$ has to be held fixed while the separate frequencies ω_n and ω_m are allowed to vary. The sum over jk is once again implied by the sum-convention. The product $E(\omega_n)E(\omega_m)$ has a time-dependence of the type $e^{-i(\omega_n + \omega_m)t}$, according to Eq. (1.21). For monochromatic input fields, one finds for sum-frequency generation

$$P_i(\mathbf{r}, \omega_3) = 2\epsilon_0 \int d\mathbf{r}' \int d\mathbf{r}'' \chi_{ijk}^{(2)}(\mathbf{r}, \mathbf{r}', \mathbf{r}'', \omega_3; \omega_1, \omega_2) E_j(\mathbf{r}', \omega_1) E_k(\mathbf{r}'', \omega_2), \quad (1.24)$$

and for SHG

$$P_i(\mathbf{r}, \omega_3) = \epsilon_0 \int d\mathbf{r}' \int d\mathbf{r}'' \chi_{ijk}^{(2)}(\mathbf{r}, \mathbf{r}', \mathbf{r}'', \omega_3; \omega_1, \omega_1) E_j(\mathbf{r}', \omega_1) E_k(\mathbf{r}'', \omega_1). \quad (1.25)$$

SHG and sum-frequency generation are investigated numerically for metal nanoparticles of different geometries in Chap. 5. To describe the nonlinear response of a metal nanoparticle, an appropriate material model has to be employed. The nonlinear model used within this thesis to describe metals is introduced in Sec. 2.2. In Sec. 2.2.5 I will present a relation between \mathbf{P}_2 and \mathbf{E} for a metal. There, it becomes apparent that the tensorial nature of the nonlinear susceptibility has to be taken into account.

For second harmonic generation from metallic nanoparticles which I investigate in this thesis, the same kind of mode-analysis as described above for SERS is helpful to determine under which circumstances strong SHG signals can be obtained. However, the selection rules, i.e. connecting the symmetry

1.4 Second Harmonic Generation and Sum-Frequency Generation

of the excited mode to the symmetry of the incoming pulse (which is trivial in the case of linear excitation), are more involved as I demonstrate using group theory in Section 3.4. Understanding this excitation process is crucial in order to make predictions regarding SHG. Additional enhancement can be obtained if the setup is tuned double-resonantly, i.e., if a resonance is available at the fundamental frequency and at the second harmonic. Extensive studies of the efficiency of nonlinear signals are carried out in this work. This is predominantly done employing a numerical method, since the nonlinear equations are difficult to tackle analytically. The results which I present in Sec. 3.4 and in Chap. 5 allow for very fundamental statements regarding the nonlinear properties of metals.

2

MATERIAL MODELS

This chapter is dedicated to the introduction of the material models for describing metals at optical frequencies, namely the Drude model and an extension thereof, the nonlocal and nonlinear hydrodynamic model which can account for local fluctuations of the density of the free valence electrons in a metal. For the latter model, two approaches to obtain an expression for the kinetic pressure of the electron gas are presented. The detailed discussions of the hydrodynamic model and its nonlocal and nonlinear properties taking place in this chapter lay the foundation of all the subsequent analytical and numerical studies performed throughout this thesis.

2.1 The Drude Model

In metals, the majority of effects associated with the interaction with an electromagnetic field are governed by the freely moving conduction electrons [17]. The Drude model described here takes only these conduction electrons into account which are subject to some damping. Drude introduced his simple, yet very successful model for the free electrons in a metal in a paper which appeared already in the year 1900 [3]. In this work, Drude speaks of a (temporally varying) “electric force” \mathbf{X} which is responsible for displacing a charge carrier:

$$m_e \frac{d^2 \mathbf{r}}{dt^2} = q \mathbf{X} - m_e \gamma \frac{d\mathbf{r}}{dt}. \quad (2.1)$$

Here, m_e is the *effective mass* of the charge carrier, q is its charge ($q = -e = -1.602... \times 10^{-19}$ C for electrons), and γ describes friction or damping. The effective electron mass is used to account for some of the collective effects, such as the formation of a positive charge cloud in the vicinity of each

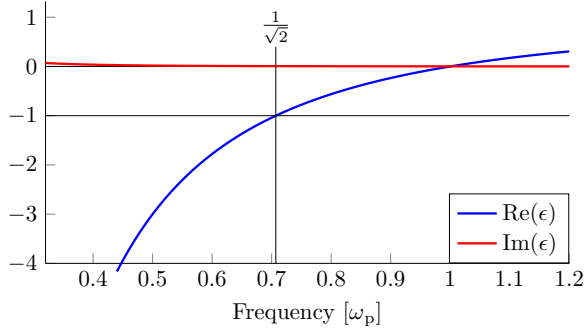


Figure 2.1: Real and imaginary part of the permittivity for a Drude metal. At $\omega = \omega_p/\sqrt{2}$ the real part of the permittivity surpasses the value of -1 (black lines), above this frequency no surface plasmons exist according to Eqs. (1.15) and (1.16).

electron. Employing such an effective mass, the electrons can be treated as free quasi-particles of mass m_e according to Eq. (2.1) with good accuracy [38].

Since in the Drude model free particles are considered, there is no restoring force. It is however interesting to note that in the original publication [3] Drude did in fact already consider the possibility of a restoring term proportional to the displacement \mathbf{r} . Such a term is used to describe interband transitions, i.e., the excitation of electrons from lower-lying bands into the conduction band within Drude-Lorentz theory [17].

From the Drude equation of motion, Eq. (2.1), one can derive a dielectric function for the Drude material [17] by assuming a harmonic time-dependence (the driving force \mathbf{X} as defined above is of course the electric field \mathbf{E})

$$\mathbf{r}(t) = \tilde{\mathbf{r}}e^{-i\omega t}, \quad \mathbf{X}(t) = \mathbf{E}e^{-i\omega t}, \quad (2.2)$$

which leads to

$$(-m_e\omega^2 - im_e\omega\gamma)\tilde{\mathbf{r}} = q\mathbf{E}. \quad (2.3)$$

The linear susceptibility $\chi^{(1)}$ connects the polarization and the electric field:

$$\epsilon_0\chi^{(1)}(\omega)\mathbf{E} = \mathbf{P}. \quad (2.4)$$

It is now assumed that the origin of the polarization lies in the formation of a number of dipoles (n dipoles per unit volume), where the dipole moment $\boldsymbol{\mu}(\mathbf{r}) = q\mathbf{r}$ is given by the displacement \mathbf{r} from Eq. (2.1):

$$\mathbf{P} = n\boldsymbol{\mu}(\mathbf{r}) = nq\mathbf{r}. \quad (2.5)$$

Equating Eqs. (2.4) and (2.5) yields

$$\frac{-q^2n}{m_e\omega^2 + i\omega\gamma m_e}\mathbf{E} = nq\mathbf{r}, \quad (2.6)$$

from which the susceptibility and the dielectric function can be directly extracted:

$$\chi^{(1)}(\omega) = \frac{-q^2n}{m_e\epsilon_0(\omega^2 + i\omega\gamma)} \quad (2.7)$$

$$\Rightarrow \epsilon_t(\omega) = 1 + \chi^{(1)}(\omega) = 1 + \frac{-q^2n}{m_e\epsilon_0(\omega^2 + i\omega\gamma)} = 1 - \frac{\omega_p^2}{\omega(\omega + i\gamma)}, \quad (2.8)$$

Where the index t stands for “transverse”, since ordinary transverse electromagnetic waves are governed by this dielectric function. Furthermore, the plasma frequency ω_p was defined as

$$\omega_p = \sqrt{\frac{q^2 n}{m_e \epsilon_0}}. \quad (2.9)$$

A typical Drude permittivity is depicted in Fig. 2.1. Note that for a typical metal $\gamma \ll \omega$ for optical frequencies, so that the limit of the so-called plasma-model without damping

$$\epsilon_t(\omega) = 1 - \frac{\omega_p^2}{\omega(\omega + i\gamma)} \xrightarrow{\gamma \ll \omega} 1 - \frac{\omega_p^2}{\omega^2} \quad (2.10)$$

can sometimes be useful.

Given such a dielectric function for a plasma model, one can now take a look at the conditions for surface plasmons which are given by Eqs. (1.15) and (1.16). If the second material is assumed to be air ($\epsilon = 1$), surface plasmons can only exist in the region where $\epsilon_t(\omega) < -1$, which is the case for

$$\omega < \omega_p / \sqrt{2} =: \omega_{sp}, \quad (2.11)$$

where I have defined the *surface plasmon frequency* $\omega_{sp} = \omega_p / \sqrt{2}$. Above this frequency, no surface modes can exist within the plasma model.

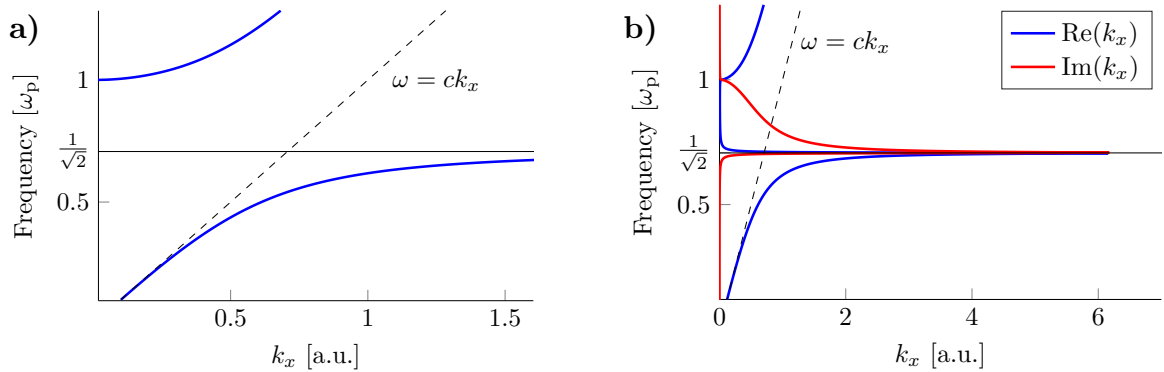


Figure 2.2: **a)** Dispersion relation for a plasma model (without damping), yielding only real values for k_x , **b)** Dispersion relation for a Drude model, curves shown for $\text{Re}(k_x)$ and $\text{Im}(k_x)$. The light line $\omega = ck_x$ is indicated by a dashed black line and the surface plasmon frequency $\omega_{sp} = \omega_p / \sqrt{2}$ by a solid black line.

In Fig. 2.2, the dispersion relation defined by Eq. (1.13) is plotted for a plasma model and for a Drude model. For the plasma model, Fig. 2.2 **a)**, there is a lower branch which initially follows the light line $\omega = ck_x$ and then approaches the surface plasmon frequency ω_{sp} . Above the plasma frequency another branch opens up, but this time Eqs. (1.15) and (1.16) are violated, k_z becomes real and radiation into the metal occurs [4, 17]. When damping is not neglected (Fig. 2.2 **b)**), there is a small imaginary contribution to k_x for both branches so that the surface modes are also slightly damped. As k_x is increased and ω approaches ω_{sp} , the imaginary part starts to grow rapidly, i.e. the losses grow very big.

By the same token, the curve for the real part of k_x bends back and finally connects to the upper branch. The modes between ω_{sp} and ω_p feature very high losses and their energy is strongly localized inside the metal [17].

Localized surface plasmons for several geometries will be discussed analytically and numerically in Chaps. 3 and 5.

2.2 The Hydrodynamic Drude Model

The hydrodynamic Drude model, just like the Drude model, describes only the free valence electrons of a metal. However, within the Drude model, all electrons were displaced collectively as the model did not allow for local fluctuations of the electron density. For very small particle sizes as in the case of SERS applications, such local density fluctuations can become important, as I will demonstrate in the analytical and numerical calculations in Chaps. 3 and 5. They are included in the hydrodynamic Drude model.

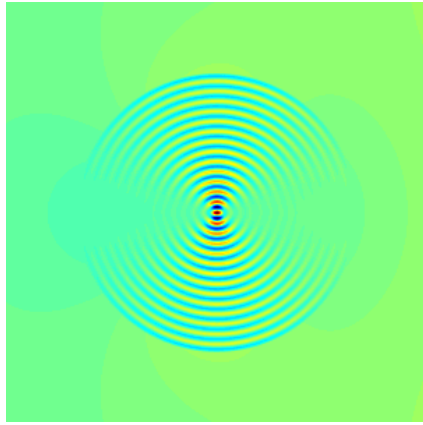


Figure 2.3: An electric field component of a bulk plasmon in a cylindrical nanowire.

i.e. sound wave-like excitations of the electron liquid, paired with a longitudinal electromagnetic field (Fig. 2.3). For vanishing \hbar (classical limit), the pressure vanishes and therefore the liquid becomes incompressible. In this case, the Drude model is recovered.

The second feature of the hydrodynamic model, besides nonlocality, is that the equations are intrinsically nonlinear. The nonlinearity is perhaps an even stronger deviation from the Drude model. Second harmonic generation from metal nanoparticles can therefore readily be discussed within this model. This is done numerically in Chap. 5.

2.2.1 The Continuity Equation and the Euler Equation

I now turn to the derivation of the hydrodynamic equations for an electron gas.

The Continuity Equation

The first equation governing such a system is the continuity equation [39]

$$\frac{\partial n}{\partial t} + \nabla \cdot (n\mathbf{v}) = 0, \quad (2.12)$$

where the particle current density can be introduced

$$\mathbf{j}_n = n\mathbf{v}. \quad (2.13)$$

Eq. (2.12) describes the conservation of the number of particles. Not only the number of particles is conserved, but also the charge and the mass contained in the system. Since I am going to consider electrodynamic effects (acting on the charge of the particles) along with thermodynamic or mechanical effects (pressure, damping, ...) it is important to keep track of all the masses and charges in the equations.

I therefore introduce the charge density ρ_c and the mass density ρ_m , via

$$n = \rho_c/q = \rho_m/m, \quad (2.14)$$

which, along with their current densities \mathbf{j}_c and \mathbf{j}_m fulfill their own continuity equations.

The Euler Equation

The second fundamental equation governing the motion of a fluid is the Euler equation. The derivation starts by stating that the total force acting on a volume containing a liquid is equal to the surface integral of this volume over the pressure, which can be written as a volume integral by means of Gauss's Theorem [39]:

$$-\oint_S p \, d\mathbf{S} = -\int_V \nabla p \, dV. \quad (2.15)$$

Here, S is the surface of the Volume V and \mathbf{S} its normal unit vector, pointing outward. The force per volume, according to Newton's Second Law is then

$$\rho_m \frac{d\mathbf{v}}{dt} = -\nabla p. \quad (2.16)$$

The delicate part of Eq. (2.16) is the total derivative $\frac{d\mathbf{v}}{dt}$ (see also Reference [40] for another insightful introduction to fluid dynamics). It is important to note that the derivative represents the change in velocity of a particle within the liquid, whereas here one needs to consider quantities which belong to a fixed point in space. These two different perspectives are known as *Lagrangian frame* (moving observer) and *Eulerian frame* (fixed observer). The total derivative can be written as

$$\begin{aligned} \frac{d\mathbf{v}}{dt} &= \frac{\partial \mathbf{v}}{\partial t} + \frac{dx}{dt} \frac{\partial \mathbf{v}}{\partial x} + \frac{dy}{dt} \frac{\partial \mathbf{v}}{\partial y} + \frac{dz}{dt} \frac{\partial \mathbf{v}}{\partial z} \\ &= \frac{\partial \mathbf{v}}{\partial t} + \left(\frac{d\mathbf{r}}{dt} \cdot \nabla \right) \mathbf{v} = \frac{\partial \mathbf{v}}{\partial t} + (\mathbf{v} \cdot \nabla) \mathbf{v}, \end{aligned} \quad (2.17)$$

where the first addend on the very right of Eq. (2.17) represents the change in velocity of a particle at a fixed position during the time dt , whereas the second addend accounts for the change of velocity at two

2 Material Models

distant points with distance dr at the very same time. I will demonstrate in Sec. 2.2.3, that this term is nonlinear (of leading order v^2) and therefore plays no role in the widely used linearized hydrodynamic model [41–43]. The hydrodynamic equations are also nonlocal equations. On a linear level, this is solely due to the pressure-gradient term which gives rise to a nonlocal dielectric function of the form $\epsilon(\mathbf{r}, \mathbf{r}', \omega)$, as I will demonstrate in Sec. 2.2.4. In Sec. 5.1.3 I will investigate the intensity-dependence of second-order quantities numerically and show that further contributions to nonlocality which are not due to the pressure term can usually be neglected. From Eqs. (2.16) and (2.17), one finds the Euler equation

$$\frac{\partial \mathbf{v}}{\partial t} + (\mathbf{v} \cdot \nabla) \mathbf{v} = -\frac{\nabla p}{\rho_m}. \quad (2.18)$$

Any additional force acting on the liquid can be added to the right hand side of Eq. (2.18):

$$\rho_m \left(\frac{\partial \mathbf{v}}{\partial t} + (\mathbf{v} \cdot \nabla) \mathbf{v} \right) = -\nabla p + \mathbf{F}. \quad (2.19)$$

The electron-liquid which I intend to describe is subject to external forces. One additional force that is needed is a damping term, which is described by a term proportional to the velocity. The damping frequency γ is introduced phenomenologically.

To describe the interaction of the liquid with an impinging electromagnetic field, a second additional force is needed, namely the Lorentz-force. The Lorentz-force term provides the coupling between the Hydrodynamic equations and Maxwell's equations (as does the current-density term in Maxwell's equations). So, finally, for the problem under discussion, one finds (assuming non-magnetic materials, $\mu_r = 1$, throughout)

$$\rho_m \left(\frac{\partial \mathbf{v}}{\partial t} + (\mathbf{v} \cdot \nabla) \mathbf{v} \right) = -\nabla p - \gamma \rho_m \mathbf{v} + \rho_c (\mathbf{E} + \mu_0 \mathbf{v} \times \mathbf{H}). \quad (2.20)$$

In order to address such problems, for example within the numerical framework, the discontinuous Galerkin time domain method, Maxwell's equations have to be solved along with the hydrodynamic equations in a self-consistent fashion. The details of this numerical scheme will be discussed in Chap. 4.

2.2.2 Thomas Fermi Theory

The model which I am going to use is based on Thomas Fermi theory. Within this model, the pressure gradient in Eq. (2.20) accounts for repulsion between the electrons. It is a macroscopic manifestation of the Pauli exclusion principle and plays a central role in the my investigations. Thomas Fermi theory is frequently used (although sometimes not explicitly stated) in the literature when calculating nonlocal characteristics of nanoparticles [41–46]. The derivation of the pressure term and its justification can be found in many textbooks on electron gas or electron liquid theory [47, 48]. The arguments are the same ones that were used by Sommerfeld and Bloch when they developed their theories to describe electrons in metals or atoms [49, 50]. However, care has to be taken since the name Thomas Fermi Theory turns out to be ambiguous when going to a linear theory as I will demonstrate in this section.

In a first approximation, it is assumed that the pressure originates from the kinetic energy of the electron gas. One can then determine p as the pressure of a Fermi gas. As a second approximation, zero

temperature is assumed. These approximations are the same ones that were made by Llewellyn Thomas and Enrico Fermi when they (independently) developed a theory to calculate the electric field in an atom in the 1920s [51, 52] – hence the name Thomas Fermi Theory. Their approximation aimed at finding a self-consistent potential which would be valid for each of the electrons independently, thus reducing the many-body problem to a single-particle problem. This is done by integrating over the coordinates of all electrons except for the one under consideration. The remaining electron then experiences the average field of all other electrons and the nucleus (or nuclei in the case of a solid). Their theory has proven quite accurate in the regime of Bohr’s Correspondence Principle, the regime of large quantum numbers, where quantum mechanical results approach those of classical mechanics [53].

I will now turn to the derivation of the pressure gradient from Eq. (2.20). The starting point is to treat the electrons as a gas which is (at least locally) uniform. In a uniform gas, there are N electrons in a given Volume V with mean density $n = \frac{N}{V}$. At zero temperature, the electrons will occupy all states in momentum space, up to the Fermi momentum p_f . This is multiplied by the volume occupied in real space to arrive at the volume of phase space which is occupied

$$V_p = \frac{4}{3}\pi p_f^3 V, \quad (2.21)$$

which corresponds to a sphere. Because of the Pauli exclusion principle, two electrons can occupy a volume of h^3 , hence

$$n = \frac{N}{V} = \frac{2}{h^3} \frac{4\pi}{3} p_f^3. \quad (2.22)$$

From this, the Fermi momentum of a free electron follows

$$p_f = \hbar \left[\frac{3}{8\pi} (2\pi)^3 \frac{N}{V} \right]^{1/3}, \quad (2.23)$$

or, correspondingly

$$k_f = \left[3\pi^2 \frac{N}{V} \right]^{1/3}. \quad (2.24)$$

Now, one has to evaluate the total kinetic energy T for N electrons with momenta \vec{p}_i

$$T = \sum_{i=1}^N \frac{p_i^2}{2m}. \quad (2.25)$$

In order to do so, the sum is transformed into an integral over a sphere in k -space, via $\sum_k \rightarrow \frac{1}{V_k} \int d^3k = \frac{V}{(2\pi)^3} \int 4\pi k^2 dk$, where one makes use of the fact that the phase space volume is spherical. In addition the sum over the two possible spins states is carried out for every value k . One then arrives at the

2 Material Models

following expression for the kinetic energy T :

$$\begin{aligned}
 T &= \sum_{|\mathbf{k}| \leq k_f, \sigma} \frac{\hbar^2 k^2}{2m_e} = 2 \cdot 4\pi \frac{V}{(2\pi)^3} \frac{\hbar^2}{2m_e} \int_0^{k_f} k^4 dk \\
 &= \frac{1}{5} \frac{V \hbar^2}{2\pi^2 m_e} \left[3\pi^2 \frac{N}{V} \right]^{5/3} \\
 &= \frac{3}{10} \frac{\hbar^2}{m_e} (3\pi^2)^{2/3} \frac{N^{5/3}}{V^{2/3}}.
 \end{aligned} \tag{2.26}$$

The pressure can now be calculated in the usual manner, by differentiating the energy with respect to the volume, keeping the particle number constant. The resulting expression for the Thomas-Fermi pressure corresponds to what was found by Bloch in his 1933-paper [50]. I will label it accordingly to distinguish it from the slightly different expression discussed in the next section which also comes out of Thomas-Fermi theory [44]. The pressure reads

$$p_{\text{Bloch}} = - \left(\frac{\partial T}{\partial V} \right)_N = \frac{1}{5} \frac{\hbar^2}{m_e} (3\pi^2)^{2/3} \left(\frac{N}{V} \right)^{5/3} =: \kappa n^{5/3}, \tag{2.27}$$

and the corresponding force density is then

$$\mathbf{F}_{\text{Bloch}} = -\nabla p_{\text{Bloch}}. \tag{2.28}$$

The last ingredient before one can start to make any calculations are the boundary conditions. Along with the usual boundary conditions of electromagnetism which are applied to the electromagnetic fields, one demands that the fluid does not leave the particle. Therefore tunneling and also spill-out is neglected. This is accomplished by imposing so-called *slip boundary conditions*, where the component of the velocity normal to the particle surface vanishes on the surface (as opposed to *no-slip* condition, where all components of the velocity vanish on the surface). As an initial condition, an initially flat distribution of charge within the particle is used which drops infinitely fast to zero at the boundary (cf. Fig. 2.4).

Having followed the above path to arrive at an expression for the Euler equation 2.19 and the Thomas Fermi pressure 2.27, I will now present a second approach to the problem. It provides further insight and also relates what is being done in this thesis to *density functional theory*.

Density Functional Theory, the Jellium Model and Thomas-Fermi Theory

It was shown by Hohenberg and Kohn [54] that any property of a system of interacting particles can be expressed in terms of a functional of the ground state density. Therefore, instead of a pressure gradient as in Eq. (2.20) one often finds a force term for the electronic repulsion that is written as functional derivative $\frac{\delta G[n]}{\delta n}$. The functional G can in principle contain correlation, exchange energy and kinetic energy of the electrons [41, 55]. The findings of Hohenberg and Kohn opened up an area of research called density functional theory. In this very active field, physicists have taken on the challenge of finding the correct functionals which properly describe the exchange correlation of the electrons. This is especially difficult to do since there is no set path to follow in order to arrive at such a functional.

If one wishes to arrive at the Euler Equation, along with an expression for Thomas Fermi pressure, one can write down the energy of the system in the form of a Bloch hydrodynamic Hamiltonian [45, 50, 56, 57]. It consists of the internal energy of the electron gas, written in terms of $G[n]$, the coupling to the electromagnetic field by means of the potentials ϕ and \mathbf{A} by means of minimal coupling and a potential V_b coming from the interaction with the background (background-background interaction is neglected):

$$H = G[n(\mathbf{r})] + \int \frac{(\mathbf{p}(\mathbf{r}) - e\mathbf{A}(\mathbf{r}))^2}{2m_e} n(\mathbf{r}) d\mathbf{r} + e \int \phi(\mathbf{r}) n(\mathbf{r}) d\mathbf{r} + e \int V_b(\mathbf{r}) n(\mathbf{r}) d\mathbf{r}, \quad (2.29)$$

where

$$\phi(\mathbf{r}) = \frac{e}{2} \int \frac{n(\mathbf{r}')}{|\mathbf{r} - \mathbf{r}'|} d\mathbf{r}', \quad V_b(\mathbf{r}) = -e \int \frac{n_b(\mathbf{r}')}{|\mathbf{r} - \mathbf{r}'|} d\mathbf{r}'. \quad (2.30)$$

Here, I have set $4\pi\epsilon_0 = 1$ and en_b is the charge density of the background. The last two terms in Eq. (2.29) can be identified with the *Hartree Potential* (without background-background interaction) [58], which describes Coulomb repulsion between the electrons and interaction of the electrons with the background¹.

Instead of solving Schrödinger's Equation at this point, one now makes a further approximation, known as *free electron gas* or *jellium model*. In this model, the nuclei are smeared out over the volume of the particle, yielding a translationally invariant system. Consequently, the distribution of the electrons also becomes smeared out [58], which makes it possible to treat them hydrodynamically as a continuum, just as it was done in the beginning of this section. Also in the same spirit as earlier, exchange and correlation terms are not included. This approximation is well-suited if the valence electrons are very weakly bound as is the case in alkali metals [59, 60]. For other metals, such as silver or gold, it represents the first extension of the simple Drude model in the regime where interband transitions play no role, incorporating nonlocal and nonlinear effects, and it leads to a number of new features which I will discuss in this thesis.

The smearing of the background results in a uniform charge distribution, replacing the electron-background-interaction term in the Hartree Potential by just a constant. The inner structure of the metal is thus removed and does not have an influence on the electrons as they move through the material. Naturally, the whole system of electrons and background has to be charge neutral. When thinking of a material that is not infinitely extended, electron-background interaction is also responsible for the electrons not leaving the nanoparticle. So the remaining effect of the electron-background potential term has to be put into the model via the boundary conditions.

The equations of motion can now be obtained by evaluating the *hydrodynamic Poisson brackets*

$$\begin{aligned} \frac{\partial \mathbf{p}}{\partial t} &= \{\mathbf{p}, H\}_{\text{HD}} \\ \frac{\partial n}{\partial t} &= \{n, H\}_{\text{HD}} \end{aligned} \quad (2.31)$$

¹Hartree's idea was to use this Hamiltonian in order to iteratively find a self-consistent solution to the one-electron Schrödinger equation. For an even more advanced theory, the single-electron wavefunctions which are solutions to this Schrödinger equation could then be combined to an N-particle wavefunction, using a Slater determinant (Hartree-Fock method) [58].

2 Material Models

where

$$\{A, B\}_{\text{HD}} = - \int \left\{ \left[\frac{\delta A}{\delta n} \nabla \cdot \frac{\delta B}{\delta \mathbf{p}} \right] + \left[\frac{\delta A}{\delta \mathbf{p}} \cdot \nabla \frac{\delta B}{\delta n} \right] + \left[\frac{\nabla \times \mathbf{p}}{n} \cdot \left(\frac{\delta B}{\delta \mathbf{p}} \times \frac{\delta A}{\delta \mathbf{p}} \right) \right] \right\} d\mathbf{r}. \quad (2.32)$$

This special formulation of Poisson brackets accounts for the transformation to Eulerian frame [57, 61–63]. Plugging the Hamiltonian 2.29 into the equations of motion yields

$$\frac{\partial n}{\partial t} = -\nabla \cdot (n\mathbf{v}) \quad (2.33)$$

$$\rho_m \left(\frac{\partial \mathbf{v}}{\partial t} + (\mathbf{v} \cdot \nabla) \mathbf{v} \right) = -n \nabla \frac{\delta G}{\delta n} + \rho_e (\mathbf{E} + \mu_0 \mathbf{v} \times \mathbf{H}) \quad (2.34)$$

with $\mathbf{E} = -\nabla \phi - \frac{\partial \mathbf{A}}{\partial t}$ and $\mu_0 \mathbf{H} = \nabla \times \mathbf{A}$ which is similar to Eq. (2.20), but with ∇p replaced by $n \nabla \frac{\delta G}{\delta n}$ (and without the damping term which is phenomenological). From Eq. (2.34) one finds that by including the Lorentz force in Equation 2.20, the electron-electron interaction term in the Hartree potential is automatically accounted for.

I would now like to turn to the pressure term in Eq. (2.34), which contains the functional $G[n]$, following Ref. [48]. Using Thomas-Fermi theory one can find a specific form of $G[n]$, which contains only the kinetic energy. This functional expresses the kinetic energy density in terms of the electron density $n(\mathbf{r})$. Above, I argued that the momentum space occupied is $\frac{4}{3}\pi p_f^3$. From this, the probability $I_{\mathbf{r}}(p)dp$ of finding an electron at position \mathbf{r} with a momentum between p and $p+dp$ (at zero temperature) can be derived. It is zero outside the Fermi-sphere and inside the Fermi-sphere it is found to be

$$I_{\mathbf{r}}(p)dp = \frac{4\pi p^2 dp}{\frac{4}{3}\pi p_f^3(\mathbf{r})}, \quad p \leq p_f(\mathbf{r}) \quad (2.35)$$

The kinetic energy density t is then

$$t = \int_0^{p_f(\mathbf{r})} n(\mathbf{r}) \frac{p^2}{2m_e} \frac{3p^2}{p_f^3(\mathbf{r})} dp = \frac{3\hbar^2}{10m_e} (3\pi^2)^{2/3} [n(\mathbf{r})]^{5/3} =: c_k [n(\mathbf{r})]^{5/3}. \quad (2.36)$$

The total kinetic energy yields

$$T[n] = c_k \int [n(\mathbf{r})]^{5/3} d\mathbf{r} \quad (2.37)$$

where the integration is performed over the the charge cloud which makes up the medium. Evaluating $\frac{\delta T[n]}{\delta n}$ results in

$$T[n + \delta n] - T[n] = \frac{5}{3} c_k \int n^{2/3}(\mathbf{r}) \delta n(\mathbf{r}) d\mathbf{r} + \dots \quad (2.38)$$

$$\Rightarrow \frac{\delta T[n]}{\delta n} = \frac{5}{3} c_k n^{2/3}. \quad (2.39)$$

Therefore, besides the Bloch-Theory above, there is now a second expression for a force coming out of Thomas Fermi theory, which I shall label DFT for density functional theory:

$$\mathbf{F}_{\text{DFT}} = -n\nabla \frac{5}{3} c_k n^{2/3}. \quad (2.40)$$

Taking a close look at the derivation which I have just outlined, one notices that the Hamiltonian 2.29 actually contains two kinetic terms. There is the minimal coupling term $\frac{(\mathbf{p}(\mathbf{r}) - e\mathbf{A}(\mathbf{r}))^2}{2m_e}$ and there is the kinetic energy density which also contains an integral over $\frac{p^2}{2m_e}$. The presence of these two different terms can be explained by the fact that the minimal coupling term is a (in some sense) macroscopic hydrodynamic term: it describes the physical behavior of the electron liquid when interacting with the electromagnetic field. The term contained in the functional G is however microscopic in the sense that it describes the behavior of a single particle making up the fluid. Once the integral over momentum space is carried out, one loses track of all these microscopic particles and arrives at an effective expression which characterizes the liquid under consideration, but does not describe single particle dynamics like the other term does.

I have now derived two different expressions for the force associated with the kinetic pressure. Both are called Thomas-Fermi in the literature. As I will show below, they agree up to 1st order perturbation theory which is why usually no distinction is made between them. Throughout this thesis, I use the Bloch-Expression. In Sec. 2.2.3 I comment on the differences between these two expressions when going to higher orders, by expanding the pressure terms in terms of the density n .

2.2.3 Perturbative Treatment of the Hydrodynamic Model

The full hydrodynamic model features nonlocal and nonlinear effects, both of which are contained in the model as it is. No further assumptions are necessary to study the nonlocal and nonlinear characteristics of this model. Specifically, having assumed a jellium model, one specific expression for the pressure, and the slip boundary conditions, both the bulk and the surface are accounted for and, in principle, higher harmonic generation can be calculated to an arbitrarily high order.

In order to study higher harmonic generation within this model, a time-domain simulation has to be performed. In Chap. 5 I will present such calculations. For very narrow-band incident pulses, the incoming signal is sufficiently small at twice the incoming frequency so that a second harmonic signal without any background can be observed. Clearly, this can only be done in such time-domain simulations (employing for instance the discontinuous Galerkin method or a finite difference time domain method). Due to the demanding nature of this problem, such computational schemes are only now emerging [M2, M3, 64–66].

Calculations employing the linearized hydrodynamic model, however, have been done for a very long time. Using the linearized model, numerical simulations become much more feasible and the model can also be evaluated in the frequency domain.

The linearized model reproduces all the linear features observed in the case of the full hydrodynamic model. Higher harmonic generation is of course not contained. In the calculations that I performed in the making of this thesis, I found no shifting, broadening or change in height of the peaks in broadband calculations which could be attributed to nonlinear terms, i.e., for a broad pulse, no intensity dependent changes between the linearized and the nonlinear model could be detected in the calculations. As I show in Sec. 5.1.3, the intensity dependence of the nonlinear terms is also restricted to the obvious

2 Material Models

scaling of the cross sections, while any additional intensity dependent shifts are negligible (or at least too small to be studied by means of the DGTD method). Thus, the full nonlinear hydrodynamic model and the linearized hydrodynamic model can be considered to deliver equivalent results for broad band calculations.

Given the importance of the linearized hydrodynamic model, I would like to discuss a perturbative expansion of the hydrodynamic equations at this point. Going beyond the linear order will reveal some further insight regarding the origin of the higher harmonic generation and shall serve as an important foundation for subsequent discussions. A perturbative treatment of the hydrodynamic equations to higher orders is also discussed in Refs. [M3, 41, 67].

Recalling the hydrodynamic equations which need to be solved,

$$\frac{\partial n}{\partial t} + \nabla(n\mathbf{v}) = 0 \quad (2.41)$$

$$\rho_m \left(\frac{\partial \mathbf{v}}{\partial t} + (\mathbf{v} \cdot \nabla) \mathbf{v} \right) = -\gamma \rho_m \mathbf{v} - \nabla p + \rho_c (\mathbf{E} + \mu_0 \mathbf{v} \times \mathbf{H}), \quad (2.42)$$

there are two possible choices for the pressure gradient. It is either given by Bloch's theory (cf. Eq. (2.27))

$$-\nabla p = \mathbf{F}_{\text{Bloch}} = -\kappa \nabla n^{5/3}, \quad (2.43)$$

or by density functional theory (cf. Eq. (2.40))

$$-\nabla p = \mathbf{F}_{\text{DFT}} = -\frac{5}{3} c_k n \nabla n^{2/3} = -\frac{5}{2} \kappa n \nabla n^{2/3}. \quad (2.44)$$

The fields constituting the hydrodynamic equations are expanded in the following manner:

$$\mathbf{E} = \mathbf{E}_0 + \mathbf{E}_1 + \dots \quad (2.45)$$

$$\mathbf{H} = \mathbf{H}_1 + \mathbf{H}_2 + \dots \quad (2.46)$$

$$n = n_0 + n_1 + \dots \quad (2.47)$$

$$\mathbf{v} = \mathbf{v}_1 + \mathbf{v}_2 + \dots \quad (2.48)$$

hence

$$j_m = m_e n \mathbf{v} = m_e n_0 \mathbf{v}_1 + m_e (n_0 \mathbf{v}_2 + n_1 \mathbf{v}_1) + \dots \quad (2.49)$$

Note that the expansion as it is written down here is not based on the smallness of a physical parameter, but simply splits the quantities in components that scale linearly, quadratically and so forth with the amplitude of the incoming electric field [67]. The assumption that

$$n_0 \gg \sum_{i=1}^{\infty} n_i \quad (2.50)$$

with

$$n_0 \gg n_1 \gg n_2 \quad (2.51)$$

is only conditionally fulfilled if the incoming field amplitude E_0 is small enough that only small departures from equilibrium are effected. An estimate for the relative magnitudes of the linear and the second order susceptibility shows that the assumption is reasonable if the nonlinearity is of electronic origin [35, 68]: The linear polarization and the second order polarization are expected to be of the same order of magnitude if the exciting field is of the order

$$E_{at} = \frac{e}{4\pi\epsilon_0 a_0^2} = 5.14 \cdot 10^{11} \text{ V/m}, \quad (2.52)$$

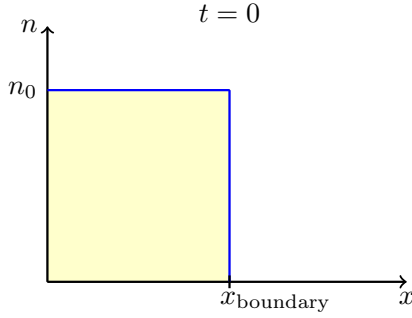


Figure 2.4: Initial density n at time $t = 0$. The density is set to n_0 inside the particle and drops sharply to zero at the boundary $x = x_{\text{boundary}}$, therefore the gradient ∇n_0 is zero everywhere as the measure of the infinitely sharp drop at the boundary is zero.

where a_0 is the Bohr radius of the hydrogen atom [35]. The mechanism described here which describes dipoles which are formed in dielectrics as a result of the electromagnetic excitation is not the same as second harmonic generation due to density fluctuations as in the hydrodynamic model. Yet, I can compare the SHG intensities of my structures to the estimate provided here. The field strengths which I employ in my calculations are 10^6 V/m and they give rise to SHG signals for which $E_1 \gg E_2$. In fact, the hydrodynamic second harmonic signals are below the estimate above for most structures. Intensities comparable to the estimate above can be reached for instance by geometric tuning (see for instance the double-resonant V-groove in Sec. 5.3) In principle, a second order quantity can exceed its linear counterpart and a third order quantity its second order counterpart if the incoming field is strong enough, but the numerical scheme will eventually become unstable as the density fluctuations become so large that the density locally drops to zero which causes the scheme to explode. At such high

intensities ($> 10^{11} \text{ V/m}$) the metal would most likely be destroyed in an experiment.

Turning to the expansion of the the hydrodynamic equations, according to the initial condition that the electron density is flat in the beginning of the simulation and sharply drops to zero at the particle boundary (Fig. 2.4), the gradient of the 0th order density vanishes:

$$\nabla n_0 = 0. \quad (2.53)$$

I start out with the treatment of the pressure gradients by expanding the exponentials of the density appearing in those terms in the following way

$$\begin{aligned} n^\alpha &= (n_0 + \underbrace{n_1 + n_2 + \dots}_{\ll n_0})^\alpha \\ &= n_0^\alpha (1 + \underbrace{\frac{n_1}{n_0} + \frac{n_2}{n_0} + \dots}_{\ll 1})^\alpha \\ &= n_0^\alpha + \alpha n_0^{\alpha-1} n_1 + \frac{1}{2} \alpha(\alpha-1) n_0^{\alpha-2} n_1^2 + \alpha n_0^{\alpha-1} n_2. \end{aligned} \quad (2.54)$$

2 Material Models

Then

$$\mathbf{F}_{\text{Bloch}} = \kappa \nabla n_0^{5/3} + \frac{5}{3} \kappa n_0^{2/3} \nabla n_1 + \frac{5}{9} \kappa n_0^{-1/3} \nabla n_1^2 + \frac{5}{3} \kappa n_0^{2/3} \nabla n_2 + \dots \quad (2.55)$$

and

$$\begin{aligned} \mathbf{F}_{\text{DFT}} = & (n_0 + n_1 + n_2) \frac{5}{2} \kappa n_0^{2/3} + \frac{5}{3} \kappa n_0^{2/3} \nabla n_1 + \frac{5}{3} \kappa n_0^{-1/3} n_1 \nabla n_1 - \\ & - \frac{5}{18} \kappa n_0^{-1/3} \nabla n_1^2 + \frac{5}{3} \kappa n_0^{2/3} \nabla n_2 + \dots \end{aligned} \quad (2.56)$$

As can be seen, the expressions agree only up to 1st order and as long as $\nabla n_0 = 0$. Going to higher orders, the terms containing ∇n_2 also agree, but the ones proportional to ∇n_1^2 have opposing signs and differ in magnitude by a factor of two. In addition, in the DFT-case, an additional term appears. While the n_2 and the n_1^2 terms both scale quadratically with the incoming field, it is not clear that they are in fact of the same order of magnitude. An investigation of these terms could certainly be interesting. In this thesis I do not perform this comparison and always use the Bloch-formulation (2.43) when performing nonlinear simulations.

The continuity equation and the Euler equation are given to 0th order by

$$\partial_t n_0 = 0, \quad (2.57)$$

$$e n_0 \mathbf{E}_0 = 0, \quad (2.58)$$

so the electric fields of 0th order also have to vanish. The 1st order equations yield (n_0 is assumed to be constant)

$$\partial_t n_1 = -\nabla \cdot (n_0 \mathbf{v}_1), \quad (2.59)$$

$$m_e n_0 \partial_t \mathbf{v}_1 = -m_e \gamma n_0 \mathbf{v}_1 - \frac{5}{3} \kappa n_0^{2/3} \nabla n_1 - e n_0 \mathbf{E}_1. \quad (2.60)$$

For the second order, one finds

$$\partial_t n_2 = -\nabla \cdot (n_1 \mathbf{v}_1 + n_0 \mathbf{v}_2) \quad (2.61)$$

and

$$\begin{aligned} m_e (n_0 \partial_t \mathbf{v}_2) + m_0 n_1 \partial_t \mathbf{v}_1 + m_e n_0 (\mathbf{v}_1 \cdot \nabla) \mathbf{v}_1 = & \\ & - m_e \gamma (n_1 \mathbf{v}_1 + n_0 \mathbf{v}_2) \\ & - \frac{5}{9} \kappa n_0^{-1/3} \nabla n_1^2 - \frac{5}{3} \kappa n_0^{2/3} \nabla n_2 \\ & - e (n_1 \mathbf{E}_1 + n_0 \mathbf{E}_2) \\ & - e n_0 \mathbf{v}_1 \times \mathbf{H}_1. \end{aligned} \quad (2.62)$$

2.2.4 The Linear Susceptibility, Bulk Plasmons and the Parameter β

I will turn to some of the properties of the linearized hydrodynamic model now. Applying the divergence operator to Eq. (2.60) and making use of Eq. (2.59), one arrives at the following equation which turns out to be very insightful (cf. Ref. [18]):

$$\begin{aligned} \nabla^2 n_1 - \frac{3m_e}{5\kappa n_0^{\frac{2}{3}}} \partial_t^2 n_1 &= -\frac{3en_0}{5\kappa m_e n_0^{\frac{2}{3}}} \nabla \cdot \mathbf{E}_1 + \frac{3\gamma m_e}{5\kappa n_0^{\frac{2}{3}}} \partial_t n_1 \\ \Rightarrow \nabla^2 n_1 - \frac{1}{\beta^2} \partial_t^2 n_1 &= -\frac{en_0}{\beta^2 m_e} \nabla \cdot \mathbf{E}_1 + \frac{\gamma}{\beta^2} \partial_t n_1, \end{aligned} \quad (2.63)$$

where, from Maxwell's equations,

$$\nabla \cdot \mathbf{E}_1 = -\frac{e}{\epsilon_0} n_1. \quad (2.64)$$

A wave equation for the density as in Eq. (2.63) describes sound waves. They are in this case driven by the divergence of the electric field on the right hand side of the equation, which is in turn given by fluctuations of the density (Eq. (2.64)), so a coupling is found between a sound wave and the electric field. Note that no magnetic field is associated with this excitation. It follows from Eqs. (2.59) and (2.64) – assuming a harmonic k -dependence and applying the divergence operators – that both the electric field and the current are longitudinal in nature. Electric field and current are effected by the electron density modulation n_1 and its time-derivative, respectively. The hybrid excitation of a sound wave and an electric field is also a plasmon polariton, but it occurs in the bulk, as opposed to the transverse surface plasmon polaritons discussed above. The parameter β introduced above can be identified with the speed of sound. It can be directly extracted from Eq. (2.63) and it is given by

$$\beta = \sqrt{\frac{5}{3} \frac{\kappa}{m_e} n_0^{\frac{2}{3}}}. \quad (2.65)$$

This parameter is of great importance when it comes to discussing the nonlocal characteristics of this model, since it determines the strength of the nonlocality or spatial dispersion and, while it is fixed to this particular value for Thomas-Fermi Theory, there are other choices of β which I will discuss in Sec. 2.2.6. It is important to note that β is related to the Fermi velocity v_f :

$$\beta^2 = \frac{5}{3} \frac{\kappa}{m_e} n_0^{\frac{2}{3}} \quad (2.66)$$

$$= \frac{1}{3} \left[\underbrace{\hbar \left(\frac{\omega_p^2 \epsilon_0 3\pi^2}{e^2 m_e^2} \right)^{\frac{1}{3}}}_{v_f} \right]^2. \quad (2.67)$$

The dispersion relation can easily be determined from Eqs. (2.63) and (2.64) (cf. Ref. [18]). Assuming harmonic solution with spatial and temporal dependence $e^{i(\mathbf{k} \cdot \mathbf{r} - \omega t)}$ and inserting the plasma frequency $\omega_p^2 = \frac{e^2 n_0}{m_e \epsilon_0}$ a Fourier transform then leads to the desired expression:

$$\beta^2 \nabla^2 n_1 - \partial_t^2 n_1 = -\omega_p^2 n_0 \nabla \cdot \mathbf{E}_1 + \gamma \partial_t n_1 \quad (2.68)$$

$$\Rightarrow \omega^2 = \omega_p^2 + \beta^2 k^2 - i\gamma\omega. \quad (2.69)$$

2 Material Models

There are two important limiting cases for Eq. (2.69). When damping is negligible so that $\gamma \rightarrow 0$ one finds ($\beta^2 k^2 \ll \omega_p^2$)

$$\omega \approx \omega_p + \frac{1}{2} \frac{\beta^2}{\omega_p} k^2. \quad (2.70)$$

This expression is equal to the condition $\epsilon(\mathbf{k}, \omega) = 0$ and I will show in the following why this condition is physically meaningful. For a local material with vanishing k or $\beta = 0$, including damping, one arrives at

$$\omega = (\omega_p^2 - \gamma^2/4)^{1/2} - i\frac{\gamma}{2} \stackrel{\gamma^2 \ll \omega_p^2}{\approx} \omega_p - i\frac{\gamma}{2}, \quad (2.71)$$

where only positive frequencies are taken into account.

A few more comments are in order regarding the speed of sound β . Within the Thomas Fermi model there is no ambiguity that parameter β has to take on the value $v_f/\sqrt{3}$. It depends on the initial density n_0 , on the plasma frequency ω_p and on the effective electron mass m_e . Therefore, three of these parameters need to be fixed (besides the damping γ which is independent) and the fourth one will be given via the relationships above. In the full hydrodynamic model, modifying β directly would mean altering the Fermi velocity and would therefore lead to an alteration of the effective electron mass, the initial density or the plasma frequency. In a linearized model, however, there are only two free parameters, namely the plasma frequency and β . In Sec. 2.2.6 I will discuss different choices of β . Besides that, in Chap. 3.2.3, I will consider β as a free parameter which can be treated perturbatively.

Now that the description of the free electrons by means of the hydrodynamic model has been discussed in detail, the steps from Sec. 1.2 are repeated for the longitudinal excitations to arrive at a dielectric function for the (linearized) hydrodynamic model. A nice account of this is given in Ref. [69]. Above, the polarization was simply given by the dipole moments which were proportional to the displacement (Eq. (2.5)). Now, according to the hydrodynamic theory, from Eq. (2.13), the time-derivative of the polarization can be written as

$$\partial_t \mathbf{P} = \mathbf{j}_c = -e \mathbf{j}_n = -ne \partial_t \mathbf{r}, \quad (2.72)$$

and therefore, by means of the continuity equation, (2.12)

$$\partial_t(en - \nabla \cdot \mathbf{P}) = 0. \quad (2.73)$$

More generally than in Eq. (2.4), the susceptibility can now not only depend on the point \mathbf{r} where the response of the material is considered, but is influenced by interactions taking place in the vicinity of this point. It is in this sense that nonlocality is introduced into the dielectric function of the material. In terms of such a nonlocal susceptibility, the (linear) polarization for an isotropic material is written as

$$\mathbf{P}_1(\mathbf{r}) = \epsilon_0 \int_V \chi^{(1)}(\mathbf{r}, \mathbf{r}') \mathbf{E}_1(\mathbf{r}') d\mathbf{r}. \quad (2.74)$$

This is equivalent to having a k -dependent permittivity or susceptibility when transforming the equations to k -space. I will demonstrate now that within the hydrodynamic model, one arrives at such a type of nonlocal or spatially dispersive dielectric function.

To extract a dielectric function, one employs the linearized Euler equation including the Lorentz force (Eq. (2.60)) and expresses the velocities in terms of the polarization. Thus rewriting Eq. (2.60), making use of Eq. (2.73), one finds

$$\partial_t^2 \mathbf{P}_1 = -\gamma \partial_t \mathbf{P}_1 + \beta^2 \nabla (\nabla \cdot \mathbf{P}_1) + \frac{e^2 n_0}{m_e} \mathbf{E}_1, \quad (2.75)$$

and, again assuming a harmonic dependence of the type $e^{i(\mathbf{k}\mathbf{r}-\omega t)}$,

$$\omega^2 \mathbf{P}_1 = -i\omega\gamma \mathbf{P}_1 + \beta^2 k^2 \mathbf{P}_1 - \frac{e^2 n_0}{m_e} \mathbf{E}_1, \quad (2.76)$$

from which the linear susceptibility follows

$$\mathbf{P}_1 = \epsilon_0 \chi^{(1)} \mathbf{E}_1 = \epsilon_0 \left(\frac{-\omega_p^2}{\omega(\omega + i\gamma) - \beta^2 k^2} \right) \mathbf{E}_1. \quad (2.77)$$

The corresponding dielectric function reads

$$\epsilon_l(k, \omega) = 1 - \frac{\omega_p^2}{\omega(\omega + i\gamma) - \beta^2 k^2}. \quad (2.78)$$

The index l stands for longitudinal, since this dielectric function accounts for the longitudinal plasmon polaritons discussed above. Such a k -dependence is known as spatial dispersion.

Note, that in the hydrodynamic model, transverse waves are also allowed, just as they were in the case of the Drude model. Therefore, one now has to distinguish between the longitudinal dielectric function (2.78) and the transverse dielectric function, given by Eq. (2.8), depending on which waves one wishes to describe. They are however not totally independent from one-another. They are coupled in a delicate way and a new boundary condition has to be found to account for the longitudinal \mathbf{E} -fields inside the particle. It turns out that this is the continuity of the normal component of the displacement field – including the longitudinal fields [43, 70]. Melnyk and Harrison showed in Ref. [70] that the normal component of both the displacement field and the charge current are continuous across the interface, the latter condition being equivalent to the usual condition of tangential \mathbf{H} being continuous. The remaining conditions for tangential \mathbf{E} and normal \mathbf{H} , which are also equivalent, remain intact as usual. As a result of this delicate coupling of the longitudinal and the transverse waves by means of the boundary conditions, the localized surface plasmon resonances are shifted. This will become apparent as I carry out some analytical calculations in Chap. 3.

Formally, the conditions are written down in the following way: For the longitudinal waves, the relations $\nabla \times \mathbf{E} = 0$ holds. Therefore, the governing equation becomes the macroscopic Maxwell equation $\nabla \cdot \mathbf{D} = 0$, assuming no free charges. Given the new dielectric function (2.78) for the longitudinal waves, I can write [18, 67, 69]

$$\nabla \cdot \mathbf{D}(\mathbf{r}, t) = \int \frac{d\mathbf{k}}{(2\pi)^{\frac{3}{2}}} \frac{d\omega}{(2\pi)^{\frac{1}{2}}} \epsilon_l(\mathbf{k}, \omega) [i\mathbf{k} \cdot \mathbf{E}(\mathbf{k}, \omega)]. \quad (2.79)$$

Since now $\mathbf{k} \cdot \mathbf{E} \neq 0$, this results in the condition

$$\epsilon_l(\mathbf{k}, \omega) = 0, \quad (2.80)$$

which implicitly defines the dispersion relation 2.69.

If a material is nonlocal a solution to the dispersion relation (2.80) can be found for any frequency ω . For real k , there are solutions above the plasma frequency ω_p . In Chaps. 3 and 5 I will show how they manifest themselves as distinct peaks (depending on the confining geometry) in the scattering or absorption spectra and as oscillations of the density and the electric field extending far into the particle. In the local case $\beta \rightarrow 0$, only one solution exists for $\omega = \omega_p$. Again, this is the classical limit of incompressibility (sending \hbar and thus the speed of sound to zero) which means that no spatial density oscillations are possible and only oscillations in time are allowed.

2.2.5 Nonlinear Susceptibility

The perturbative approach can also be used to express the second order nonlinearity in terms of a nonlinear polarization [71–74]. In Sec. 1.4, the wave-mixing processes were described in terms of a nonlinear susceptibility, which was given by

$$P_i(\mathbf{r}, \omega_3) = \epsilon_0 \int d\mathbf{r}' \int d\mathbf{r}'' \chi_{ijk}^{(2)}(\mathbf{r}, \mathbf{r}', \mathbf{r}'', \omega_3; \omega_1, \omega_1) E_j(\mathbf{r}', \omega_1) E_k(\mathbf{r}'', \omega_1), \quad (2.81)$$

with $\omega_3 = 2\omega_1$. The second order nonlinear polarization for a hydrodynamic gas can be shown to have the form [71]

$$\mathbf{P}(\mathbf{r}, \omega_3) = \alpha_1 (\mathbf{E}(\mathbf{r}, \omega_1) \cdot \nabla) \mathbf{E}(\mathbf{r}, \omega_1) + \alpha_2 \nabla (\mathbf{E}(\mathbf{r}, \omega_1) \cdot \mathbf{E}(\mathbf{r}, \omega_1)) + \alpha_3 \mathbf{E}(\mathbf{r}, \omega_1) (\nabla \cdot \mathbf{E}(\mathbf{r}, \omega_1)), \quad (2.82)$$

where the prefactors α_1 – α_3 can be determined from the hydrodynamic equations [71–73]. Most notably, the third term is zero for transverse waves since they yield $\nabla \cdot \mathbf{E} = 0$. It only contributes if density fluctuations are present (cf. Eq. (2.63)). Below the plasma frequency, they occur primarily at the surface as I will demonstrate in Chap. 5. Therefore, this term is often considered to describe “surface contributions” to the nonlinearity, whereas the other terms describe “bulk contributions”. Note, that within this thesis, no such formulation of the nonlinearity is employed. Rather, for the numerical simulations, the full set of equations, without any further assumptions, is used. Therefore, both contributions are fully contained as longitudinal and transverse fields are included. The distinction between bulk and surface contributions makes sense if one takes an approach where the two have to be separated, but in reality one cannot exist without the other. For the nonlinear calculations performed here, I employ a finite volume method which describes both the bulk and the surface and does therefore not rely on any assumptions or approximations.

I would also like to comment that in the presence of bulk plasmons, above the plasma frequency, the second term from Eq. (2.82) starts to contribute in the bulk. This makes the SHG mechanism even more involved. Since such processes are beyond the optical regime they are not important here, but the effect of these processes becomes visible in Sec. 5.1.2.

2.2.6 The Importance of the Hydrodynamic Model: Applicability and Extensions

Extensions of the Linearized Hydrodynamic Model

The debate about the validity of the hydrodynamic model is an important one. It clearly represents the nonlocal extension of the ubiquitous Drude model, which is still the method of choice for many applications. However, at small particle sizes nonlocal properties become important. This can be explained by

the interplay between damping, i.e. the mean free path of the electrons, and the particle size [75]. Since the bulk plasmons are subject to damping, they only start to suffer geometry-dependent effects (such as a bulk-mode in a cylindrical structure) when the particle is small enough so that a bulk plasmons can actually "feel" the confinement in the particle, i.e. the plasmons don't experience too much damping when traveling from one side of the particle to the other. The bulk plasmons are experimentally observable in small structures [76] and their description is one of the most obvious and most important advantages of the hydrodynamic model over a normal Drude mode.

The issue becomes much more complicated when going to structures where the boundary becomes more important or quantum mechanical effects start to set in. An example of such structures are dimer structures with very small particle separation of less than a nanometer, where a comparison to time dependent density functional theory calculations shows qualitative but not quantitative agreement [77]. This is not surprising, since a semi-classical model is not expected to perform very well in this regime.

However, as I have shown above, there are many attempts to remedy the shortcomings of the description of the surface which lead to better agreement with quantum descriptions [45, 78].

Redirecting attention to the bulk-part of the method, it is important to discuss the value of the speed of sound β in the plasma. While the value calculated above is consistent within Thomas-Fermi theory, taking a look at the problem from a slightly different angle reveals that $\beta = v_f/\sqrt{3}$ would actually have to be considered a low-frequency limit for frequencies that are much lower than the damping γ of the system, which is clearly not the case for optical frequencies which are three orders of magnitude above the damping of a typical noble metal. The argument goes as follows [79, 80]²:

Given an adiabatic process, the pressure is proportional to n^m where m depends on the degrees of freedom f , via $m = (f + 2)/f$. For low frequencies and high damping, collisions dominate and the motion becomes very random, resulting in $f = 3$ for a three-dimensional gas. For high frequencies, the collisions, the movement is so fast and the distance traveled within one cycle become so small that collisions become negligible and the motion is predominantly given by the direction of the electric field, therefore reducing the degrees of freedom to $f = 1$. From this, one finds

$$\beta = \begin{cases} v_f/\sqrt{3}, & \omega \ll \gamma \\ v_f\sqrt{3/5}, & \omega \gg \gamma \end{cases}. \quad (2.83)$$

According to these findings, the qualitative behavior will be the same in both cases, but the Thomas Fermi limit $\omega \ll \gamma$ underestimates the nonlocal effects when applying it to optical frequencies. Most publications that are concerned with the linearized hydrodynamic model simply assume the high frequency value, whereas I choose to stick to the value obtained above, also for the linearized calculations, in order to be consistent with Thomas Fermi theory on both the linear and nonlinear level – keeping in mind that the results obtained within this thesis with respect to nonlocality might therefore be just a lower limit.

As a matter of fact, both limits have to break down when $\omega \approx \gamma$ and there exists a further generalization, based on the Boltzmann equation, which results in a complex-valued, frequency-dependent $\beta(\omega)$. The theory is discussed in detail by Halevi in Ref. [79]. The model includes the effect of collisions by means of a correction which was proposed by Mermin. On a linear level, it results in an expression for

²Note that the discussion can be found in the 2nd edition of the book by J. D. Jackson [80], but has been taken out of the third edition of the book.

2 Material Models

β which reads

$$\beta^2(\omega) = \frac{\frac{3}{5}\omega + \frac{1}{3}i\gamma}{\omega + i\gamma} v_f^2. \quad (2.84)$$

For very high or very low frequencies it tends to the two known real-valued limiting cases from Eq. (2.83). In Ref. [79] the expression (2.84) is inserted into the permittivity (2.78) and then the implicit definition of the dispersion relation (2.80) is used. The author arrives at

$$\omega(\omega + i\gamma)^2 - \omega_p^2(\omega + i\gamma) - \left(\frac{3}{5}\omega + \frac{1}{3}\gamma\right) v_f^2 k^2 = 0, \quad (2.85)$$

which can be expanded if the expression for ω for vanishing k , Eq. (2.71) is used in the last term. The dispersion relation then reads

$$\omega \approx \omega_p + \frac{3}{10} \frac{v_f^2}{\omega_p} k^2 - i\frac{\gamma}{2} + i\frac{\gamma}{2} \frac{4}{15} \frac{v_f^2}{\omega_p^2} k^2. \quad (2.86)$$

Here, the first two terms are just the dispersion relation as in Eq. (2.70) for a nonlocal model with β given by its high-frequency value. The third term is the phenomenological damping as in Eq. (2.71). However, the last term is a k -dependent damping term which was not present in the previous theories. It accounts for Landau damping which describes a loss of energy of the plasma wave to surrounding particles or quasi-particle excitations which have a velocity similar to the phase velocity of the plasma wave [81, 82]. In the present model, the Landau damping also depends on the damping γ and is therefore collision-modified.

A similar generalization of the nonlocal hydrodynamic model to complex-valued, frequency-dependent β was presented in Ref. [83].

Interband Transitions

I have not touched upon interband transitions in this chapter. The problem here is that a description of interband transitions that would be suitable to go along with the nonlocal and nonlinear hydrodynamic model which I am employing would in itself have to be nonlinear. The incorporation of interband transitions into nonlocal frameworks by means of a method presented by Liebsch [84] yields very good results [45]. Since the nonlinear aspects of the hydrodynamic Drude model, which are one of the main objectives of this work, are much more involved and such an extension will not be aimed at here. The model without interband transitions gives rise to a manifold of new phenomena on the linear and on the nonlinear level which need to be understood and are conceptually interesting so they deserve a thorough investigation.

Quantum Corrections and the Von-Weizsäcker Extension

An extension to the kinetic energy functional was suggested by von Weizsäcker. It features an additional term which contains a gradient correction to the Thomas-Fermi functional of the form [85, 86]

$$T_W[n] = \lambda \frac{1}{8} \int \frac{|\nabla n|^2}{n} d\mathbf{r}. \quad (2.87)$$

In the language of density functional theory it is the next correction to the hydrodynamic Drude model and it can account for an electron spill-out. Such corrections containing the gradient of the density can be important in regions of high density fluctuations near the surface. Effectively the hard-wall boundary condition is lifted and the density goes smoothly to zero at the particle interface [45]. This spill-out becomes important within about 1\AA of the surface [87]. It was shown by Toscano *et al.* [45] that this advanced model features Bennett-resonances that are otherwise not present in hard-wall models and leads to a correction of the (size-dependent) shifts of the dipole resonances in cylindrical metal nanowires: While the hydrodynamic Drude model with hard walls inevitably leads to a blue-shift as the radius is decreased, the model including spill-out can lead to a red-shift [45]. Toscano *et al.* found a blue-shift for a silver nanowire when decreasing the particle size (linear with the inverse radius) and a red-shift for a sodium nanowire which is in agreement with experimental observations [45]. To my knowledge, the shift of the higher order modes within this model has not yet been investigated.

In a quantum mechanical description of a gap-system, tunneling is expected, which would give rise to short-circuiting between two particles that are in close proximity. How close the particles would have to be is a matter of debate. Time-dependent density functional theory calculations suggest that the separations need to be below one nanometer [88], which is much more than the Von-Weizsäcker spill-out can account for.

A publication by Mortensen *et al.* [83] suggests that effects commonly attributed to short-circuiting in *ab-initio* calculations – most notably the suppression of the dipole plasmon resonance (which is not present in local calculations or in the hydrodynamic Drude model) – can be accounted for by introducing a complex-valued β in a similar fashion as in the aforementioned approach by Halevi [79]. In fact, Mortensen and coworkers argue that quantum mechanical tunneling (reported to occur in the picosecond range) is likely to be too slow to be mediated by optical excitations (in the femtosecond range) and AC tunneling currents have also not been confirmed experimentally. Therefore, an additional damping mechanism is a more likely explanation for the broadening.

Concluding Remarks

Publications that are concerned with (a linearized version of) the hydrodynamic model for plasmons have been and continue to be appearing in abundance. The linearized model can be treated in both time- and frequency domain and an extended Mie-theory and an electrostatic formulation exist (both of which will be discussed in Chap. 3 of this thesis). The linearized model with numerous possible extensions regarding electron density profiles, interband transitions or Landau damping continues to be of importance, as it has proven to point us in the right direction, while being computationally much more feasible than density functional theory calculations which can typically not describe plasmonic nanoparticles with a typical size of some ten nanometers. With the large number of new Ansatzes described above [M2, M3, 45, 79, 83], and ever better computing clusters, this is clearly not the end of the story and the hydrodynamic model will become more and more useful to make both qualitative and quantitative predictions.

Since nonlocality depends on the size of the particle (cf. Sec. 2.2.6) and can therefore in principle be made visible in an experiment by studying the size-dependence, nonlocality cannot simply be turned off in an experiment as it can be done in a numerical simulation. Numerical simulations therefore provide a way to look for qualitative modifications of the spectra or field distributions which arise due to the nonlocality and provide fundamental theoretical insight. The spectrum of a simple single scatterer, such

2 *Material Models*

as a sphere or a cylinder, is usually not diverse enough to exhibit such interesting features effected by nonlocality. A very interesting system whose spectra and field distributions are much more complex but can still be understood analytically, is the cylindrical dimer. The investigations of such a system in Chaps. 3 and 5 lie at the heart of this thesis.

The second feature of this model, nonlinearity opens up even more opportunities. The hydrodynamic model, being the simplest nonlinear extension of the Drude model, makes it possible to gain insight into nonlinear processes and allows for fundamental statements regarding the excitation of plasmonic modes by nonlinear processes. Such considerations are also carried out in Chap. 5.

3

CHAPTER 3

ANALYTICAL CONSIDERATIONS

In this Chapter, I present analytical scattering calculations employing the linearized hydrodynamic model or the Drude model on the level of electrostatic theory or Mie theory. The analytical solutions not only serve as reference solutions to validate the numerical methods I use later on, but also provide significant insight regarding the theory that is employed. They allow me to discuss limiting cases in a much better way than numerical calculations and, most importantly, are of help when it comes to interpreting the numerical results. In the simple case of a single cylinder, a full analytical Mie-solution including nonlocal effects is available, which is presented here. For the more complicated setup of a cylindrical dimer, a solution within local electrostatic theory is presented. All considerations are made for infinitely extended structures that can effectively be treated as two-dimensional. In the last section, I discuss the hydrodynamic equations employing group theory. This is done by determining the symmetry point group of a given geometrical setup. The action of the spatial derivatives occurring within the hydrodynamic and the Maxwell equations is determined for this point group, which can be used to link the symmetries of the modes excited by second order processes to the symmetries of the incident pulse.

3.1 The Material Parameters

In Chap. 2 I discussed the hydrodynamic material model with transverse and longitudinal dielectric functions

$$\epsilon_t(\omega) = 1 - \frac{\omega_p^2}{\omega(\omega + i\gamma)}, \quad (3.1)$$

$$\epsilon_l(\omega, k) = 1 - \frac{\omega_p^2}{\omega(\omega + i\gamma) - \beta^2 k^2}. \quad (3.2)$$

I will now introduce a set of parameters which I am going to use throughout this thesis. It is based on the parameters for silver presented in the landmark paper by Johnson and Christy [89], which provides parameters for a number of noble metals. As pointed out in Sec. 2.2.6, interband transitions are not going to be discussed in this thesis, but only a Drude material and a hydrodynamic Drude material which includes nonlinear and nonlocal effects. Therefore, I use only the Drude-contribution of the dielectric function extracted from Ref. [89] and simply dismiss the Lorentz terms accounting for interband transitions. This results in the following values

$$\omega_p = 1.39 \cdot 10^{16} \text{ s}^{-1}, \quad (3.3)$$

$$\gamma = 3.23 \cdot 10^{13} \text{ s}^{-1}, \quad (3.4)$$

$$m_e = 0.96m_0 = 8.7450 \cdot 10^{-31} \text{ kg}, \quad (3.5)$$

where $m_0 = 9.1094 \cdot 10^{-31} \text{ kg}$ is the free electron mass. As discussed in Sec. 2.2.3, the system is fully defined by these three parameters, since the equilibrium electron density and the Fermi velocity can be calculated:

$$n_0 = \epsilon_0 m_e \omega_p^2 / e^2 = 5.828 \cdot 10^{28} \text{ m}^{-3}, \quad (3.6)$$

$$v_f = \hbar \left(\frac{\omega_p^2 \epsilon_0 3\pi^2}{e^2 m_e^2} \right)^{1/3} = 1.4464 \cdot 10^6 \text{ m s}^{-1}. \quad (3.7)$$

The set of parameters obtained this way is consistent with the values found elsewhere in the literature, which were obtained from different experiments. See for instance Ashcroft and Mermin [90], where the values are given as $n_0 = 5.86 \cdot 10^{28} \text{ m}^{-3}$ and $v_f = 1.39 \cdot 10^6 \text{ m s}^{-1}$.

Note that by dismissing the Lorentz terms, silver is only well-described in the low-frequency regime. Specifically, the important transition from $\text{Re}(\epsilon) < 0$ to $\text{Re}(\epsilon) > 0$ which happens at the plasma frequency ω_p for a Drude metal is shifted to a lower frequency when interband transitions are included, i.e. the resonances are also redshifted and bulk plasmons start to appear at a lower frequency. In principle, the shifts could be accounted for by using a different “effective plasma frequency”, yet this would not correctly describe the physical situation since an alteration of the plasma frequency would result in incorrect electron density. While resonances can be shifted this way, this would happen through the wrong physical mechanisms. The shifts that should be coming from interband transitions would instead be mediated by free electrons. This being said, the model can be considered rather generic. The observations made in this thesis are of relevance for any noble metal in a long wavelength limit and for alkali metals. The features discussed persist regardless of the actual values for all the materials that are

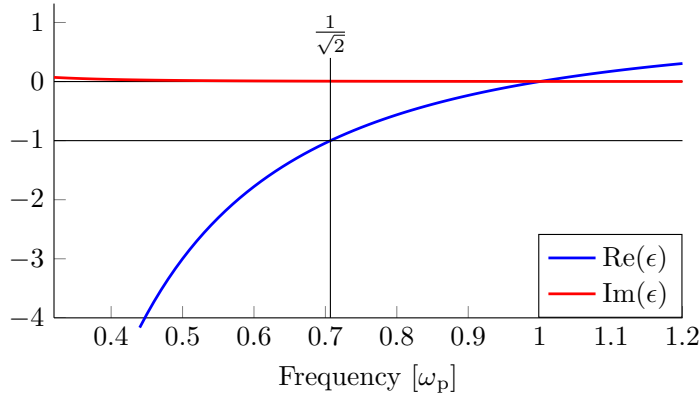


Figure 3.1: Real and imaginary part of the permittivity $\epsilon_t(\omega)$.

above ω_p . In this regime, $\gamma \ll \omega$ and therefore, the limit of the plasma model, Eq. (2.10), with a purely real dielectric function already makes it possible to draw important conclusions.

commonly treated as Drude metals in the literature (for instance for Gold as in Refs. [42, 46, 91, 92], for Aluminum as in Ref. [93], or for Sodium as in Refs. [43, 94]). I will therefore state all frequencies in units of the plasma frequency, on the one hand because it is far more insightful to relate all effects to this important quantity, and on the other hand to underline the general nature of these effects. The dielectric function is displayed in Fig. 3.1.

Note that the frequency range of interest here ranges from about $0.5\omega_p$ to just

3.2 Analytical Treatment of a Single Cylinder

3.2.1 Extended Mie Theory for a Nonlocal Material

As a starting point for my considerations, I use the analytical considerations made by Ruppin [43]. It is based on the standard Mie theory for a cylinder as described for instance in [95]. Mie theory provides a rigorous scattering theory for a cylinder (or a sphere) by solving Maxwell's Equations with the appropriate boundary conditions. I will only give a short outline of how this is done and refer the reader to Ref. [95]. To arrive at a solution for the scattering problem, the scalar wave equation is solved in the appropriate coordinates. The fields \mathbf{E} and \mathbf{H} can be rigorously constructed from these solutions and the boundary conditions can be applied.

I will now present the most relevant details from Ref. [43] where the solution for a single cylinder, described by a nonlocal dielectric function is given. I consider an infinite cylindrical nanowire of radius a which is described by the dielectric functions from Eqs. (3.1) and (3.2). It is surrounded by air with $\epsilon = 1$. When dealing with a nonlocal material, a longitudinal \mathbf{E} -field arises that needs to be described. Modified matching conditions are needed in order to account for this field. Since $\mathbf{E}_l \parallel \mathbf{k}$, there is no \mathbf{B} -field associated with the longitudinal fields (cf. Sec. 2.2.3). Inside the cylinder, where both transverse and longitudinal modes exist, the fields are expanded in cylindrical Bessel functions J_n , since they remain regular in the origin. Here, $n \in \mathbb{N}^+$ is the mode index. The transverse modes fulfill

$$k_t^2 = \frac{\omega^2}{c^2} \epsilon_t(\omega), \quad (3.8)$$

and the longitudinal modes obey the implicit dispersion relation

$$\epsilon_l(k_l, \omega) = 0 \quad \Rightarrow \quad k_l^2 = \frac{\omega(\omega + i\gamma)}{\beta^2} \epsilon_t(\omega). \quad (3.9)$$

3 Analytical Considerations

It is useful to introduce the quantity ζ which relates k_l and k_t :

$$\zeta(\omega) = \frac{\omega}{\omega + i\gamma} \frac{\beta^2}{c^2} \quad (3.10)$$

$$\Rightarrow k_l = \frac{\omega}{c} \sqrt{\frac{\epsilon_t}{\zeta(\omega)}} = k_t / \sqrt{\zeta}. \quad (3.11)$$

With this, the solutions for inside the cylinder are given by

$$J_n(k_t r) \big|_{r < a} \text{ for transverse waves,} \quad (3.12)$$

$$J_n(k_l r) \big|_{r < a} \text{ for longitudinal waves.} \quad (3.13)$$

Outside of the cylinder, no longitudinal modes exist. Bessel functions J_n describe the incident waves and Hankel functions H_n the scattered waves. The dispersion is given by the free-space dispersion

$$k_0 = \omega/c. \quad (3.14)$$

Thus,

$$J_n(k_0 r) \big|_{r > a} \text{ for incident waves,} \quad (3.15)$$

$$H_n(k_0 r) \big|_{r > a} \text{ for scattered waves.} \quad (3.16)$$

The matching conditions which I presented in Section 2.2.4 can now explicitly be written down in the following way [43, 70]:

Continuity of the E-field component parallel to the surface:

$$\underbrace{J'_n(k_0 a)}_{\text{outside incoming}} + \underbrace{a_n H'_n(k_0 a)}_{\text{outside scattered}} = \underbrace{g_n J'_n(k_t a)}_{\text{inside transverse}} - \underbrace{\frac{in}{k_0 a} h_n J_n(k_l a)}_{\text{inside longitudinal}}. \quad (3.17)$$

Continuity of the H-field component normal to the surface:

$$\underbrace{J_n(k_0 a)}_{\text{outside incoming}} + \underbrace{a_n H_n(k_0 a)}_{\text{outside scattered}} = \underbrace{\sqrt{\epsilon_t} g_n J_n(k_t a)}_{\text{inside transverse}}. \quad (3.18)$$

Continuity of the displacement current normal to the surface (additional boundary condition):

$$\underbrace{\frac{n}{k_0 a} J_n(k_0 a)}_{\text{outside incoming}} + \underbrace{\frac{n}{k_0 a} a_n H_n(k_0 a)}_{\text{outside scattered}} = \underbrace{\frac{n}{k_t a} g_n J_n(k_t a)}_{\text{inside transverse}} - \underbrace{i \frac{k_l}{k_0} h_n J'_n(k_l a)}_{\text{inside longitudinal}}. \quad (3.19)$$

One arrives at the following scattering coefficients [43]:

$$a_n = - \frac{[c_n + J'_n(k_t a)] J_n(k_0 a) - \sqrt{\epsilon_t} J_n(k_t a) J'_n(k_0 a)}{[c_n + J'_n(k_t a)] H_n(k_0 a) - \sqrt{\epsilon_t} J_n(k_t a) H'_n(k_0 a)},$$

$$c_n = \frac{n^2}{k_l a} \frac{J_n(k_l a)}{J'_n(k_l a)} \frac{J_n(k_t a)}{k_t a} [\epsilon_t - 1]. \quad (3.20)$$

The local model is restored for $c_n = 0$.

These coefficients now depend on the nonlocal parameter β through k_l . Note that they are still coefficients of the scattered and hence transverse field modes which exist below the plasma frequency, i.e., the spectra at frequencies below ω_p are influenced by nonlocality. While there are no oscillatory longitudinal modes below the plasma frequency, there are evanescent longitudinal modes with almost purely imaginary k_l which cause this shift [75]. The scattering and extinction spectra [95] are given by

$$\sigma_{\text{scat}} = \frac{2}{k_0 a} \sum_{n=-\infty}^{\infty} |a_n|, \quad \sigma_{\text{ext}} = \frac{2}{k_0 a} \sum_{n=-\infty}^{\infty} \text{Re } a_n, \quad (3.21)$$

from which one can also compute the absorption spectrum $\sigma_{\text{abs}} = \sigma_{\text{ext}} - \sigma_{\text{scat}}$. Note that the a_n are complex-valued and have poles in the complex frequency plane. Unlike a resonator made up of perfect mirrors, energy is radiated and, in addition, the materials are lossy (cf. Appendix A). The imaginary part is small and I will neglect it here in the discussion of finding the mode-frequencies, it should however be kept in mind that a larger imaginary part (a small Q-factor) corresponds to stronger dissipation and yields a broader peak in the spectrum [96]. This is discussed in Appendix A in the context of quasinormal modes and I will touch upon this subject again in the discussion of the numerical results in Chap. 5.

Discussion of the Spectra

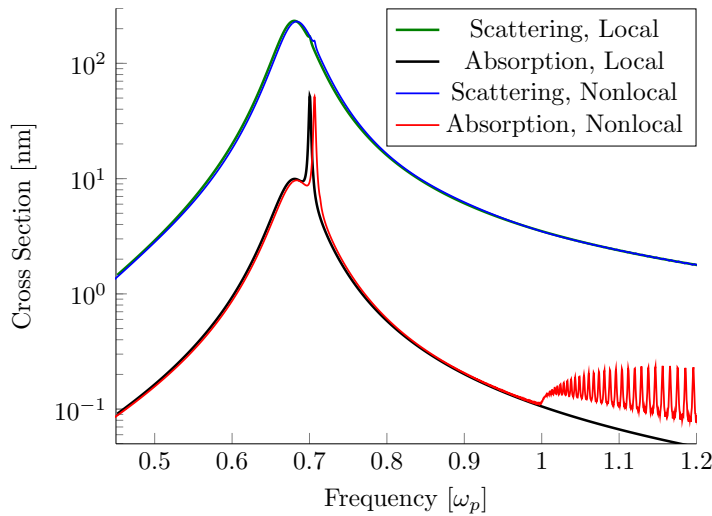


Figure 3.2: Scattering and Absorption spectra for a Drude silver cylinder of radius 10 nm. The results were obtained with Mathematica [97]. For this setup, prominent dipole and quadrupole resonances are found, the first contributing strongly to the scattering cross section and the latter dominating the absorption spectrum. The nonlocal spectra are blueshifted with respect to the local spectra.

The spectra which are obtained by means of Eq. (3.21) are displayed in Fig. 3.2 for a cylinder of radius $a = 10$ nm, both for the local and the nonlocal case. The dipole peak (with $n = 1$) of the nonlocal spectrum is blueshifted with respect to the local spectrum by

$$\delta\omega(n = 1) \approx 0.003\omega_p, \quad (3.22)$$

which corresponds to less than one nanometer when converting the frequency to wavelengths. There is also a reduction in magnitude from the local to the nonlocal spectrum. Here, I will focus on the shift, but below in Sec. 3.2.3 the influence on the height of the peaks is also investigated and it becomes important again when I discuss field enhancement in nonlocal materials in Sec. 5.2.5. While in this setup only contributions of the dipole and the quadrupole mode are visible, it is insightful to take a close look at the a_n

3 Analytical Considerations

that constitute the spectra. In Fig. 3.3I), the positions of the maxima for several modes a_n from Eq. (3.20) are displayed for the local and the nonlocal case. The corresponding calculations have been performed with Mathematica [97]. Let me define the frequencies of the peaks of the a_n on the real frequency axis as ω_n^{\max} , so $a_1(\omega)$ has a maximum for $\omega = \omega_1^{\max}$, which is the dipole resonance.

Taking a look at all the a_n and their resonance frequencies ω_n^{\max} , one makes an interesting observation: For both the local and the nonlocal model, the a_n shift to the blue for increasing n . However, for the local model, there is an upper bound. In the local model, it is approached as early as for $n = 3$. It is given by the surface plasmon frequency $\omega_{sp} = \omega_p/\sqrt{2}$. However, for the nonlocal model, the maximum of each a_n is shifted with respect to that of a_{n-1} . There is no upper limit to this shift and even the plasma frequency does not set a bound to this behavior. Fig. 3.3II) shows the difference between the local and the nonlocal calculation, which is given by

$$\delta\omega(n) = a_n^{\text{nonlocal}} - a_n^{\text{local}}. \quad (3.23)$$

While this difference $\delta\omega(n)$ is small for the first few n (which are the ones dominating a spectrum), it grows approximately linear. I performed a fit to these differences and found the functional dependence to be

$$\delta\omega(n) = 6.08 \cdot 10^{-6} n^2 + 0.00304 n + 1.95 \cdot 10^{-4}. \quad (3.24)$$

This means that the quadrupole peak shifts approximately twice as much as the dipole peak when going from a local to a nonlocal material model and it means that the resonance frequencies for higher n are not bounded. There are surface modes that exist above the plasmon frequency $\omega_{sp} = \omega_p/\sqrt{2}$ and in principle even beyond the plasma frequency ω_p . While the contribution to the spectra of the higher order modes is very small in highly symmetric structures such as cylinders excited by plane waves, it was pointed out by Christensen et al. [93] in the context of nanospheres, that by introducing a zero- or one-dimensional source, these resonances can be made visible.

These findings could also be of importance in the context of the spaser [99, 100]. Spaser stands for surface plasmon amplification by stimulated emission of radiation. In such a spaser, the decay of dye molecules acting as emitters in the vicinity of a metallic nanosphere produces localized surface plasmons. Therefore, an efficient coupling between the emitters and the dipole mode of the nanosphere is desired. Decay into all other modes is radiation loss. Within semi-classical spaser theory [101, 102] using a nonlocal material model, it was shown [102] that higher order modes act as important loss channels which would impede spasing for the setup under consideration in Ref [100]. In the local case where all of the modes cluster at the surface plasmon frequency ω_{sp} , even high order modes have a significant overlap with the dipole mode and therefore add to the loss. In the calculations presented in Ref. [102], as many as 300 modes were added up in order to obtain a reliable result¹ for the loss. As I have demonstrated, in a nonlocal model, the modes are spaced out, thus the overlap between higher order modes and the dipole mode becomes insignificant and much less than 300 modes are expected to contribute to the loss. The structures studied in the above-mentioned works are in fact only 7 nm in radius, they will, according to the findings presented here, show nonlocal behavior. While spasing is believed to be out of reach for the parameters used in Ref. [100] within a local model, the absence of many of the loss-channels in a nonlocal model could be an argument in favor of the highly disputed setup.

¹convergence of the result was checked in the sense that it was made sure that adding another mode to the calculation would not change the result on the level of the desired precision.

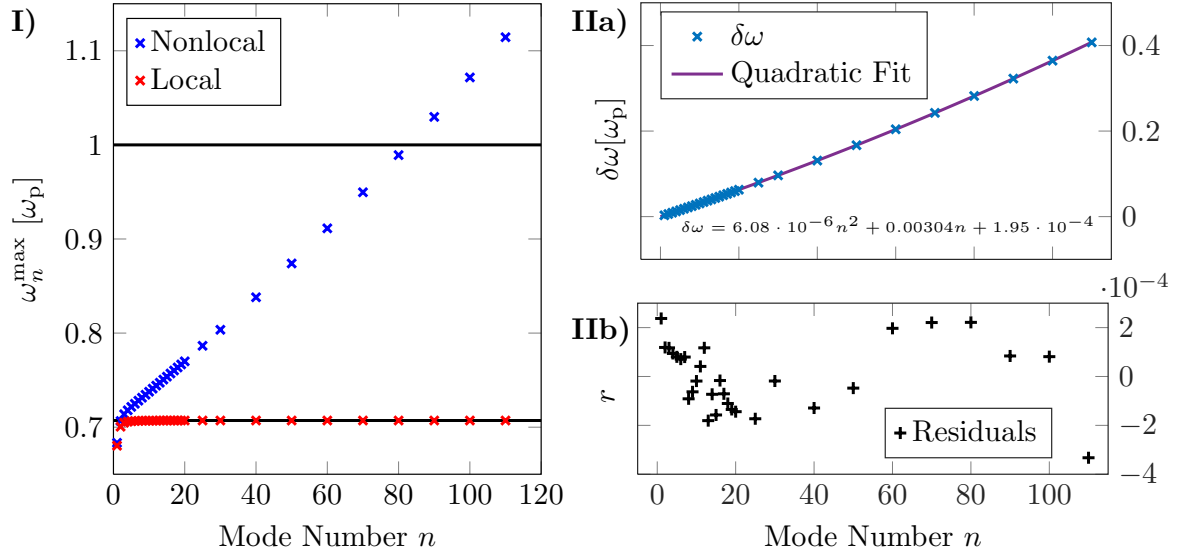


Figure 3.3: **I)** The frequencies of the maxima of the Mie coefficients (Eq. (3.20)), ω_n^{\max} , are plotted over the mode number n for a Drude silver cylinder of radius 10 nm. The horizontal lines indicate the plasma frequency and the plasmon frequency $\omega_p/\sqrt{2}$. The latter poses an upper bound to the positions of the maxima of the local Mie coefficients, which lie just below $\omega_p/\sqrt{2}$ for the first few n and then quickly approach this value. The nonlocal Mie coefficients are not bounded and extend beyond the plasma frequency. They follow a behavior which looks linear at first sight. The results were obtained with Mathematica [97] **IIa)** The difference between the nonlocal and the local results from **I)** is shown and a quadratic fit was performed. The difference is approximately linear in n with a small quadratic correction. The fit for the frequency shift is given by $\delta\omega = 6.08 \cdot 10^{-6}n^2 + 0.00304n + 1.95 \cdot 10^{-4}$ **IIb)** The residuals for the quadratic fit from **IIa)** are displayed. The error of the fit is well below 1 ‰ for the whole range of n under consideration. The fit was performed with Matlab [98].

3.2.2 Asymptotic Behavior

To further investigate the shift of the Mie scattering coefficients, I will make some analytical considerations for the limiting case $n \gg 1$, for which an approximation for the Bessel functions exists.

The maxima of Eq. (3.20) can be determined analytically by searching for solutions of the equation

$$[c_n(\omega) + J'_n(k_t a)]H_n(k_0 a) - \sqrt{\epsilon_t(\omega)}H'_n(k_0 a)J_n(k_t a) = 0. \quad (3.25)$$

In the nonlocal case the equation for the resonances can be rewritten as

$$\frac{n^2}{k_l a} \left(\frac{J'_n(k_l a)}{J_n(k_l a)} \right)^{-1} \left(\frac{\epsilon_t(\omega) - 1}{k_0 a \sqrt{\epsilon_t(\omega)}} \right) + \frac{J'_n(k_t a)}{J_n(k_t a)} - \sqrt{\epsilon_t(\omega)} \frac{H'_n(k_0 a)}{H_n(k_0 a)} = 0, \quad (3.26)$$

and in the local case

$$\frac{J'_n(k_t a)}{J_n(k_t a)} - \sqrt{\epsilon_t(\omega)} \frac{H'_n(k_0 a)}{H_n(k_0 a)} = 0. \quad (3.27)$$

3 Analytical Considerations

For metals like silver $\gamma/\omega_p \sim 10^{-3}$ and $c/\omega_p \sim 20$ nm. The solutions are going to be near the surface plasmon frequency $\omega_{sp} = \omega_p/\sqrt{2}$ and thus $\omega_n \lesssim \omega_p$. This means that if the radius a is of the order of a few nanometer it follows that $|k_0 a| \ll 1$. Below the plasma frequency $\text{Re}[\epsilon_t(\omega)] < 0$ while above $\text{Re}[\epsilon_t(\omega)] > 0$ and $|\epsilon_t(\omega_p)| \sim \gamma/\omega_p$. In addition, in the range of frequencies under consideration, $\zeta(\omega) \sim \beta^2/c^2 \ll 1$. Let me consider the case where $|\epsilon_t(\omega)|$ is of the order of unity. This means that $|k_t a| \ll 1$. For high order modes (large n), the Bessel and Hankel functions can be approximated as [103]

$$J_n(z) \stackrel{n \gg 1}{\approx} \frac{1}{\sqrt{2\pi n}} \left(\frac{ez}{2n}\right)^n \quad (3.28)$$

$$Y_n(z) \stackrel{n \gg 1}{\approx} -\sqrt{\frac{2}{\pi n}} \left(\frac{ez}{2n}\right)^{-n} \quad (3.29)$$

$$H_n^{(1)}(z) = J_n(z) + iY_n(z) \stackrel{n \gg 1}{\approx} -i\sqrt{\frac{2}{\pi n}} \left(\frac{2n}{ez}\right)^n \left[1 + \frac{i}{2} \left(\frac{ez}{2n}\right)^{2n}\right]. \quad (3.30)$$

In this limit, the logarithmic derivatives give

$$\frac{J'_n(z)}{J_n(z)} = \frac{d}{dz} \ln[J_n(z)] \approx \frac{n}{z}, \quad (3.31)$$

$$\frac{H'_n(z)}{H_n(z)} = \frac{d}{dz} \ln[H_n(z)] \approx -\frac{n}{z}. \quad (3.32)$$

This means that in the local case $c_n(\omega) \rightarrow 0$ one finds

$$\frac{1}{\sqrt{\epsilon_t(\omega)}} + \sqrt{\epsilon_t(\omega)} = 0 \Rightarrow \epsilon_t(\omega) = -1; \quad \omega \approx \omega_{sp} = \frac{\omega_p}{\sqrt{2}}, \quad (3.33)$$

which was to be expected from Fig. 3.3. Therefore, for large n the same value is obtained as in the electrostatic limit, but in the present example of a cylinder of 10 nm radius, the approximation breaks down for small n . Explicitly, for small arguments,

$$J_n(z) \stackrel{|z| \ll \sqrt{n+1}}{\approx} \frac{1}{n!} \left(\frac{z}{2}\right)^n, \quad (3.34)$$

$$Y_n(z) \stackrel{|z| \ll \sqrt{n+1}}{\approx} \begin{cases} \frac{2}{\pi} \left(\ln \left[\frac{z}{2} \right] + \gamma \right) & n = 0 \\ -\frac{(n-1)!}{\pi} \left(\frac{2}{z} \right)^n & n \neq 0 \end{cases}, \quad (3.35)$$

which, for $n \neq 0$, once again leads to Eq.(3.33), showing that in small radius limit all resonances collapse into the resonance for $n = 1$.

Let me move on to the nonlocal contributions. Taking a look at the arguments of the functions, one

finds $|k_l a| \gg 1$ since $\zeta \approx \beta^2/c^2 \ll 1$. For very large arguments the approximation reads

$$J_n(z) \stackrel{|z| \gg 1}{\approx} \begin{cases} \sqrt{\frac{1}{2\pi z}} e^{i(z - n\frac{\pi}{2} - \frac{\pi}{4})} & \text{for } \text{Im}[z] < 0 \\ \sqrt{\frac{1}{2\pi z}} e^{-i(z - n\frac{\pi}{2} - \frac{\pi}{4})} & \text{for } \text{Im}[z] > 0 \end{cases} \quad (3.36)$$

$$\Rightarrow \frac{d}{dz} \ln[J_n(z)] \approx \begin{cases} i \left(1 + \frac{i}{2z}\right) & \text{for } \text{Im}[z] < 0 \\ -i \left(1 - \frac{i}{2z}\right) & \text{for } \text{Im}[z] > 0 \end{cases}. \quad (3.37)$$

Choosing the solution for $\text{Im}[z] > 0$ (see Eq.(3.40)), together with the same approximation for the local case ($n \neq 0$) leads to

$$i \frac{n}{k_l a} \left(1 + \frac{i}{2k_l a}\right) \left(\frac{\epsilon_t(\omega) - 1}{k_0 a \sqrt{\epsilon_t(\omega)}}\right) + \frac{1}{k_t a} + \sqrt{\epsilon_t(\omega)} \frac{1}{k_0 a} = 0. \quad (3.38)$$

Some further simplifications yield

$$\epsilon_t(\omega) = -\frac{1 - i \frac{n}{k_l a}}{1 + i \frac{n}{k_l a}} \approx -1 + i \frac{2n}{k_l a}, \quad (3.39)$$

where -1 on the right hand side of Eq. (3.39) represents the local solution and $i \frac{2n}{k_l a}$ is a nonlocal correction. Thus one can calculate a nonlocal correction that depends on n and then add it to the actual local solution, rather than adding it to the approximate local solution $\epsilon_t(\omega) = -1$. Dissipation is still neglected and $\zeta(\omega) \sim \beta^2/c^2$. Consider now the solution ω_{sp} of $\epsilon_t(\omega) = -1$. In a linear approximation, it is assumed that the solutions of the previous equations have the form $\omega_n = \omega_{\text{sp}}(1 + \delta_n)$ with $|\delta_n| \ll 1$. Thus,

$$\epsilon_t(\omega_n) \approx -1 + \omega_{\text{sp}} \epsilon'_t(\omega_{\text{sp}}) \delta_n \quad (3.40)$$

and, directly from Eq. (3.11), using Eq. (3.40), it follows that

$$k_l \approx i \frac{\omega_{\text{sp}}}{\beta} \left[1 + \left(1 - \frac{\omega_{\text{sp}}}{2} \epsilon'_t(\omega_{\text{sp}}) \right) \delta_n \right] \quad (3.41)$$

and therefore one arrives at

$$\delta_n \approx \frac{2n\beta}{\omega_{\text{sp}} a} \left[\omega_{\text{sp}} \epsilon'_t(\omega_{\text{sp}}) + \frac{2n\beta}{\omega_{\text{sp}} a} \left(1 - \frac{1}{2} \omega_{\text{sp}} \epsilon'_t(\omega_{\text{sp}}) \right) \right]^{-1} \approx \frac{2n\beta}{a \omega_{\text{sp}}^2 \epsilon'_t(\omega_{\text{sp}})} \ll 1. \quad (3.42)$$

In the non-dissipative limit $\omega_{\text{sp}} \epsilon'_t(\omega_{\text{sp}}) \sim 4$, which leads to

$$\omega_n = \omega_{\text{sp}} + \frac{2\beta}{a \omega_{\text{sp}} \epsilon'_t(\omega_{\text{sp}})} n \approx \omega_{\text{sp}} + \frac{\beta}{2a} n. \quad (3.43)$$

3 Analytical Considerations

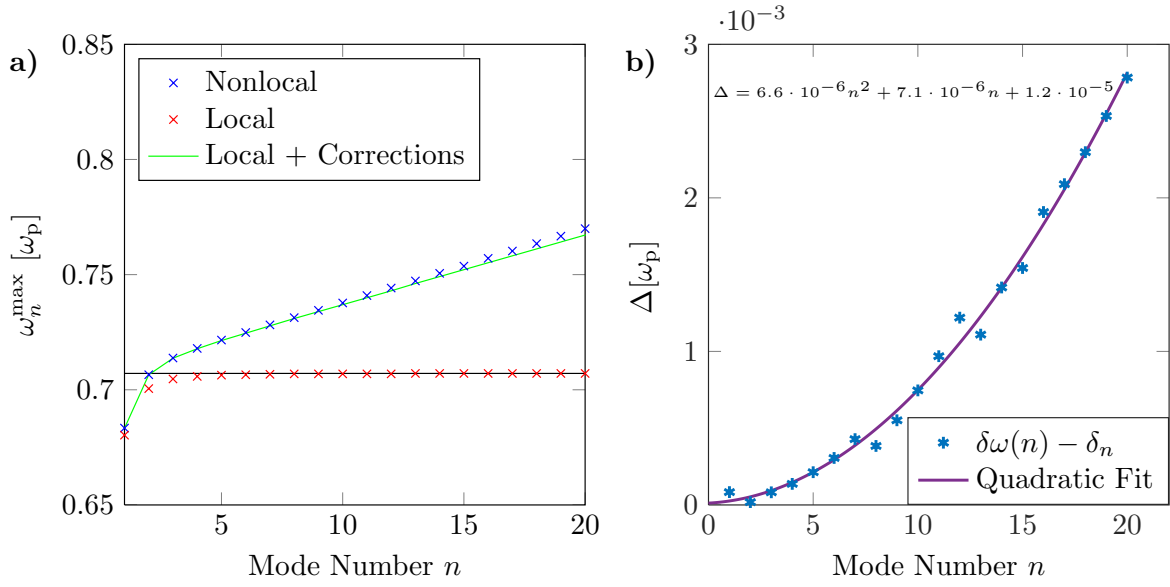


Figure 3.4: **a)** The frequencies of the maxima of the Mie coefficients (Eq. (3.20)), ω_n^{\max} , are plotted over the mode number n for a Drude silver cylinder of radius 10 nm as in Fig. 3.3. The green line displays the local values which have been corrected according to Eq. (3.44). Even though n assumes only discrete values, a line is used as a guide to the eye. **b)** The absolute difference between the asymptotic correction δ_n and the de facto difference between the local and the nonlocal Mie solution $\delta\omega(n)$ is depicted over n . While the differences are small, it can be seen that the missing shift is well described by a quadratic contribution.

Hence, in a first approximation, nonlocality introduces a shift in frequency which grows linearly with n . As was also pointed out by Christensen [93], the plasma frequency ω_p does not pose a limit to the blue shift.

The findings from above explain the small blue shift of the dipole or quadrupole resonance of a conventional scattering or absorption spectrum of a single circular cylinder that is illuminated by a Gaussian pulse. Let me proceed to make a more quantitative statement regarding the approximations which I have just performed. As I pointed out earlier, the local part in Eq. (3.39) is clearly off for the first few n . Since I am not interested in an approximate solution to the local part, I will use the nonlocal correction on the non-approximate solution to the local solution, i.e., identify the δ_n with $\delta\omega(n)$ from Eq. (3.23):

$$\omega_n \approx \omega_{sp} + \frac{\beta}{2a}n \rightarrow \omega_{sp,n} + \frac{\beta}{2a}n, \quad (3.44)$$

where $\omega_{sp,n}$ is the solution to Eq. (3.27). For the material model at hand and a cylinder of radius $a = 10$ nm, the shift is given by

$$\delta_n = \frac{\beta}{2a}n = 0.003004\omega_p, \quad (3.45)$$

which agrees well with the linear contribution to the fit above in Fig. 3.3. The results of Eq. (3.44) are displayed in Fig. 3.4, along with the ω_n^{\max} from the Mie calculations.

Entering the Electrostatic Regime

As a second example, I study the nonlocal spectra for a cylinder of 2 nm radius for which I calculate the frequency shifts to be

$$\delta_n = 0.015020\omega_p. \quad (3.46)$$

In Fig. 3.5 the spectra are shown. In Fig. 3.5 **b**) a quadrupole resonance is found in the absorption

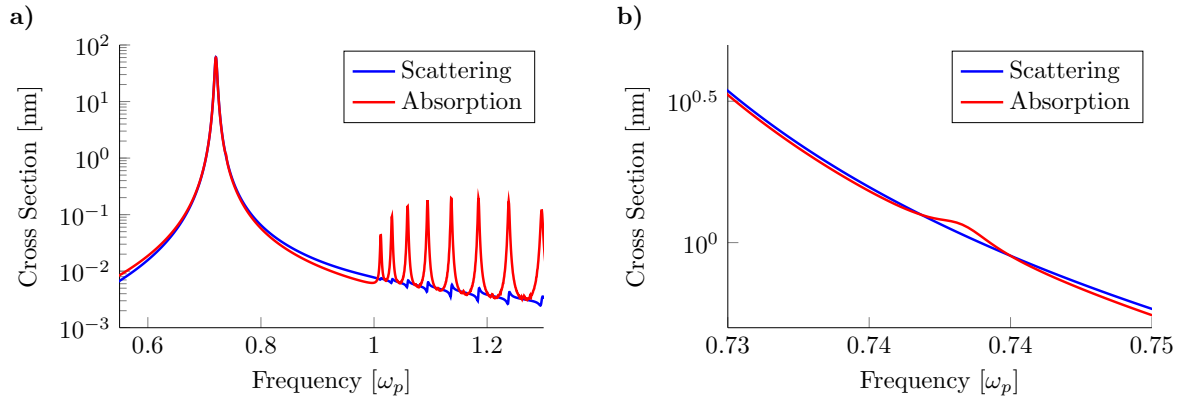


Figure 3.5: **a)** The nonlocal spectra for a cylinder of radius 2 nm are displayed using a logarithmic scale for the y-axis. The bulk plasmons are very prominent in such a small structure. In **b)** a zoom is provided which shows that a small quadrupole resonance is present in the absorption cross section.

spectrum, which would coincide with the main dipole peak in a local theory. The position of the dipole and the quadrupole peak match the prediction according to Eq. (3.44), as can be seen from Fig. 3.6. It can also be seen from Fig. 3.6 **a)** that this example is well-described by the electrostatic limit as all the local ω_n^{\max} are approximately at ω_{sp} (see Sec. 3.2.5). However, since the effects of nonlocality are stronger in such a small system, the asymptotics are less accurate than in the case of the 10 nm cylinder above, as can be seen from Fig. 3.6 **b)**.

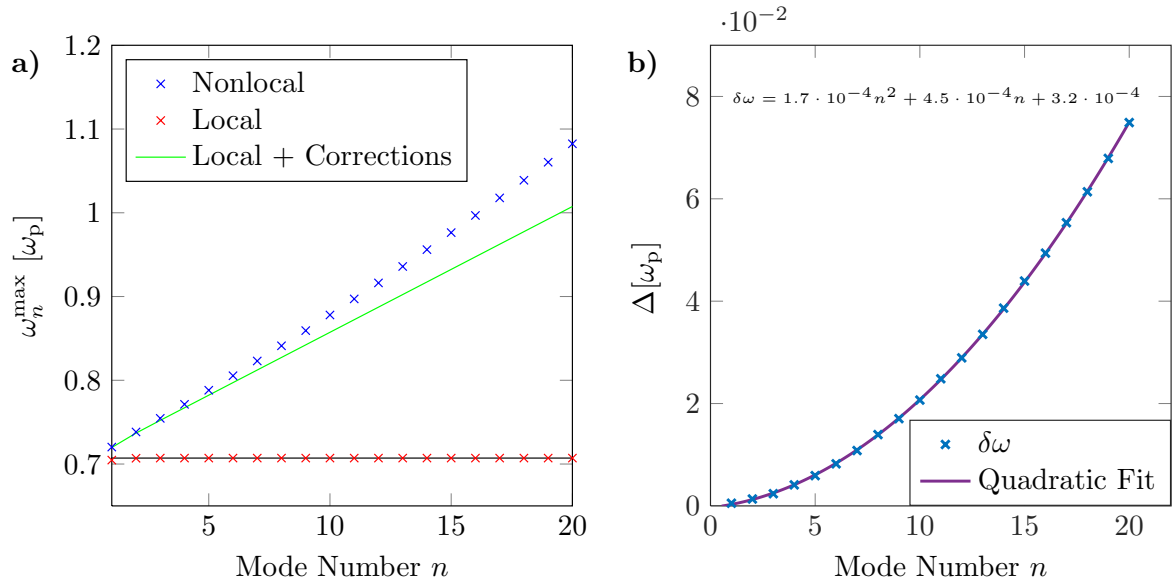


Figure 3.6: As in Fig. 3.4, the positions of the maxima of the Mie coefficients are displayed, this time for radius 2 nm. This is deeper in the electrostatic regime, as all the local coefficients have their maxima near the plasmon frequency ω_{sp} . The green line again displays the frequencies calculated from 3.44.

3.2.3 Perturbative Treatment of the Parameter β

In this work, the parameter β was determined to be $\beta_{TF} = \sqrt{\frac{1}{3}}v_f$ from Thomas Fermi theory. As pointed out, the high-frequency limit $\beta = \sqrt{\frac{3}{5}}v_f$ is also frequently found in the literature. Since different values for β are being used, I now go ahead and consider β as a free parameter which determines degree of nonlocality, and study its influence on the spectra as it is varied. To do this, I investigate how it affects the magnitude and the position of the peaks in the cross sections. Above, in Eq. (3.44), I have already derived an approximate formula for the shift of the n^{th} mode

$$\omega_n \approx \omega_{sp,n} + \frac{\beta n}{2a}, \quad (3.47)$$

which can be interpreted as an equation for $\omega_n(\beta)$, where the shift grows linearly in β . Writing $\beta = \beta_{TF} \cdot x$ yields

$$\omega_n \approx \omega_{sp,n} + \frac{\beta n}{2a} \quad (3.48)$$

$$= \omega_{sp,n} + \frac{\beta_{TF} n}{2a} x, \quad (3.49)$$

where x is varied between 0 and 1. The expected slope is

$$\frac{\beta_{TF} n}{2a} x = 0.00300 n \omega_p x. \quad (3.50)$$

In Fig. 3.7 the spectra are displayed for different values of beta, varying between $\beta = 0$ and $\beta = \beta_{TF}$, using the Mie scattering algorithm from above. In Fig. 3.8 the spectral positions and heights of the maxima of the spectra from Fig. 3.7 are displayed, along with their linear regressions.

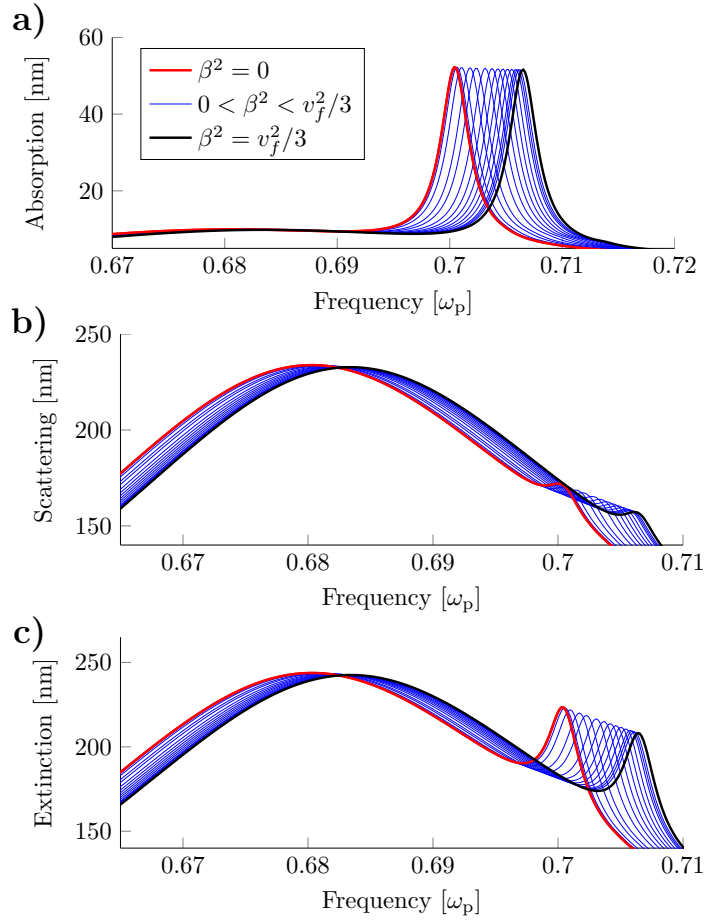


Figure 3.7: Influence of the nonlocal parameter β on the cross sections. **a)** Absorption **b)** Scattering **c)** Extinction. The parameter β is varied between 0 and $v_f/\sqrt{3}$.

3 Analytical Considerations

The linear regressions yield

	Linear Regression	R^2
Scattering Max. Value	$233.8085 - 1.0730x$	1.0000
Scattering ω_{\max}	$0.6803\omega_p + 0.0031\omega_p x$	0.9988
Extinction Max. Value	$243.7446 - 1.1758x$	1.000
Extinction ω_{\max}	$0.6803\omega_p + 0.0031\omega_p x$	0.9987
Absorption Max. Value	$52.1803 - 0.6296x$	0.9782
Absorption ω_{\max}	$0.7004\omega_p + 0.0061\omega_p x$	0.9994

which is in good agreement with Eq. (3.50): For the scattering and the extinction cross section, the maximum value is the dipole peak (and the slope of $0.0031\omega_p$ is approximately the expected slope for $n = 1$). For the absorption cross section the maximum value is at the quadrupole peak and I find the slope $0.0061\omega_p \approx 0.0030 \cdot 2\omega_p$, i.e., the expected slope for $n = 2$. Note that the numerically obtained values for the frequencies of the maxima in Fig. 3.7 are limited by the frequency discretization within the numerical solver which was chosen to be $1.8 \cdot 10^{-4}\omega_p$.

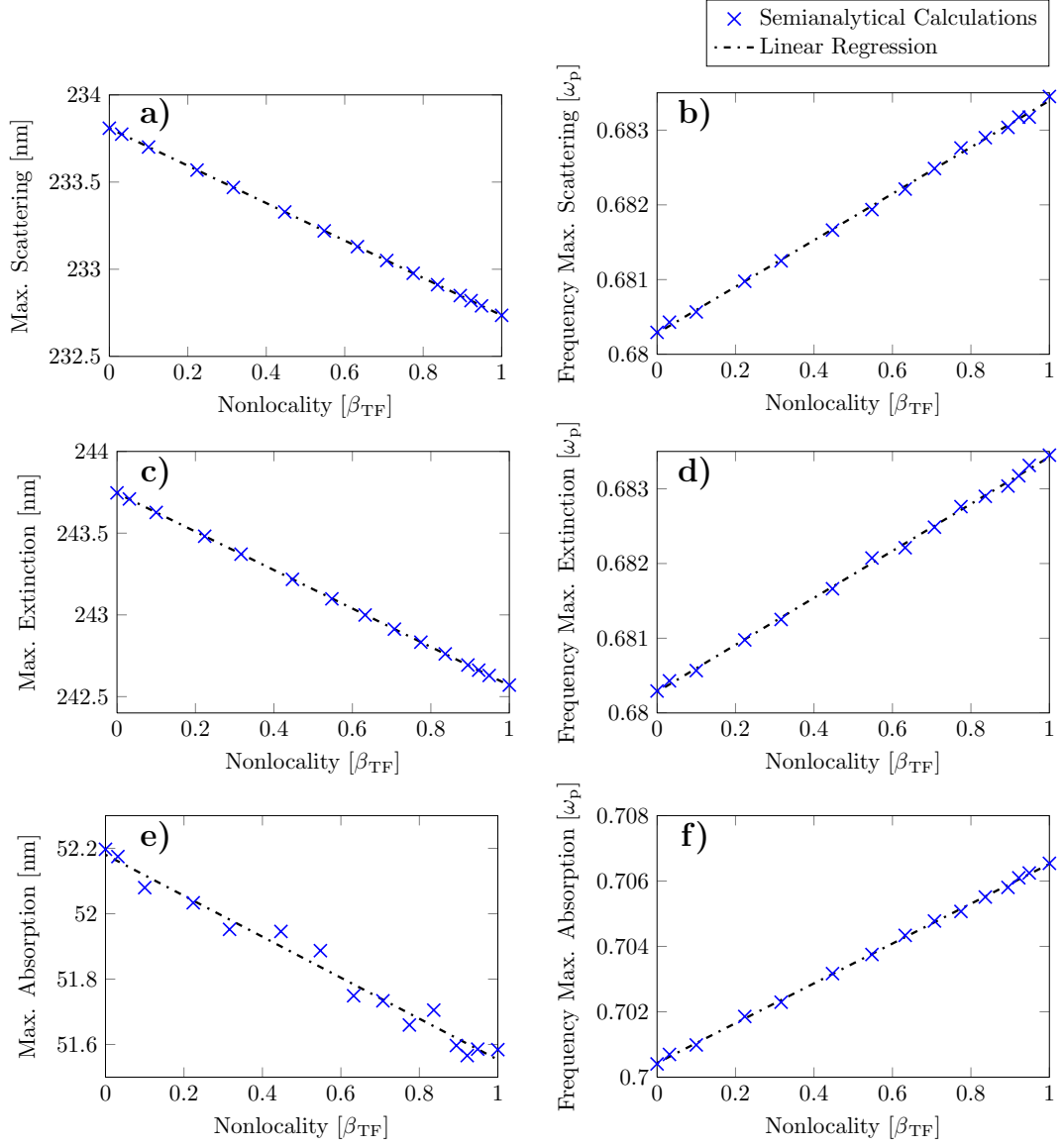


Figure 3.8: Linear Regressions studying the influence of the degree of nonlocality on the spectra

3.2.4 Bulk Plasmons

Having discussed the surface plasmon resonances, I now turn to the bulk modes which exist above the plasma frequency. Let me recall the equation for the scattering coefficients 3.20:

$$a_n = -\frac{[c_n + J'_n(k_t a)]J_n(k_0 a) - \sqrt{\epsilon_t} J_n(k_t a) J'_n(k_0 a)}{[c_n + J'_n(k_t a)]H_n(k_0 a) - \sqrt{\epsilon_t} J_n(k_t a) H'_n(k_0 a)},$$

$$c_n = \frac{n^2}{k_l a} \frac{J_n(k_l a)}{J'_n(k_l a)} \frac{J_n(k_t a)}{k_t a} [\epsilon_t - 1], \quad (3.51)$$

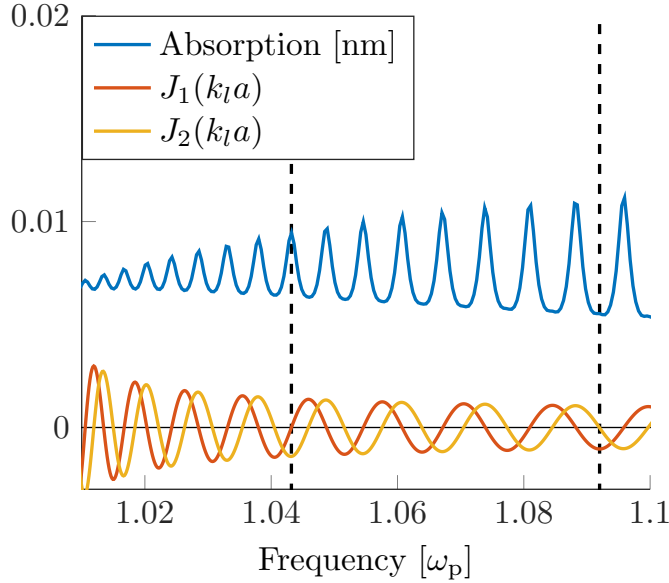


Figure 3.9: Absorption spectrum for a Drude silver cylinder of radius $a = 10$ nm above the plasma frequency, displaying Bulk plasmons, along with the derivatives of the Bessel functions $J'_n(k_l a)$ with $n = 1, 2$. The bulk plasmon resonances occur at $J'_n(k_l a) = 0$. The vertical lines serve as a guide to the eye to relate a zero-point of the $J'_n(k_l a)$ to a peak in the spectrum. The results were obtained with Mathematica [97].

lines in Fig. 3.9 relate one of the main peaks and one of the intermediary peaks to the zero points of $J'_1(k_l a)$ and $J'_2(k_l a)$ respectively.

Above the plasma frequency, the $J_n(k_l a)$ oscillate while $J_n(k_0 a)$, $J_n(k_t a)$ and $H_n(k_0 a)$ are monotonic and do not change sign in the frequency range of interest. Therefore the scattering coefficients exhibit maxima when the β -dependent term c_n diverges, which happens under the condition

$$J'_n(k_l a) = 0. \quad (3.52)$$

The oscillatory behavior of $J_n(k_l a)$ results in an infinite number of resonances for every a_n . All a_n with even n have their resonances at the same positions while the resonances of the a_n with odd n are shifted with respect to those with even n . In Fig. 3.9 the absorption spectrum displaying bulk plasmon resonances is depicted, along with the functions $J'_n(k_l a)$ for $n = 1, 2$. The main contribution to the absorption spectrum comes from $n = 1$, therefore the peaks in the spectrum are found where $J'_1(k_l a) = 0$. In principle, there are intermediary peaks where $J'_2(k_l a) = 0$. For the setup under consideration, these intermediary peaks are however barely visible. The vertical dashed

3.2.5 Electrostatics

Even though the “full problem” was solved above using an extended Mie-Theory, I would like to discuss nonlocal electrostatics at this point – for the following two reasons: Firstly, it is interesting to see which mechanisms persist in an electrostatic theory (e.g. the blue shift) and therefore determine how good the electrostatic approximation is for the problem at hand. Secondly, this serves as a preparation for the discussion of the cylindrical dimer below. For the dimer, the electrostatic local theory is fairly straightforward, but a full Mie-theory and a nonlocal electrostatic theory are problematic. Therefore, it is important to learn as much as possible about the electrostatics, in order to be able to deduce as much as possible from the local theory of the cylindrical dimer.

Before I set out to do any calculations I would like to clarify what I mean by electrostatics since this can in the present case be a source of confusion. Whenever I speak of electrostatics I imply that I solve Laplace’s equation for the electrostatic potential V , with the corresponding boundary conditions for a particle. Thus, the electric field becomes curl-free. I go however beyond the frequency-independent full electrostatic case (as if one were to apply a constant voltage to a capacitor) in several ways: First of all, by applying the boundary conditions, the permittivity used to describe the material (in all cases the previously introduced Drude metal) introduces a frequency dependence which yields frequency-dependent solutions for the modes. Secondly, I consider all higher order modes, regardless of their symmetry, also those modes that cannot be excited by a static electric field.

In this section I apply this protocol to a single cylinder with radius R and a dielectric function $\epsilon(\omega)$, embedded in a constant background material with ϵ_M :

$$\Delta V = 0, \quad (3.53)$$

such that

$$V_i(R) = V_o(R), \quad (3.54)$$

$$\epsilon(\omega) \frac{\partial V_i}{\partial r} \Big|_R = \epsilon_M \frac{\partial V_o}{\partial r} \Big|_R. \quad (3.55)$$

Here, Eq. (3.54) ensures that the potential is continuous across the surface, while Eq. (3.55) takes care of the discontinuity in the normal component of the \mathbf{E} -field on the particle boundary.

Solutions of the Laplace equation in Cylindrical coordinates separate:

$$V(r, \phi) = R(r)\Phi(\phi). \quad (3.56)$$

The Ansatz (see, for instance [104])

$$\Phi(\phi) = A \cos k\phi + B \sin k\phi, \quad k = 0, 1, 2, \dots \quad (3.57)$$

$$R(r) = r^n, \quad n = \pm k \quad (3.58)$$

$$R(r) = C \ln r + D, \quad k = 0 \quad (3.59)$$

leads to

$$\frac{\epsilon(\omega)}{\epsilon_M} R^{n-1} = -R^{n-1}, \quad (3.60)$$

$$\Rightarrow \frac{\epsilon(\omega)}{\epsilon_M} = -1, \quad (3.61)$$

3 Analytical Considerations

independent of n . This is in contrast to the solution for a sphere, where a dependence on a quantum number l is found: $\frac{\epsilon\omega}{\epsilon_M} = -\frac{l+1}{l}$. The solutions of Eq. (3.61) are just the ω_n^{\max} from Sec 3.2.2. This means that in the electrostatic limit, all modes are found at the surface plasmon frequency $\omega_{sp} = \omega_{\text{plasma}}/\sqrt{2}$, which I have already demonstrated to be a good approximation in the case of a 2 nm cylinder (cf. Fig. 3.6).

The potentials possess specific symmetries and will therefore be excited depending on the symmetries of an incident light pulse. Note that only the dipole mode is “fully electrostatic” in the sense that its symmetry is such that it could be excited by means of a static electric field in a capacitor. To excite the quadrupole mode, a more complicated excitation such as a propagating light pulse is needed (see Sec. 3.4). The potentials for sine and cosine, for $k = 1, 2$ are displayed in Fig. 3.10. They lead to fields which show the typical dipole and quadrupole field distributions.

Nonlocal Electrostatics

An electrostatic theory including nonlocal effects in the case of a sphere was given by Dasgupta, Fuchs and Claro [105, 106]. In the following derivations I am strictly following Ref. [105], but with the spherical functions replaced by the cylindrical functions to account for the quasi two-dimensional case. More generally than in the local case above, a \mathbf{k} -dependent longitudinal dielectric function $\epsilon(\mathbf{k}, \omega)$ has to be considered now and the matching conditions at the particle boundary have to be modified accordingly. The inclusion of the nonlocal effects in a nonlocal theory formulated by means of potentials is not straightforward.

Outside of the cylinder the potential is in general still expanded in a 2π -periodic angular part (which is again quantized due to the periodicity) and, as above, a power-law for the radial part (from now on, $\epsilon_0 = 1$ and the surrounding medium is assumed to be air with $\epsilon_M = 1$)

$$V(\mathbf{r}) = b_l r^{-l} e^{il\phi}, \quad l \in \mathbb{N}^+ \quad (3.62)$$

and, in vacuum, the displacement field outside is simply

$$\mathbf{E}(\mathbf{r}) = \mathbf{D}(\mathbf{r}) = -\nabla V(\mathbf{r}) = l b_l r^{-l-1} e^{il\phi}. \quad (3.63)$$

Inside, in the electrostatic case,

$$\nabla \times \mathbf{E} = 0, \quad (3.64)$$

and

$$\nabla \cdot \mathbf{D} = 0. \quad (3.65)$$

To find a potential formulation for the nonlocal boundary conditions, one formally introduces surface charges at the interface $r = a$ in such a way that the tangential component of \mathbf{D} is left continuous at the boundary and the normal component is discontinuous, thus, violating Eq. (3.65) on the boundary and acting as a source for \mathbf{D} .

In the electrostatic limit, Eq. (3.64) holds everywhere. Therefore one can introduce a potential function inside the cylinder which is given by

$$\mathbf{D}(\mathbf{r}) = -\nabla V_{\mathbf{D}}(\mathbf{r}), \quad (3.66)$$

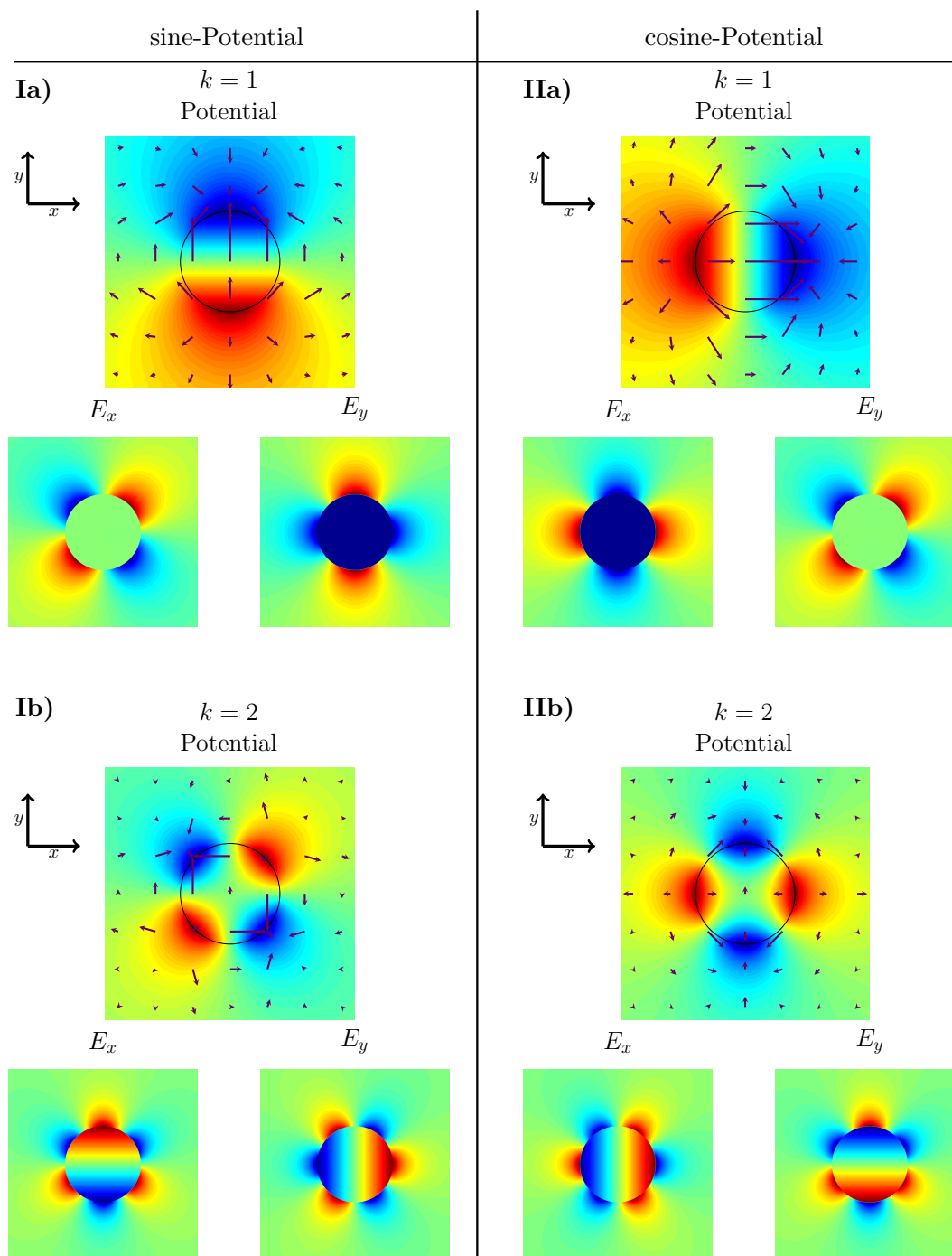


Figure 3.10: Dipole ($k = 1$) and quadrupole ($k = 2$) potentials and field distributions for a single cylinder from electrostatic theory, for the two symmetry classes of potentials.

3 Analytical Considerations

regardless of $\epsilon(\mathbf{k}, \omega)$, and its Fourier transform

$$V_{\mathbf{D}}(\mathbf{k}) = \frac{1}{2\pi} \int V_{\mathbf{D}}(\mathbf{r}) e^{-i\mathbf{k}\mathbf{r}} d^2\mathbf{r}. \quad (3.67)$$

In the same manner, a Fourier transform can be defined $V(\mathbf{k})$ of $V(\mathbf{r})$. Because of Eqs. (3.64) and (3.65), this potential also fulfills the Poisson equation

$$\nabla^2 V(\mathbf{k}) = 0, \quad (3.68)$$

inside and outside of the cylinder, but not at the surface, where there are non-vanishing charge terms on the right hand side of 3.68. Their angular dependence has to be the same as the angular dependence of the fields inside and outside. Just as in Eq. (3.62), a general 2π -periodic angular function $c_l e^{-il\phi}$ is used as an Ansatz. The charges are confined to the surface by multiplying with a delta function $\delta(r - a)$. Putting it all together results in the following expression in k -space:

$$-k^2 V_{\mathbf{D}}^l(\mathbf{k}) = \frac{c_l}{2\pi} \int_0^\infty \int_0^{2\pi} \delta(r - a) e^{-il\phi} e^{-ikr \cos(\theta - \phi)} r dr d\phi, \quad (3.69)$$

where $\mathbf{r} = (r, \phi)$ and $\mathbf{k} = (k, \theta)$. Expanding the exponential function in cylindrical coordinates, known as Jacobi-Anger expansion [107], and evaluating the r -integral, yields

$$-k^2 V_{\mathbf{D}}^l(\mathbf{k}) = \frac{c_l}{2\pi} \int_0^{2\pi} a e^{-il\phi} \sum_{n=-\infty}^{\infty} (-i)^n e^{-in\theta} J_n(ka) e^{in\phi} d\phi \quad (3.70)$$

$$= \frac{c_l a}{2\pi} \sum_{n=-\infty}^{\infty} e^{-in\theta} (-i)^n J_n(ka) \underbrace{\left[\frac{2 \sin[(n-l)\pi]}{(n-l)} \right]}_{=2\pi \delta_{ln}} \quad (3.71)$$

$$= c_l a e^{-il\theta} (-i)^l J_l(ka). \quad (3.72)$$

I can now write

$$V_{\mathbf{D}}^l(\mathbf{k}) = c_l a e^{-il\theta} (-i)^l J_l(ka) / k^2 \quad (3.73)$$

and the potential for \mathbf{E} inside the cylinder is given by

$$V^l(\mathbf{k}) = V_{\mathbf{D}}^l(\mathbf{k}) / \epsilon(\omega, \mathbf{k}). \quad (3.74)$$

Transforming back to real space, yields

$$V^l(\mathbf{r}') = \frac{c_l a}{2\pi} (-i)^l \int_0^\infty \int_0^{2\pi} \frac{e^{-il\theta} J_l(ka) e^{ikr' \cos(\theta - \phi')}}{k^2 \epsilon(k, \omega)} k dk d\theta \quad (3.75)$$

$$= \frac{c_l a}{2\pi} (-i)^l \int_0^\infty \int_0^{2\pi} \frac{J_l(ka)}{k \epsilon(k, \omega)} \sum_{m=-\infty}^{\infty} (i)^m J_m(kr') e^{i(m-l)\theta} e^{-im\phi'} dk d\theta \quad (3.76)$$

$$= c_l a e^{il\phi'} \int_0^\infty \frac{J_l(ka) J_l(kr')}{k \epsilon(k, \omega)} dk, \quad (3.77)$$

and, using (see [108], p. 405)

$$\int_0^\infty \frac{J_\nu(at)J_\nu(bt)}{t} dt = \frac{(a/b)^\nu}{2\nu}, \quad (3.78)$$

it follows that

$$V_{\mathbf{D}}^l(\mathbf{r}) = c_l a e^{-il\phi} \int_0^\infty \frac{J_l(kr)J_l(ka)}{k} dk \quad (3.79)$$

$$= c_l a e^{-il\phi} \frac{(r/a)^l}{2l} \quad (3.80)$$

$$= \frac{c_l e^{-il\phi}}{2l} \frac{r^l}{a^{(l-1)}}. \quad (3.81)$$

Hence,

$$\partial_r V_{\mathbf{D}}(\mathbf{r}) = c_l e^{-il\phi} \frac{r^{(l-1)}}{2a^{(l-1)}}. \quad (3.82)$$

In order to match the fields at the boundary, one has to match V_{outside} with $V_{\text{inside}} = V_{\mathbf{D}}/\epsilon$, and $-\partial_r V = E_r = D_r$ on the outside with $-\partial_r V_{\mathbf{D}} = D_r$ on the inside (the angular dependence can be dropped since it is the same everywhere):

$$b_l a^{-l} = c_l a \int_0^\infty \frac{J_l^2(ka)}{k \epsilon(k, \omega)} dk, \quad (3.83)$$

$$b_l l a^{-l-1} = -c_l \frac{a^{(l-1)}}{2a^{(l-1)}} = -\frac{c_l}{2}. \quad (3.84)$$

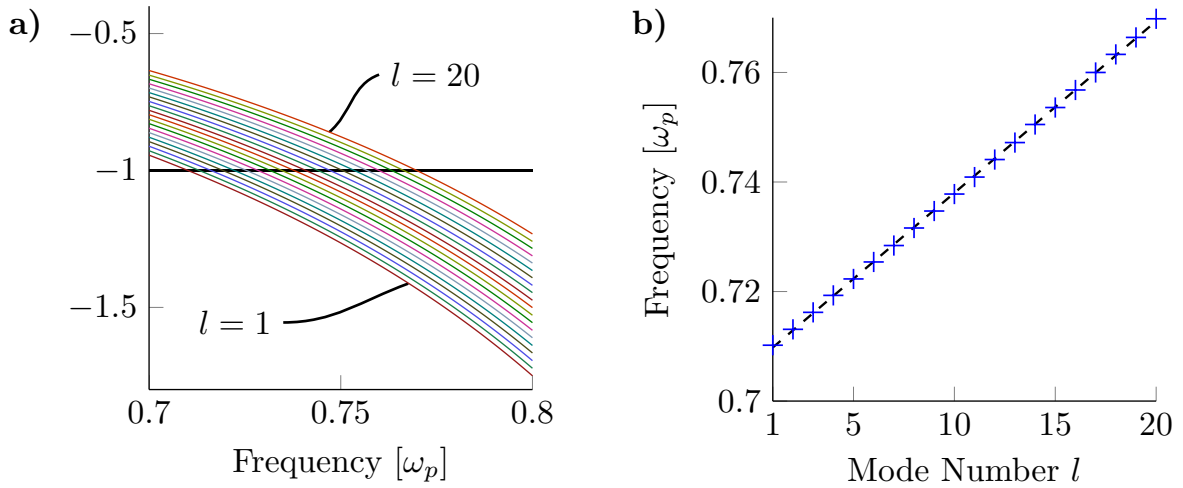


Figure 3.11: a) Graphical solution of Eq. (3.85) b) Linear Regression for the solutions from a) over the mode number l . The dependence is linear in the regime under consideration, for $l = 1 \dots 20$. The frequency ω solving Eq. (3.85) is given by $\omega = .7066\omega_p + .0031\omega_p \cdot l$ with $R^2 = .9999$.

3 Analytical Considerations

Thus, one has to solve

$$-1 = 2l \int_0^\infty \frac{J_l^2(ka)}{k \epsilon(k, \omega)} dk, \quad (3.85)$$

which be done numerically for the real part, for instance using the Gauss-Kronrod quadrature function of MATLAB [98]. The shift for the modes obtained from Eq. (3.85) in Fig. 3.11 is found to be $0.0031\omega_p$ which agrees once again with the asymptotic value from Sec. 3.2.2 which was found to be $0.00300\omega_p$ (Eq. (3.45)) and the shift found for the full Mie calculation $0.00304\omega_p$ (Eq. (3.24)).

3.3 Electrostatic Treatment of a Cylindrical Dimer

3.3.1 Introduction to Bicylindrical Coordinates

As shown above, the problem of a single cylinder can be treated analytically in many ways. For the nonlocal case, there is both a full Mie-solution and an electrostatic formulation. Going to a more complicated setup such as a cylindrical dimer means giving up many of the symmetries which simplified the treatment of the cylindrical setup. At the heart of the analytical treatment of a dimer structure lies a conformal map which provides a transformation between a strip of \mathbb{R}^2 and a dimer (Fig. 3.12). The Laplace-operator bears a complicated form in these transformed coordinates. As I will show shortly, in the most general case of a Poisson equation with sources, the operator does not separate. For the electrostatic case $\Delta V = 0$ however, the Laplace operator becomes particularly simple, which allows us to solve the problem at hand and draw important conclusions which will be of great use when interpreting the numerical findings for a cylindrical dimer in Chap. 5.2.

A general introduction to different coordinate systems is given in Ref. [109] and a very detailed account of bipolar coordinates can be found in Ref. [110], but also the considerations done by Ruppin for two spheres in Ref. [111] serve as a good guideline. I will follow these works in the following sections. The bicylindrical coordinates u and ξ are one of many possible extensions of bipolar coordinates. Just as for cylindrical coordinates, the third dimension is given by z . Bipolar coordinates can also be extended to treat bispherical or toroidal systems and thus are a powerful tool to treat a multitude of different geometries [110].

In a plane, the transformation between cartesian coordinates and bipolar coordinates is given by

$$x = a \frac{\sinh \xi}{(\cosh \xi - \cos u)}, \quad (3.86)$$

$$y = a \frac{\sin u}{(\cosh \xi - \cos u)}. \quad (3.87)$$

Since bipolar coordinates feature two poles, there is one additional free parameter called a . It determines the distance between the two foci that lie at $\pm a$. The coordinates ξ and u are built around these two foci. For any specific setup of two circles with their respective radii and a given distance between them, there is only one solution for a . The ξ -level curves are non-concentric circles around the foci (in a close zoom in on one of the foci, ξ looks similar to r in cylindrical coordinates, however approaching one of the foci, means approaching $\pm\infty$, rather than zero) and the u -level curves are truncated circles that connect the two foci (u takes the place of the angular variable ϕ in cylindrical coordinates, when zooming in on

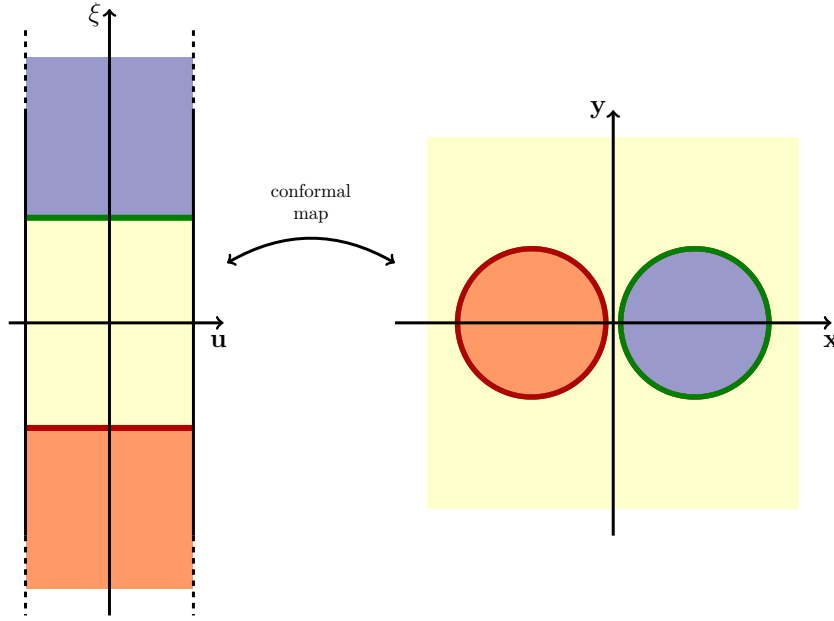


Figure 3.12: A conformal map provides a transformation between two cylinders and a strip of \mathbb{R}^2 . The horizontal lines (green and red) are mapped onto the surfaces of the two cylinders. The space extending beyond the lines, towards positive and negative infinity, is mapped into the cylinders and the space between the lines represents all of the surrounding space.

one of the foci – it runs from 0 to 2π). The values of the coordinates ξ and u in a cartesian coordinate system are depicted in Fig. 3.13.

It is possible to determine a for any specific problem via the center points of the two cylinders, $x_{c_{1/2}}$ and the radii $R_{1/2}$:

$$x_{c_{1/2}} = \frac{a}{\tanh \xi_{1/2}}, \quad R_{1/2} = \frac{a}{|\sinh \xi_{1/2}|}. \quad (3.88)$$

In this thesis, I consider radii $R_1 = R_2 = 10$ nm and a gap of 2 nm, corresponding to $x_{c_{1/2}} = \pm 11$ nm. Then,

$$\xi_{1/2} = \pm \text{Arcosh} \left(\frac{x_c}{R} \right) = \pm 0.443568245... \quad (3.89)$$

$$a = 4.582575... \text{ nm}. \quad (3.90)$$

3.3.2 Conformal Maps

In the last section I introduced the bicylindrical coordinates and from Figs. 3.12 and 3.13 one can gain some intuition for them. In order to work further with these coordinates, i.e. define differential operators or implement them in a computer program, it is helpful to define the bicylindrical coordinates as a conformal map, i.e. an analytic mapping, where cartesian space is interpreted as the complex plane,

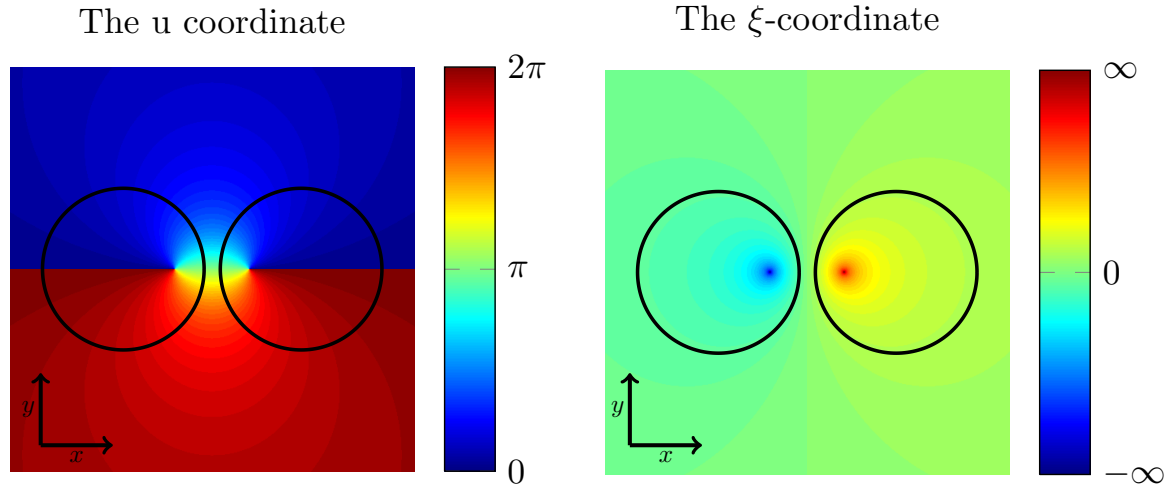


Figure 3.13: On the left, the u -coordinate is depicted, which runs from 0 to 2π – clockwise around the left focus which lies on the negative x -axis, and counterclockwise around the right focus on the positive x -axis (note however, that moving along a ξ -level line (a circle), u looks distorted towards the center of the plot, compared to the actual angle-variable ϕ in cylindrical coordinates). On the right, the ξ -coordinate is displayed which runs from $-\infty$ (left focus) to $+\infty$ (right focus). $\xi = 0$ represents both the y -axis and all of spatial infinity. The black circles represent the cylindrical dimer setup which I investigate in this thesis.

$z = x + iy$, and the general mapping is of the form

$$w = f(z) \quad (3.91)$$

$$= u + iv = f(x + iy). \quad (3.92)$$

In technical terms, a conformal map is a diffeomorphism (a bijective, differentiable mapping between manifolds whose inverse is also differentiable) which preserves the metric up to a scale. This means that under a conformal mapping, angles are preserved [112].

To gain some insight, I will take a small detour and discuss polar coordinates as a conformal map first.

Polar Coordinates as a Conformal Map

Let me start by considering a mapping

$$w = f(z) = \ln(z). \quad (3.93)$$

This can be rewritten

$$x + iy = e^{u+iv} = e^u (\cos v + i \sin v), \quad (3.94)$$

which resembles very much the well-known polar coordinates, but with e^u in lieu of ρ or r :

$$\begin{pmatrix} x \\ y \end{pmatrix} = e^u \begin{pmatrix} \cos v \\ \sin v \end{pmatrix}. \quad (3.95)$$

By performing a simple substitution, one obtains the ubiquitous polar coordinates, but that is not what I will do now and it will become apparent shortly, why the current form can be advantageous. The variable u now ranges from $-\infty$ to $+\infty$, whereas ρ or r assume only positive values, as they simply represent the distance from the origin. The variable v which takes on the role of ϕ , is found only as an argument of 2π -periodic trigonometric functions and therefore runs only from 0 to 2π (or from $-\pi$ to $+\pi$ if this convention is better suited for the problem at hand).

The main difference between the representation 3.95 and the usual form of polar coordinates becomes apparent when taking a look at the metric. The Jacobian is

$$J_{\text{conformal}} = \begin{pmatrix} e^u \cos(v) & -e^u \sin(v) \\ e^u \sin(v) & e^u \cos(v) \end{pmatrix}, \quad (3.96)$$

as opposed to

$$J_{\text{polar}} = \begin{pmatrix} \cos(\phi) & -r \sin(\phi) \\ \sin(\phi) & r \cos(\phi) \end{pmatrix} \quad (3.97)$$

for polar coordinates. Since the exponential function remains unaltered upon derivation, one realizes immediately that 3.96 looks more symmetric than 3.97 and the respective metric tensors $g = J^T J$ yield:

$$g_{\text{conformal}} = \begin{pmatrix} e^{2u} & 0 \\ 0 & e^{2u} \end{pmatrix} = \begin{pmatrix} h_u^2 & 0 \\ 0 & h_v^2 \end{pmatrix} =: h^2 \mathbb{1}, \quad (3.98)$$

and

$$g_{\text{polar}} = \begin{pmatrix} 1 & 0 \\ 0 & r^2 \end{pmatrix} = \begin{pmatrix} h_r^2 & 0 \\ 0 & h_\phi^2 \end{pmatrix}. \quad (3.99)$$

Comparing Eqs. (3.98) and (3.99), it becomes apparent why the transformation 3.93 is a conformal map which only rescales the metric, while polar coordinates are not. The entries h_i are just the scaling factors between the contravariant component and the unit-vector component of a given vector \mathbf{V} :

$$\mathbf{V} = V^i \frac{\partial}{\partial x^i} = V^i e_i = V^i h_i \hat{e}_i. \quad (3.100)$$

The symmetric metric has an immediate effect on the differential operators in the respective coordinates: The familiar form of the gradient, the divergence etc. in cylindrical or spherical coordinates is very asymmetric. The divergence acting on a vector $\mathbf{V} = V^i e_i = V^u e_u + V^v e_v = V^r e_r + V^\phi e_\phi$ is written as (using Einstein's sum convention)

$$\nabla \cdot \mathbf{V} = \frac{1}{\prod_i h_i} \partial_n \left[\left(\prod_n h_n \right) V^n / h_n \right], \quad (3.101)$$

3 Analytical Considerations

and the gradient of a function f

$$\nabla f = \frac{1}{h_i} (\partial_i f) \mathbf{e}_i. \quad (3.102)$$

When solving an electrostatic problem, the Laplacian is needed. It reads

$$\Delta f = \frac{1}{\prod_i h_i} \partial_n \left[\frac{\prod_i h_i}{h_n^2} \partial_n f \right], \quad (3.103)$$

which, in the symmetric case 3.98 yields simply

$$\Delta f = \frac{1}{h^2} \left[\partial_u^2 f + \partial_v^2 f \right]. \quad (3.104)$$

In the case of a homogeneous equation, one can get rid of the prefactor $1/h^2$ and the equation takes the same form as in cartesian coordinates and one can easily write down the harmonic solutions. However, it has to be kept in mind that, unlike in cartesian coordinates, v is limited from $-\pi$ to π and only 2π -periodic solutions are allowed.

3.3.3 Bicylindrical Coordinates as a Conformal Map

The bicylindrical coordinates introduced above via 3.86 and 3.87 are already a conformal map that can be written as

$$w = f(z) = -i \ln \left(\frac{z+a}{z-a} \right), \quad (3.105)$$

and the metric is

$$g = h^2 \mathbb{1} = \left(\frac{a}{\cosh \xi - \cos u} \right)^2 \mathbb{1}. \quad (3.106)$$

Therefore, the Laplace Operator reads

$$\Delta f = \left(\frac{\cosh \xi - \cos u}{a} \right)^2 \left[\partial_\xi^2 f + \partial_u^2 f \right], \quad (3.107)$$

which, again, separates in the case of the electrostatic Poisson equation $\Delta V = 0$:

$$V = f_1(\xi) f_2(u), \quad (3.108)$$

and has the harmonic solutions

$$f_1 = [\sinh k\xi, \cosh k\xi] \quad \text{or} \quad [e^{k\xi}, e^{-k\xi}] \quad (3.109)$$

$$f_2 = [\sin ku, \cos ku] \quad \text{or} \quad [e^{iku}, e^{-iku}]. \quad (3.110)$$

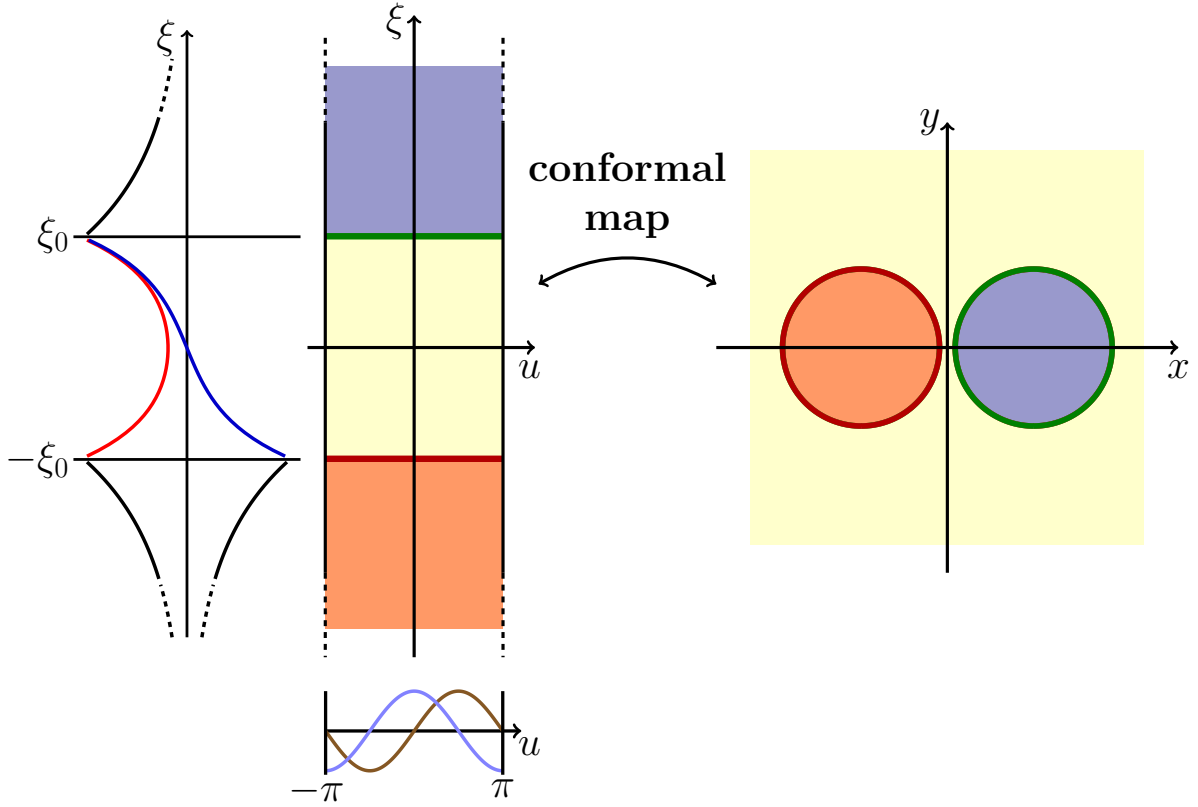


Figure 3.14: The conformal map for bicylindrical coordinates is depicted along with the possible solutions of Laplace's equation in ξ - and u -coordinates for $l = 1$.

The solutions for the electrostatic potential given by Eqs. (3.109) and (3.110) are depicted in Fig. 3.14 for the specific case of a bicylindrical setup. For the ξ -coordinate between the cylinders hyperbolic sine and hyperbolic cosine are possible solutions. Inside the cylinders the solutions have to be exponentially decaying to avoid singularities. The variable u takes on the role of the azimuthal coordinate ϕ in cylindrical coordinates and the solutions have to be 2π -periodic, thus k is quantized. Symmetrical considerations make it possible to split the problem into 4 categories, combining the solutions $\sin(ku)$ or $\cos(ku)$ with $\sinh(k\xi)$ or $\cosh(k\xi)$. In Fig. 3.15, I display the 4 types of potentials, along with their gradients, shown as arrows (which correspond to the electric field), for $k = 1$. In Fig. 3.16, the x - and y -components of the electric fields are displayed. The field distributions are also important for the discussion of the numerical results in Chap. 5, since they are accessible in the discontinuous Galerkin time domain method. The four symmetry categories can be identified as pertaining to the dihedral symmetry point-group D_2 . More specifically, each potential represents one of the four irreducible representations of this group. A thorough discussion of the symmetries is presented in the next section.

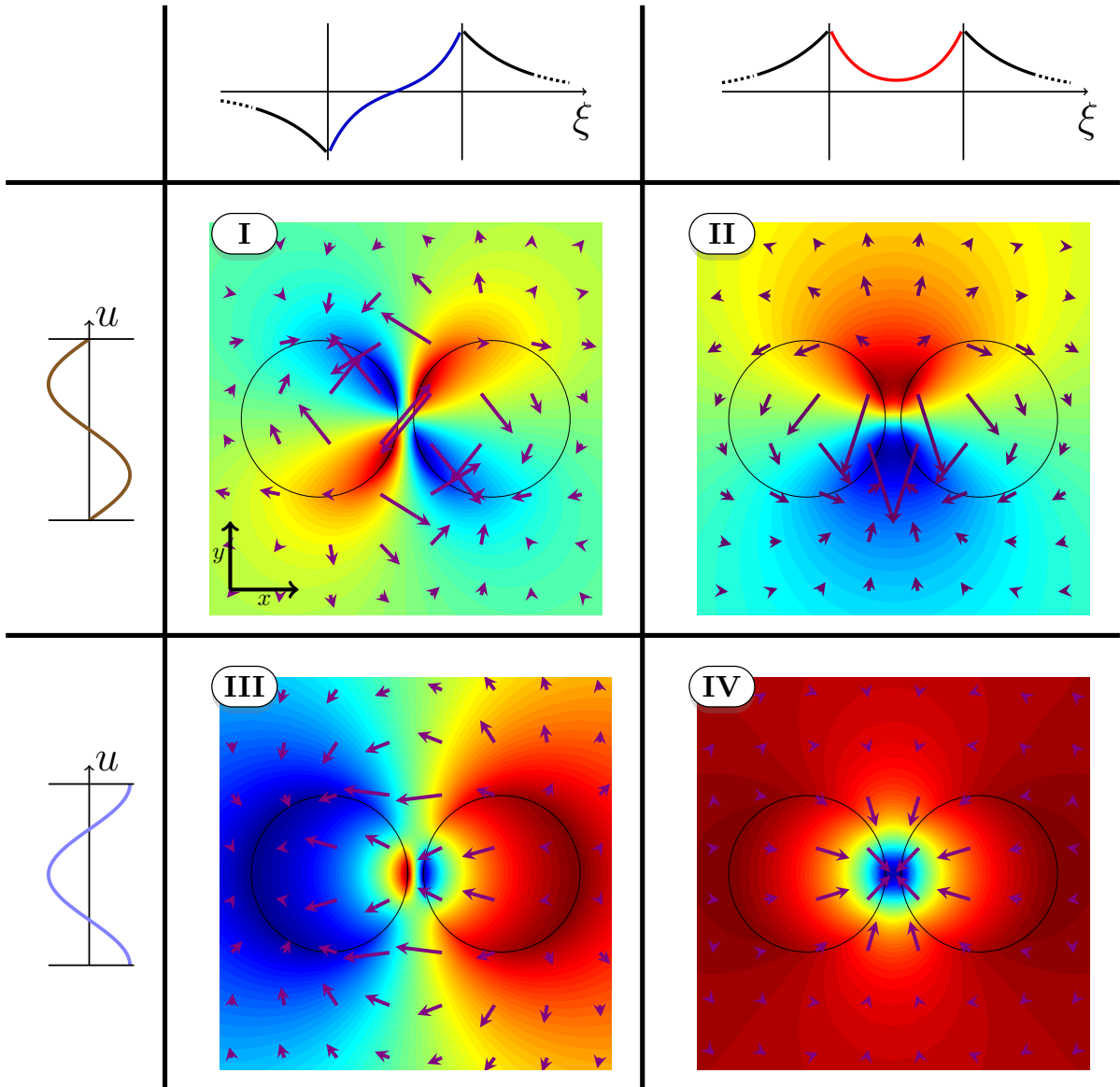


Figure 3.15: The four different types of electrostatic potentials which can be constructed in bi-cylindrical coordinates. I categorize them in four classes, labeled I-IV.

Again, as for the cylinder in Sec. 3.2, I now solve for the modes, via

$$V_i(\pm\xi_0) = V_o(\pm\xi_0), \quad (3.111)$$

$$\epsilon(\omega) \frac{\partial V_i}{\partial \xi} \Big|_{\pm\xi_0} = \epsilon_M \frac{\partial V_o}{\partial \xi} \Big|_{\pm\xi_0}, \quad (3.112)$$

where i stands for inside the cylinder (where the permittivity is given by $\epsilon(\omega)$) and o stands for outside

where the surrounding medium shall be air with $\epsilon_M = 1$. The azimuthal variable u plays no role

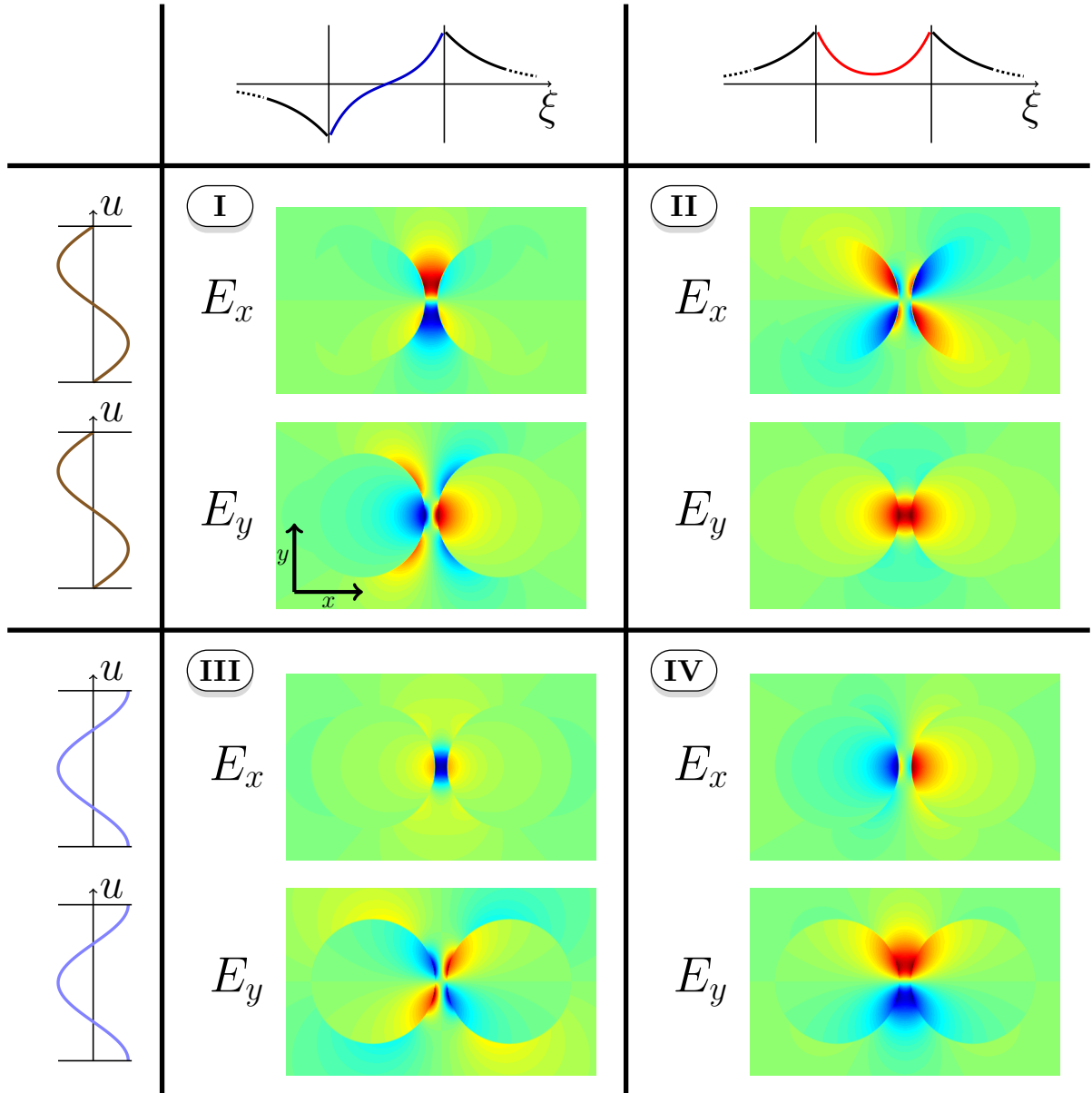


Figure 3.16: Electric field components corresponding to the four different types of potentials from Fig. 3.15.

in the boundary problem, since the u -dependence is the same everywhere in space, so the sine- and cosine-solutions are degenerate in frequency. According to Fig. 3.14, exponentially decaying solutions $e^{k\xi}, e^{-k\xi}$ are needed inside the cylinders and hyperbolic functions $\sinh k\xi, \cosh k\xi$ in all the rest of

3 Analytical Considerations

space. Inserting this into Eqs. (3.111) and (3.112), the solutions are

$$\begin{aligned}\epsilon(\omega) &= -\coth(k\xi_0) \quad \text{for sinh-type solutions,} \\ \epsilon(\omega) &= -\tanh(k\xi_0) \quad \text{for cosh-type solutions.}\end{aligned}\tag{3.113}$$

For $k \rightarrow \infty$, they both tend to $\epsilon(\omega) = -1$, which is the same as in the case of a single cylinder. Thus, the limiting frequency is the surface plasmon frequency ω_{sp} . However, now there are two solutions for

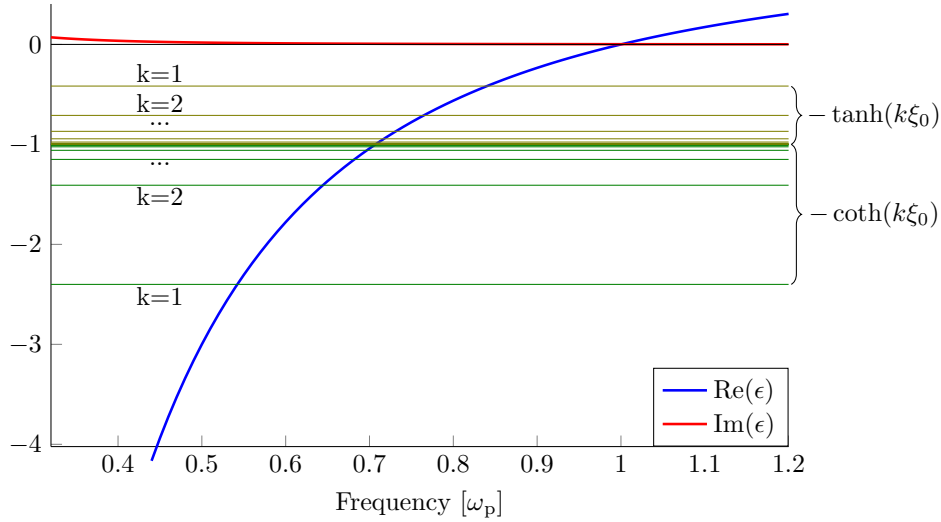


Figure 3.17: Graphical solution for the frequencies of the modes of a cylindrical dimer within electrostatic theory, as given by Eq. (3.113).

each k , one above and one below the limiting frequency ω_{sp} , which is a typical hybridization effect. The frequencies corresponding to the modes k (the graphical solutions to Eq. (3.113)) are depicted in Fig. 3.17.

The excitation of these modes, based on the symmetries of the incoming light pulse, is discussed in the next section, for linear and nonlinear processes.

In Sec. 5.2 I perform numerical simulations for such a setup to test this theory, which can be done by analyzing the spectra and the field distributions. Furthermore, the influence of nonlocality and nonlinearity in such a system will be investigated numerically.

3.4 Group Theoretical Considerations

Group-theory is a very helpful tool in categorizing the modes and drawing important conclusions in the context of the hydrodynamic model which will become important in the context of second harmonic generation in Chap. 5. By inspecting the gradients (the arrows) in Fig. 3.15, one expects that solutions of class II can be excited by a Gaussian wave packet which is incident from the left or right (\mathbf{k} parallel to the dimer axis) and class III by a wave which is rotated by 90 degrees (\mathbf{k} perpendicular to the dimer axis). Furthermore, class I should be excited for both angles of incidence, as long as there are retardation effects, i.e. the extent of the dimer cannot be too small, compared to the wavelength of the incoming

light. Class IV is a “dark mode” which should be forbidden altogether. I now present some more rigorous considerations which put the mode-selection process that I just described on more solid ground. Employing the symmetries of the hydrodynamic and Maxwell equations the mode selection rules can also be found for the SHG signal. I start out with the cylindrical dimer, then I discuss the single cylinder finally present calculations for a V-groove.

3.4.1 Cylindrical Dimer

The cylindrical dimer features a number of symmetries which can be exploited to make statements about the selection of modes under certain excitations. The foundations of group theory which I use in this section can be found for instance in Refs. [113, 114].

The cylindrical dimer geometry which is infinitely extended in z -direction is mapped onto itself by virtue of four different symmetry operations: a rotation around the z -axis by 180 degrees (C_2 -symmetry), mirroring on the xz -plane (σ_{xz} -symmetry) and mirroring on the yz -plane (σ_{yz} -symmetry), and, obviously, the identity operation I . This corresponds to the symmetry point-group C_{2v} [115]. In the present case of an infinitely extended system with $\partial_z F = 0$ for any quantity F , this is not only isomorphic but even equivalent to the dihedral-group D_2 . This group is abelian and the character table of D_2 or C_{2v} can be written in the following form:

$C_{2v} = D_2$	I	$C_2(z)$	$\sigma_{xz} = C_2(x)$	$\sigma_{yz} = C_2(y)$
A	1	1	1	1
B_1	1	1	-1	-1
B_2	1	-1	1	-1
B_3	1	-1	-1	1

I write the transformation behavior of a quantity, e.g. a field component F as $\mathcal{T}[F]$, i.e. $\mathcal{T}[F]$ specifies under which transformation the field is mapped onto itself. The direct sum-symbol \oplus indicates an addition or superposition of transformation behaviors where all signs and magnitudes are dropped. As an example, a field component of an incoming field, E_{y1} , which transforms as a superposition of a symmetry of type A and a symmetry of type B_2 is written as

$$\mathcal{T}[E_{y1}] = A \oplus B_2. \quad (3.114)$$

The dimer itself thus transforms as A . The four types of electrostatic potentials each pertain to one of the symmetry classes, i.e. irreducible representations from the character table. Their symmetries can be easily identified by inspection. They are given in Fig. 3.18. The two-dimensional nabla-operator transforms as

$$\mathcal{T}[\nabla] = \begin{pmatrix} \mathcal{T}[\partial_x] \\ \mathcal{T}[\partial_y] \end{pmatrix} = \begin{pmatrix} B_2 \\ B_3 \end{pmatrix}. \quad (3.115)$$

The multiplication rules can be readily extracted from the character table by multiplying the elements in the same column and identifying the results with one of the four possible symmetry classes.

3 Analytical Considerations

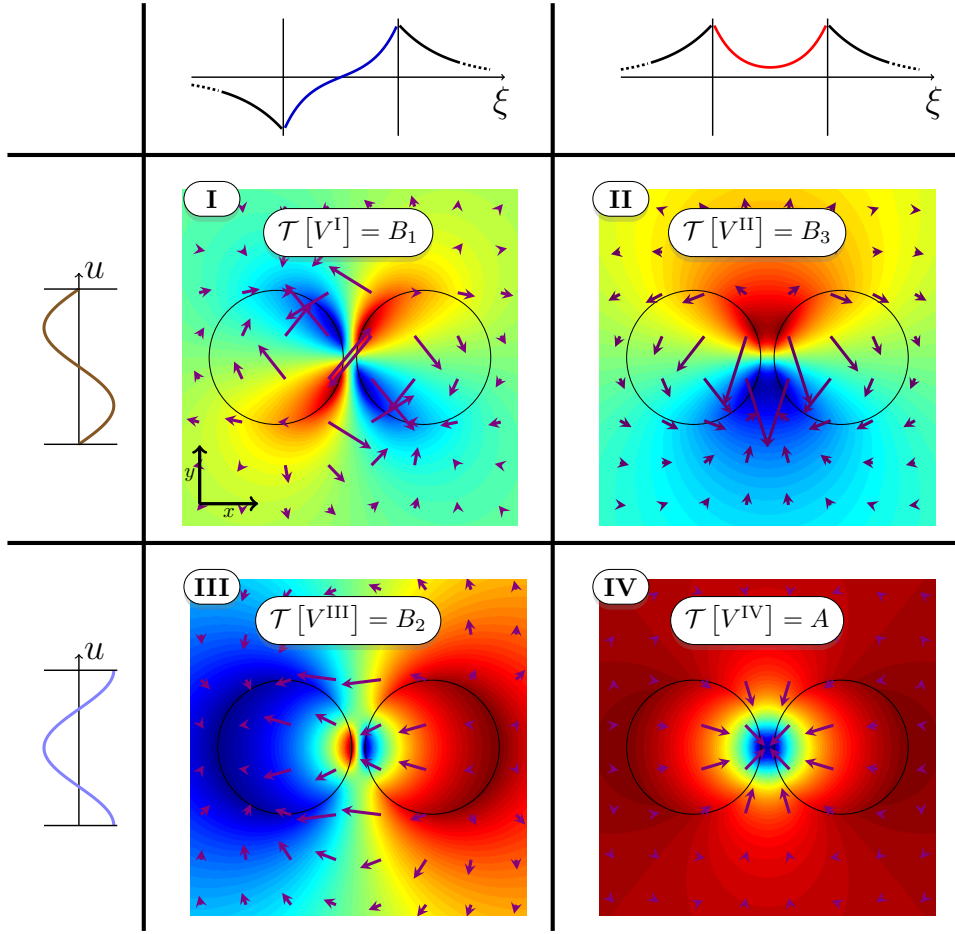


Figure 3.18: Potentials $V^I - V^{IV}$ of the four classes of modes of a cylindrical dimer and their symmetries.

The rules yield ($i, j, k = 1, 2, 3$, mutually exclusive)

$$B_i B_j = B_j B_i = B_k \quad \text{and cyclic,} \quad (3.116)$$

$$B_i A = B_i, \quad (3.117)$$

$$B_i^2 = A, \quad (3.118)$$

$$A^2 = A. \quad (3.119)$$

With the multiplication rules, the symmetries of the potentials, and those of the nabla-operator at hand, it is easy to determine the symmetries of the electric field components of the modes, i.e. express them

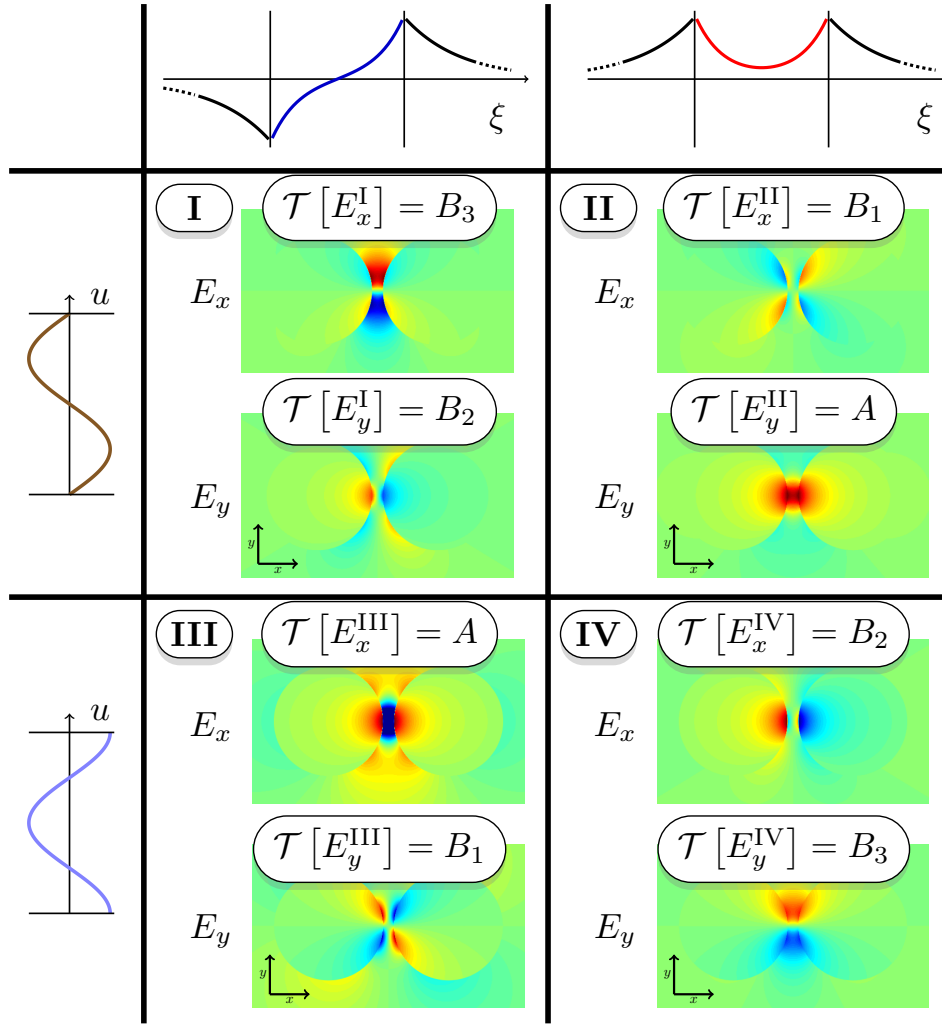


Figure 3.19: Electric field components of the four classes of modes of a cylindrical dimer and their symmetries.

in terms of irreducible representations:

$$\mathcal{T}[\mathbf{E}^I] = \mathcal{T}[\nabla] \mathcal{T}[V^I] = \begin{pmatrix} B_2 \\ B_3 \end{pmatrix} B_1 = \begin{pmatrix} B_3 \\ B_2 \end{pmatrix}, \quad (3.120)$$

$$\mathcal{T}[\mathbf{E}^{II}] = \mathcal{T}[\nabla] \mathcal{T}[V^{II}] = \begin{pmatrix} B_2 \\ B_3 \end{pmatrix} B_3 = \begin{pmatrix} B_1 \\ A \end{pmatrix}, \quad (3.121)$$

$$\mathcal{T}[\mathbf{E}^{III}] = \mathcal{T}[\nabla] \mathcal{T}[V^{III}] = \begin{pmatrix} B_2 \\ B_3 \end{pmatrix} B_2 = \begin{pmatrix} A \\ B_1 \end{pmatrix}, \quad (3.122)$$

$$\mathcal{T}[\mathbf{E}^{IV}] = \mathcal{T}[\nabla] \mathcal{T}[V^{IV}] = \begin{pmatrix} B_2 \\ B_3 \end{pmatrix} A = \begin{pmatrix} B_2 \\ B_3 \end{pmatrix}. \quad (3.123)$$

3 Analytical Considerations

The field distributions, identified with their respective irreducible representations are shown in Fig. 3.19.

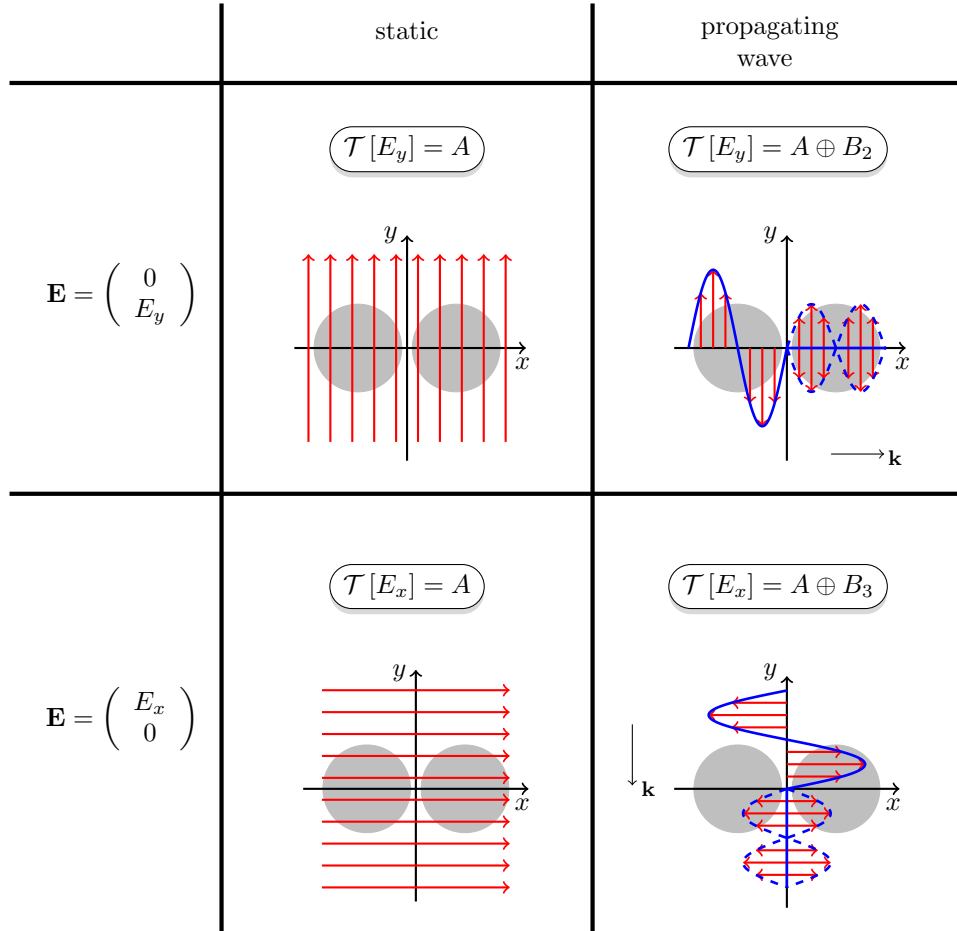


Figure 3.20: This schematic depicts the symmetries for a fully static field (left column) and for a propagating wave packet (at a fixed time). The symmetries of the static fields are always given by the irreducible representation A as they are homogeneous in space. A pulse propagating in x -direction is homogeneous in y -direction and changes its phase along x , therefore it can be constructed out of a superposition of A and B_2 . Likewise, a pulse propagating in y -direction is constructed out of A and B_3 . (Caution: do not apply the symmetry operation to the direction of the arrows but only to their position.)

To excite the modes, the incident wave has to match the symmetry of the field components. In the DGTD simulations performed later on, the incoming waves are propagating in x - or y -direction and the electric field lies in the xy -plane, the magnetic field points in z -direction. Such a propagating wave packet, to which one can assign a frequency and a temporal width is beyond zeroth order electrostatics, where only static electric fields, such as a static field in x -direction or a static field in y -direction are allowed. The symmetries of a wave packet propagating in either direction, thus showing different phases at different points in space, can however still be decomposed into their irreducible representations. The

schematic in Fig. 3.20 illustrates how this can be done.

The static case is homogeneous in space. The dynamic case for each of the polarizations $\mathbf{E} = E_x \mathbf{e}_x$ and $\mathbf{E} = E_y \mathbf{e}_y$ ($\mathbf{e}_{x,y}$ denote the unit vectors in x and y direction) is in both cases constructed out of the symmetry of the static case and one additional component. For propagation along the x -axis, the signal changes in the x -direction and is homogeneous along y , yielding a B_2 -symmetry and vice versa for propagation along the y -axis. The smaller the plasmonic particle becomes, the further the electrostatic regime is entered (the phase-change across the particle becomes smaller), reducing to the static A -contribution. Combining the symmetry considerations above and the solutions from Eq. (3.113), one expects the following results when impinging a Gaussian beam on such a dimer setup: For incidence along the dimer axis, there should be solutions of class I and of class II, hence, solutions below and above ω_{sp} , whereas for incidence perpendicular to the dimer axis, the solutions will be of class I and of class III (both of which lie below ω_{sp}). The following table sums up these findings:

	sinh (low frequency)	cosh (high frequency)
sin	class I excitation from both directions (retardation needed)	class II excitation along dimer axis
cos	class III excitation perpendicular to dimer axis	class IV “dark mode”

In Sec. 5.2.2, I show that the class I contributions do in fact grow smaller when the size of the particle is reduced. Here I will not comment further on the respective magnitudes (I will leave this part to the numerical method) but only use the notation introduced above, employing the direct sum sign \oplus , dropping all magnitudes.

It is now time to dive into the hydrodynamic and the Maxwell equations. Having defined the nomenclature and the necessary symbols, it is possible to derive the symmetries of higher order quantities in terms of those of known quantities.

The uniform equilibrium density has the same symmetry as the dimer itself

$$\mathcal{T}[n_0] = A, \quad (3.124)$$

which I will plug into the equations right away to simplify them. The time-derivative does not alter the (spatial) symmetry.

3 Analytical Considerations

The first equation I would like to analyze is the first order continuity equation:

$$\partial_t n_1 = -\nabla \cdot (n_0 \mathbf{v}_1) \quad (3.125)$$

$$\Rightarrow \mathcal{T}[n_1] = \begin{pmatrix} B_2 \\ B_3 \end{pmatrix} A \mathcal{T}[\mathbf{v}_1] \quad (3.126)$$

$$\Rightarrow \mathcal{T}[n_1] = B_2 \mathcal{T}[v_{1x}] \oplus B_3 \mathcal{T}[v_{1y}]. \quad (3.127)$$

The Euler equation yields

$$m_e n_0 \partial_t \mathbf{v}_1 = -m_e \gamma n_0 \mathbf{v}_1 - \frac{5}{3} \kappa n_0^{\frac{2}{3}} \nabla n_1 - e n_0 \mathbf{E}_1 \quad (3.128)$$

$$\Rightarrow \mathcal{T}[v_{1x}] = B_2 \mathcal{T}[n_1] \oplus \mathcal{T}[E_{1x}] \quad (3.129)$$

$$\mathcal{T}[v_{1y}] = B_3 \mathcal{T}[n_1] \oplus \mathcal{T}[E_{1y}]. \quad (3.130)$$

Inserting Eq. (3.127) into Eqs. (3.129) and (3.130) leads to

$$\begin{aligned} \mathcal{T}[v_{1x}] &= B_2 B_2 \mathcal{T}[v_{1x}] \oplus B_2 B_3 \mathcal{T}[v_{1y}] \oplus \mathcal{T}[E_{1x}] \\ &= B_1 \mathcal{T}[v_{1y}] \oplus \mathcal{T}[E_{1x}] \end{aligned} \quad (3.131)$$

$$\mathcal{T}[v_{1y}] = B_1 \mathcal{T}[v_{1x}] \oplus \mathcal{T}[E_{1y}], \quad (3.132)$$

which makes it possible to express the velocity components in terms of the electric fields

$$\begin{aligned} \mathcal{T}[v_{1x}] &= \mathcal{T}[E_{1x}] \oplus B_1 \mathcal{T}[E_{1y}] \\ \mathcal{T}[v_{1y}] &= \mathcal{T}[E_{1y}] \oplus B_1 \mathcal{T}[E_{1x}]. \end{aligned} \quad (3.133)$$

These relations simply show that the movement of the particles which are driven by the electric field, given by v_{1i} has the same symmetry as E_{1i} ($i = x, y$). This is easily fulfilled if the second field component E_{1j} ($j = y, x$) is zero. In the case of the dimer modes, $E_{1j} \neq 0$, but then $\mathcal{T}[E_{1j}]$ is not independent of $\mathcal{T}[E_{1i}]$. The two are connected through the electrostatic potential. Since the gradient operator is given by $\mathcal{T}[\nabla] = (B_2 \ B_3)^T$, the relation

$$\mathcal{T}[E_{1x}] = B_2 \mathcal{T}[V] = B_1 B_3 \mathcal{T}[V] = B_1 \mathcal{T}[E_{1y}] \quad (3.134)$$

holds, in agreement with Eq. (3.133).

Another sanity check of the procedure can be done by combining Eq. (3.133) with the continuity equation, Eq. (3.127). One then finds

$$\mathcal{T}[n_1] = B_2 \mathcal{T}[E_{1x}] \oplus B_3 \mathcal{T}[E_{1y}]. \quad (3.135)$$

Equation (3.135) shows that the first order density has the same symmetry as the electrostatic potential

$$\mathcal{T}[n_1] = \mathcal{T}[V], \quad (3.136)$$

which has to be true, because the excess charges give rise to the potentials and therefore must have the same symmetries. This is also demonstrated numerically in Chap. 5.

Before I can move on to the second order equations, I need to determine the symmetry of the magnetic field (for the polarization employed here, there is only the H_z -component), which is a necessary ingredient for the second order Euler equation. It is straightforwardly extracted from one of Maxwell's curl equations:

$$\partial_t \mathbf{H}_1 = -\nabla \times \mathbf{E}_1 \quad (3.137)$$

$$\implies \mathcal{T}[H_{1z}] = B_3 \mathcal{T}[E_{1x}] \oplus B_2 \mathcal{T}[E_{1y}]. \quad (3.138)$$

The second order continuity equation reads

$$\partial_t n_2 = -\nabla \cdot (n_1 \mathbf{v}_1 + n_0 \mathbf{v}_2) \quad (3.139)$$

$$\begin{aligned} \implies \mathcal{T}[n_2] &= \mathcal{T}[n_1] \left[B_2 \mathcal{T}[v_{1x}] \oplus B_3 \mathcal{T}[v_{1y}] \right] \\ &\quad \oplus A \left[B_2 \mathcal{T}[v_{2x}] \oplus B_3 \mathcal{T}[v_{2y}] \right] \end{aligned} \quad (3.140)$$

$$\stackrel{3.135, 3.133}{\implies} \mathcal{T}[n_2] = \left[B_2 \mathcal{T}[E_{1x}] \oplus B_3 \mathcal{T}[E_{1y}] \right]^2 \oplus B_2 \mathcal{T}[v_{2x}] \oplus B_3 \mathcal{T}[v_{2y}] \quad (3.141)$$

$$\stackrel{3.134}{\implies} \mathcal{T}[n_2] = \left[\mathcal{T}[E_{1x}] \right]^2 \oplus B_2 \mathcal{T}[v_{2x}] \oplus B_3 \mathcal{T}[v_{2y}]. \quad (3.142)$$

3 Analytical Considerations

The second order Euler equation is given by

$$\begin{aligned}
& m_e(n_0\partial_t\mathbf{v}_2) + m_0n_1\partial_t\mathbf{v}_1 + m_en_0(\mathbf{v}_1 \cdot \nabla)\mathbf{v}_1 \\
& = -m_e\gamma(n_1\mathbf{v}_1 + n_0\mathbf{v}_2) \\
& \quad - \frac{5}{9}\kappa n_0^{-1/3}\nabla n_1^2 - \frac{5}{3}\kappa n_0^{2/3}\nabla n_2 \\
& \quad - e(n_1\mathbf{E}_1 + n_0\mathbf{E}_2) \\
& \quad - en_0\mathbf{v}_1 \times \mathbf{H}_1
\end{aligned} \tag{3.143}$$

$$\begin{aligned}
& \xrightarrow{x\text{-component}} \mathcal{T}[v_{2x}] \oplus \mathcal{T}[n_1]\mathcal{T}[v_{1x}] + \left[B_2\mathcal{T}[v_{1x}] \oplus B_3\mathcal{T}[v_{1y}] \right] \mathcal{T}[v_{1x}] \\
& = \mathcal{T}[n_1]\mathcal{T}[v_{1x}] \oplus \mathcal{T}[v_{2x}] \oplus B_2 \left[\mathcal{T}[n_1] \right]^2 \oplus B_2\mathcal{T}[n_2] \\
& \quad \oplus \mathcal{T}[n_1]\mathcal{T}[E_{1x}] \oplus \mathcal{T}[E_{2x}] \oplus \mathcal{T}[v_{1y}]\mathcal{T}[H_{1z}]
\end{aligned} \tag{3.144}$$

$$\begin{aligned}
& \xrightarrow{3.1343, 133} B_2 \left[\mathcal{T}[E_{1x}] \right]^2 = B_2 \left[\mathcal{T}[E_{1x}] \right]^2 \oplus \mathcal{T}[v_{2x}] \oplus B_2 \left[\mathcal{T}[E_{1x}] \right]^2 \oplus B_2\mathcal{T}[n_2] \\
& \quad \oplus B_2 \left[\mathcal{T}[E_{1x}] \right]^2 \oplus \mathcal{T}[E_{2x}] \oplus B_1\mathcal{T}[E_{1x}]\mathcal{T}[H_{1z}] \\
& = \mathcal{T}[v_{2x}] \oplus B_2\mathcal{T}[n_2] \oplus \mathcal{T}[E_{2x}].
\end{aligned} \tag{3.145}$$

This results in an expression for $\mathcal{T}[v_{2x}]$ and by repeating the same procedure for the y -component, one arrives at

$$\mathcal{T}[v_{2x}] = B_2 \left[\mathcal{T}[E_{1x}] \right]^2 \oplus B_2\mathcal{T}[n_2] \oplus \mathcal{T}[E_{2x}], \tag{3.146}$$

$$\mathcal{T}[v_{2y}] = B_3 \left[\mathcal{T}[E_{1x}] \right]^2 \oplus B_3\mathcal{T}[n_2] \oplus \mathcal{T}[E_{2y}]. \tag{3.147}$$

Inserting both into Eq. (3.142) yields

$$\mathcal{T}[n_2] = \left[\mathcal{T}[E_{1x}] \right]^2 \oplus B_2\mathcal{T}[E_{2x}], \tag{3.148}$$

which establishes a connection between the second order density and electric field and the first order electric field. The second order density and electric field are connected in an easy way by Gauß' law

$$B_2\mathcal{T}[E_{2x}] \oplus B_3B_1\mathcal{T}[E_{2x}] = \mathcal{T}[n_2], \tag{3.149}$$

where I have made use of the fact that the second order electric field components are connected in the same way as those of first order since the orders decouple in the curl-equation. Thus I can finally write down the relation between the first order and the second-order electric field:

$$\mathcal{T}[E_{2x}] = B_2 \left[\mathcal{T}[E_{1x}] \right]^2. \tag{3.150}$$

Let me apply this to the case of the symmetries of the dimer-modes. For a wave packet propagating in y -direction, the symmetry of the electric field is given by (cf. Fig. 3.20)

$$\mathcal{T}[E_{x,\text{inc}}] = \mathcal{T}[E_{1x}] = A \oplus B_3, \quad (3.151)$$

which is compatible with modes of class I and II that are both excited in this case. Calculating the second order fields

$$\mathcal{T}[E_{2x}] = B_2 [A \oplus B_3]^2 = B_2(A \oplus B_3) = B_2 \oplus B_1, \quad (3.152)$$

reveals that those are precisely the other two symmetries, i.e. the modes of class II and IV. Repeating the exercise for the other angle of incidence is straightforward: Starting with

$$\mathcal{T}[E_{y,\text{inc}}] = A \oplus B_2, \quad (3.153)$$

the modes of class I and II are excited, which must have first order E_x -fields of the type

$$\mathcal{T}[E_{1x}] = B_1 \oplus B_3 \quad (3.154)$$

and

$$\mathcal{T}[E_{2x}] = B_2 [B_1 \oplus B_3]^2 = B_2(A \oplus B_2) = B_2 \oplus A. \quad (3.155)$$

Now the selection rules for the modes of the cylindrical dimer rest on more solid ground. The group-theoretical considerations reveal that for second harmonics the modes which are excited are precisely the ones which were excluded in the linear case.

3.4.2 SHG from a Single Cylinder

In Fig. 3.10, I presented the field images for a single cylinder for the dipole and quadrupole mode, for the two possible degenerate solutions employing sine and cosine respectively for the azimuthal variable.

For an incoming waves that is propagating in x -direction and an electric field in y -direction, the sine-modes from Fig. 3.10 **I** can be excited, according to Fig. 3.20.

The dipole mode which is excited thus has a potential which fulfills the B_3 symmetry. Therefore the fields must have the symmetries

$$\mathcal{T}[\mathbf{E}_{\text{dipole}}] = \begin{pmatrix} B_2 \\ B_3 \end{pmatrix} B_3 = \begin{pmatrix} B_1 \\ A \end{pmatrix}. \quad (3.156)$$

As can be seen, this mode is easily excited, even by a static field, through the A -symmetry in the E_y -component. The second harmonics of this distribution would have the x -component given by

$$\mathcal{T}[\mathbf{E}_{x,\text{dipole,SHG}}] = B_2[B_1]^2 = B_2. \quad (3.157)$$

However, as can be readily seen from Fig. 3.10, a dipole mode can under no circumstances have an electric field component featuring a B_2 symmetry, as they are always of type A or B_1 .

The quadrupole potential however has a B_1 -symmetry, thus

$$\mathcal{T}[\mathbf{E}_{\text{quadrupole}}] = \begin{pmatrix} B_2 \\ B_3 \end{pmatrix} B_1 = \begin{pmatrix} B_3 \\ B_2 \end{pmatrix} \quad (3.158)$$

(it is excited by means of the B_2 symmetry in the E_y -component of a dynamic pulse) and

$$\mathcal{T}[\mathbf{E}_{x,\text{quadrupole,SHG}}] = B_2[B_3]^2 = B_2, \quad (3.159)$$

which is only fulfilled for the rotated mode, i.e., using the sine instead of the cosine solution.

Thus it is to be expected that SHG at the dipole frequency has to be suppressed in a single cylinder.

3.4.3 SHG from a V-Groove

The findings from the previous sections can now be applied to other systems of lower symmetry. A v-groove structure as in Fig. 3.21, i.e. an antenna with a v-shaped cut on one side is an ideally-suited system as it breaks the high symmetry of the dimer as it cannot be mirrored upside down. The structure is seemingly more complicated than the cylindrical dimer because of the lower symmetry. From a group-theoretical point of view, it turns out that its symmetries are fully contained in the theory above: The V-groove is only mapped onto itself by mirroring or rotating on the y -axis which corresponds to a simple C_2 point group. Therefore, the other operations have to be eliminated from the character table and one arrives at a character table that is actually simpler than the one before:

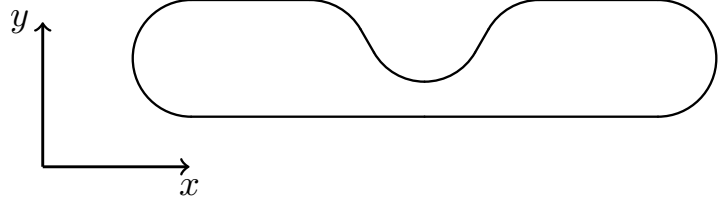


Figure 3.21: Schematic of a V-groove structure

C_2	I	$C_2(z)$	$C_2(x)$	$C_2(y)$
A	1	-	-	1
B_1	1	-	-	-1
B_2	1	-	-	-1
B_3	1	-	-	1

Thus there are only two symmetries left and the other two symmetries from the dimer geometry can be identified as

$$B_1^{D_2} \equiv B_2^{D_2} \equiv B^{C_2}, \quad (3.160)$$

$$A^{D_2} \equiv B_3^{D_2} \equiv A^{C_2}. \quad (3.161)$$

By making the corresponding replacements in the equations for the dimer one readily obtains the symmetries for the first and second order fields: For a wave propagating in y -direction, with the \mathbf{E} -field polarized in x -direction, along the long axis of the V-groove, one finds

$$\mathcal{T}[E_{x,\text{incoming}}^{\text{dimer}}] = \mathcal{T}[E_{1x}^{\text{dimer}}] = A^{D_2} \oplus B_3^{D_2} \longrightarrow \mathcal{T}[E_{1x}^{\text{V-groove}}] = A^{C_2} \quad (3.162)$$

and therefore

$$\mathcal{T}[E_{2x}^{\text{V-groove}}] = B^{C_2} [A^{C_2}]^2 = B^{C_2}(A^{C_2}) = B^{C_2}. \quad (3.163)$$

Which shows that for this angle of incidence the nonlinearly excited modes are not the ones which are excited linearly. For the other angle of incidence, the mode symmetry is given by

$$\mathcal{T}[E_{1x}^{\text{dimer}}] = B_1^{D_2} \oplus B_3^{D_2} \longrightarrow \mathcal{T}[E_{1x}^{\text{V-groove}}] = B^{C_2} \oplus A^{C_2} \quad (3.164)$$

and

$$\mathcal{T}[E_{2x}^{\text{V-groove}}] = B^{C_2} [B^{C_2} \oplus A^{C_2}]^2 = B^{C_2}(A^{C_2} \oplus B^{C_2}) = B^{C_2} \oplus A^{C_2}. \quad (3.165)$$

So for this angle of incidence, both classes of modes are excited on both the linear and the nonlinear level. These predictions are also confirmed numerically in Chap. 5.3.

4

CHAPTER 4

THE DISCONTINUOUS GALERKIN TIME DOMAIN METHOD

This chapter deals with the numerical scheme that is employed in this thesis. The discontinuous Galerkin time domain (DGTD) method which I used was written over the years in the group of Prof. Busch and consecutively extended and improved by generations of students and researchers. The basics of this method are amply discussed in various PhD-theses, most notably Refs. [116, 117], as well as in Ref. [118]. After some comments on why this particular method is a suitable choice for my purposes, I discuss those features that are important for the very calculations done within the thesis. I discuss the important new features concerning the hydrodynamic model and the challenges that come with it. For a very thorough discussion of the implementation of the hydrodynamic model, I refer the reader also to Ref. [73]. The derivation of the correct form of the hydrodynamic equations in dimensionless units, finding and implementing analytical test cases and ensuring convergence, as well as applying the method to new systems were my main contributions. These aspects are also discussed here.

4.1 Numerical Simulations of Plasmonic Nanoparticles

In the previous chapters it became apparent that the analytical possibilities to treat plasmonic structures are limited to highly symmetric structures. To treat more complicated systems such as dimers, one has to resort to numerical methods that are suitable to solve Maxwell's equations in arbitrary geometries. The discontinuous Galerkin time domain method is a finite element method which calculates the time-evolution of a set of equations for a physical system which is represented by an unstructured mesh.

In this thesis, I aim at pointing out the most prominent features which arise due to nonlocality and nonlinearity in the hydrodynamic equations and which make it possible to experimentally check the

validity of the model used here. Those are qualitative and quantitative changes due to nonlocality and the excitation of plasmonic modes by nonlinear processes. The strongest influence is thereby found in more complicated structures, whose modes exhibit complicated field distributions and whose spectra are more diverse than those of simple cylinders or spheres. Therefore, I have to resort to a numerical method.

The discontinuous Galerkin time domain method (DGTD) is thereby particularly well-suited to treat the hydrodynamic equations which I introduced in Chap. 2. The method can be used to study arbitrary geometries and analytically solvable test cases for simple structures allow for a validation of the method. The unstructured mesh allows for a very good approximation of all physical systems considered, As the mesh elements can be made very small, even circular structures can be well-approximated without the need for curved elements. The equations that are fed into the DGTD method have to describe the time-evolution in conservation form. Such a formulation can be found for Maxwell's curl equations. The hydrodynamic equations which I introduced in the preceding chapters are naturally formulated in such a fashion.

Furthermore, time-domain methods provide the possibility to directly investigate the nonlinear properties of the hydrodynamic equations by solving the full set of nonlinear equations [M2, M3], without having to make any further assumptions about the nonlinear source terms as it was sometimes done in the past [119, 120]. In practice, besides the limitations of the model itself, there are computational limits to the hydrodynamic calculations as well, since a treatment of nonlocality (which includes bulk plasmons of very small wavelengths) usually calls for sub-nanometer resolution, but especially the DGTD method, which employs an unstructured mesh that can be refined where necessary [118] has shown good convergence behavior for such structures [M2], making the method well-suited to study plasmonic structures of realistic size.

Nonetheless, the approach is sometimes criticized for providing only qualitative results, but no authoritative quantitative predictions [77]. Many of the shortcomings of the model are being addressed in recent publications, such as the treatment of the particle boundary [45, 78], interband transitions [45, 84] or frequency-dependent nonlocality and Landau damping [79, 83] and show better agreement with experimental results [45]. While for very small structures and sub-nanometer gap-structures, time-dependent density functional theory methods may be the method of choice [77, 88], they are not feasible for the structures considered here. With the aforementioned recent developments on the forefront of semi-classical simulations of plasmonic systems and their versatility in dealing with complicated geometrical structures thanks to ever better computers, there is once again an increased interest in simulation techniques which employ the hydrodynamic Drude model and extensions thereof [M2, M3, 41, 45, 67, 69, 77–79, 83, 93, 119–121]. In the present work, the contribution to this long list of recent improvements on modeling with the hydrodynamic Drude model lies in solving the full hydrodynamic equations with all their nonlinear terms, while employing a simple model without interband transitions or soft walls. Such schemes have recently gained popularity as commercial DGTD software has become available and computers are becoming fast enough to treat comparably large systems [M2, M3, 64–66]. While this model will not provide a very good description of a metal at very high frequencies, the findings are of fundamental importance. Especially the selection rules for nonlinear excitation of modes which are discussed numerically in Chap. 5 are fundamental mechanisms.

4.1.1 Implementation of Maxwell's Equations and the Hydrodynamic Equations

To write down the equations under consideration in the way they are implemented in the DGTD method, supervectors containing for instance all of the field components of the electric and the magnetic field are constructed. These supervectors are written in Fraktur, while “physical” two- or three-dimensional vectors are kept in boldface, as before. Vectors of Supervectors are indicated by an arrow. Some of the derivations of this section and the following section were also published in the supplementary material of one of my own publications, Ref. [M2], but this chapter goes slightly further, in order to briefly introduce all concepts used in the numerical investigations of this thesis. The DGTD method is designed to solve continuity equations of the form [M2, 73, 118]

$$\partial_t \mathbf{u}(\mathbf{r}, t) + \vec{\nabla} \cdot \vec{\mathfrak{f}}(\mathbf{u}, \mathbf{r}, t) = \mathfrak{g}(\mathbf{r}, t), \quad \mathbf{r} \in \Omega \subseteq \mathbb{R}^n, \quad (4.1)$$

for $n = 2$ or 3 dimensions on a finite domain Ω with surface $\partial\Omega$. Here, $\mathbf{u}(\mathbf{r}, t)$ is a density, $\mathfrak{f}(\mathbf{u}, \mathbf{r}, t)$ is the corresponding flux, and $\mathfrak{g}(\mathbf{r}, t)$ represents a source term. These equations of motion are subject to boundary conditions on the surface of the domain:

$$\mathbf{u}(\mathbf{r} \in \partial\Omega, t) = \mathfrak{h}_{\partial\Omega}(\mathbf{r}, t), \quad (4.2)$$

and to initial conditions

$$\mathbf{u}(\mathbf{r}, t = 0) = \mathfrak{h}_0(\mathbf{r}). \quad (4.3)$$

For the hydrodynamic equations, i.e. the continuity equation 2.12 and the Euler equation 2.19, which represent particle and momentum conservation respectively, this yields

$$\begin{aligned} \mathbf{u}^{(HD)} &= \begin{bmatrix} \rho \\ \mathbf{j} \end{bmatrix}, \\ \vec{\mathfrak{f}}^{(HD)} &= \begin{bmatrix} \mathbf{j} \\ \frac{1}{\rho} \mathbf{j} \otimes \mathbf{j} + p \mathbb{1} \end{bmatrix}, \\ \mathfrak{g}^{(HD)} &= \begin{bmatrix} \delta\rho \\ \mathbf{F} \end{bmatrix}. \end{aligned} \quad (4.4)$$

Here, $\delta\rho$ represents a source of particles (in the present case non-existent) and \mathbf{F} is the force density that acts as a source or sink of momentum from or to another physical (sub-)system, e.g., the previously discussed damping term or the Lorentz force.

For the Maxwell equations a slightly modified continuity equation is needed [118]

$$\hat{Q} \partial_t \mathbf{u} + \vec{\nabla} \cdot \vec{\mathfrak{f}}(\mathbf{u}) = \mathfrak{g}, \quad (4.5)$$

where

$$\begin{aligned}
 \hat{Q} &= \begin{bmatrix} \epsilon(\mathbf{r}) & 0 \\ 0 & \mu(\mathbf{r}) \end{bmatrix}, \\
 \mathbf{u}^{(EM)} &= \begin{bmatrix} \mathbf{E}(\mathbf{r}, t) \\ \mathbf{H}(\mathbf{r}, t) \end{bmatrix}, \\
 \mathbf{g}^{(EM)} &= \begin{bmatrix} -\mathbf{j}(\mathbf{r}, t) \\ 0 \end{bmatrix}, \\
 \vec{\mathbf{f}}^{(EM)} &= \begin{bmatrix} -\hat{\mathbf{e}} \times \mathbf{H}(\mathbf{r}, t) \\ \hat{\mathbf{e}} \times \mathbf{E}(\mathbf{r}, t) \end{bmatrix}, \\
 \hat{\mathbf{e}} &= \begin{bmatrix} \mathbf{e}_x \\ \mathbf{e}_y \\ \mathbf{e}_z \end{bmatrix}.
 \end{aligned} \tag{4.6}$$

Within DGTD, the computational domain is subdivided into a set of finite elements. The whole procedure can be done for different dimensionalities. Triangles are used for $d = 2$, tetrahedra for $d = 3$. The various fields are expanded into Lagrange polynomials L_i which are defined on n nodal points \mathbf{r}_j on each element by means of

$$L_i(\mathbf{r}_j) = \delta_{ij}, \quad i, j = 1, \dots, n, \tag{4.7}$$

i.e. they are zero at all but one nodal points. Therefore, the expansion coefficients \tilde{u}_i , \tilde{f}_i , and \tilde{g}_i of \mathbf{u} , $\vec{\mathbf{f}}$, and \mathbf{g} are given by the field value at the position \mathbf{r}_i :

$$\mathbf{u}(\mathbf{r}_k) = \tilde{u}_j \cdot L_j(\mathbf{r}_k) = \tilde{u}_j \delta_{jk} = \tilde{u}_k. \tag{4.8}$$

By increasing the order of the Lagrange polynomials, the number of nodal points and therefore the spatial discretization is increased.

To solve the conservation equations Eq. (4.1) and 4.5 numerically, an approximation has to be found which minimizes the residual to these equations (I will drop the \hat{Q} in the equations since it provides no further insight and I will not perform a thorough derivation of a formulation of Maxwell's Equations in the DGTD, as this can be found in many other sources [73, 116, 117, 122, 123]).

$$\partial_t \mathbf{u} + \vec{\nabla} \cdot \vec{\mathbf{f}}(\mathbf{u}) - \mathbf{g} = \text{res}. \tag{4.9}$$

This is done by introducing a basis of test-functions. Choosing the same functions as test-functions as for the expansion above in Eq. (3.40) is called the *Galerkin choice* [124]. On the volume of a given element, denoted by Ω^k , the residuum is the minimized if it is orthogonal to the function space:

$$\int_{\Omega^k} d^d r \left(\partial_t \mathbf{u} + \vec{\nabla} \cdot \vec{\mathbf{f}}(\mathbf{u}) - \mathbf{g} \right) \cdot L_i(\mathbf{r}) = \int_{\Omega^k} d^d r \text{res} \cdot L_i(\mathbf{r}) = 0. \tag{4.10}$$

All considerations above were made locally on one single element. The connection between these elements is done by introducing a *numerical flux*. An upper index k ($k = 1, \dots, N$) is introduced to label the N elements.

The numerical flux then acts as a source or drain in the conservation equations and connects the elements consistently, in the sense that if the density is reduced in one element, this density has to be added to the neighboring elements [73]. Expanding the conservation equations yields

$$\int_{\Omega^k} d^d r \partial_t \tilde{u}^k L_i^k + \vec{\nabla} \cdot \left(\vec{f}^k L_i^k \right) - \tilde{g} L_i^k = 0. \quad (4.11)$$

Now the product rule is carried out for the divergence term and the part containing the divergence of the flux is moved to the right hand side of the equation

$$\int_{\Omega^k} d^d r \partial_t \tilde{u}^k L_i^k + \vec{f}^k \vec{\nabla} \cdot L_i^k - \tilde{g} L_i^k = - \int_{\Omega^k} d^d r \left(\vec{\nabla} \cdot \vec{f}^k \right) L_i^k. \quad (4.12)$$

In a next step, Gauß' law is applied on the right hand side and the physical flux \vec{f}^k is replaced by the numerical flux \vec{f}^*

$$\int_{\Omega^k} d^d r \partial_t \tilde{u}^k L_i^k + \vec{f}^k \vec{\nabla} \cdot L_i^k - \tilde{g} L_i^k = - \int_{\partial\Omega^k} d^{d-1} r \hat{n} \cdot \vec{f}^* L_i^k, \quad (4.13)$$

where \hat{n} is a supervector containing outward normal vectors on the element Ω^k . Eq. (4.13) is called the weak formulation which is employed for the hydrodynamic equations[125], in conjunction with a so-called Lax-Friedrich flux. A discussion of different fluxes follows below. The hydrodynamic equations are solved only within the plasmonic particle and at the surface, slip boundary conditions are employed which ensure that the normal component of the velocity vanishes at the surface.

For the Maxwell equations, the strong formulation is utilized[118, 126], employing an upwind flux (again, to be discussed below). The strong formulation is obtained by integrating the divergence term in Eq. (4.13) by parts and again applying Gauß' law:

$$\int_{\Omega^k} d^d r \left(\partial_t \tilde{u}^k + \vec{\nabla} \cdot \vec{f}^k - \tilde{g} \right) L_i^k = \int_{\partial\Omega^k} d^{d-1} r \hat{n} \cdot \left(\vec{f}^k - \vec{f}^* \right) L_i^k. \quad (4.14)$$

The expansions, in the weak or the strong formulation, are now inserted into Eq. (4.10).

To treat the problem numerically the occurring integrals of products of basis functions are written as matrix-entries:

$$\begin{aligned} M_{ij}^k &= \int_{\Omega^k} L_i L_j d^n r, \\ \vec{S}_{ij}^k &= \int_{\Omega^k} \vec{\nabla} L_i L_j d^n r, \\ F_{ij}^k &= \int_{\partial\Omega^k} L_i L_j d^{n-1} r. \end{aligned}$$

Here, the matrix with matrix elements M_{ij}^k is block-diagonal and the individual blocks can easily be inverted. The weak formulation, used for hydrodynamics, is then written as:

$$\partial_t \tilde{u}_i^k = - \left(M^{-1} \right)_{il}^k \vec{S}_{jl}^k \vec{f}_j^k + \tilde{g}_i^k - \left(M^{-1} \right)_{il}^k F_{lj}^k \left(\vec{n} \cdot \vec{f}_j^* \right). \quad (4.15)$$

For further details on the implementation of the strong formulation used for Maxwell's equations, see Refs. [73, 117, 122, 123]. The differential equation Eq. (4.15) now has to be evolved in time. This is done via a 14-stage 4th-order low-storage Runge-Kutta scheme [117, 118, 123]. I will not provide a detailed description of this scheme here. It is however important for my purposes that the scheme represents an explicit time-stepping scheme which is conditionally stable, i.e. the time step Δt cannot be chosen arbitrarily large in order for the scheme to remain stable. This is of practical relevance: For my purposes, to resolve for instance bulk plasmons, very fine spatial discretizations are required. This means that extremely small elements are needed. This must limit the time step, as can be readily motivated in the language of finite difference schemes [125]: The time-step Δt and the distance between nodes in the spatial grid Δx define a so-called *grid speed*. If the wave-propagation speed exceeds the grid speed the method becomes unstable. For the DGTD method, the grid speed is therefore given by the shortest distance between two nodal points within an element. For an unstructured mesh, it is quite involved to reliably determine this distance and choose a corresponding time-step [118].

Finally, I would like to comment on the different types of fluxes which can be employed. The choice of the numerical flux which ensures that the solutions are not only local but global solutions can be important, as it has to be made sure that the scheme is both convergent and consistent [73, 122]. The simplest choice is the central flux which is given by

$$\hat{\mathbf{n}} \cdot \vec{\mathbf{f}}^* = \frac{1}{2} \left(\hat{\mathbf{n}} \cdot \vec{\mathbf{f}}^{k=-} + \hat{\mathbf{n}} \cdot \vec{\mathbf{f}}^{k=+} \right), \quad (4.16)$$

where the index $k = -$ denotes the element under consideration and $k = +$ denote the neighboring element. The central flux is energy-conserving. While energy-conservation is of course desirable from a physical point of view, an alternative choice of flux, the upwind flux¹, is often employed. It introduces numerical dissipation into the system. It can be written as [118]

$$\hat{\mathbf{n}} \cdot \left(\vec{\mathbf{f}}^k - \vec{\mathbf{f}}^* \right) = \left(\frac{1}{\bar{Z}} \left(\alpha [\Delta \mathbf{E} - \hat{\mathbf{n}} (\hat{\mathbf{n}} \cdot \Delta \mathbf{E})] + Z^+ \hat{\mathbf{n}} \times \Delta \mathbf{H} \right) + \frac{1}{\bar{Y}} \left(\alpha [\Delta \mathbf{H} - \hat{\mathbf{n}} (\hat{\mathbf{n}} \cdot \Delta \mathbf{H})] + Y^+ \hat{\mathbf{n}} \times \Delta \mathbf{E} \right) \right), \quad (4.17)$$

where

$$Z^\pm = \frac{1}{Y^\pm} = \sqrt{\frac{\mu^\pm}{\epsilon^\pm}}, \quad (4.18)$$

$$\bar{Z} = Z^+ + Z^-, \quad \bar{Y} = Y^+ + Y^-, \quad (4.19)$$

$$\Delta \mathbf{E} = \mathbf{E}^+ - \mathbf{E}^-, \quad \Delta \mathbf{H} = \mathbf{H}^+ - \mathbf{H}^-. \quad (4.20)$$

The parameter α which must lie between 0 and 1 for a stable scheme, determines the strength of the upwind term, $\alpha = 0$ recovers the central flux. For finite difference schemes a central flux in fact leads to unconditional instability, whereas within the DGTD method a central flux can in principle be employed and leads to a stable and converging scheme [127, 128]. However, the upwind flux $\alpha = 1$ exhibits optimal convergence rates and strongly damps unphysical spurious modes due to the numerically introduced dissipation [118, 129].

¹The term upwind originates from the fact that to derive this flux, spatial derivatives are calculated by means of one-sided (rather than central) approximations, on grid points which lie *upwind* (or *upstream*) from the space point under consideration [125].

For the hydrodynamic equations, numerical dissipation is introduced by the so-called Lax-Friedrichs flux [125], which provides even stronger numerical dissipation. Here, the central flux is corrected by a term that is proportional to the maximum speed of sound in the surrounding elements [73]. It is implemented as [M2, 73]:

$$\hat{\mathbf{n}} \cdot \vec{f}^* = \frac{1}{2} \left(\hat{\mathbf{n}} \cdot \vec{f}^{k=-} + \hat{\mathbf{n}} \cdot \vec{f}^{k=+} \right) + \frac{\alpha}{2} \max_{\partial\Omega^\pm} \left(|\mathbf{v}| + \sqrt{\left| \frac{mp}{n} \right|} \right) \Delta u \quad (4.21)$$

where a central flux is corrected by the local maximal linearized speed of sound on the surface in question. Here, m is the adiabatic index $m = \frac{f+2}{f}$ which was discussed in Sec. 2.2.6, p is the pressure, n the electron number density and

$$\Delta u = u^+ - u^-. \quad (4.22)$$

Note that since the computational domain cannot be infinitely large, at the boundaries of the system, special boundary conditions are needed. The system can either be made periodic by identifying the two boundaries on opposite sides, or reflecting boundary conditions (perfect electric conductor or perfect magnetic conductor) or absorbing boundary conditions (Silver-Müller) can be introduced. They correspond to artificially introduced fields E^+ and H^+ in Eq. (4.17) which are chosen the following way:

Boundary Condition	E^+	H^+
Perfect Electric Conductor	$-E^-$	H^-
Perfect Magnetic Conductor	E^-	$-H^-$
Silver-Müller	$-E^-$	$-H^-$

4.1.2 Dimensionless Units

In numerical calculations, the different orders of magnitude appearing in the hydrodynamic equations and Maxwell's equations pose practical problems. To remedy this, all quantities are cast into dimensionless units, and characteristic scales are introduced. For my simulations, the characteristic length scale is $l_0 = 1$ nm. Likewise, a characteristic electromagnetic field $E_0 = 10^9$ V/m is introduced. Based on these rescaling factors, scaling factors are obtained for all other physical quantities, such as time, magnetic and electric field, the electron charge density $\rho \equiv \rho_c = qn$ electron current density $\vec{j} = \rho v$. Note that now, for purpose of rescaling and consequently implementation, only the charge density $\rho \equiv \rho_c$ is employed, rather than the number or mass density. Spatial and temporal derivatives have to be rescaled accordingly. The rescaling of all relevant quantities which are implemented is listed in the table below :

SI-Quantity	Rescaled Quantity	Rescaling Factor
\mathbf{r}	$\tilde{\mathbf{r}} = \mathbf{r}/l_0$	$l_0 = 1$ nm
t	$\tilde{t} = t/t_0$	$t_0 = l_0/c$
\mathbf{E}	$\tilde{\mathbf{E}} = \mathbf{E}/E_0$	$E_0 = 10^9$ V/m
\mathbf{H}	$\tilde{\mathbf{H}} = \mathbf{H}/H_0$	$H_0 = E_0 \sqrt{\epsilon_0/\mu_0}$
\mathbf{j}	$\tilde{\mathbf{j}} = \mathbf{j}/j_0$	$j_0 = H_0/l_0$
ρ	$\tilde{\rho} = \rho/\rho_0$	$\rho_0 = j_0/c$
∇	$\tilde{\nabla} = l_0 \nabla$	$1/l_0$
∂_t	$\partial_{\tilde{t}} = t_0 \partial_t$	$1/t_0$

The original hydrodynamic equations for the electron fluid, including damping and the Lorentz force as external forces, read as

$$\partial_t \rho = -\nabla \cdot \mathbf{j} \quad (4.23)$$

$$\begin{aligned} \partial_t \mathbf{j} = & -\frac{1}{\rho} (\mathbf{j} \cdot \nabla) \mathbf{j} - \frac{q}{m} \nabla p - \gamma \mathbf{j} + \\ & + \frac{q}{m} (\rho \mathbf{E} + \mu_0 \mu_r \mathbf{j} \times \mathbf{H}), \end{aligned} \quad (4.24)$$

Upon rescaling, these equations are recast into the form

$$\begin{aligned} \partial_{\tilde{t}} \tilde{\rho} = & -\tilde{\nabla} \cdot \tilde{\mathbf{j}}, \\ \partial_{\tilde{t}} \tilde{\mathbf{j}} = & -\frac{1}{\tilde{\rho}} (\tilde{\mathbf{j}} \cdot \tilde{\nabla}) \tilde{\mathbf{j}} - \frac{\kappa}{mc^2} \left(\frac{\rho_0}{q} \right)^{\frac{2}{3}} \tilde{\nabla} \tilde{\rho}^{\frac{5}{3}} - \frac{l_0}{c} \gamma \tilde{\mathbf{j}} \\ & + \frac{ql_0 E_0}{mc^2} (\tilde{\rho} \tilde{\mathbf{E}} + \mu_r \tilde{\mathbf{j}} \times \tilde{\mathbf{H}}), \end{aligned} \quad (4.25)$$

which provides the necessary prefactors for the numerical implementation of the various terms in the hydrodynamic equations.

4.2 Aspects of Numerical Simulations with the DGTD Method

4.2.1 Total Field-Scattered Field Formalism and On-The-Fly Fourier Transform

Injecting Gaussian Wave Packets

The light pulses which I use in my simulations are Gaussian wave packets propagating in a given direction. I usually consider two-dimensional systems, i.e. systems that are infinitely extended in z -direction. In two dimensions, Maxwell's equations decouple into two polarizations. The one relevant for the excitation of surface plasmons has an electric field which lies in the xy -plane and H therefore only has a z -component. A incoming pulse that is propagating in x -direction in free space has only an E_y -component and the electric and magnetic field are invariant in y - and z -direction which means the pulse has a spatially homogeneous profile. This pulse is injected at the boundary between the total field and the scattered field-region (Fig. 4.1), propagating within the total field region where it can interact with a scatterer. The analytical solution of the unperturbed pulse is subtracted again at the contour between the total field and the scattered field region, i.e. if no scatterer is present, no fields radiate into the scattered field region (hence the name). So once again the flux is artificially modified at the boundary, employing the analytically calculated fields of the incoming pulse [118, 130].

On-The-Fly Fourier Transform

Naturally, in a time-domain simulation all quantities are time-resolved and while it is sometimes insightful to study the dynamics of a process, frequency resolved quantities such as scattering spectra

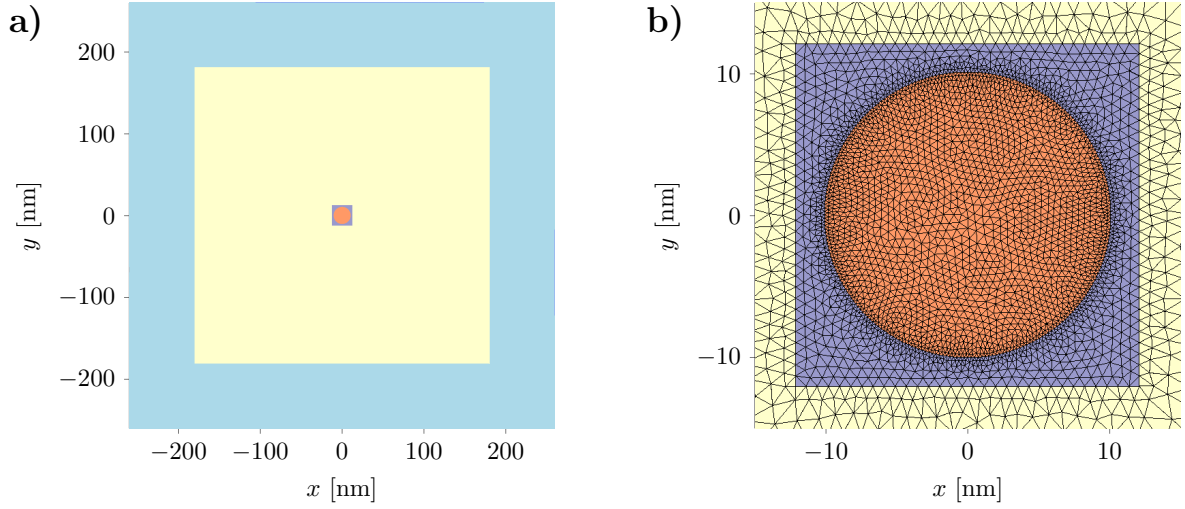


Figure 4.1: **a)** The computational domain for a typical scattering simulation, using a total field scattered field formalism: The scatterer (orange) is surrounded by the total field region (purple). The scattered field region (yellow) is large to keep evanescent fields from entering the perfectly matched layers (blue), which represent an unphysical absorbing material to mimic infinite space. **b)** The unstructured mesh in the vicinity of the scatterer. The field is injected at the boundary between the total field region (purple) and the scattered field region (yellow). The unstructured mesh features is extremely fine within the scatterer, especially near the boundaries.

or the field distributions at a given frequency are often more interesting, be it for comparison with an experiment, experimental design purposes or simply to extract information for a theoretical study as in the the case of the present thesis.

Luckily, the Fourier transform

$$\tilde{f}(\omega) = \int_{-\infty}^{\infty} f(t) e^{i\omega t} dt \quad (4.26)$$

can be approximated by its discrete form [118]

$$\tilde{f}(\omega) \approx \Delta t \sum_{i=1}^T f(t_i) e^{i\omega t_i} \quad (4.27)$$

for a total of T time steps which can in principle have different lengths t_i . This straightforwardly provides an update scheme for the Fourier transformed field at frequency ω_j

$$\tilde{f}^{t_k}(\omega_j) = \tilde{f}^{t_{k-1}}(\omega_j) + \Delta t_k f(t_k) e^{i\omega_j t_k} \quad (4.28)$$

which now depends on the current simulation time t_k . This is known as the *on-the-fly Fourier transform*. It converges under the condition that the fields are initially zero and decay to zero again at the end of the simulation for $t = T$. The error then only depends on the step size Δt which, as I argued before,

will be very small in all of my simulations. The big advantage of the approximation scheme Eq. (4.28) is that only one previous time-step has to be kept in memory. Therefore the evaluation of Eq. (4.28) can be performed at many different frequencies ω_j and space points with little numerical effort. This is extremely important as calculations of spectra which are supposed to resolve numerous features require a large number of frequencies and field distributions on the other hand require a large number of space points. It is one of the advantages of a time-domain simulation that a single pulse can in principle contain as many frequencies as one likes, therefore, all Fourier-transformed fields and spectra can be extracted from a single calculation. In practice it is important to choose long enough simulation times to ensure that no fields are left in the system at the end of the simulation and hence at the end of the Fourier transform. Specifically, I found bulk plasmon oscillations in nonlocal simulations to stay in the system for a very long time.

Calculating Cross Sections

In scattering experiments, scattering and absorption cross sections are recorded, rather than field distributions which are usually not accessible. They are also one of the most important quantities in my investigations. The cross sections are given by integrating the total power flux through the total field-scattered field contour. The power flux per time and area, i.e. the time-averaged Poynting vector is given by

$$\mathbf{S}(\omega) = \frac{1}{2} \text{Re} [\mathbf{E}(\omega) \times \mathbf{H}^*(\omega)] \quad (4.29)$$

which can be evaluated at all nodes on the total field-scattered field contour, employing the fields obtained by the on-the-fly Fourier transform [118]. The flux-component normal to the total field-scattered field surface is then integrated spatially and normalized to the flux associated with the incoming field which then yields the cross section. Having access to the total fields and the scattered fields at the position of this contour makes it possible to distinguish between the scattered flux and the absorbed flux:

$$C^{\text{scat}}(\omega) = \frac{\int_{\text{tfsf}} \mathbf{n} \cdot \mathbf{S}^{\text{scat}}(\omega) d^2r}{\int_{\text{tfsf}} \mathbf{n} \cdot \mathbf{S}^{\text{inc}}(\omega) d^2r} \quad (4.30)$$

$$C^{\text{abso}}(\omega) = -\frac{\int_{\text{tfsf}} \mathbf{n} \cdot \mathbf{S}^{\text{tot}}(\omega) d^2r}{\int_{\text{tfsf}} \mathbf{n} \cdot \mathbf{S}^{\text{inc}}(\omega) d^2r}. \quad (4.31)$$

Comment on Nonlinear Scattering Simulations

The total field-scattered field formalism relies on the linearity of Maxwell's equations, as the fields are written as a sum of incoming and scattered field. This raises the question whether it is legitimate to perform nonlinear simulations. In Chap. 5 I will present nonlinear simulations which show second harmonic generation. For these kinds of calculations, I run spectrally sharp, quasi-monochromatic pulses which generate two well-separated signals: one at the incoming frequency which is the linear signal – it is the same signal one would obtain by means of a linearized method so the approach is in order – and one at twice the frequency which is the SHG signal. At the frequency of the nonlinear signal, by construction, there will be negative absorption which will equal the nonlinear scattered signal. Of

course, it makes no sense to normalize this signal to the flux of the incoming fields, since the incoming field is essentially zero at this frequency. Therefore, it is divided by the value of the incoming flux:

$$C^{\text{SHG}}(2\omega) = \frac{\int_{\text{tfsf}} \mathbf{n} \cdot \mathbf{S}^{\text{scat}}(2\omega) d^2r}{\int_{\text{tfsf}} \mathbf{n} \cdot \mathbf{S}^{\text{inc}}(\omega) d^2r} = \frac{\int_{\text{tfsf}} \mathbf{n} \cdot \mathbf{S}^{\text{tot}}(2\omega) d^2r}{\int_{\text{tfsf}} \mathbf{n} \cdot \mathbf{S}^{\text{inc}}(\omega) d^2r}. \quad (4.32)$$

$$(4.33)$$

In practice, I normalize the SHG signal to the maximum value of the linear spectrum. If numerous spectrally sharp calculations are performed at different frequencies, the envelope of the resulting SHG signals gives a full SHG spectrum which is physically meaningful.

4.2.2 Material Assignments

Metals

The hydrodynamic equations of course represent one possibility to implement a (Drude-)metal. Choosing $\beta = 0$ reproduces precisely the results from the Drude model. Implementing these equations to simulate a local material would however be somewhat of an overkill. However, in time-domain, one cannot simply feed a table of values into the code in order to describe the permittivity of a dispersive material. The frequency-dependent permittivity gives rise to a convolution in time-domain which can be implemented – or circumvented – by means of so-called auxiliary differential equations [118, 130]. This can be done if an analytical expression is known – usually given by a fit to the measured material parameters, in practice restricted to a small frequency range of interest to yield a better fit. For the Drude model I have already introduced the relation (Eq. (2.8))

$$\epsilon(\omega) = 1 + \chi(\omega) = 1 - \frac{\omega_p^2}{\omega(\omega + i\gamma)}. \quad (4.34)$$

Here, the value 1 could be replaced by a more general fitting value which represents the background permittivity ϵ_∞ . Starting out with the constitutive relation in frequency domain

$$\mathbf{D}(\omega) = \epsilon(\omega)\mathbf{E}(\omega), \quad (4.35)$$

yields

$$\mathbf{D}(t) = \int_{-\infty}^t \epsilon(t - t')\mathbf{E}(t') dt' \quad (4.36)$$

in time-domain. Inserting Eq. 4.34 into Eq.4.35 gives

$$-i\omega\mathbf{D}(\omega) = -i\omega\mathbf{E}(\omega) + \underbrace{-i\omega\chi(\omega)}_{\mathbf{j}(\omega)}. \quad (4.37)$$

The last term is interpreted as a polarization current. In time domain, Eq. (4.37) then reads

$$\partial_t \mathbf{D}(t) = \partial_t \mathbf{E}(t) + \mathbf{j}(t) \quad (4.38)$$

and, explicitly inserting the expression for χ from Eq. 4.34, yields an equation for the auxiliary current $\mathbf{j}(\omega)$,

$$-i\omega\mathbf{j}(\omega) = \omega_p^2\mathbf{E}(\omega) - \gamma\mathbf{j}(\omega), \quad (4.39)$$

which results in an auxiliary differential equation for the current in time domain that has to be solved alongside the Maxwell equations:

$$\partial_t\mathbf{j}(t) = \omega_p^2\mathbf{E}(t) - \gamma\mathbf{j}(t). \quad (4.40)$$

The current then couples to Maxwell's equations in the usual manner. This expression is actually equivalent to the expression for \mathbf{j} which is obtained from Euler's equation when setting $\beta = 0$. However, the second hydrodynamic equation, the continuity equation for n , does not need to be implemented in this description since the electron density is constant.

For local calculations done within this work, I employed this kind of implementation of the Drude model since the corresponding calculations are faster than running a hydrodynamic model with $\beta = 0$.

More sophisticated material models include interband transitions by adding (an arbitrary number of) Lorentz oscillators to the Drude permittivity [118].

Perfectly Matched Layers

To mimic infinite, non-periodic space in a finite volume method, the fields have to be terminated at the end of the computational domain. Above, I described absorbing boundary conditions which make the fields disappear at the outer boundary by means of Silver-Müller boundary conditions. They are however not perfectly absorbing, especially if the wave does not impinge normally on the surface. Therefore, an additional material layer is added which represents an (unphysical) absorbing material, designed to dissipate all of the radiation which penetrates the area. At the same time, it is important that no reflection occurs as the wave enters this material. Here, an implementation of the so-called uniaxial perfectly matched is employed [118, 131]. The material features anisotropic material parameters

$$\underline{\epsilon}' = \underline{\Lambda}\epsilon, \quad \underline{\mu}' = \underline{\Lambda}\mu, \quad \underline{\Lambda} = \begin{pmatrix} \frac{s_y s_z}{s_x} & 0 & 0 \\ 0 & \frac{s_x s_z}{s_y} & 0 \\ 0 & 0 & \frac{s_x s_y}{s_z} \end{pmatrix}, \quad (4.41)$$

with the PML parameters

$$s_i = 1 - \frac{\sigma_i}{i\omega}. \quad (4.42)$$

The parameter σ_i effects damping in i -direction, hence the name uniaxial. By matching the impedances between the physical material and the PMLs, back reflection is minimized. In practice, due to numerical errors, back reflection occurs and the right choice of parameters is a trade-off between the material's ability to absorb (and hence the thickness needed to achieve a good result) and reflection [117].

4.3 Convergence of the Hydrodynamic DGTD Method

When doing numerics, it is important to determine how much trust can be put into the method at hand. It is essential to be able to give an estimate of the error and determine the regimes and setups for which the method is valid. In this section I will present the procedure used in the making of this thesis to ensure that the results are reasonable and trustworthy and show examples of the convergence studies which I have done.

The values a produced by the method will depend on many parameters that affect the accuracy of the method. In the present case, the spatial resolution, given by the size of the largest mesh element h (I choose this to be the largest edge length of all triangles in a given area) and the polynomial order p , has the strongest influence on the accuracy of the result and on the run-time (there is always a trade-off between the two), but of course one has to keep in mind that there are other parameters, such as the time step which will eventually limit the accuracy of the result. An analysis of the error depending on the largest mesh element size h and the polynomial order p (hp -convergence) lies at the heart of the validation of a numerical scheme exhibiting this kind of convergence, such as the DGTD method. A method is convergent with a limit a_0 , if

$$|a_h - a_0| \longrightarrow 0, \text{ for } h \rightarrow 0. \quad (4.43)$$

For bulk media, the convergence of the DGTD method is exponential in the polynomial order p and polynomial in h , i.e. the hp -convergence behavior can be written as

$$|a_h - a_0| \leq Ch^\alpha, \quad (4.44)$$

where C is a constant. The exponential convergence behavior in p was shown to be of order $\alpha = p + 1$ [116, 132].

The parameters h and p both describe how well the bulk is refined (while of course only h has an influence of the surface description). Therefore, the typical hp -convergence behavior of a discontinuous Galerkin method is only obtained for rectangular test systems where no additional error from the surface-description comes into play and it was shown to be fulfilled for the Maxwell solver of an older version of the code which was used in this thesis for a metallic cavity [116]. In this work it was also determined that the error is dominated by the spatial resolution and that for any time-step which provided a stable scheme, there was practically no influence of the time-step on the error. In an ideal world, neglecting the fact that other parameters such as machine precision and the time-step play a role, $a_{h \rightarrow 0}$ is then the "physically correct" value. For any method one intends to use, it is good to have at least one case where a reference solution, i.e. a physically correct value, is available. In the present case this is the cross section of the infinitely extended cylinder. In principle, the concept of convergence has nothing to do with the existence of a physically correct value. When going to a new, more complicated system, convergence has to be investigated again to make sure that the new setup doesn't impose additional difficulties which require a different set of parameters to obtain converging behavior. This can be done either by comparing the results of two consecutive calculations to one-another or by comparing to a very accurate reference calculation with small h and high p (Note that especially small h is important to avoid errors stemming from the description of the geometry). The fact that the method converged towards the physically correct value in the test case then allows the user to trust that, given that convergence can be achieved, the method also converges to the physical value in the case where no reference

solution is available. However, one has to keep in mind that because of limitations coming from other sources of error than the one under investigations, in practice, the method will never converge exactly to the analytical value.

I would now like to apply this type of convergence study to the hydrodynamic Maxwell equations in the DGTD method. In Chap. 3 the main focus was on the study of scattering and absorption cross sections and I will continue to consider them in the following chapters. Therefore it makes sense to study the convergence behavior of these very quantities (for which there are analytical reference solutions), even though they are integrated quantities which undergo some post-processing which can lead to a larger error originating from sources other than the spatial resolution (incidentally, the error could also decrease, due to the addition of partial errors with different signs).

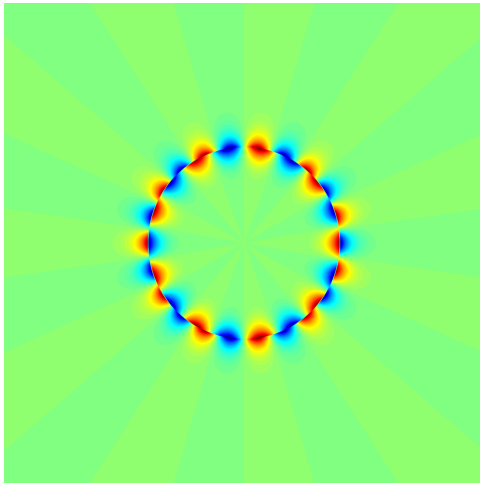


Figure 4.2: One electric field component for a high order surface mode ($k = 10$), calculated electrostatically as described in Sec. 3.2.5.

The infinite cylinder for which I have already presented the analytical solution, being one of the very few systems for which a reference solution is available, shall serve as the starting point for my convergence study. Fig. 4.2 displays one field component for a high order surface mode. To resolve the surface mode, not surprisingly, the surface region is the most important region. Part of the error of the surface mode comes from the surface discretization (i.e. that the mesh actually describes a polygon and not a circle) and part comes from the bulk refinement (in the vicinity of the surface).

However, since the DGTD method is a volume method and I am using only regular triangles without curved lines, it is impossible to just refine the surface without refining the bulk regions in the vicinity of the surface (the opposite would be possible). Netgen, the meshing program which I employed for most of my calculations [133], features *uniform refinement*, which increases the bulk refinement by halving every element and also smoothens the surface (the elements are not simply cut in half, but the approximation of the circular surface becomes better with every refinement). By employing this options, the contributions of bulk and surface cannot be separated and therefore *hp*-convergence behavior as in the case of a bulk structure cannot be expected. For the surface modes, such a uniform refinement is not strictly necessary, as it would be sufficient to refine the mesh only near the surface. I have chosen to use uniform refinement where ever possible, since it is better controlled than refining only the surface region. Also, it is then possible to study the convergence behavior of the bulk plasmons using the same calculations. Also, the initial discretization of the surface is in all cases already very fine, so that the error from the surface is small to begin with. For the convergence study of the second harmonic signal I have chosen to refine only the surface region because the simulations are in general longer and full uniform refine would be too costly, as I will elaborate below.

4.3.1 First Order Quantities

Surface Plasmon Resonances

I now present the convergence studies for the cross sections of the single cylinder which I discussed analytically in Sec. 3.2. Extracting these quantities from the DGTD method is somewhat involved as I have shown in the first sections of this chapter. Since the cross sections are frequency-space quantities, they are calculated by an on-the-fly Fourier transform which is carried out over the whole run-time of the numerical experiment. This means, they also follow a certain convergence behavior in simulation time (when the simulation time is too short, this usually results in unphysical “ripples” appearing in the spectrum). I choose a very long simulation time of over 330 fs (compared to a temporal pulse width of under 1 fs for the broad band excitations) and I have checked that in this realm, the run-time no longer influences the result on the order of the desired accuracy. The TfSf contour is a quadratic box of 24 nm edge length and the PMLs start beyond 180 nm in all four directions and have a thickness of 80 nm. The value I will actually look at in the convergence study is the height of certain important peaks of the spectra, such as the maximum value of scattering or absorption cross section or the height of bulk plasmon peaks. For simplicity, I choose to consider only single points, rather than considering a domain of many frequencies or integrating over them, which would mean that one would in some cases have to deal with line crossings. This also seems to be a good measure for the error since at these maximum points the deviation between the numerical and the analytical value usually reaches a maximum.

I am not interested in the frequencies of the peaks here: the frequency axis has a limited resolution which I have chosen as approximately $10^{-3} \omega_p$. At this resolution, when going to higher discretizations in h and p , no more change is detected in the position of the maximum. The accuracy of the peak position can therefore be taken to be better than $\pm 0.001 \omega_p$. To study the convergence of the surface plasmon resonances, I investigate the behavior of the maximum of the scattering cross section (which is the dipolar resonance) and of the maximum of the absorption cross section (which is the quadrupolar resonance). The convergence plots are depicted in Fig. 4.3. For second, third and fourth order polynomials the error – depending on the size (maximum edge length) of the largest element within the cylinder – is given in a double-logarithmic plot. Note that I choose to plot the error against the largest bulk element, rather than the largest element on the boundary, in the spirit of the uniform bulk-refinement which is applied. The curves would not look very different if I chose the surface element instead, since both are halved simultaneously, only the numbers on the x -axis would change. In this convergence study I cannot distinguish between the bulk and the surface effects, but the x -axis label is not intended to imply that the contribution of the bulk to the error is larger or more important than the contribution of the surface to the error. Since a uniform bulk-refinement quickly leads to an enormous number of mesh elements and extremely small mesh elements (which in turn lead to very small time-steps), I can only do two refinement-steps. The starting mesh for 2^{nd} - and 3^{rd} -order polynomials has a maximum edge length inside the cylinder of 1.36 nm which is then subsequently reduced to 0.68 and 0.34 nm. For 4^{th} -order polynomials the parameters above would result in unfeasible simulation times, therefore I start out with a bulk discretization of 2 nm which is then halved to 1 nm and finally 0.5 nm.

For the scattering cross sections the error is already very small for the coarsest mesh: about three percent for the second order polynomials and just above one percent for the other two polynomial orders. For third and fourth order meshes, a minimal value for the error of 0.85 % is already reached after the first refinement and the slopes which are determined to be $\alpha \approx 0.4$ in both cases are rather flat,

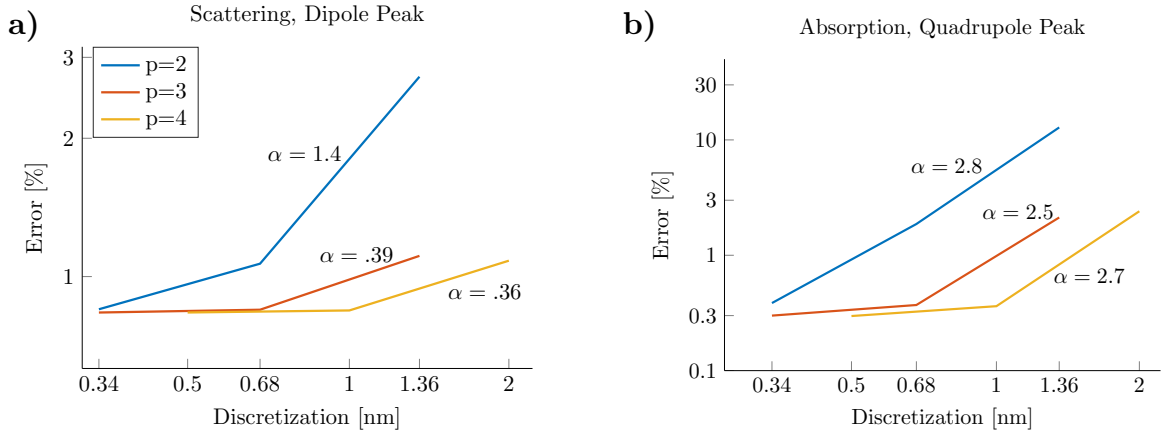


Figure 4.3: *hp*-convergence plots for uniform refinement of the bulk. The error is given with respect to the analytical reference solution from Ref. [43]. **a)** Convergence of the dipole peak in the scattering cross section. **b)** Convergence of the quadrupole peak in the absorption cross section. The slope, corresponding to the polynomial order α , is indicated only for the steepest line segment for each polynomial order.

further refinement does not reduce the error any more. Even for second order polynomials a slope of only 1.4 nm is found in the first refinement and significant flattening as the mesh is refined a second time. This means that beyond that, other factors limit the accuracy of the simulation, such as the simulation time, the size of the computational domain (which influences the result through backscattering from the PMLs), the Runge-Kutta-Scheme or even rounding-errors in the post-processing of the data (on-the-fly-Fourier transform, calculation of Poynting fluxes from the fields, normalization to the incident spectrum). For second order polynomials, there is some additional decrease when refining the mesh a second time, but the slope is significantly reduced, yielding the same minimal value for the error as for the other two polynomial orders.

For the absorption cross section the initial error is higher than for the scattering cross section, yielding about 12 % for second order polynomials and 2.5 % for third and fourth order polynomials for the coarsest meshes. Again, for third and fourth order polynomials the minimal error which is found to be 0.3 % and hence smaller than in the case of the scattering is already reached after a single refinement step. For second order polynomials this value is reached only after the second refinement. It is noteworthy that the quadrupole peak in the absorption depends stronger on the bulk refinement than the scattering peak: the initial error is larger and the final error smaller than in the case of the scattering. The slopes are steeper and thus the polynomial order is higher.

A steady decrease in error as in Fig. 4.3 is exactly the kind of convergence behavior one would like to see in order to trust a method. The final errors of below 1 % are well acceptable, in view of the multitude of parameters which are limiting factors in this case. In a separate study (not shown), I could clearly identify backscattering, i.e. the choice of the right PML parameter as well as a large enough distance of the PMLs from the scatterer as the main source of error. A poorer choice of PMLs lead to errors of 3 – 5%. The current setup with errors of below 1% is acceptable and appears to be a good compromise between accuracy and computational efficiency. By keeping the same PML parameters for

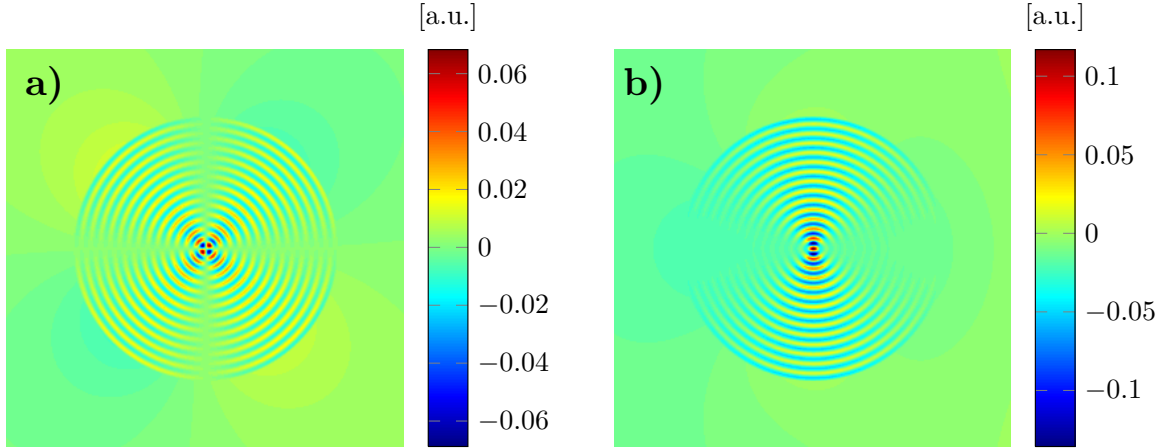


Figure 4.4: **a)** Real part of E_x and **b)** real part of E_y for a high order bulk plasmon resonance at $\omega = 1.129 \omega_p$. The typical pattern of maxima and minima extending into the particle requires high spatial resolution to be resolved.

other geometries, it is safe to say that the “final” error (for extremely good h and p) will also lie below 1%. This is of course under the assumption that this final error can be reached in finite simulation times.

As a final remark on the convergence of the surface plasmon resonances I would like to state that I have checked for third order polynomials that also for a mesh which is only refined in the vicinity of the surface while keeping the bulk region rather coarse (≈ 3 nm edge lengths in the center), the error of scattering and absorption also drops below 1% for 0.5 nm mesh elements in the surface region. Thus, a full uniform refinement of the whole mesh is not necessary to obtain good results. However, attempting to resolve bulk plasmons this way is hopeless, therefore I have used uniform refinement here, in order to be able to use the results from the same calculations in the convergence studies of the bulk plasmons in the next section.

Bulk Plasmon Resonances

The longitudinal bulk plasmons which exist in the hydrodynamic model are standing wave patterns which correspond to the geometry of the particle. In Fig. 4.4 the electric field components of one of these bulk modes are displayed. For this frequency, they feature approximately thirty maxima and minima across the diameter of the particle. Therefore it is obvious that sub-nanometer resolution, by means of small h or high p , is required. As I have shown in Chap. 2, they exist above the plasma frequency and every mode manifests itself in a peak in the absorption spectrum. In Fig. 4.5, the absorption cross sections are shown for a few select mesh sizes and polynomial orders, along with the analytical reference solution. Low polynomial orders and coarse meshes quickly fail to resolve these bulk plasmons correctly, but for fourth order polynomials and a maximal mesh element size of 0.5 nm, the DGTD method seems to nicely reproduce the analytical spectra, even up to $1.2 \omega_p$, but since the peaks are small in magnitude, the relative error quickly grows very large. I now conduct a convergence check, just as I have done it above in the case of the surface plasmon peaks for two select frequencies (these frequen-

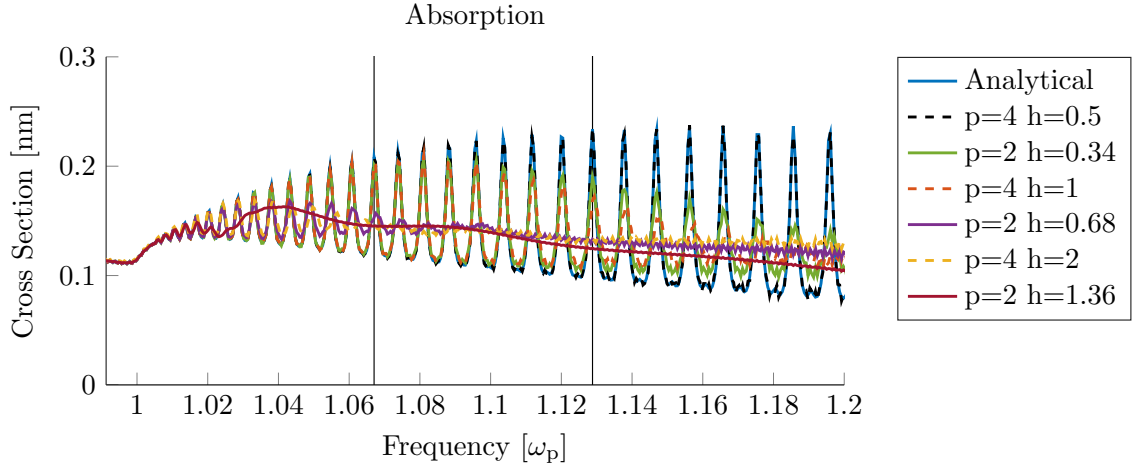


Figure 4.5: Absorption spectra showing bulk plasmons for different polynomial orders and mesh refinements. The vertical lines indicate the frequencies for which the full convergence check is conducted below.

cies are indicated by the vertical lines in Fig. 4.5). As pointed out, I can use the same meshes as in the previous section for the surface modes. The convergence check is displayed in Fig. 4.6. The initial errors – which are the same for all polynomial orders in both cases and are found to be approximately 30% for the first peak and 45% for the second peak – have to be interpreted with care: They actually correspond to complete absence of the bulk plasmons. The effect of the bulk refinement is very strong in both cases, as one would expect. For the lower frequency, errors of the order of a few percent can be reached by using a very fine mesh. Below a certain value for h , all three polynomial orders exhibit comparable slopes of $\alpha \approx 3$. This is surprising in view of an expected convergence with $\alpha = p + 1$. Surely, the study here is very limited due to the small number of data points. Unfortunately, more data points are not feasible, so the actual value of α obtained here is perhaps not very meaningful. Still, the fact that a steep slope is obtained suffices to show that the method actually enters a converging regime. For the higher frequency, where the mode features even more maxima and minima, the error remains large for second order polynomials. For third and fourth order polynomials it drops to about ten percent. It is important to keep in mind that for these extremely high bulk modes the error is of the order of ten percent. Nonetheless, the peaks are present in the spectra and indicate the correct frequencies of the modes.

For reasons I have pointed out, the method does not show the theoretically expected slopes in the convergence plots. However, the method is well-behaved for both bulk and surface plasmon resonances upon h -refinement. According to the findings from this chapter, for every geometry one should confirm that the change in result for surface plasmons drops drastically when going beyond a certain discretization. Then, the error on the surface plasmons on a linear level will be of the order of 1%. For the bulk plasmon modes, the regime where the change in result suddenly drops can practically not be entered (in realistic simulation times). The error will therefore in practice be on the order of 10%. Higher order bulk plasmon modes exhibit a significantly larger error than low order bulk plasmon modes.

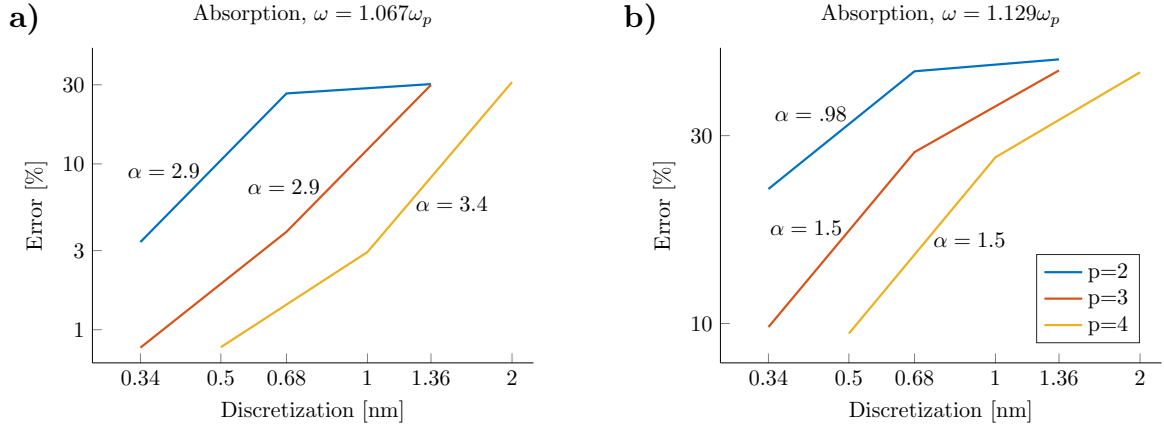


Figure 4.6: *hp*-convergence plots of the bulk plasmon peaks at two different frequencies for uniform refinement of the bulk. The error is given with respect to the analytical reference solution from Ref. [43]. The slope, corresponding to the polynomial order α , is indicated only for the steepest line segment for each polynomial order.

4.3.2 Second Harmonics

Having investigated the convergence of the method on a linear level, I will now move on to the second order quantities. In Sec. 2.2.3 I demonstrated that the hydrodynamic equations are intrinsically nonlinear and I have shown how they can be expanded into the higher nonlinear orders. I would now like to demonstrate the convergence of second harmonic cross sections which are constituted by the fields \mathbf{E}_2 and \mathbf{H}_2 .

For the second order quantities I have no reference solution, but given the good convergence behavior on a linear level (and assuming that the equations are correctly implemented), I have reason to believe that, if the method shows convergence on a nonlinear level, it will also converge to the physically correct value. To show this convergence, I will do two things: I will compare the results from an *hp*-refinement study to a numerical reference solution and I will analyze the change in result when going from one refinement to the next, making sure that the changes grow smaller with each refinement (a *soft* convergence study). The numerical reference solution that I use is the 4th-order solution with the very fine mesh from the hard convergence studies above, in Sec. 4.3.1. The maximal edge length in the center of the bulk is 0.5 nm and the surface elements are of 0.16 nm. But using it as a reference comes at a price: I can of course no longer use it for the convergence study itself and I need to use a different set of meshes. Ideally, not only three, but four meshes to have one additional data point for a soft convergence study. The meshes I use for the convergence study are generated with Trelis [134]. The coarsest mesh has elements of size 2 nm and is then subsequently refined, but only in the vicinity of the surface, since the modes excited by SHG are also surface modes and this is where the largest contribution is expected. Even for the finest mesh, the elements in the center are still of 1 nm but surface elements are of 0.25 nm. This has the advantage that less elements are needed in total and therefore the run times are significantly shorter. However, the refinement is not as well-controlled as in the case of the uniform refinement.

For the simulations of the second harmonics, I employ spectrally sharp Gaussian pulses, which cor-

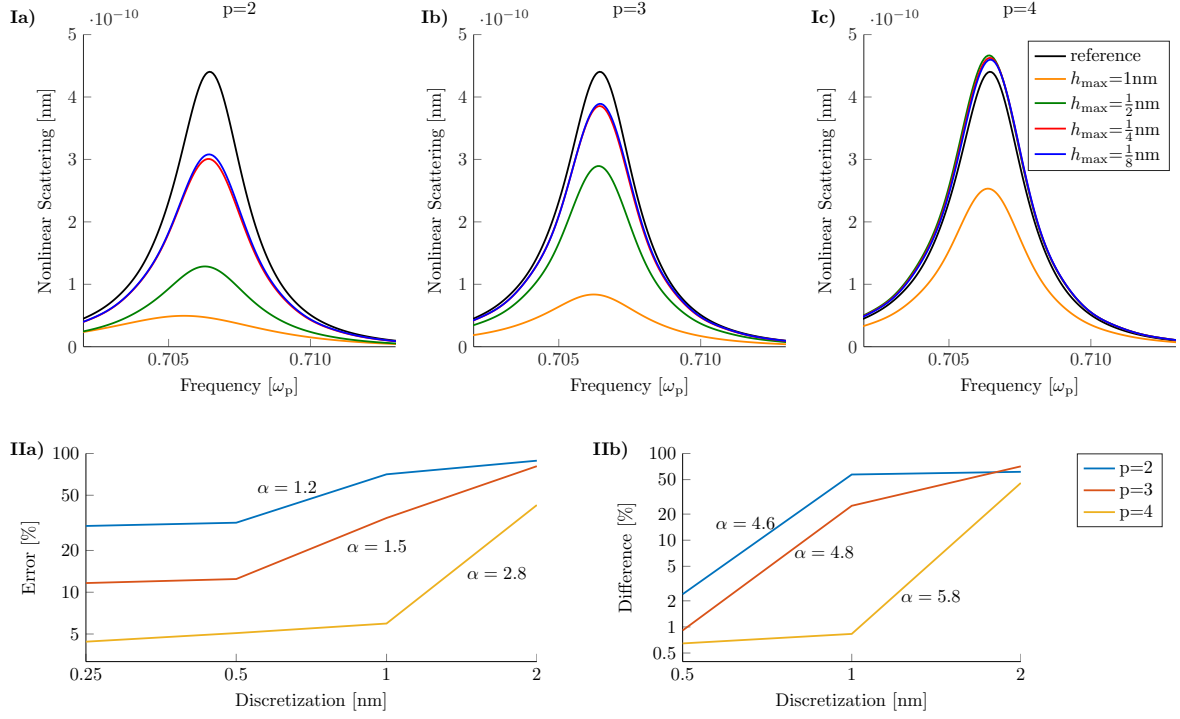


Figure 4.7: **I)** Second harmonic scattering signal for different polynomial orders and different refinements of the mesh near the surface, along with a reference solution. **IIa)** Double-logarithmic plot of the error of the calculations with respect to the numerical reference solution (maximal edge length in the bulk 0.5 nm, length of the surface elements 0.16 nm). **IIb)** Double-logarithmic plot of the change of a calculation with respect to the previous calculation.

respond to temporally long pulses. I have chosen a pulse width of 13.3 fs which is sufficiently sharp so that the fundamental signal is numerically zero at the position of the second harmonic. for my purposes, in the units used here, this means that the signal is below 10^{-15} (cf. Sec. 5.1.2, Fig. 5.5). Because of the long incoming pulses and due to the small magnitude of the second harmonic signals long run-times are necessary – otherwise one finds ripples on the spectra because the excitations have not fully decayed. These long run times make the convergence checks of the second harmonics more difficult. In the case of the cylinder a comparably strong signal is obtained at the quadrupole frequency and the field distribution is also a quadrupole field-distribution. Therefore a discretization near the surface seems justified.

The results of this convergence test are displayed in Fig. 4.7. The incoming signal is at half the frequency of the quadrupole resonance and the signal is detected at the quadrupole resonance. Figs. 4.7 **Ia)**-**c)** show the SHG-spectra for the three different polynomial orders and for the different meshes along with the reference solution. For second and third order polynomials, the SHG spectra are much too small at first. They slowly approach the reference value from below. Even for the finest mesh the error remains large, at above 30% and above 10%, respectively. For fourth order polynomials, which naturally resolve the bulk better than the other two polynomial orders, the error is initially also quite large (30%), but already after first refinement it drops significantly to about 5%. A close look at Fig. 4.7 **Ic)** reveals an interesting behavior: The solution overshoots the analytical reference solution, but then moves back in the correct direction, bringing the spectra back down to the reference value, steadily decreasing the error. It becomes clear from Fig. 4.7 **Ila)** and **b)** that the changes grow so small that the error will remain at its value just under 5%, so once again the result is limited by the bulk refinement. With some optimism, the overshooting-behavior can however be considered a lucky feature: one could view it as providing an upper bound to the second harmonic signal, as it is unlikely that the maximum will start growing again upon further refinement. This would however have to be checked if one was aiming for even higher levels of accuracy.

Comparing the different polynomial orders, most notably the errors for the different polynomial orders in Fig. 4.7 **Ila)**, one makes an important discovery: While the errors do not change much anymore between the two finest discretizations within each of the polynomial orders, there are still big differences in error between the different polynomial orders. Thus, a refinement of the surface or of the bulk in the vicinity of the surface no longer suffices to improve the result, but a better bulk resolution (going to a higher polynomial order) still has a big impact on the result. Thus, one can conclude that bulk refinement does play a big role for the second harmonic signal, limiting the accuracy of the result to about 10% for third order polynomials and to about 5% for fourth order polynomials when only the surface is refined, with respect to a fourth order calculation with a very fine mesh everywhere. Thus, also on the level of second harmonics, the method is well-behaved. For calculations of second harmonics in the following chapters I will always use meshes with a very fine bulk region and third or fourth order polynomials for which I can now state the error to be of the order of only a few percent.

5

NUMERICAL RESULTS

This chapter is dedicated to numerical investigations of several plasmonic nanostructures by means of the discontinuous Galerkin time domain method. Within this method, the fully nonlinear and nonlocal material model can be employed. The analytical reference calculations for the local and the nonlocal material as well as the convergence tests from the preceeding chapters lay the foundations for the investigation of more complicated structures which takes place in this chapter. Besides the scattering and absorption cross section, there are other quantities of interest that are accessible within the DGTD method, such as the fluctuation of the electron density and the field distribution and field enhancement. After a discussion of scattering and SHG from a single cylinder, I turn to more complicated setups, such as a cylindrical dimer, a V-groove and a bow-tie. The findings are compared to the analytically obtained results from Chap. 3. All considerations, except where otherwise noted, are done for quasi two-dimensional structures that are infinitely extended in z -direction and the polarization is the one which is relevant in the context of plasmons, where the magnetic field points in z -direction.

5.1 Cylinder

5.1.1 Linear Scattering Simulations

A natural starting point for my numerical investigations is once again the circular cylinder with radius 10 nm which I already discussed analytically in Chap. 3. I employ the hydrodynamic material model with the same parameters as in Sec. 3.1. The numerical setup and the mesh which I use in this section is shown in Fig. 5.1. The TFSF contour is kept close to the particle, so that errors from the propagation through the coarsly meshed free space are kept to a minimum. The PMLs are kept very far from the scatterer in this example, to make sure that no evanescent fields reach into the PML region.

5 Numerical Results

The particle is illuminated by a broad-band light pulse with Gaussian shape. It possesses a temporal width of $1/3$ fs which corresponds to a very broad spectral width of $1.36 \omega_p$ and is centered approx-

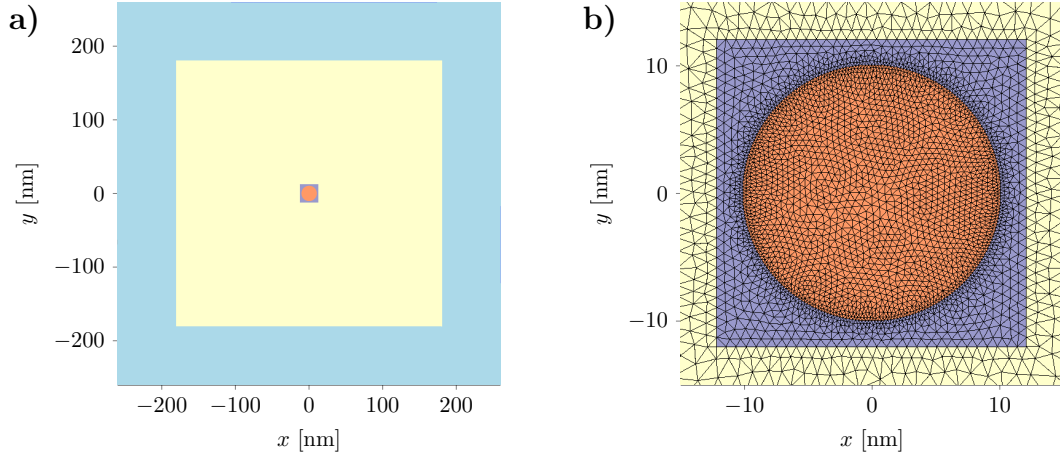


Figure 5.1: a) The TFSF setup used in the calculations of this section. b) The mesh in the center of the numerical setup, near the cylindrical scatterer. The maximal edge length within the cylinder is 0.54 nm.

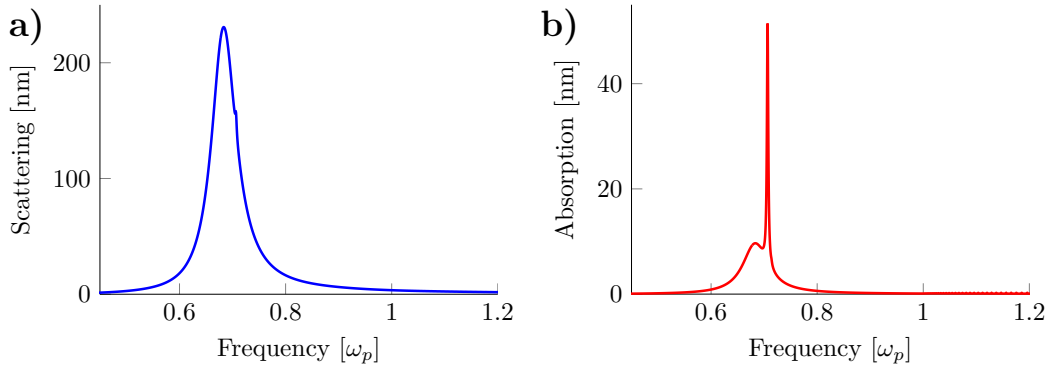


Figure 5.2: a) Scattering and b) absorption for a single cylinder with radius 10 nm. The scattering spectrum is dominated by a broad dipole peak and exhibits a small quadrupole resonance. The absorption spectrum features a broad (low Q -factor) dipole peak and a very pronounced (high Q -factor) sharp quadrupole peak.

imately at the plasmon frequency ω_{sp} . The spectra are normalized to this incoming pulse shape. The total simulation time was over 330 fs and therefore much longer than the exciting pulse. Thus at the end of the simulation the fields in the system have decayed to the point where they are numerically zero. I have already demonstrated the convergence characteristics of this system in Chap. 4 and discussed the spectra of the structure in Chap. 3. Scattering and absorption are displayed again in Fig. 5.2. To discuss the features of this spectrum I recall the concept of quasinormal modes which I already

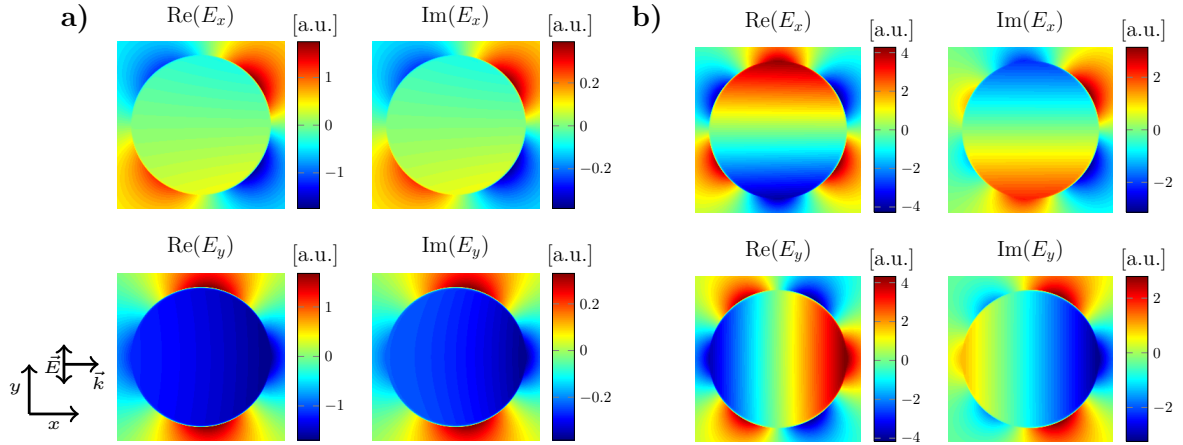


Figure 5.3: Real and imaginary part of the electric field distributions for both components E_x and E_y for **a)** dipole and **b)** quadrupole resonance frequency. The direction of the incident field and the polarization is depicted by the arrows on the lower left.

mentioned in Chap. 3 and which is introduced in more detail in Appendix A. Such modes pertain to a complex frequency and the Q-factor, which describes the dissipation of the mode through radiation and absorption, has to do with the imaginary part of the mode-frequency: A high-Q mode (small

imaginary part, sharp peak) dissipates slower than a low-Q mode with a larger imaginary part [96]. The scattering spectrum is in the present case dominated by a broad dipole peak and the absorption spectrum features a broad dipole peak with a low Q-factor and a very sharp and pronounced quadrupole peak with a high Q-factor. By the widths of the dipole and quadrupole resonances for the present system one can deduce that the energy dissipates much faster for the dipole mode. In Fig. 5.3 the Fourier transformed field distributions at the real frequencies of the dipole and quadrupole peak are displayed. They have been calculated by means of the on-the-fly Fourier transform (cf. Sec. 4.2.1). They resemble the analytically calculated field distributions from electrostatic theory that were displayed in Fig. 3.10, but are not exactly the same. For the dipole frequency,

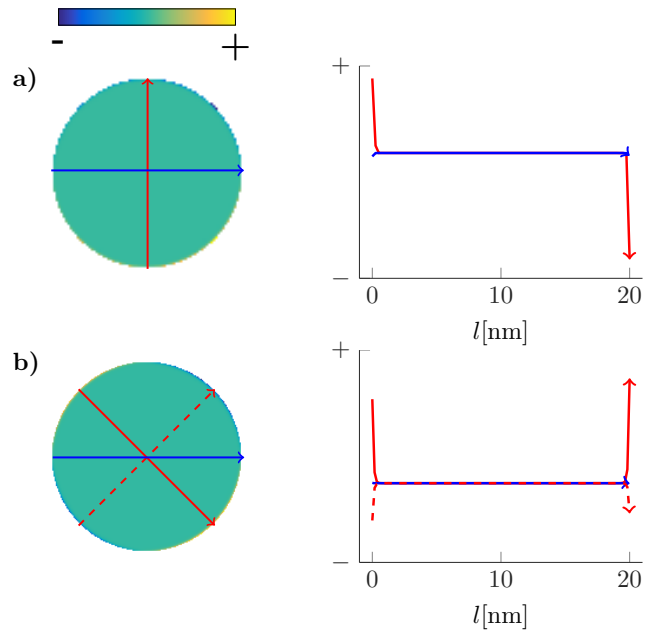


Figure 5.4: Real part of the Fourier transformed density fluctuations for **a)** dipole and **b)** quadrupole resonance frequency. On the right, the density is displayed along the different paths l shown on the left, in the corresponding colors.

the field distribution from the DGTD simulation is that of a “pure” mode (as in Fig. 3.10) since the quadrupole peak is so sharp that it does not influence the field distribution at the dipole frequency. For the quadrupole resonance this does not hold: The imaginary part of the Fourier transformed electric field shows a significant distortion, due to the overlap with the low-Q dipole mode. Next, I shall turn to an investigation of the electron density fluctuations in the cylinder. This quantity is important in the context of the hydrodynamic model since it represents in itself the big difference between the hydrodynamic model and the ordinary Drude model, where spatial density fluctuations are neglected. In a similar way as for the electric fields above, I present the on-the-fly Fourier transform of the fluctuations in the density in Fig. 5.4 for the dipole and the quadrupole frequency. For better visibility, the density fluctuations along line cuts through the particle are also displayed in Fig. 5.4. They are typical dipole and quadrupole distributions. The density fluctuations occur exclusively very close to the particle surface, where the electron liquid is being pressed against the hard walls by means of the electric force acting on it. Since the fluctuations happen on such an extremely small scale of well below a nanometer, the images of the resulting potentials and fields look just like the ones from the local or the electrostatic case (which represent the limiting case of a fluctuation on an infinitesimally small length). This makes it possible to compare the field images obtained in the local case to those from electrostatics, which is useful when it comes to distinguishing and categorizing the fields. They share the symmetries with the electrostatic potentials which I have presented in Sec. 3.2.5, Fig. 3.10. This was also found by the group theoretical symmetry considerations which I presented in Sec 3.4 and is physically explained by the fact that the displaced charges give rise to the potentials.

5.1.2 Second Harmonics

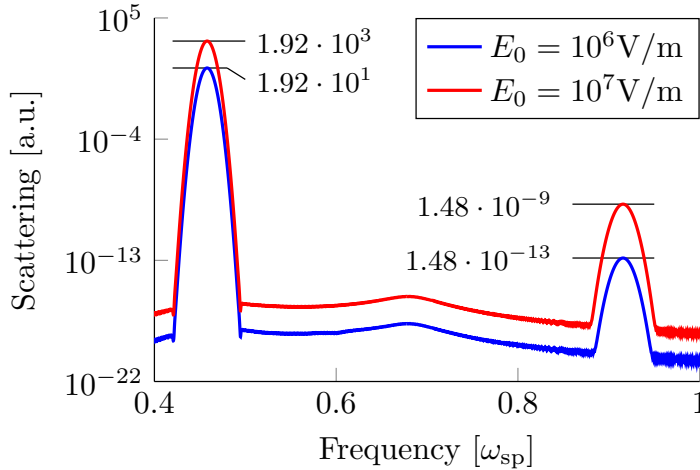


Figure 5.5: Scattering signal for a spectrally sharp pulse impinging on a cylinder. The second harmonic scattering flux increases by four orders of magnitude when the linear signal is increased by two orders of magnitude.

In Sec. 2.2 I discussed the nonlinear nature of the hydrodynamic model. Here, I present some calculations showing SHG for a single cylinder. The first simulations of this kind with the present method were published in Ref. [M2] and then later used in the making of Ref. [M3] and [M4]. Employing the full hydrodynamic model, it is in principle possible to extract terms of arbitrarily high order. Time domain simulations are naturally well-suited for the calculation of higher harmonics since they make it possible to solve the full set of the hydrodynamic and Maxwell’s equations for (in principle) all frequencies at the same time and therefore allow for mixing or doubling of frequencies as it is contained in the equations. As I already described in Sec. 4.3.2, an incident pulse is used

that is spectrally sharp, so that it does not interfere with the higher harmonic signal. In this thesis, I used a pulse of temporal width 13.3 fs for all nonlinear calculations, which corresponds to a spectral width of $0.034 \omega_p$. In Fig. 5.5 a full scattering spectrum for a nonlocal simulation with incidence frequency $\omega_{in} \approx 0.46 \omega_p$ is shown. One can see that the linear signal decays sharply in the vicinity of ω_{in} and does not influence the spectrum at the second harmonic signal at $2\omega_{in}$. The extremely small cross sections of 10^{-12} might look strange as a numerical result at a first glance, given that they are comparable to machine precision, but please note that these are cross sections which are not directly calculated in the numerical scheme. What is calculated are the fields. They are typically of the order of 10^{-3} for a second

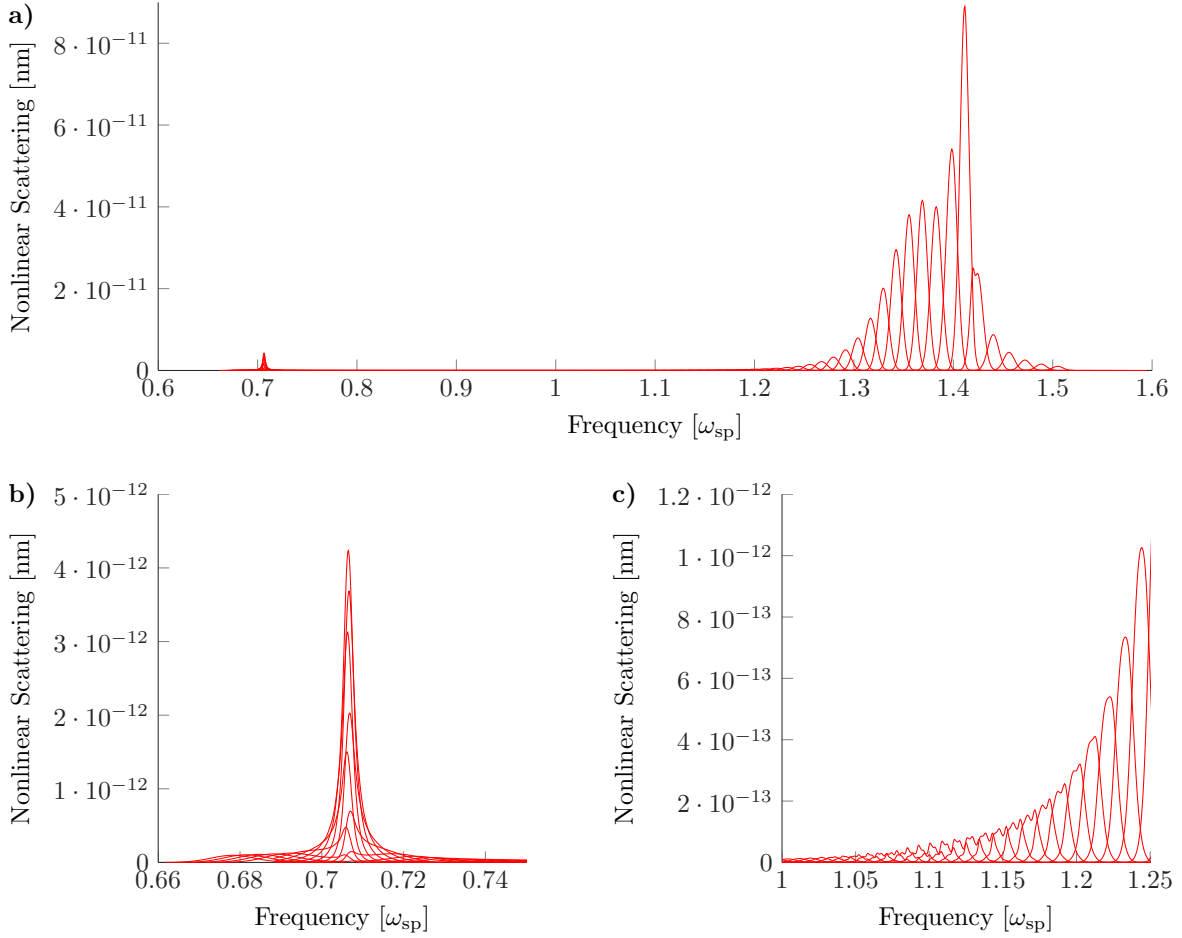


Figure 5.6: **a)** A full SHG-scan for a single cylinder, from below the dipole resonance to above twice the quadrupole resonance. The SHG signal around $2\omega_{sp}$ is much stronger than the one near ω_{sp} and resembles the linear absorption spectrum with a broad (dipole) and a sharp (quadrupole) resonance. **b)** Zoom on the dipole and quadrupole resonance near ω_{sp} . A very sharp peak is found that lies exactly at the quadrupole frequency. **c)** Zoom on the SHG spectrum just above the plasma frequency. Up to about $1.2 \omega_p$ small ripples are visible due to bulk plasmons. For higher frequencies the bulk plasmons are no longer resolved and the ripples disappear.

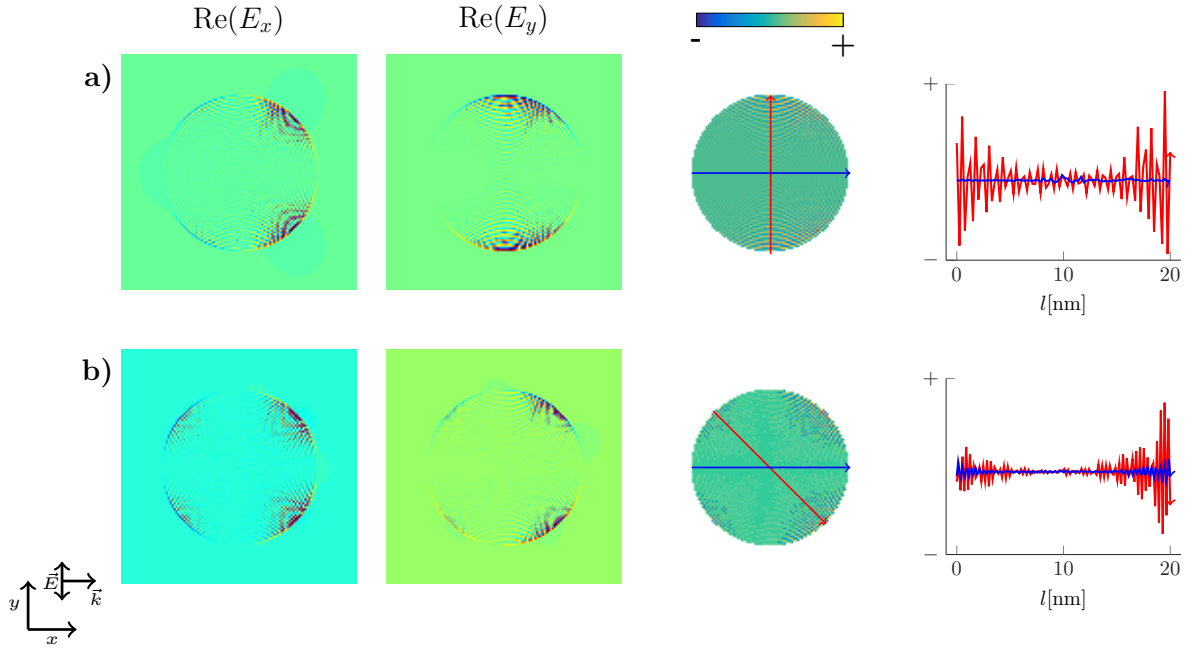


Figure 5.7: Fourier transformed images of the second harmonic fields and density fluctuations at **a)** twice the dipole frequency and **b)** twice the quadrupole frequency.

harmonic signal. The fluxes scale quadratically with the fields and are then normalized to the incident intensity, which generates these extremely small cross sections. Numerically speaking, there is however no problem with these numbers since their smallness arises only in the post-processing.

The linear signals in the spectra in Fig. 5.5 scale quadratically with the incoming field (since they are poynting fluxes which are proportional to $\mathbf{E} \times \mathbf{B}$). The second harmonic signal at $2\omega_{\text{in}}$ hence scales with the fourth power. I can now compare the SHG efficiency of the cylinder within the hydrodynamic model to the estimate given by Eq. (2.52). There, an incident field strength of $E_0 = 10^{11} \text{ V/m}$ was needed so that the linear and the second harmonic signal are of the same order of magnitude. According to the values from Fig. 5.5, for the system considered here, a field strength of $E_0 = 10^{13} \text{ V/m}$ would yield comparable linear and SHG intensities. As I will show later, the SHG intensity depends strongly on the geometry.

I would like to point out that between the linear signal and the SHG signal, there is a small bump near ω_{sp} which is simply due to the well-known dipole resonance of the cylindrical scatterer. This kind of bump (which I confirmed to scale just like the linear signal with the intensity) was mistakenly called a “fractional harmonic” in a recent publication by Krasavin et al. [65]. According to the authors of this work, this peak is due to the exponent in the Thomas Fermi pressure term. However, the numerical results presented in this very same work contradict this hypothesis since the peak persists, even in the absence of the Thomas Fermi pressure term – and it is found exactly at the frequency of a pronounced resonance in the linear spectrum of their structure.

Having confirmed the scaling behavior of the higher harmonics, I would like to move on to the investigation of full second harmonic spectra, i.e. cover a larger frequency range. This is perhaps one of the

weaker point of this approach since it requires running dozens of separate calculations. With the spectrally sharp (temporally long) pulses and the high resolutions required for bulk plasmons, a single calculation for a complicated structure can take several days. Fig. 5.6 shows such a full second harmonic scan of a single cylinder over a large frequency range, with SHG-frequencies from just below the dipole resonance to well above twice the quadrupole frequency.

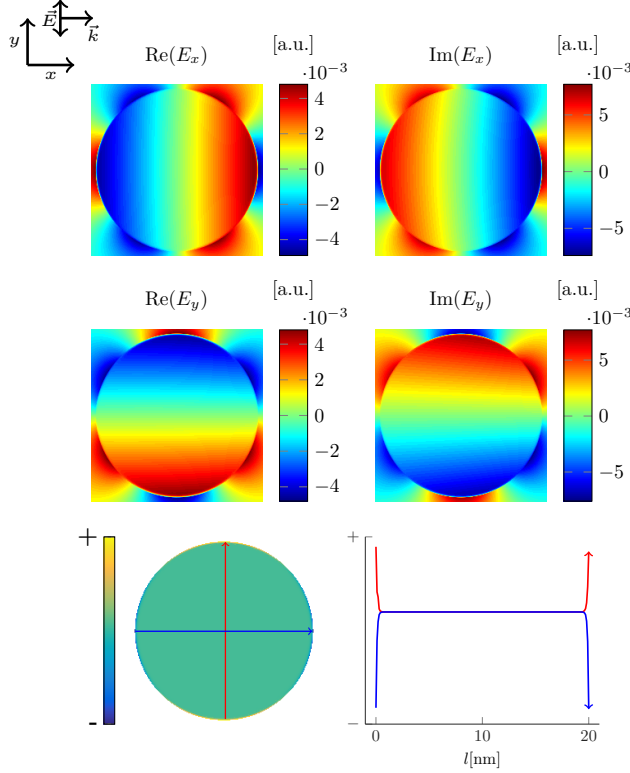


Figure 5.8: Second harmonic fields and density fluctuations near the plasmon frequency of a single cylinder. The signal is found at the quadrupole frequency.

The first thing to note in the broad band SHG-spectrum is that the signal around $2\omega_{sp}$ is over an order of magnitude larger than the signal at ω_{sp} . There are two possible explanations for this: either it is more advantageous to have a resonance at the incoming frequency than having one at the second harmonic, or the presence of bulk plasmons serves as an additional source of non-linearity (cf. 2.2.5). The signal at $2\omega_{sp}$ resembles very much the linear absorption spectrum from Fig. 5.2 b). It features a broad peak at twice the dipole frequency and a much sharper and higher peak at a twice the quadrupole frequency. In Fig. 5.7 the field distributions and the density fluctuations at the frequencies of these peaks are displayed. I show only the real part of the fields, since the imaginary part contains no additional information. As pointed out, at these high frequencies there are bulk plasmons present, as can be seen in the field- and density-plots do show bulk plasmons. The presence of these bulk plasmons makes a straightforward mode-categorization difficult. The images at twice the dipole frequency are somewhat easier to analyze since the dipole signal has less overlap with the quadrupole signal. While the field images only slightly resemble the field distributions from Fig. 3.10 Ia), the strength of the density fluctuations actually seems to follow the magnitude of the potential in Fig. 3.10 Ia). The same holds for the density fluctuations at twice the quadrupole frequency in Fig. 5.7b) – it follows the potential in Fig. 3.10 Ib). It is however difficult to categorize the field distributions. For this particular example, the field plots are not very clear and difficult to analyze. It is likely that the modes excited here are the same ones that are excited at half the frequency in the linear case (Fig. 3.10 Ia) and Ib)), overlaid with excitations of bulk-modes. This suggests that the SHG mechanism is strongly influenced by the presence of bulk plasmons and is not the one which was analyzed group-theoretically in Sec. 3.4. For the mechanism described there, only those modes that are dark on the linear level are excited via SHG.

I now turn to the peak near the plasmon frequency ω_{sp} . While the spectrum does not resemble the absorption spectrum as much as the one at $2\omega_{sp}$, the highest peak is still exactly at the quadrupole

frequency. An analysis of the fields and density fluctuations at this frequency is given in Fig. 5.8 and allows for a clear statement: The mode shows a quadrupole field distribution and density fluctuation. This was to be expected from the frequency at which it was found. And it is in fact the previously dark quadrupole mode from Fig. 3.10 **IIb**). Thus, all the predictions from Sec. 3.4 are confirmed: The dipole mode is suppressed because the symmetry relation which has to hold between the exciting pulse and the SHG signal cannot be fulfilled for a dipole mode in the case of a single cylinder. The symmetry relations are however fulfilled by the dark quadrupole mode excited here.

5.1.3 Origin and Intensity Dependence of Higher Order Terms

Before I turn to more complicated structures, I will dedicate this section and the next to discuss some general properties of the nonlinear hydrodynamic model, employing the example of a single cylinder. In the second order hydrodynamic equations 2.61 and 2.62, the terms containing products of first order quantities which act as sources for the second harmonics can be considered individually [M3].

These terms are the convective term, the pressure term, and two Lorentz force terms, one containing the electric field and one containing the magnetic field. Two questions arise in the context of the nonlinear hydrodynamic equations: Firstly it is interesting to study their respective contributions to the second harmonic signal. Secondly, one can investigate if there is an additional intensity dependent effect besides the obvious scaling.

To address the first question, a numerical framework is needed which allows us to separate the different contributions to the higher order terms. Dan-Nha Huynh implemented a perturbative version of the hydrodynamic DGT code which makes it possible to separate the contributing second order terms. Some findings on the contributions of the separate terms for different structures have already been published in a paper written by Dan-Nha Huynh and myself [M3]. The second question, regarding the intensity dependence of higher order terms, arises for the following reason: The nonlocal parameter β , as I have shown in Chap. 2, comes out of the (linearized) pressure gradient term in the hydrodynamic equations. The linear scattering spectra for a particle made up of such a nonlocal material are altered (shifted) and the alteration is proportional to the magnitude of the nonlocal parameter. If there are nonlinear corrections to the pressure gradient term, and hence corrections to β , this will have an additional effect on the spectra. Since this is a second order effect, it is expected to be intensity dependent. This question has not been addressed in the above-mentioned work and I would like to discuss it here briefly.

Fig. 5.9 shows the spectra including only one of the four different terms which contribute to the second harmonic spectrum, as well as a spectrum containing all of the contributions. All of this is done for two different incoming field intensities at the frequency of the quadrupole resonance which provides the strongest SHG signal. I want to stress that the considerations made here are only done for this one resonance frequency and would in principle have to be repeated for other frequencies to paint a full picture. From Fig. 5.9 **I**) it can be seen that in the present case the convection term contributes the most to the nonlinear spectrum. It is followed by the pressure term contribution and finally by the electric and magnetic contributions which are of similar magnitude.

Studying the intensity dependence of these terms to the point where corrections to the nonlocality become visible poses a severe numerical challenge. The effects are in fact extremely small. To make them visible, several orders of magnitude in the incoming field intensity need to be bridged. The results from Fig. 5.9 were obtained using incoming pulses of $E_0 = 10^4$ V/m and $E_0 = 10^7$ V/m. It can be seen in Fig. 5.9 **I**) that the high-intensity spectrum containing all of the source terms experiences a red-shift,

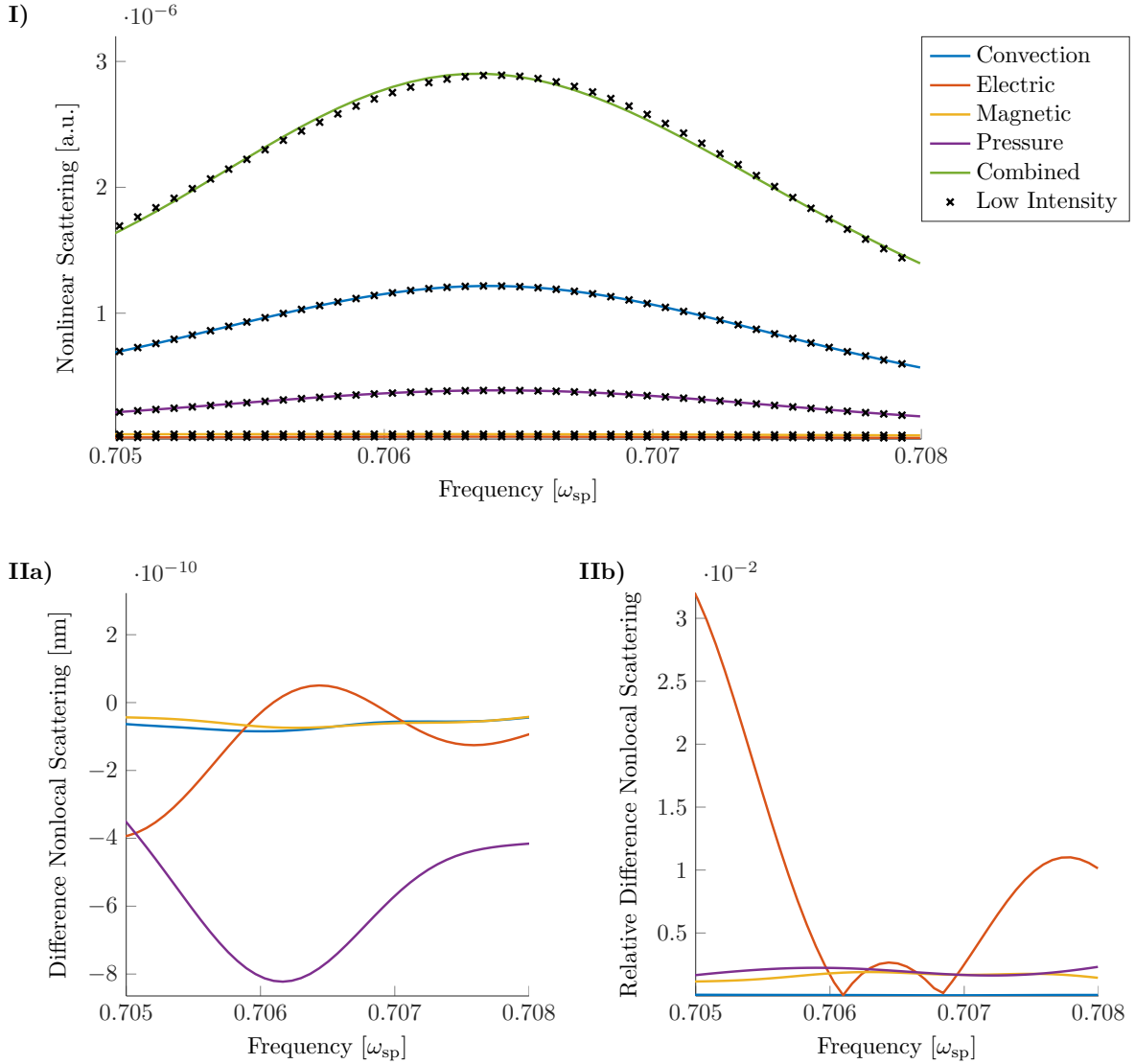


Figure 5.9: I) The contributions to the second harmonic scattering spectrum of a single cylinder are shown for two different frequencies, the solid lines are for an incident field strength of $E_0 = 10^7$ V/m and the crosses for corresponding simulations with $E_0 = 10^4$ V/m. In IIa) and b) the absolute and relative difference between the calculations with the two different intensities are shown for each of the contributions.

i.e. a shift in the opposite direction of the original blue-shift that was introduced by adding nonlocality on the linear level. Looking at Fig. 5.9 II), the origin of the shift can be attributed to the pressure term which undergoes the strongest intensity-dependent modification in absolute numbers. The electric field term is the only other term that is significantly influenced by the intensity, in relative numbers the electric term is even influenced the strongest.

While the discussion of the intensity dependence as presented here is far from complete and would be an interesting topic to address both numerically and analytically, perhaps in a perturbative fashion, I would like to conclude the numerical investigations at this point by stating that for our purposes these shifts and corrections to the nonlocality can safely be neglected. I.e. the linearized pressure term is responsible for all nonlocal effects and nonlinear corrections need not be taken into account. This is important as it justifies comparing nonlinear resonances to those resonances obtained from linear or broad-band calculations, which I will do extensively in the following sections.

5.2 Cylindrical Dimer

5.2.1 Local Case

In this section I turn to a numerical investigation of the dimer structure which I discussed analytically in the electrostatic limit in Sec. 3.3. It consists of two cylinders of 10 nm radius with a gap of 2 nm. In order to do so, I will first calculate the local spectra and interpret them with the help of the analytical findings from Sec. 3.3 and by using a second numerical method, a quasinormal mode calculator (cf. Appendix A) as well as the group-theoretical considerations from Sec. 3.4) and then discuss the nonlocal and nonlinear properties. Let me recall the solutions for the frequencies of the modes of the dimer system, which were given by

$$\begin{aligned}\epsilon(\omega) &= -\coth(k\xi_0) \quad \text{for sinh-type solutions} \\ \epsilon(\omega) &= -\tanh(k\xi_0) \quad \text{for cosh-type solutions}\end{aligned}\tag{5.1}$$

Both the sinh- and cosh-type solutions are then combined with either a sine- or a cosine-function for the “azimuthal” part, yielding a total of 4 classes of solutions which belong to the symmetry point group D_2 (cf. Sec. 3.3.3 and Sec. 3.4):

	sinh (low frequency)	cosh (high frequency)
sin	class I excitation from both directions (retardation needed)	class II excitation along dimer axis
cos	class III excitation perpendicular to dimer axis	class IV “dark mode”

The graphical solutions for Eq. (5.1) are displayed again in Fig. 5.10. They can now be compared to the numerical simulations. The total field region of the mesh which was employed for all the calculations is displayed in Fig. 5.11. The scatterer is meshed with a very high resolution so that high order surface plasmons can be resolved.

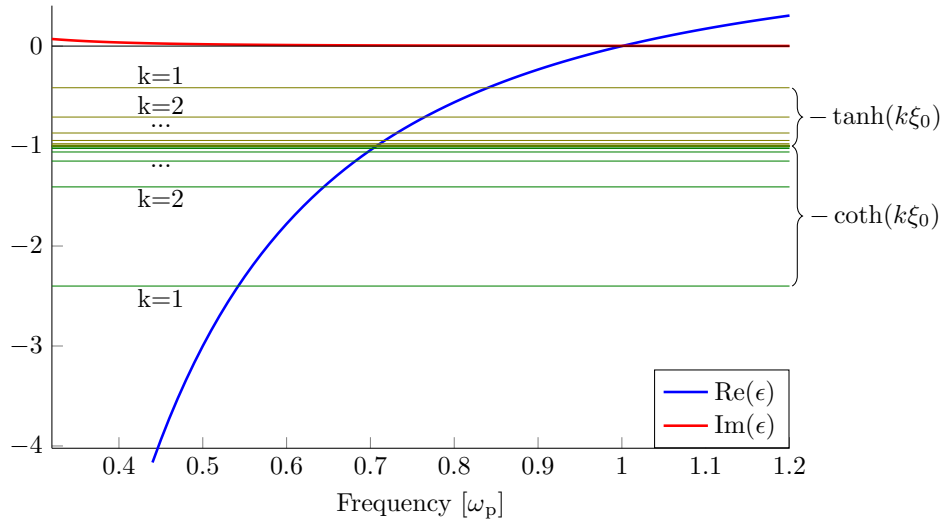


Figure 5.10: Graphical solution for the frequencies of the modes of a cylindrical dimer within electrostatic theory, as given by Eq. (5.1).

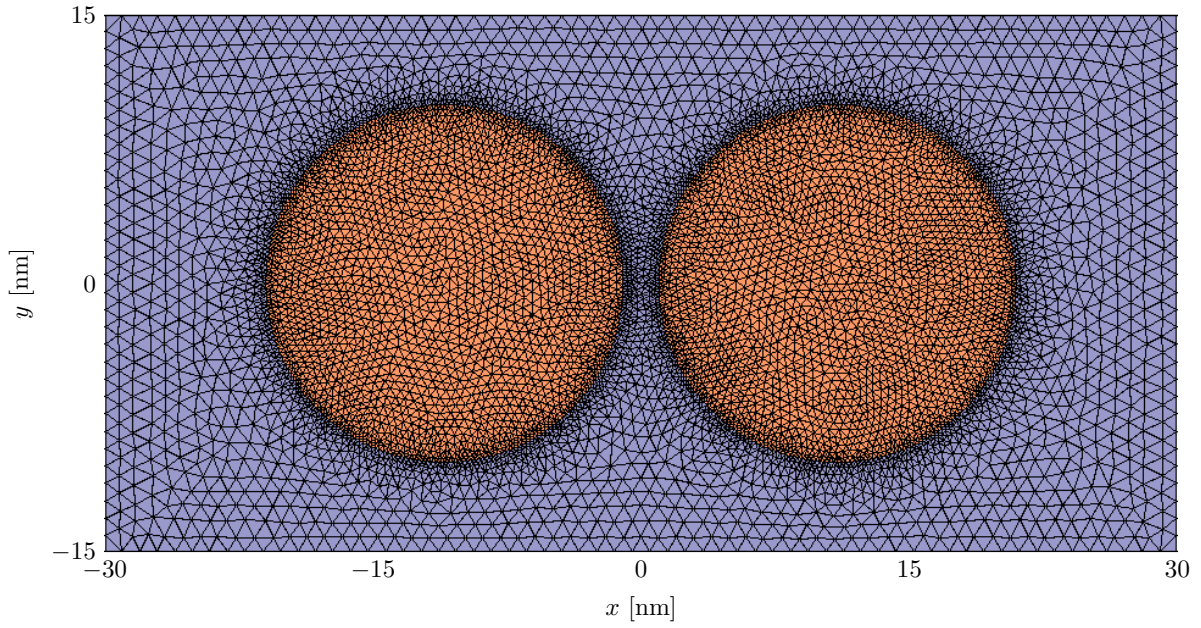


Figure 5.11: The total field region containing the dimer scatterer of the mesh which was employed for the bowtie calculations. The maximal edge length within the scatterer is 0.8 nm. The scattered field region (not shown) extends to $\pm 250 \text{ nm}$ in every direction and beyond that, there are 100 nm of PMLs in every direction (not shown).

5 Numerical Results

In Fig. 5.12 I present the scattering spectra which were obtained by means of the DGTD method, along with the analytically obtained electrostatic solutions from Fig. 5.10. As expected from the underlying symmetries (Sec 3.4), the spectrum for the illumination with \mathbf{k} perpendicular to the dimer axis (incidence from the top in Fig. 5.11) features only modes below the plasmon frequency, i.e. of class III and class I – the latter because the structure is large enough not to be too far in the electrostatic limit. For incidence with \mathbf{k} along the dimer axis (incidence from the left in Fig. 5.11) the spectrum exhibits resonances above and below ω_{sp} . The frequencies calculated by electrostatic theory do not quite match the frequencies at which the resonances are actually found. This is also because the structure is too large to be accurately described within electrostatics. However, for the lowest order modes $k = 1, 2$ the peaks are well-separated from all other peaks and can be clearly identified. They exhibit in fact the expected symmetries which can be seen by inspecting the field images. The degeneracy, for instance of the $k = 1$ modes of class I and III, which was found in electrostatic theory, is lifted in the numerical simulation, making it possible to access the field images of both of these modes.

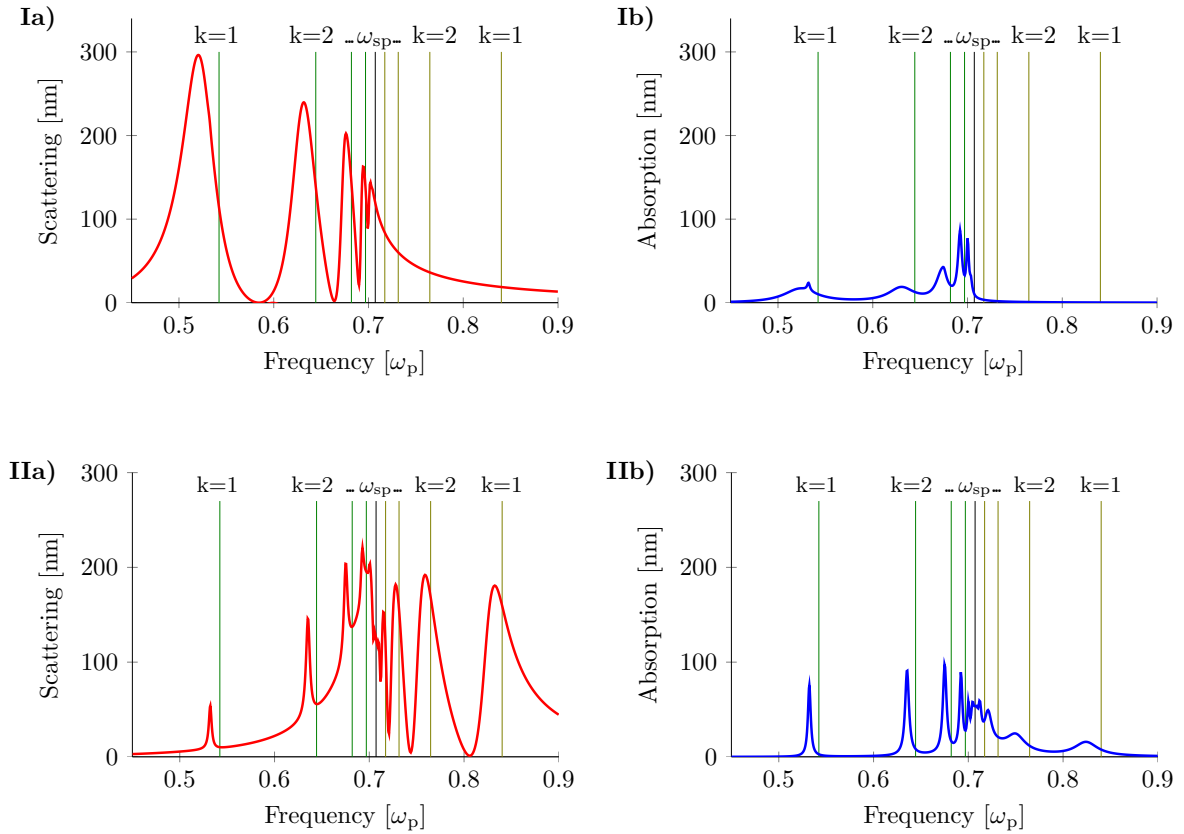


Figure 5.12: Scattering and absorption spectra for a cylindrical dimer under illumination perpendicular to the dimer axis (**Ia**) and (**Ib**)) and under illumination along the dimer axis (**IIa**) and (**IIb**)). The vertical lines indicate the frequencies of the modes from Fig. 5.10 and the plasmon frequency.

In Fig. 5.13 the same spectra as in Fig. 5.12 are displayed again, but this time they are compared to the spectral location of the quasinormal modes in the complex frequency plane (cf. Appendix A). The peaks in the scattering and absorption spectra are found at frequencies at which resonances are expected from the quasinormal mode calculations. Modes with a high Q-factor (small imaginary part in the quasinormal mode calculation) provide sharper spectral peaks in the scattering calculations. Both

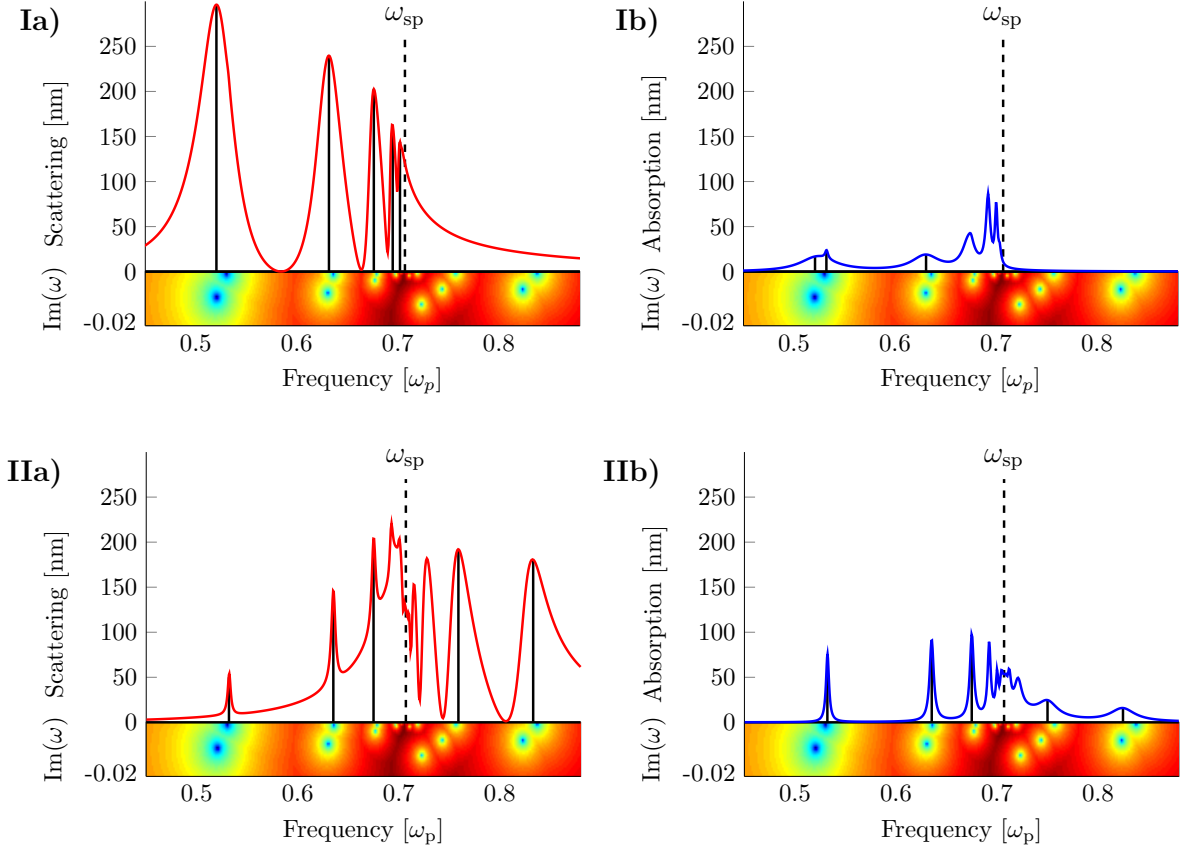


Figure 5.13: Scattering and absorption spectra as in Fig. 5.12 and the spectral location of the quasinormal modes of the cylindrical dimer. The vertical black lines serve as guides to the eye and show that the two numerical schemes are in good agreement.

methods agree well for the lower order modes. For higher orders, the quasinormal mode calculations which employ regular cylindrical coordinates fail to resolve the modes. From the quasinormal mode calculation it becomes once again apparent that the sine-cosine degeneracy is lifted: The clearest example is again the low-frequency $k=1$ mode which is found just above $0.5\omega_p$. Here, two quasinormal modes are found, one at a slightly lower frequency with a large imaginary (low Q-factor) part and one at a higher frequency with a very small imaginary part (high Q-factor). The low-Q mode dominates the scattering spectrum under perpendicular incidence in Fig. 5.13 **Ia**) and the high-Q mode is found in the scattering spectrum for incidence along the dimer axis Fig. 5.13 **IIa**). Additionally, the high-Q mode is also present in the absorption-spectrum for perpendicular incidence, i.e., it is excited from both

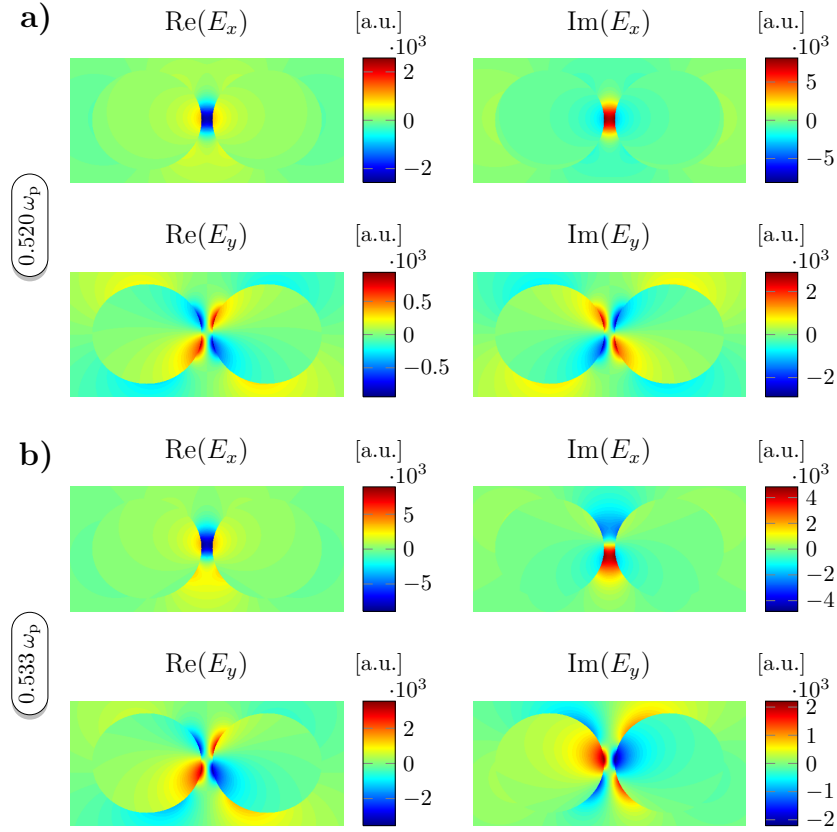


Figure 5.14: Field images for the $k = 1$ modes, incidence orthogonal to the dimer axis. **a)** At $0.520\omega_p$ a pure mode of class III is excited. **b)** At $0.533\omega_p$ a mode of class I is expected, but due to the low Q -factor of the mode at $0.520\omega_p$, there is a significant overlap between both modes. The real part resembles in this case the class III mode and the imaginary part the class I mode.

directions. From the analytical considerations made earlier it was found that the high- Q mode must be of class I and the low- Q mode of class III. This is also confirmed by the field images in Figs. 5.14 and 5.15 **a)**. Furthermore, from Fig. 5.13 **IIIb)** it can be deduced that the high-frequency modes of class II which are excited for incidence along the dimer axis have a lower Q -factor and a lower frequency than the dark modes which are not excited. The field images for the high-frequency class II-mode are displayed in Fig. 5.15 **b)**.

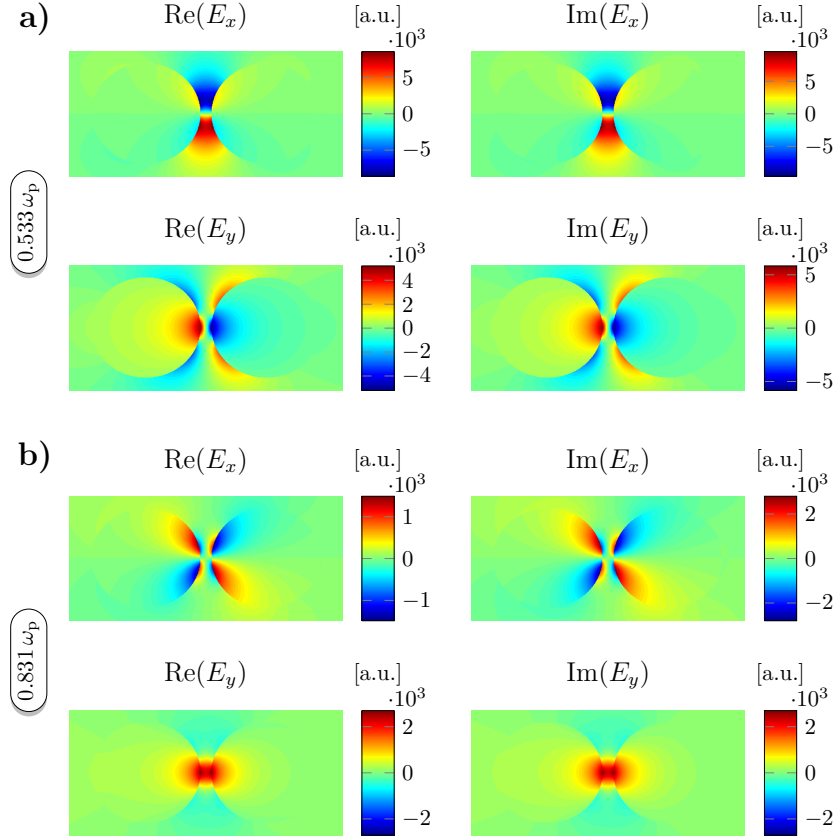


Figure 5.15: Field Images for the $k = 1$ modes, incidence along the dimer axis. **a)** A pure class I mode is found at $0.533\omega_p$ since modes of class III are forbidden. **b)** A pure mode of class II is excited at $0.831\omega_p$. It is only allowed under this angle of incidence.

5.2.2 Nonlocal Case

In the simple case of the cylinder, the frequencies of the modes are increasingly blue-shifted with increasing k , when nonlocality is introduced (Sec. 3.2). In the case of a dimer where the modes with

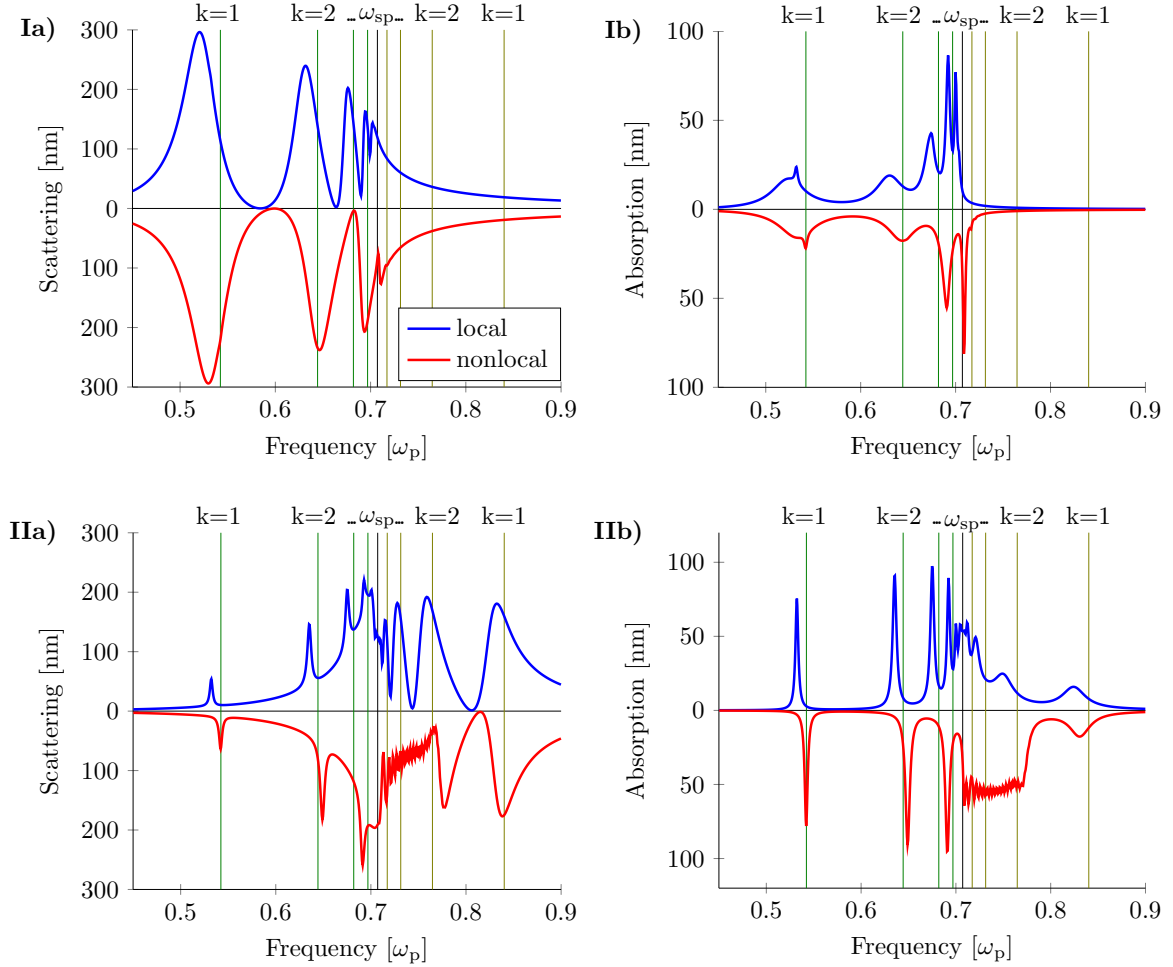


Figure 5.16: **a)** Scattering and **b)** absorption spectra of a cylindrical dimer, for incidence perpendicular to the dimer axis (**I**) and along the dimer axis (**II**). Calculations were done for a local and a nonlocal material model. For better visibility, the nonlocal spectra are plotted upside down. The nonlocal spectra are blueshifted.

lowest k are found at both ends of the spectrum it is likely that the same kind of behavior is observed. In Fig. 5.16 the effect of nonlocality on the scattering and absorption spectra for both angles of incidence is shown. Once again, a blueshift is observed. The following table displays the shifts for the lowest orders $k = 1, 2, 3$, where possible. Since only numerically calculated spectra are available, only the peak positions of the first two or three k can be extracted, due to the overlap of the spectral peaks:

class I	$k = 1$	blueshift: $0.0096\omega_p$
	$k = 2$	blueshift: $0.0143\omega_p$
	$k = 2$	blueshift: $0.0155\omega_p$
class II	$k = 1$	blueshift: $0.0072\omega_p$
	$k = 2$	blueshift: $0.0178\omega_p$
class III	$k = 1$	blueshift: $0.0100\omega_p$
	$k = 2$	blueshift: $0.0148\omega_p$
	$k = 3$	blueshift: $0.0148\omega_p$

Once again the tendency is that the shift increases as k is increased, The information available here is not enough to make a statement on whether this shift grows once again linearly with increasing k . From the table, the shift rather seems to saturate. The shift does however have a significant influence on the spectra in the case where the light pulse impinges in the direction of the dimer axis (Fig. 5.16 II): A number of ripples appear just above the plasmon frequency ω_{sp} and extend approximately to the frequency where the class II, $k = 2$ would be expected. In the local case, I already showed that for this system all modes of higher orders ($k \gtrsim 4$) are found very close to the plasmon frequency ω_{sp} , so clearly the ripples are an effect of blueshifted higher order modes. From the information available here, it is however not clear whether the modes of class II or the modes of class III or a combination of both are responsible for this significant change in the spectrum. Given that in the case of orthogonal incidence (Fig. 5.16 I), where modes of class I and III are available, no such effect is observed, it might be due to the class II modes. In any case, this presents a severe qualitative change in the spectrum when going from a local to a nonlocal description. Possibly the presence or absence of these modes, slightly above the plasmon frequency, and the strong absorption that comes with it could be a promising feature to determine the validity of the nonlocal hydrodynamic model in an experiment.

It is also noteworthy that the field distributions in the nonlocal case for a “pure” mode, such as one of the $k = 1$ -mode, are only very slightly modified when comparing them to the local spectra. Quantitatively, a reduction in field strength is observed, but qualitatively they still resemble the field images from the local case or the analytical electrostatics. This means that in the nonlocal case, the findings from electrostatics can still straightforwardly serve to identify and categorize the modes. The field images were also consulted to identify the shifted modes in the table above.

As a final important remark regarding the effects of nonlocality, I would like to point out that the effects described above cannot be captured by determining a so-called centroid of charge [135]. The idea behind this very simplified model is that spectral shifts could be introduced by determining an effective particle size (depending on the material parameters) and performing local calculations employing this newly calculated size. While it is possible to move around the resonances of for instance a dimer structure by manipulating the size of the particles and their separation, this approach fails to correctly represent any of the effects discussed here: As I have pointed out in Sec. 3.2.2, for a very small single cylinder the local model becomes increasingly independent of particle size (electrostatic limit). This is however precisely the regime where nonlocal effects are strongest, so attempting to achieve this shift by reducing the size of the particle must fail. But not only are the resonances shifted more than could be accounted for by a simple modification of the particle size, they are also shifted into a region which is entirely forbidden for surface plasmons in a single cylinder, namely into the regime between ω_{sp} and ω_p . The third aspect is the relative spectral position of the different resonances which is fundamentally different in a nonlocal model as I have also shown. It was shown by Toscano et al. [45] that for some

5 Numerical Results

setups the (size-dependent) blue-shift of the dipole resonance which is observed when employing hard wall boundary conditions is in fact turned into a (size-dependent) red shift when assuming the more physical situation of electron spill-out. To my knowledge, the influence of the boundary conditions on the higher order modes has not yet been investigated and it would be insightful to investigate which kind of shift is experienced by the quadrupole resonance. It should be clear from the discussions in this chapter that if a “centroid of charge”-approach, i.e. size modification, should be successful to correct the shift of the dipole resonance, the nonlocal model would still have to be employed, rather than the local model, in order to account for the positions of the higher order modes.

Nonlocal Cylindrical Dimer in the Electrostatic Limit

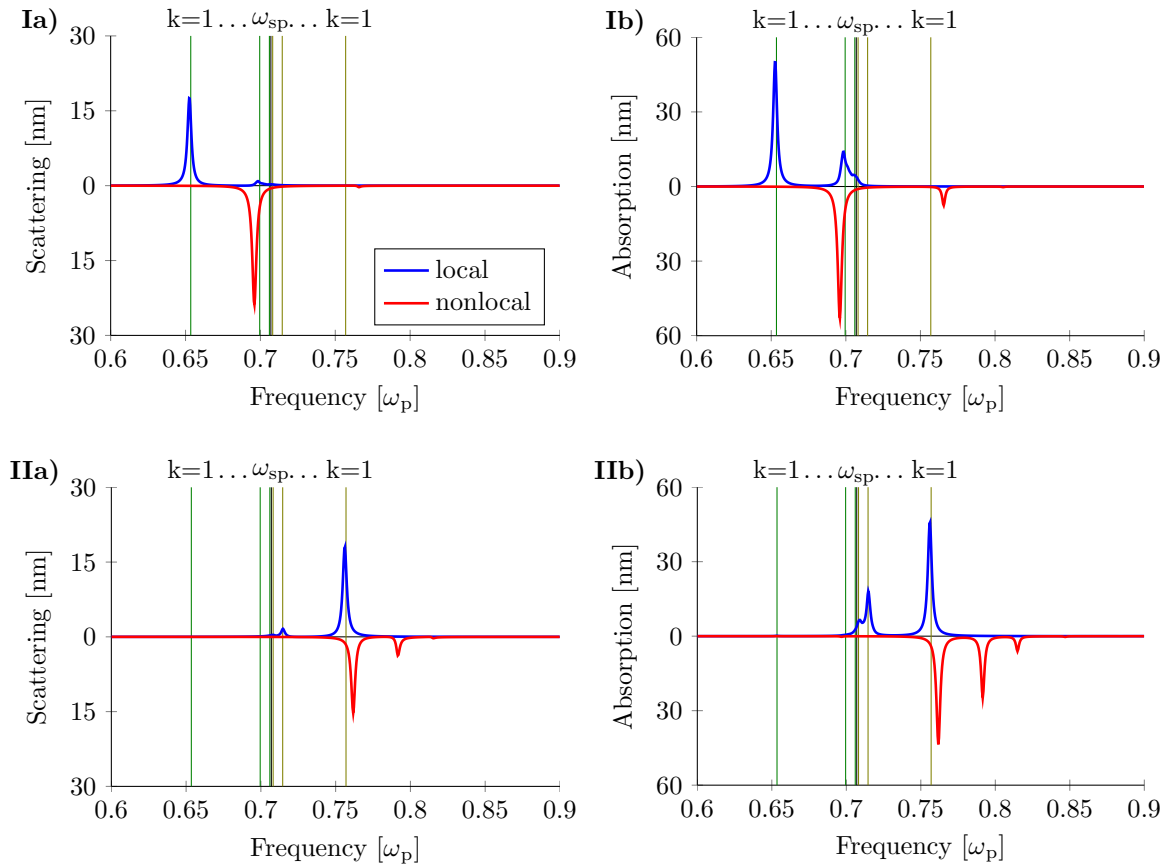


Figure 5.17: Local and nonlocal scattering and absorption spectra. **I)** Incidence perpendicular to the dimer axis. **II)** Incidence along the dimer axis.

In the previous considerations regarding a cylindrical dimer with 10 nm radius, the electrostatic theory provided valuable insight, but the frequencies of the modes which were calculated analytically could only serve to identify the mode number, but were not a good estimate of the actual frequency (Fig. 5.12). I pointed out that 10 nm are too large to be actually considered an electrostatic limit in the sense that

the spectral positions of the modes are not correctly represented by the electrostatic approach presented above. In Fig. 5.17 the spectra for a much smaller dimer of 2 nm radius and 1 nm separation are displayed, both for the local and for the nonlocal material model. I already showed that in the case of the single cylinder particles of 2 nm radius are well described by electrostatics. The analytically calculated frequencies of the modes are now clearly a much better fit (Fig. 5.17). It is also noteworthy that for incidence along the dimer axis (Fig. 5.17 **II**) there are now only strong peaks above the plasmon frequency, meaning that the modes of class I for which retardation is necessary, are heavily suppressed in this limit (cf. Sec. 3.4 for the group-theoretical interpretation of this effect). As discussed, while the electrostatic approach becomes more accurate, the nonlocality grows stronger in such small structures, as the length scale on which the plasma waves are damped away becomes comparable to the particle dimensions. In Figs. 5.17 **I**), a significant blueshift of the peaks to frequencies well beyond the plasmon frequency can be observed. More interestingly, in Figs. 5.17 **II**) for modes of class II, where higher order modes lie at lower frequencies in the local case, it can be seen that for such strong nonlocality as in the present case, the spectra are actually reversed, as the blueshift increases with the mode number. This can be seen even better in the logarithmic representation in Fig. 5.18 **b**). One can also see a strongly suppressed mode of class I below the plasmon frequency and very pronounced bulk plasmons above the plasma frequency. As above for the large dimer, I will extract the shift, depending on the mode number, for the three available classes of modes:

class I	$k = 1$	blueshift: $0.0432\omega_p$
class II	$k = 1$	blueshift: $0.0055\omega_p$
	$k = 2$	blueshift: $0.0769\omega_p$
	$k = 3$	blueshift: $0.1062\omega_p$
	$k = 4$	blueshift: $0.1400\omega_p$
	$k = 5$	blueshift: $0.1770\omega_p$
class III	$k = 1$	blueshift: $0.0435\omega_p$
	$k = 2$	blueshift: $0.0671\omega_p$
	$k = 3$	blueshift: $0.1003\omega_p$
	$k = 4$	blueshift: $0.1368\omega_p$
	$k = 5$	blueshift: $0.1758\omega_p$

As before, in the case of the cylinder in Chap. 3, the shift $\delta\omega(k)$ can be fitted by a quadratic function. For class III this yields

$$\delta\omega = 0.0024k^2 + 0.019k + 0.021 \quad (5.2)$$

and for class II

$$\delta\omega = 0.0019k^2 + 0.024k + 0.051. \quad (5.3)$$

For the second fit, shift of $k = 1$ has been neglected since it represents an inexplicable outlier. The fits for both classes of modes are comparable, and the linear contribution exceeds the quadratic contribution by an order of magnitude in both cases.

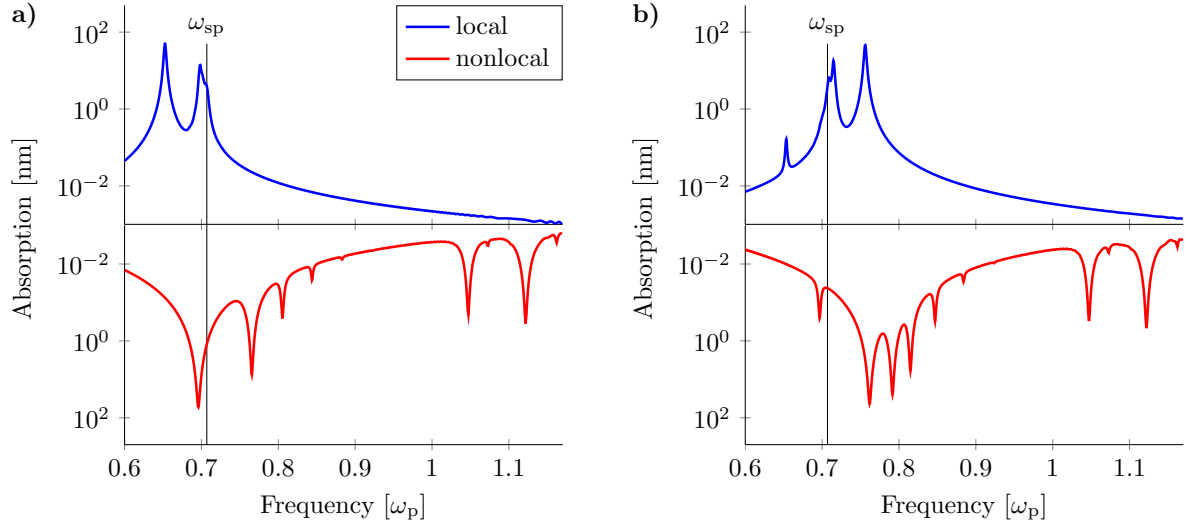


Figure 5.18: Local and nonlocal absorption spectra (logarithmic plot). **a)** Incidence perpendicular to the dimer axis. **b)** Incidence along the dimer axis.

5.2.3 Nonlinear Scattering

In Fig. 5.19 the nonlinear scattering spectra for the large dimer of radius 10 nm are presented, for both angles of incidence.

The group theoretical considerations from Sec. 3.4 suggest that for each angle of incidence, two classes of modes are excited by SHG: Precisely the ones that are not excited linearly. Thus if the modes of class I and III were excited linearly, the SHG signal must pertain to modes II and IV, etc. And, in fact, for both angles, a strong signal is found near the high-frequency $k = 1$ line. It is at a slightly higher frequency than the $k = 1$ peak from the class II mode which was excited in the linear case. From the quasinormal mode calculations in Fig. 5.13 it can be seen that the high-frequency $k = 1$ -modes of class II and IV are no longer degenerate when going beyond electrostatics and it could be seen that the dark class IV mode does indeed possess a higher energy than the class II mode. This already suggests that the mode which is excited via SHG is the previously dark class IV mode. Note that in Sec. 5.1.3 I demonstrated that intensity-dependent shifts due to nonlocal effects of higher order can be neglected. Therefore it is justified to compare the peaks in the nonlinear spectrum to the frequencies of the modes calculated employing a linear theory. The field images in Fig. 5.20 confirm this. Thus the group theoretical approach once again predicts the behavior correctly.

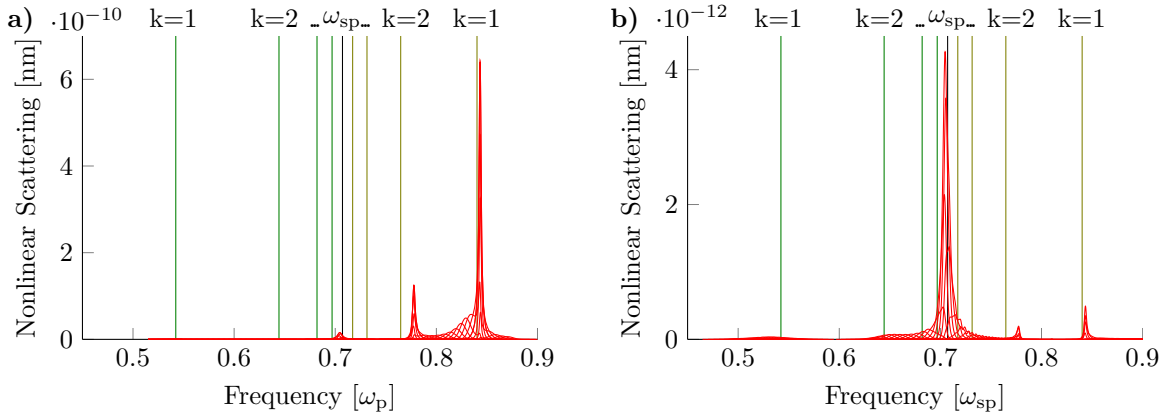


Figure 5.19: Nonlinear scattering for **a)** perpendicular incidence and **b)** incidence along the dimer axis. Several calculations with sharp pulses were performed to scan a broad frequency range. The positions of the resonances from electrostatic theory are displayed by vertical lines.

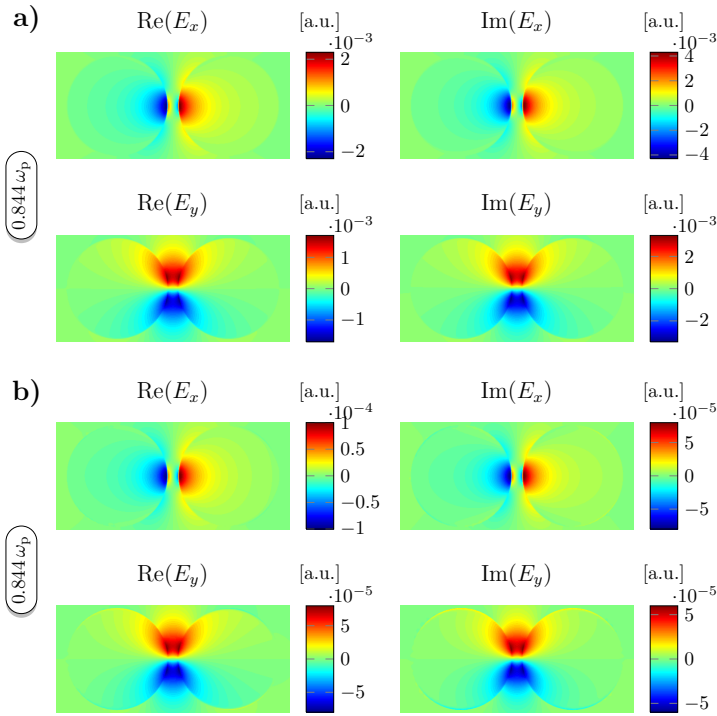


Figure 5.20: Field distributions at the highest frequency second harmonic signal. **a)** Perpendicular incidence **b)** Incidence along the dimer axis. Both times the dark mode of class IV is excited.

It is striking that while for perpendicular incidence the highest peak is found at the high frequency $k = 1$ -line while for incidence along the axis, the strongest peak is found in the middle. A closer look reveals why this is the case: For perpendicular incidence (5.19 a)), there is also a noticeable SHG-signal just to the left of the very strong peak. It corresponds to the frequency of the class II $k = 1$ mode which is dark for this angle of incidence. At the same time there are no modes at all below the plasmon frequency in the SHG spectrum. For the other angle of incidence (5.19 b)), the $k = 1$ mode of class IV is very isolated. The modes of class II are not available for SHG in this case because they are not dark. However, modes are found below the plasmon frequency. They are rather weak, but a zoom in on the low-frequency $k = 1$ line reveals that a signal is in fact present (cf. Fig. 5.21). The field image confirms that this mode is of class III which is

5 Numerical Results

dark for this angle of incidence. The very high peak near ω_{sp} in 5.19 **b)** can be explained by the availability of many dark modes (from class III below and class IV above the plasmon frequency) in the vicinity of ω_{sp} .

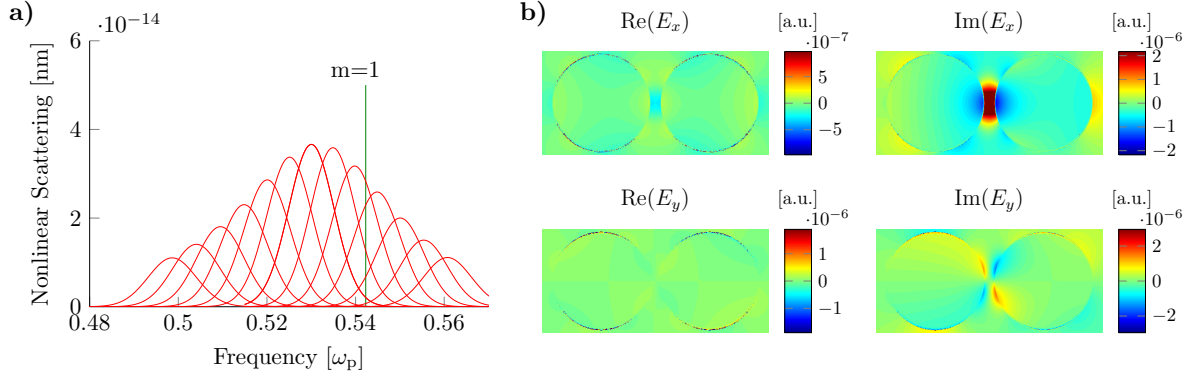


Figure 5.21: **a)** Zoom on the low-frequency peak of the SHG spectrum of the dimer and illumination along the dimer axis. **b)** Field distribution at the highest peak of the spectrum. The scale has been reduced by a factor two for better visibility. The mode is class III, $k = 1$. A comparably strong field is found at the boundary of the particle.

The field images of the class III mode in Fig. 5.21 **b)** still have to be discussed. Compared to the field images for the high frequency modes the signal is now much weaker. One notices strong fields at the very edge of the particle. The fields there are actually off the scale of the colorbar which has been reduced by a factor two. Therefore, these fields at the edges exceed those fields constituting the mode by a factor of 2 or more. The mode is only well visible in the imaginary part. The strong fields near the edge are visible in all four pictures. Nevertheless, the mode-profile that is then produced is that of a regular mode which lives inside and outside the geometry. As in all other cases, the field profile looks just like a linearly produced mode. Whether the fields near the surface are a physical effect that hint at a larger SHG contribution coming from electron density fluctuations near the surface, or whether this is a numerical artefact which is visible in this case due to the smallness of the SHG signal cannot be clarified with the information at hand.

5.2.4 Electron Density Fluctuations for the Dimer Modes

By now I have identified all possible modes in the dimer system and shown a way to excite them. In the process, I displayed the corresponding field images which were sufficient for the discussions. I now present the electron density fluctuations which correspond to the modes. Not only for completeness' sake, but also because they allow for some physical arguments which explain where the hybridization comes from and how the degeneracy of the sine- and cosine-modes is lifted when going beyond the electrostatic limit.

In Fig. 5.22 the density fluctuations are displayed for the four $k = 1$ modes. With this, it is possible to draw a revised version of the schematic from the introductory chapter, Fig. 1.4. In order to do so, each of the two cylinders making up the dimer is seen as a single dipole, rather than considering the whole system as a dipole. This leads to the schematic presented in Fig. 5.23. Now, in addition to the modes

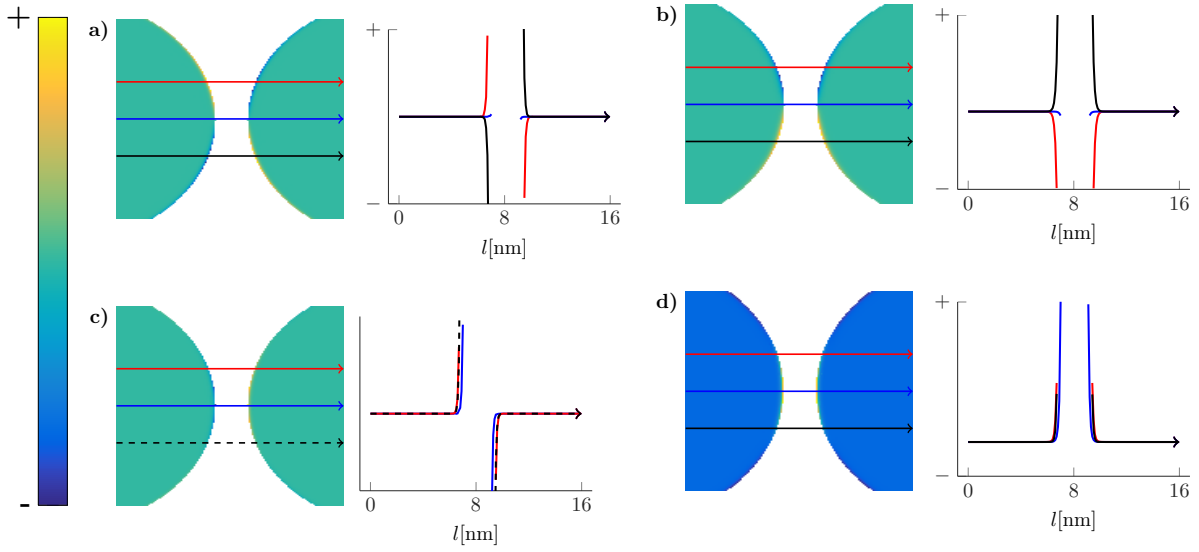


Figure 5.22: Fourier transform of the electron density fluctuations for the four $k = 1$ modes, calculated with the DGTD method. The fluctuations are plotted along the lines across the gap in the left of each subfigure, in the corresponding color. **a)** Class I **b)** Class II **c)** Class III **d)** Class IV. They exhibit the same symmetries as the electrostatic potentials from Fig. 3.15.

II and III, for which the whole system could essentially be viewed as one dipole (and illustrated by a single arrow), there are two additional configurations which are beyond what I earlier called the “fully electrostatic case”, i.e. what could be excited by an electric field in a capacitor. It can be seen that the low energy modes I and III are attracting dipoles and therefore energetically favorable. The configurations II and IV are repulsing dipoles, and therefore found at high energies. This picture intuitively describes the hybridization and completes the irreducible representation of the point-group of the dimer which

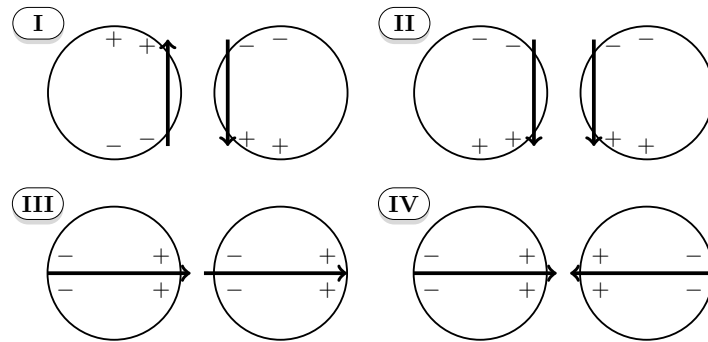


Figure 5.23: Schematic of the charge movement in a dimer, corresponding to the four classes of modes. **a)** Class I **b)** Class II **c)** Class III **d)** Class IV. This figure is an extension of Fig. 1.4 and, in addition to the fully electrostatic modes II and III includes the remaining two configurations which complete the point group of the dimer.

was incomplete in Fig. 1.4. The symmetries of the density fluctuations are again those of the potentials from Fig. 3.15 (cf. Sec. 3.4).

From the spectra and the quasinormal mode calculations (Fig. 5.13) it can also be seen that the newly added configurations I and IV lie at slightly higher energies than their counterparts with similar energies and possess a higher Q-factor. The reason for this lies in the fact that they are not simple dipoles and therefore do not radiate as strongly, i.e., the energy does not dissipate as quickly. Furthermore, also as a consequence of going beyond the fully static limit, the actual length of the dipole becomes important (in the electrostatic limit all length scales vanish), which is the reason why mode III, which is a very long dipole and thus radiates strongly, must have a lower Q-factor than mode II (cf. Fig. 5.13).

5.2.5 Field Enhancement in a Dimer for a Local and a Nonlocal Material

In the previous sections of this Chapter, in the context of the integrated quantities, i.e. scattering and absorption, I have already taken a look at the field distributions for a given frequency, in order to characterize the modes by comparing them to the analytically calculated field distribution. As discussed in the Introduction (Sec. 1.3), physicists are often interested in the field distribution, since hotspots featuring extremely high field values serve to enhance the Raman signal of a probe that is placed near such a hotspot. Then, the physical quantity which is of importance here is the absolute value of the electric field (the field intensity), normalized to the incoming field, or, as described in detail in Sec. 1.3, the SERS-Factor

$$M_{\text{SERS}} = \left(\frac{|E_s|}{|E_0|} \right)^4. \quad (5.4)$$

This section is dedicated to an investigation of the field enhancement from obtained for a dimer structure. To study field enhancement, the field distributions are analyzed and the influence of nonlocality is investigated. It was often pointed out that a nonlocal description will lead to a reduced field enhancement in gap structures [46, 136, 137]. For a local description, singular behavior occurs in the limit of particles touching at a single point [138]. This unphysical behavior is remedied in the nonlocal description, which allows for varying charges within the particle, resulting in a “smearing” of the charge distribution [136].

In Sec. 3.2.3 I have demonstrated that the spectra also show a noticeable reduction when going from a local to a nonlocal description, so a reduction of field enhancement is not surprising at this point. However, the preceding studies showed that cylindrical dimers feature a multitude of different modes, all of them with different field distributions. Clearly, the field enhancement must be reduced at the hotspot (where the particles are touching) due to the smearing effect, but in view of the complicated field distributions in a dimer system and the significant alteration of the spectra when going to a nonlocal description, a more thorough investigation is needed, both space- and frequency-resolved.

I will start out with a frequency-resolved analysis of the field enhancement at two important space points in the gap, namely at the center point between the two cylinders and at a point on the surface of one of the cylinders, lying on the dimer axis. For many modes the strongest field enhancement is found in the gap, so I will start out by investigating this region. I distinguish between the two points in order to show that the exact position can make a big difference. Also, in SERS molecules are adsorbed at the surface of the particles, rather than floating in the space between them. Fig. 5.24 shows the SERS

factors at these two points, for the two different angles of incidence investigated before, for a local and a nonlocal material model. In the following investigations, I mark the value of 10^6 as the critical value above which single molecule detection is possible. The first and most obvious thing to see from

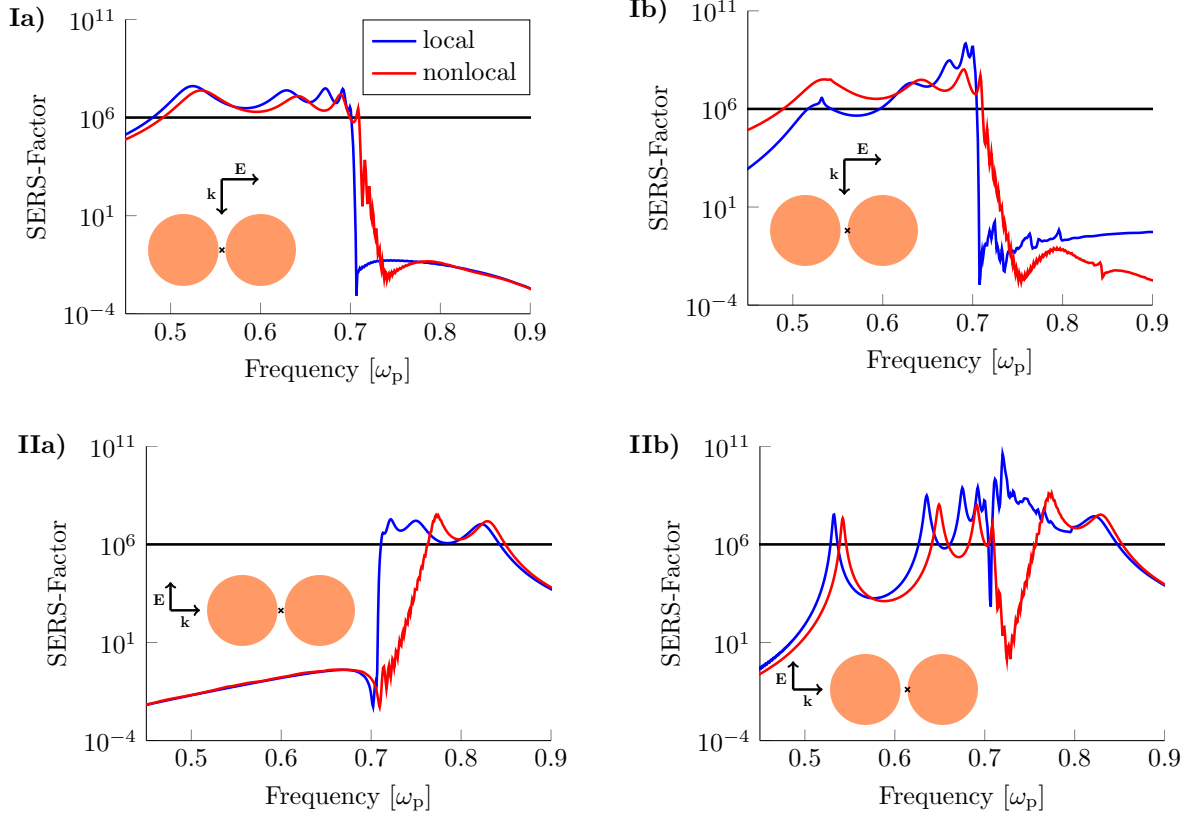


Figure 5.24: This figure displays the field enhancement over frequency measured at two different points in space, for two different angles of incidence, for both the local and the nonlocal material model. **I)** Incidence perpendicular to the dimer axis. **II)** Incidence along the dimer axis. **a)** Center point. **b)** Point on the surface of a cylinder, on the dimer axis. The horizontal black line marks the value 10^6 .

Fig. 5.24 is that field enhancement occurs in those frequency-regions where modes are excited: For perpendicular incidence (Fig. 5.24 **Ia**)), predominantly modes of class III which lie below the plasmon frequency are excited. This is also the frequency range of strongest field enhancement. For a local model the enhancement drops sharply as the plasmon frequency is reached. For a nonlocal material, the peaks are blueshifted and slightly reduced in magnitude. The drop at ω_{sp} is significantly less abrupt, due to the presence of a multitude of blue-shifted higher order modes just above ω_{sp} . A similar behavior is observed in Fig. 5.24 **Ib**): strong field enhancement is found at the positions of the local or nonlocal modes respectively. However, the common assumption that the field enhancement is always reduced in a nonlocal model does not hold at this spacepoint. The local spectrum shows weak field enhancement at low frequencies and for every higher mode the enhancement becomes stronger until it drops sharply

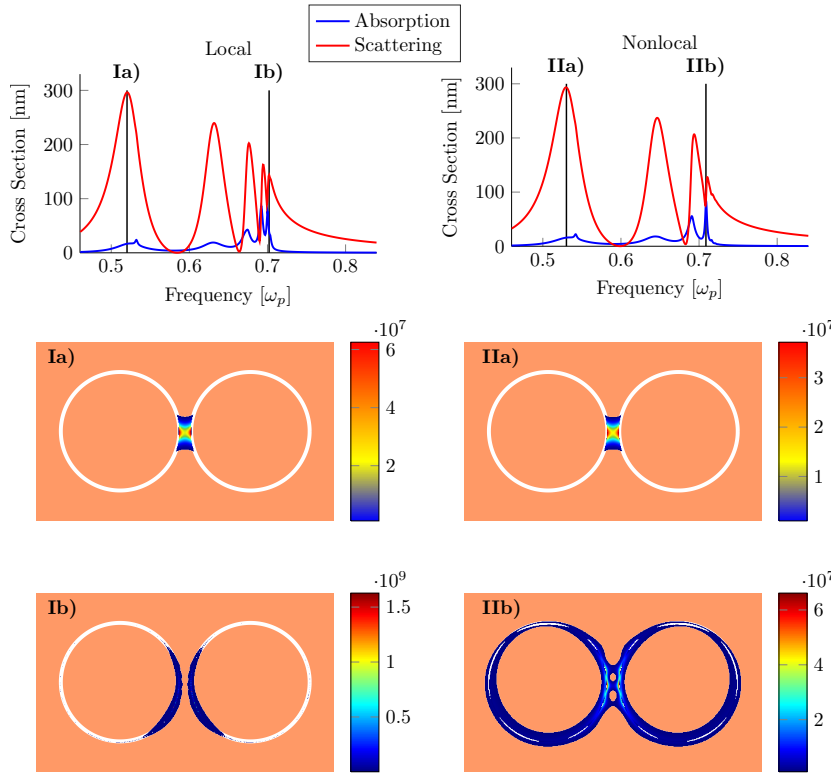


Figure 5.25: SERS-active area of a dimer, perpendicular incidence, at the frequencies indicated by the vertical lines in the spectra. Only those regions where the SERS-factor exceeds 10^6 are color-coded.

of the modes in the nonlocal case: In the local case many modes coincide at ω_{sp} , all of these modes together generate fields that are still strong enough to effect SERS-activity. Above that frequency, there are modes of low order which have field distributions that are strong at the center point and also effect SERS-activity. In the nonlocal case, the modes are blueshifted and above the plasmon frequency there are numerous high order modes (which have field distributions that are not particularly strong in the center, as I will show below, in Figs. 5.25 and 5.26). They are all at different frequencies and therefore do not add up to reach the SERS-active regime. Only as the very low order modes (which have strong fields in the center) just below $0.8\omega_p$ are reached, the configuration becomes SERS-active. In Fig. 5.24 IIb), close to the surface, the behavior is similar to the behavior in Fig. 5.24 IIa), however, some SERS-activity is found below the plasmon frequency where modes of class I are excited. This means that the field distributions associated with these modes are such that they provide large fields at the boundary but virtually no field at all at the center point, as we know from Fig. 5.24 IIa) (see also Figs. 5.25 and 5.26). The field enhancement of the class I modes is blueshifted and reduced in the nonlocal case. A drop in field enhancement is found in the local case at ω_{sp} , where all the high order modes lie. In the nonlocal case, this drop covers a much broader frequency range due to the shifting of those modes.

at ω_{sp} . For the nonlocal model, this is not the case. Rather, the field enhancement is approximately the same for all the modes lying below the plasmon frequency, i.e. for the high modes near ω_{sp} the field enhancement is still reduced compared to the local model, but for the lowest mode the field enhancement is actually increased. In Fig. 5.24 IIa), for incidence along the dimer axis where modes of class II are excited which lie above the plasmon frequency, strong field enhancement is found at the plasmon frequency and above in the local case. In the nonlocal case, however, the field enhancement increases slowly starting at ω_{sp} and only gradually reaches the value of 10^6 . This can be explained by the shifting

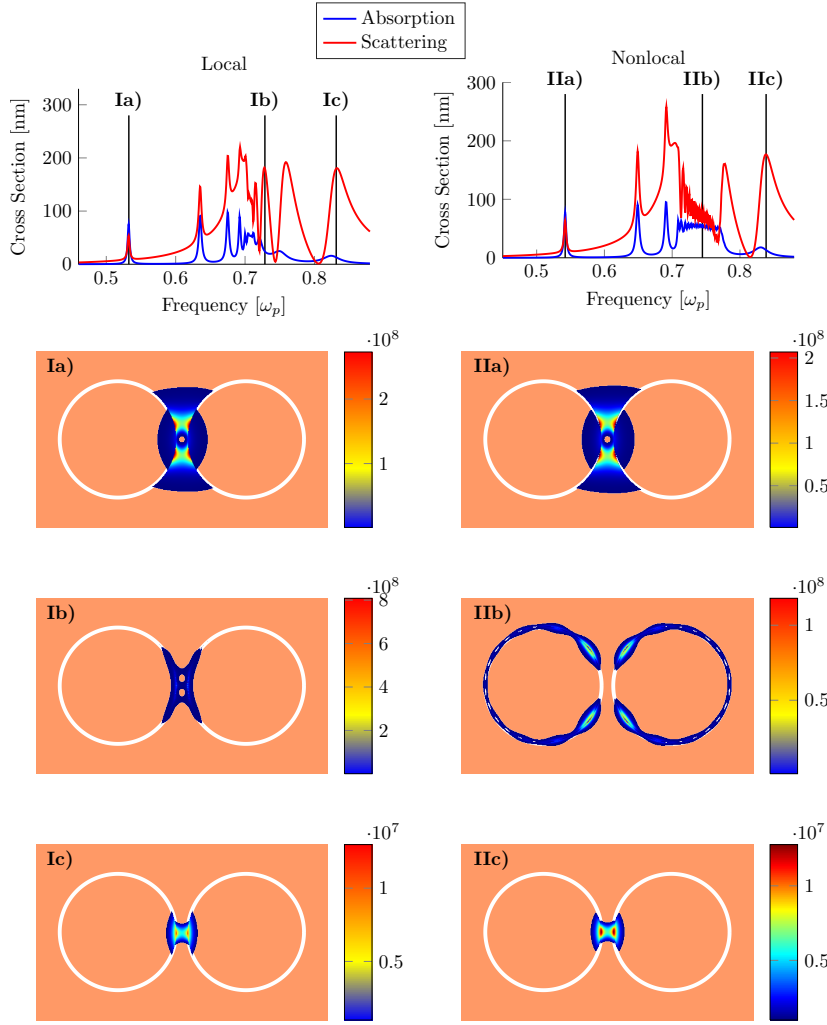


Figure 5.26: SERS-active area of a dimer, incidence along the dimer axis, at the frequencies indicated by the vertical lines in the spectra. Only those regions where the SERS-factor exceeds 10^6 are color-coded.

in the spectra which are displayed in the top part of the figure. The first field distribution is for the strong dipole peak. Sers-activity is only found in the gap between the two cylinders. The strongest fields are very close to the cylinder surfaces. The maximum field enhancement drops by about a factor of two when going from a local to a nonlocal model, but the SERS-active area remains unaltered and the field distributions do not change. The second set of images, Fig. 5.25 **Ib)** and **IIb)** were recorded at the peaks lying the farthest to the blue in the spectrum. Here, in the proximity of ω_{sp} the shifts due to non-locality are the strongest. Correspondingly the influence of nonlocality is much more pronounced than at the dipole frequency: the maximum field enhancement drops by almost two orders of magnitude, but the structure remains SERS-active. In fact, the area where the SERS factor exceeds 10^6 is significantly larger in the nonlocal case. While SERS-activity is only found where they cylinders are facing each

From the preceding discussion it has become clear, that an investigation of the field distributions is necessary. Clearly, this cannot be done for all frequencies, but I have chosen a few select frequencies which will provide sufficient insight. To analyze the spatial dependence, I plot the SERS factor at a given frequency. To visualize the changes in SERS activity when going from a local to a nonlocal material model, only those areas where the SERS factor exceeds the value of 10^6 are color-coded.

The regions where the SERS factor is below that value are kept in orange, thus only the area that is actually SERS-active is displayed. The position of the two cylinders is indicated by two white rings. First, I take a look at the case of incidence orthogonal to the dimer axis. In Fig. 5.25 the field distributions are displayed at two different frequencies – the frequencies are marked by vertical lines

other and only very close to the surfaces of the two cylinders in the local case, the SERS-active area reaches in a ring-shape all the way around the two cylinders and protrudes further into the gap, giving rise to SERS-activity in the center point in the nonlocal case. Assuming that the enhancement of 10^6 is enough for the purposes of a given experiment, the nonlocality is actually beneficial: The exact position of the molecule does not matter as much as in the local case. It can even be placed on the surface of one of the cylinders, away from the gap and still be detected. Thus, the statement that field enhancement drops in the presence of nonlocality remains true, but it is only half of the story. When going to the other angle of incidence, in Fig. 5.26 for the lowest frequency dipole peak there is also almost no change in field enhancement between the local and the nonlocal model (Fig. 5.26 **Ia**) and **IIa**). This suggests that not the absence of singularities in a nonlocal model, but rather the relative shift of modes is primarily responsible for the reduced field enhancement. Due to the peculiar shape of the mode, there is virtually no field in the center point – a feature which is shared by all modes of class III, which explains the sudden drop at the plasmon frequency in Fig. 5.24 **IIa**). This is an important example for why it is important to analyze the mode profile, rather than assuming that field enhancement must be strong in the gap region. An analysis of the center point or even of the fields along a line connecting the two cylinders is by no means enough to gain a thorough understanding of the field enhancement in dimer structures. The same is true when moving to the middle of the spectrum, near ω_{sp} (Fig. 5.26 **Ib**) and **IIb**): In the nonlocal model the fields for this mode (as for the other modes in the vicinity which are not shown) is concentrated in the gap. For the nonlocal model, this is the area where the strong shifts of the modes occur, resulting in numerous ripples in the spectrum. It turns out that the field enhancement for this frequency is less than one order of frequency below that of the local model at a similar frequency, but the field distribution is such that SERS activity is actually only found on the outward facing parts of the cylinder, sparing the gap altogether. The third set of images (Fig. 5.26 **Ic**) and **IIc**) pertains to the highest frequency peak, which is again a first order mode (of class II). The field shows a weak dependence on nonlocality (a slight enlargement of the region of highest field enhancement and almost no drop in magnitude), the distribution is comparable to that of the first order mode under the other angle of incidence but it penetrates further into the particle.

In conclusion, the common notion that nonlocality will lead to reduced maximum field enhancement for a given mode is certainly true, but the impact of nonlocality on the field distributions is very involved and of course highly dependent on the structure in question so that a thorough space- and frequency-resolved investigation is necessary for every new structure. The dimer is a perfect example for the complicated nature of these effects and provided a lot of inside since its modes can be well understood.

5.3 Double Resonant SHG from a V-Groove

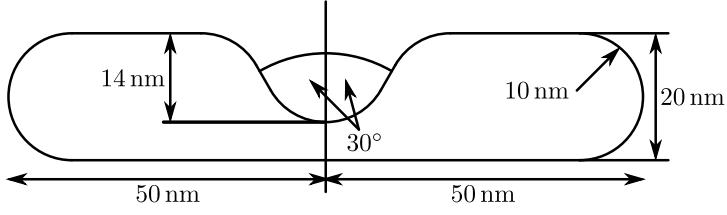


Figure 5.27: Sketch of the V-groove geometry, designed by Andreas Hille.

Another structure which I investigated during my time as a doctoral student was a so-called V-groove. It was designed by Andreas Hille and some aspects of SHG from this structure have already been discussed in a publication [M2]. This discussion however still lacked the thorough mode analysis which I am about to present. The V-groove is a two-dimensional structure, 100 nm by 20 nm, with a V-shaped cut-

out on one side (Fig. 5.27). The idea behind the design is to have a low frequency resonance pertaining to the full length of the system (100 nm) and higher frequency resonances pertaining to the two shorter pieces to the left and to the right of the groove. If the dimensions are chosen appropriately, one can find a resonance at ω_0 so that there is also a resonance at $2\omega_0$. In this sense, the structure is geometrically tuned to be double-resonant. Part of the mesh which was employed for the numerical simulations is shown in Fig. 5.28.

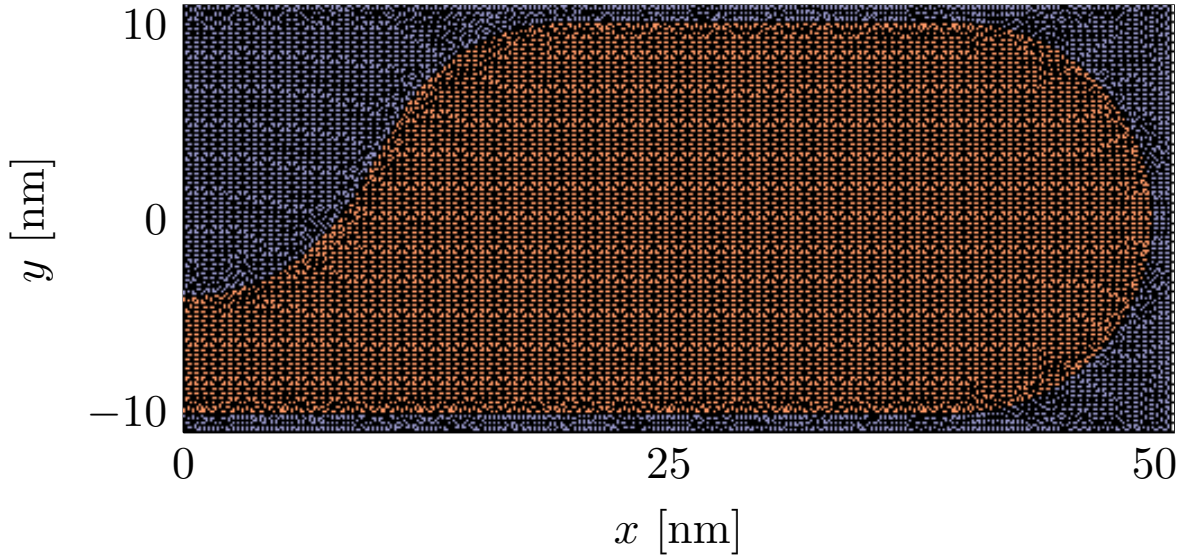


Figure 5.28: Part of the mesh used for the V-groove calculations. For better visibility, only one half of the total field region is displayed. The maximal edge length within the scatterer is 0.65 nm. The scattered field region (not shown) extends to ± 350 nm in x direction and ± 250 nm in y direction, beyond that, there are 50 nm of PMLs in every direction (not shown).

As mentioned in Sec. 3.4, the V-groove has certain similarities to a dimer but features lower symmetry because it cannot be mirrored upside down. Formally, the V-groove corresponds to the symmetry point-group C_2 (Sec 3.4). Due to the lower symmetry, there are only two different classes of modes. I recall

5 Numerical Results

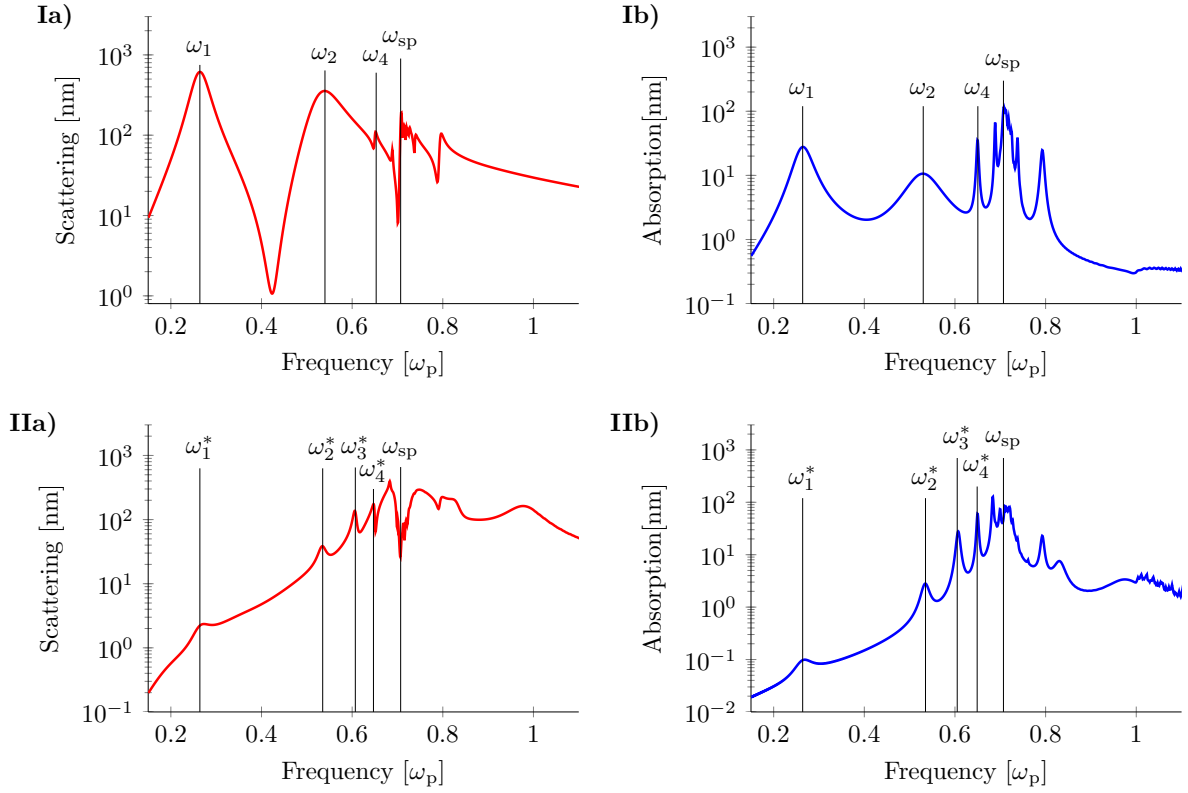


Figure 5.29: Logarithmic plot of the linear spectra of the V-groove. **I)** incidence along the short axis (from the top in Fig. 5.27), **II)** incidence along the long axis (from the left in Fig. 5.27). The resonances indicated by vertical lines will be of importance in the discussion of SHG.

the findings from Sec. 3.4 for the excitation of modes in a V-groove structure: For incidence from the top (Fig. 5.27), i.e. with the \mathbf{E} -field polarized in x -direction and the k -vector pointing downward, only one class of modes (class I) is excited. If the incidence is rotated by 90 degrees, both classes, class I and II, are excited. For the second harmonic signals the situation is as follows: For incidence from above (along the short axis) the nonlinearly excited modes are of class II, i.e. precisely those modes that were not excited linearly. For angle from the left, along the long axis, where there are modes of class I and II on a linear level, the SHG signal also features modes of both classes I and II.

The linear spectra are displayed in Fig. 5.29. Close inspection of the spectra reveals that for at every frequency at which there is a resonance in Fig. 5.29 **I)**, there is also a resonance in Fig. 5.29 **II)**, but the inverse does not hold. This backs the group theory which suggested that both classes of modes are excited for incidence along the long axis, while only one class is excited for incidence along the short axis. All peaks in the spectra in Fig. 5.29 **I)** must pertain to class I. Three of the those peaks in question are labeled by ω_1 , ω_2 and ω_4 .

On the other hand, the peaks in Fig. 5.29 **II)** could in principle be either from class I or from class II. The peaks labeled by ω_1^* , ω_2^* and ω_4^* are found at the same frequencies as ω_1 , ω_2 and ω_4 . Therefore, they are either the same modes of class I which were excited by the other angle of incidence, or they

are modes from class II which are found at the same frequency. Only for the peak labeled by ω_3^* it is obvious that it must belong to a class II mode, since there is no peak to be found at the same frequency for the other angle of incidence. Below, an analysis of the SHG spectra makes it possible to determine whether the starred peaks pertain to class I or class II.

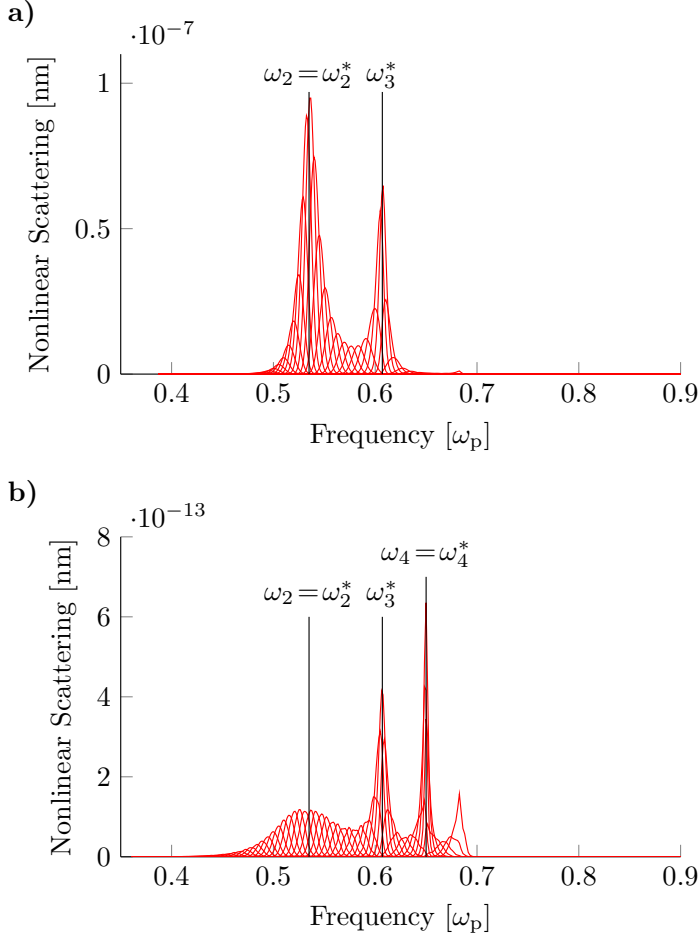


Figure 5.30: SHG from a double resonant V-groove. **a)** Incidence along the short axis. Strong double resonant behavior is found as the linear signal coincides with ω_1 . **b)** Incidence along the long axis. Double-resonant enhancement is not found as the ω_1^* resonance on the linear level for this angle of incidence is weak. Note that the linear signal is only rastered across the ω_1 peak, from $0.25\omega_p$ to $0.35\omega_p$ to capture double resonant behavior. This is not a full frequency scan.

$\omega_2 = \omega_2^*$ and ω_3^* . Above, I already pointed out that ω_3^* is with certainty a mode of class II, which is dark for this angle of incidence. Therefore a SHG signal is expected. The fact that there is also a resonance at

The frequencies $\omega_2 = \omega_2^*$, $\omega_3 = \omega_3^*$ and $\omega_4 = \omega_4^*$ are at approximately twice the frequency of ω_1 . Thus, sending in a light pulse near ω_1 , generating a second harmonic signal at those peaks, will be a double-resonant excitation.

For incidence from the top the linear signal at ω_1 is very strong, which yields a strong double-resonance, while for the other angle of incidence the signal (ω_1^*) is extremely small and therefore the effect of double-resonance is weak, if not negligible. This is shown in Fig. 5.30. For incidence from the top there is strong SHG enhancement, yielding a signal which is approximately five orders of magnitude larger than the signal for the other angle of incidence. For the single cylinder, a resonance at the incoming frequency has been shown to give rise to strong SHG fields (Fig. 5.6) – over an order of magnitude stronger than if the resonance is at the SHG frequency. Here, a combination of both leads to significant enhancement. The SHG efficiency for this type of excitation is actually comparable to the estimate for dielectrics which was given in Eq. (2.52). If the incoming field was increased to 10^{11} V/m the SHG signal and the linear signal would be of the same order of magnitude. Having taken note of the strength of the SHG signal, the mode analysis of the SHG signals still has to be done. Two very pronounced peaks are found in 5.30 a) at the frequencies

5 Numerical Results

$\omega_2 = \omega_2^*$ means that the ω_2^* peak comes from a class II mode which is degenerate in frequency with the class I mode ω_2 . The fact that there is no SHG signal at ω_4^* on the other hand means that ω_4^* is the same class I mode as ω_4 . The SHG signal for the other direction of incidence, Fig. 5.30 b) exhibits peaks at all three frequencies $\omega_2 = \omega_2^*$, $\omega_3 = \omega_3^*$ and $\omega_4 = \omega_4^*$. This confirms once again the group-theoretical prediction that modes from both symmetry classes are excited linearly and nonlinearly for this angle of incidence, i.e. the mode ω_3^* which is clearly of class II is excited linearly and nonlinearly and so is the mode ω_4 which was identified as a class I mode. Obviously the mode $\omega_2 = \omega_2^*$ also delivers a signal since it is a mixed signal of a class I and a class II signal at the same frequency.

5.4 Sum-Frequency Generation from a Bow-Tie Antenna

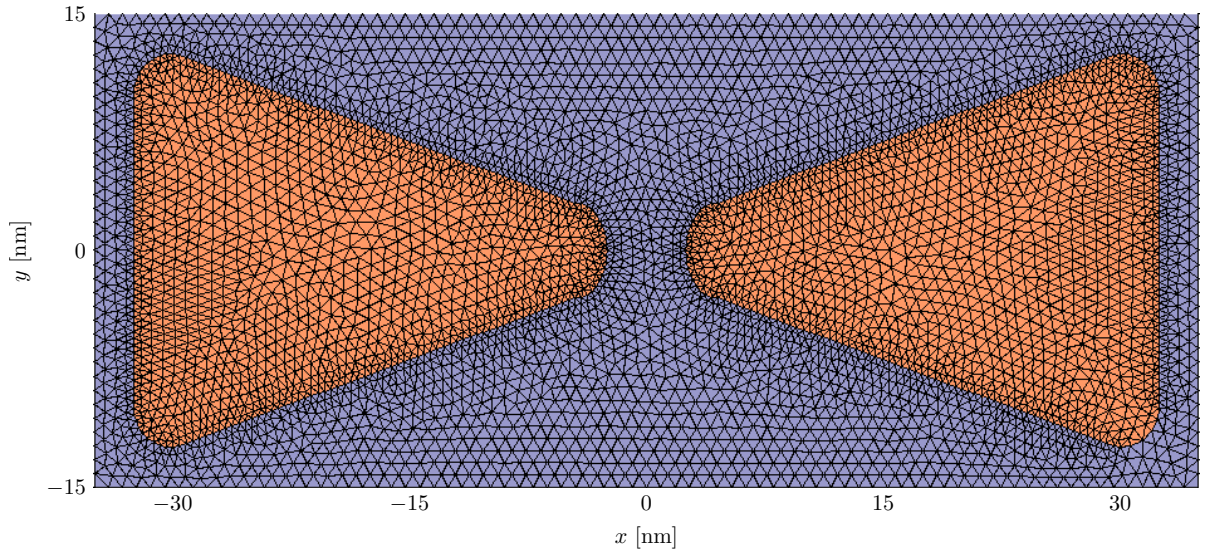


Figure 5.31: The total field region containing the bowtie scatterer of the mesh which was employed for the bowtie calculations. The maximal edge length within the scatterer is 1.3 nm. The scattered field region (not shown) extends to ± 250 nm in every direction and beyond that, there are 100 nm of PMLs in every direction (not shown).

In the preceding section, I showed that by double resonant tuning much larger SHG cross sections can be achieved. It might however be the case that a strong higher harmonic signal is desired, yet it is not possible to perform geometric tuning. This could be because one is limited to a certain structure, or because it is technically not feasible to modify the structure correspondingly. One can then make use of three-wave mixing in a broader sense: Instead of having an incoming signal at ω' and an second harmonic signal at $2\omega'$, one uses two incoming pulses at ω', ω'' , which results in three second order signals:

$$\omega', \omega'' \longrightarrow 2\omega', 2\omega'', \omega' + \omega''. \quad (5.5)$$

This type of three-wave mixing was investigated in a joint publication with Dan-Nha Huynh [M3]. To conduct this study, we employed a bow-tie structure which I designed on the basis of the dimer. It

consists of two triangles with rounded corners. The gap is 5 nm, the base of the triangles (y -direction) is 25 nm and the height is 30 nm. The total field region of the mesh employed for the calculations is displayed in Fig. 5.31. The material model is the same as before, but the bow-tie is embedded in a background material with a constant ϵ_{bg} of 2.25. This background medium shifts the plasmon frequency to the red, away from interband transitions, via

$$\epsilon(\omega) = -\epsilon_{bg}, \quad (5.6)$$

$$\rightarrow \omega = 0.555\omega_p. \quad (5.7)$$

The slightly larger gap than in the case of the dimer makes this structure more experimentally realistic and the shift due to the background medium bring the resonances into a regime where the use of a simple Drude model without interband transitions is a better fit.

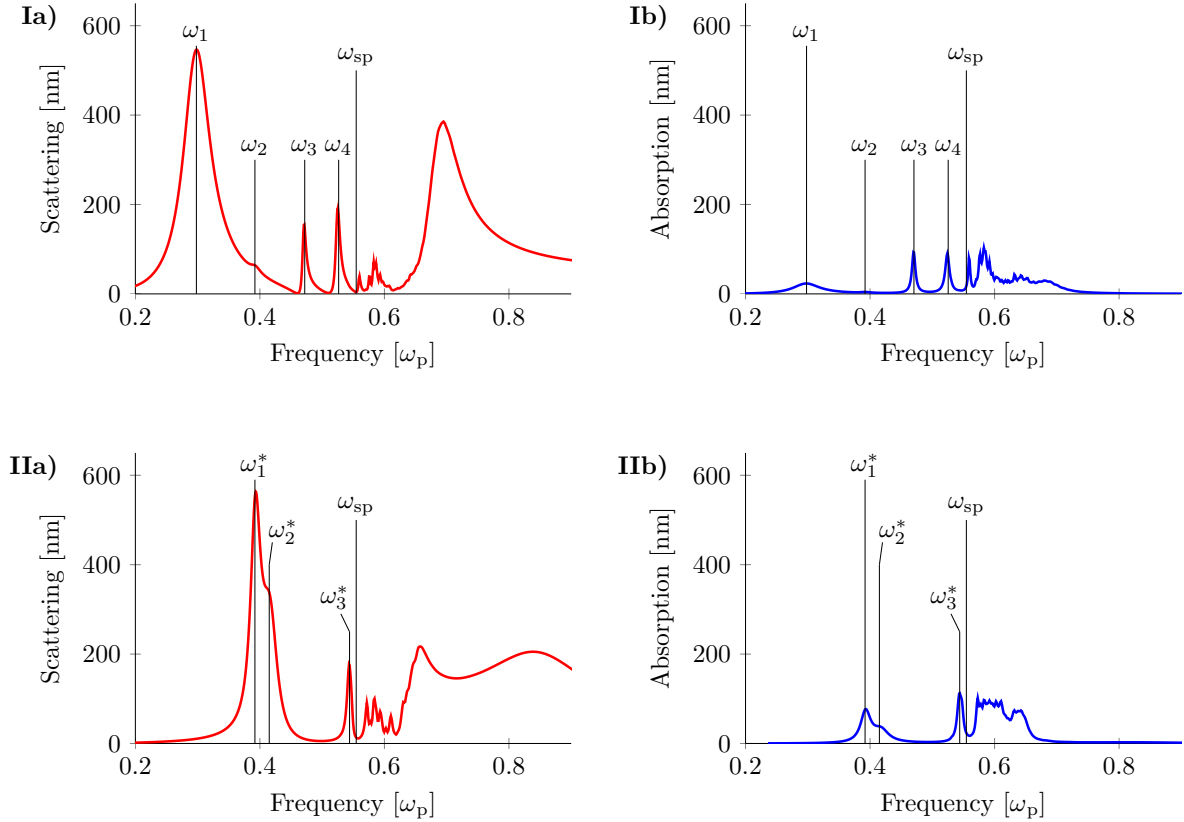


Figure 5.32: Scattering and absorption spectra for the bowtie displayed in Fig. 5.31, employing a nonlocal material model. **I)** Incidence from the top. **II)** Incidence from the side. For incidence from the top, a strong scattering peak, labeled ω_1 is found. One of the incident pulses for the wave-mixing calculations will be kept on this resonance.

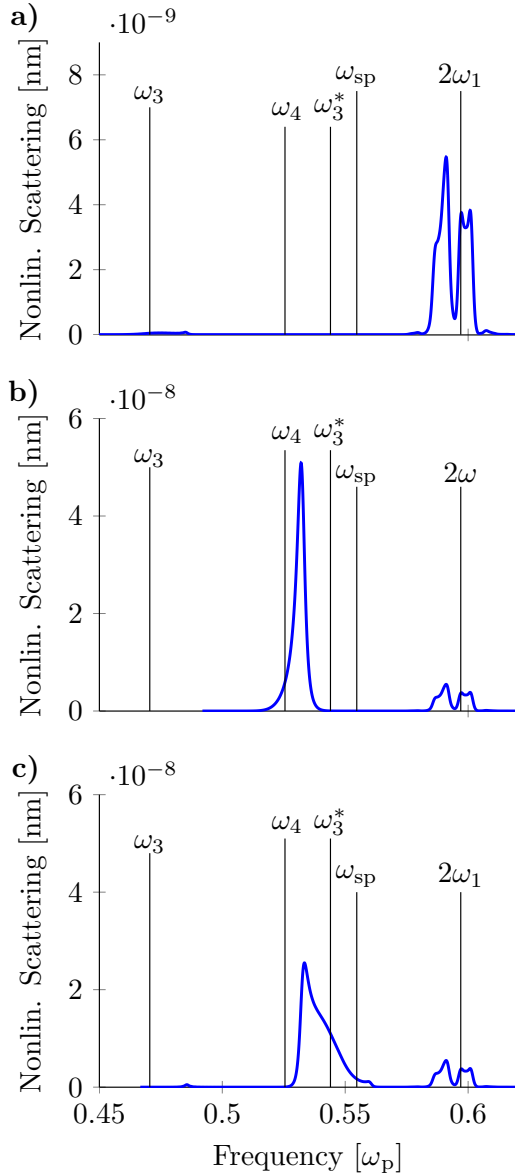


Figure 5.33: Sum-frequency generation from a bow-tie. One of the incoming pulses is always on resonance with the dipole resonance ω_1 , the second incoming pulse is chosen so that the sum-frequency is resonant with **a)** ω_3 **b)** ω_4 **c)** ω_3^* .

Another interesting observation can be made from Fig. 5.33 **b)** where the mixing signal coincides with ω_4 : The pattern at $2\omega_1$ persists as it should, but at ω_3 there is no mixing signal. Rather, a very strong

Knowing the group theoretical selection rules which were employed in the preceding Sections, the studies from Ref. [M3] can now be repeated in a more rigorous fashion. The bow-tie also belongs to the dihedral point group, thus there have to be four classes of modes. However, they cannot be constructed as in the case of the dimer since there is no corresponding conformal map to solve the electrostatic problem of such a complicated structure. As in the case of the dimer, it can be expected that one of these classes will remain dark for all angles of incidence upon linear excitation. Furthermore, as in the case of the dimer, the modes which are excited linearly and nonlinearly for one specific angle of incidence can be expected to be mutually exclusive.

The spectra of the bow-tie are displayed in Fig. 5.32. They bear some similarities to the dimer spectra: The spectra extend to both sides of the plasmon frequency and just above the plasmon frequency, there is a multitude of modes. At the position of the strong low-frequency resonance ω_1 for incidence from the top, there is no resonance for incidence from the side.

Previously, in the case of the V-groove, the incoming pulse was on resonance with the lowest frequency peak. Now, two pulses are injected, one from the top and one from the bottom, one of which is chosen to coincide with the low frequency peak ω_1 and the second one is chosen such that the mixing signal $\omega' + \omega''$ lies at a desired frequency, for instance at a resonance ω_3 or ω_3^* . The results are presented in Fig. 5.33. This time, because of the slightly lower resolution of the mesh, the calculations were carried out with 4th-order polynomials. In Fig. 5.33 **a)**, the mixing signal coincides with ω_3 which is a bright mode for this angle of incidence. The signal is very weak, as expected, since if there is a mode which is bright for linear excitation for this angle of incidence, according to the selection rules of the dihedral group, it must hence be dark for SHG. The SHG signal at $2\omega_1$ is much stronger and shows a distinct pattern of 4 peaks, which indicates that there are a number of dark modes in the vicinity of $2\omega_1$ (possibly the ripples in the vicinity of $0.6\omega_p$ in Fig. 5.32 **II**).

signal ($\sim 5 \cdot 10^{-8}$), which is of the order of magnitude of the double-resonant signals for the V-groove in Sec. 5.3) is found slightly to the blue from ω_4 which confirms the existence of a dark mode and thus a class of modes that is excited within neither of the spectra in Fig. 5.32. This is also confirmed by Fig. 5.33 c). Here, the mixing signal coincides with the dark mode ω_3^* and a signal is in fact produced at ω_3^* , but the much stronger dark mode which tweaked the spectrum in Fig. 5.33 b) overshadows the signal at ω_3^* . The signal at ω_3^* manifests itself merely as a shoulder to the stronger signal slightly to the red. Thus, for a bow-tie there are dark modes which are not excited by a Gaussian pulse for either of the directions of incidence, as it was the case for the class IV modes of the dimer. For both the bow-tie and the dimer these modes show the strongest second harmonic signal. In the wave-mixing setup presented here, where one of the incoming pulses coincides with the dipole resonance, the signal is two orders of magnitude stronger than in the case of the dimer where the linear signal was off-resonant.

In this study, I only investigated pulses incident from opposite directions which means they excited the same kinds of modes. In the previous sections I demonstrated that the types of modes which are excited nonlinearly depend on the symmetries of the modes at the linear level and thus on the incoming pulses. Rotating one of the incoming pulses by 90 degrees in a wave-mixing setup would mean that the two pulses excite different kinds of modes on the linear level and the mixing-signal would possibly no longer have any symmetry constraints in terms of which modes could be excited. A careful study of the selection rules for incoming pulses with different symmetry, as well as an investigation of “triple resonant” structures which feature resonances for both incoming pulses and for the mixing signal are certainly interesting configurations for future investigations.

5.5 Three-Dimensional Structures

The DGTD method is of course in principle not limited to two-dimensional structures. Also, an analytical solution just like the one for a cylinder, presented in Chap. 3 exists and can be found in Ref. [75]. However, a three-dimensional calculation is computationally much more demanding than a two-dimensional calculation and for extensive frequency scans, such systems are not feasible with the code at hand on computers existing today. As a proof of principle, I would still like to present a 3d calculation here. Fig. 5.34 displays the extinction spectrum for a 10 nm sphere, using the same nonlocal material model as above, once as calculated by means of the formula given by Rupp in Ref. [75] and once calculated by the DGTD method. The mesh that was used featured a maximum element edge length of 2.6 nm inside the sphere. relative error between these two calculations at the dipole peak is around 10 %.

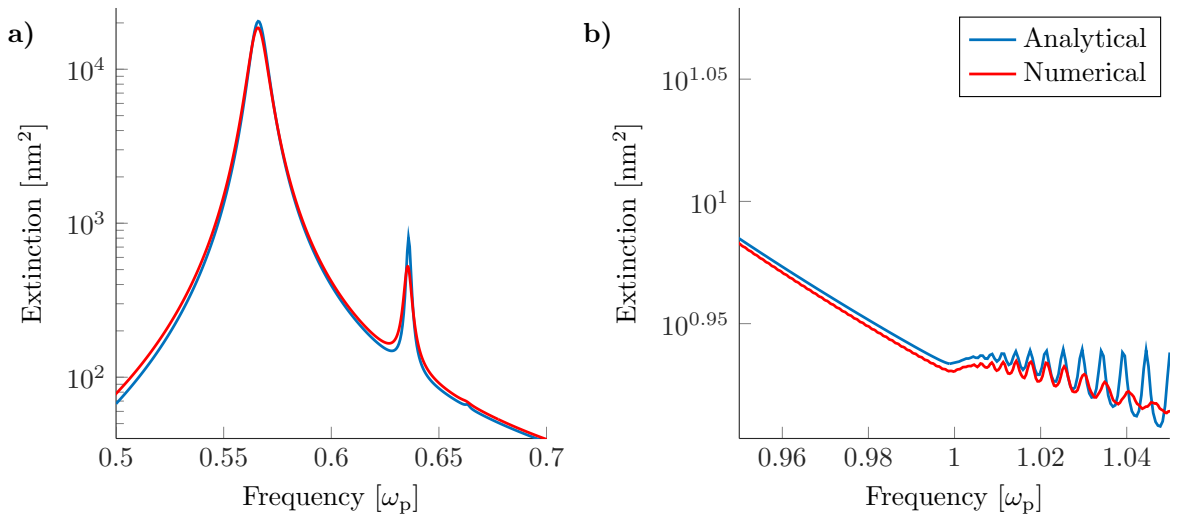


Figure 5.34: Extinction spectrum for a sphere with radius 10 nm, calculated analytically and numerically for a nonlocal material. **a)** near the plasmon frequency and **b)** near the plasma frequency. The positions of the peaks coincide well, however the height differs. For the analytical simulation, a hexapolar peak is visible which is almost completely missing in the numerical result. The positions of the first few bulk plasmon resonances also given correctly by the numerical simulation, but higher orders are not well resolved.

6

SUMMARY AND CONCLUSIONS

Summary

In this thesis, I presented studies of different types of plasmonic nanoparticles, both analytical and numerical. The main focus was to study the influence of nonlocality and nonlinearity as contained within the hydrodynamic model.

A careful introduction of how bulk and surface plasmon polaritons are described within the material models used, namely the Drude model and the hydrodynamic Drude model, was provided in Chap. 2. The derivations of these models are important both in order to gain a deeper understanding of the origin of the effects contained within the models, but also in order to understand their capabilities and limitations. I pointed out an ambiguity in the definition of the hydrodynamic pressure, and presented possible extensions of the hydrodynamic model. I also commented on the similarities and differences between the hydrodynamic model and density functional theory.

The full hydrodynamic model cannot be treated analytically. Only for the linearized hydrodynamic model – which features nonlocality but no higher harmonic generation – analytical solutions exist for simple structures such as a cylindrical nanowire. The solutions for a cylindrical nanowire, both employing Mie theory and in the electrostatic approximation, were presented in Chap. 3. I studied the asymptotic behavior of spectral shifts that are induced by nonlocality and investigated the validity of the electrostatic limit, including nonlocality. This provided important insight which can be used to interpret numerically obtained results for structures that are no longer fully analytically treatable. One structure which cannot be treated analytically using the hydrodynamic model is the ubiquitous cylindrical nanowire dimer. However, this system can be studied analytically in the electrostatic limit, employing a local material model. I performed such an analysis and classified the modes which pertain to such a dimer system. This was then also used for the interpretation of the numerical findings. A further analytical study, based on group theory was also performed. By interpreting the hydrodynamic equations and Maxwell's equations in terms of the symmetry point group imposed on the equations by the particle geometry, connections can be made between the symmetries of the incident pulse and the modes which

are excited, both by linear and nonlinear processes. This allows for important predictions for SHG.

In Chap. 4, I introduced the DGTD method, which I showed to be an adequate scheme for studying plasmonic particles, employing the hydrodynamic model. The analytical studies from Chap. 3 were used as reference solutions for the numerical method. I demonstrated the importance of extensive convergence studies. While they did not exhibit the same convergence rate as studies conducted for rectangular systems, they showed satisfactory convergence behavior. I showed that these studies have to be repeated for each new geometry, since every setup will have its own very specific requirements regarding spatial resolution. The error on the nonlinear level was found to be larger than on the linear level when employing the same mesh and polynomial order. While the discretization in the vicinity of the surface was important to achieve good results, the bulk also had to be well-resolved in order to achieve sufficient accuracy.

An extensive numerical study of different systems was then presented in Chap. 5. Starting out with the single cylinder, I presented scattering calculations, showed electric field distributions and density fluctuations and studied second harmonic generation (SHG). The selection rules for second harmonic generation which I presented in Sec. 3.4 were confirmed. Similar considerations as for the cylinder were then carried out for the cylindrical dimer. Nonlocality was investigated first, making use of the analytical findings from Chap. 3 and comparing to numerical simulations employing a quasinormal mode solver (App. A). Despite the lack of an analytical reference solution for nonlocal or nonlinear materials, the previous analysis of the modes of a dimer made it possible to interpret all of the features of the linear and the nonlinear spectra. The linear modes of the dimer were then analyzed under the aspect of field enhancement which is important for surface enhanced Raman spectroscopy (SERS). The mode analysis and selection rules were once again helpful tools, as the field distributions of the different modes were found to differ strongly. This way, configurations for specifically high field enhancement were determined and the influence of nonlocality on the enhancement was studied. I then investigated more complicated structures such as a v-groove and a bowtie. Both structures turn out to be related to the cylindrical dimer: the v-groove belongs to a lower symmetry group which is a subgroup of that of the dimer and can thus be studied in the same manner. For both structures double-resonant three-wave mixing was investigated (having a resonance at both the incoming frequency and the SHG frequency), which was found to have a strong impact on the SHG efficiency.

Conclusions and Outlook

In my studies of plasmonic nanoparticles, I have shown the importance of understanding the modes of a nanoparticle in order to predict their excitation and explain and understand the spectra and field distributions. The field distribution of every mode is thereby imposed by the geometry and the mode selection is given by its excitation (symmetry of the exciting field, linear or nonlinear process). The frequency associated with the mode on the other hand is introduced by the material model. This means that alterations in field enhancement due to nonlocality are primarily due to the fact that the frequencies of the modes are shifted with respect to each other. Corrections due to a different treatment of the surface and the absence of singularities in the hydrodynamic model were found to only have a small effect. While analytical possibilities, especially to treat nonlocal or nonlinear materials for complicated structures, are limited, I have demonstrated that a careful analysis of the modes in the electrostatic limit – which can be done for a dimer – is sufficient to gain a good understanding of the modes. In

conjunction with the analytical understanding of nonlocality gained in the context of a single cylinder (for which the electrostatic limit was investigated as well) and a numerical analysis which allowed for a comparison of the local and the nonlocal material model, even the nonlocal spectra could be understood. The group theoretical approach (Sec. 3.4) make it possible to predict the excitation of modes for linear and nonlinear processes and represents one of the key findings of my work. The approach turned out to be useful even for more complicated structures where the electrostatic modes are not available: For structures of lower symmetry than the dimer, such as the V-groove, the selection rules are contained within those of the dimer and allow for a full explanation of the numerically obtained linear and nonlinear spectra. Furthermore, the procedure presented in this thesis provides a guideline on how to treat different structures with other symmetries. The scheme can be repeated for different point groups, describing for instance multimers of more than two symmetrically arranged cylinders (which are then represented by non-abelian groups) and it can be extended to third or even higher harmonics.

The DGTD method was found to be capable of treating complicated nanostructures. The method can therefore be useful both to support theoretical efforts, as in the case of dimers which are analytically treatable to some extent, and for experimental design or interpretation purposes. Structures of realistic sizes can be handled in 2d while for 3d structures additional effort must be put into the development of more potent codes. An inclusion of curved elements would give access to more complicated structures and better convergence rates.

From the numerical investigations, it became apparent that for particles sizes of some ten nanometers, which are experimentally feasible, nonlocality starts to become important and hence a nonlocal hydrodynamic model (or an extension thereof) must be used. The nonlocality resulted in shifts of the modes, the shift being stronger for higher order modes, thus spectra and field enhancement were significantly altered.

In numerical simulations of SHG, all previously mentioned selection rules were confirmed. The simulations however also provided a quantitative prediction for the mode excitation, both for linear and nonlinear processes. Double resonance was found to yield strong enhancement of the second harmonic signal. The symmetries can be exploited further to achieve even stronger enhancement. An analysis of the sum-frequency signal of incoming pulses which are orthogonal to each other could yield double-resonant enhancement without the symmetry constraint.

I mentioned possible extensions of the numerical method which have been shown to lead to better agreement with experimental results. Those include soft boundaries which become important for very small particles and small gaps, the inclusion of interband transitions to accurately treat frequencies near the plasma frequency, and the generalized non-local optical response theory which has been found to deliver qualitatively better results for gap-structures.

The results from the numerical investigations presented here were obtained with a rather generic model and excluding interband transitions and cannot be expected to be quantitatively accurate. However, for silver the frequency regime of the surface plasmon resonances is in fact well described by a Drude model. In order to obtain results which are in quantitative agreement with an experiment, a fit to the parameters obtained for the exact sample under consideration has to be performed. Yet, I was able to show a number of qualitative features which can be verified experimentally and which will remain valid regardless of the parameters used.

The dimer system with its four distinct classes of modes is an ideal test system. The field distributions of the different modes pertaining to a dimer system as a property of the geometry persist regardless of the material model. Since all the modes of the system are known, by performing a frequency- and

6 *Summary and Conclusions*

space-resolved scan of field intensities, a mode analysis which goes beyond scattering or absorption spectra can be performed. The frequencies at which the modes are found (and, very notably, whether they overlap or are shifted apart) differ for the local and the nonlocal material model. Such a scan can therefore provide information about the validity of the models. Electron energy loss spectroscopy could yield sufficiently good spatial resolution and frequency resolution in the desired frequency range [139]. Furthermore, the SHG selection rules for the dimer system can be tested experimentally.

A

QUASINORMAL MODE CALCULATIONS

Plasmonic nanoparticles act as resonators which support electromagnetic modes with standing wave patterns, according to their symmetry. Since the electromagnetic energy in real systems is known to dissipate from the nanoparticles, either by radiation or by absorption in the material, a mode of a realistic system cannot be simply defined as in the case of a cavity with perfect electric conductors as boundaries. Plasmonic nanoparticles therefore represent leaky cavities which possess modes at complex frequencies, as the eigenvalue problem is rendered non-Hermitian. That the eigenfrequencies of the modes have to be complex for a lossy material can be easily seen from the imaginary contribution of a damping term to the Drude permittivity. But even the modes of non-lossy media have complex eigenfrequencies, due to their radiative nature. This is modeled mathematically by employing a radiation condition for outgoing waves instead of a conventional boundary condition. The imaginary part of the eigenfrequencies must be negative to ensure causality. Such modes are called quasinormal modes [140]. They can be characterized by their quality factor (Q -factor) which provides a measure for the energy loss per cycle [141–143]. The Q -factor of a mode found at the complex frequency ω_m is given by

$$Q = -\frac{\text{Re}(\omega_m)}{2\text{Im}(\omega_m)}. \quad (\text{A.1})$$

As a consequence of employing the radiation condition, the modes diverge at infinity. They can however still be normalized and a generalized mode volume can be defined [96, 142]. One possible way of calculating quasinormal modes is given by [142]

$$\mathbf{f}(\mathbf{r}, \omega) = \left(\frac{\omega}{c_0}\right)^2 \int_V \mathbf{G}^B(\mathbf{r}, \mathbf{r}', \omega) \Delta\epsilon(\mathbf{r}', \omega) \mathbf{f}(\mathbf{r}', \omega) d\mathbf{r}'. \quad (\text{A.2})$$

Here, $\Delta\epsilon(\mathbf{r}', \omega) = \epsilon_r(\mathbf{r}, \omega) - \epsilon_B$ is the difference between the permittivity $\epsilon_r(\mathbf{r}, \omega)$ which defines the geometry of the nanostructure and the constant background permittivity ϵ_B . $\mathbf{G}^B(\mathbf{r}, \mathbf{r}', \omega)$ is the electromagnetic Green's tensor. The fields \mathbf{f} , the eigenfunctions of the equation, are the quasinormal modes.

To solve, Eq. (A.2), Kristensen et al. used an approach where the quasinormal modes are calculated iteratively, starting from an initial guess, as self-consistent solutions to the integral equation, for a scattering problem with no incident field [96]. The scheme is described in more detail in the references already mentioned above [141–143]. As a basis for the expansion of the fields, Kristensen employs cylindrical wave functions which renders the method particularly useful for the problems investigated in this thesis. Quasinormal mode calculations and complex spectra in this thesis were calculated with the code of Kristensen [141, 142].

The fact that the modes are solutions to a scattering problem without an incoming field means that they are not subject to any symmetry constraints (cf. Sec. 3.4). i.e., all modes from all irreducible representations are obtained at once. Therefore the numerical procedure can provide a full plot, containing the positions of all modes (also the “dark modes”) in the complex frequency plane. These plots are of great value in the discussions of the mode-selection on a linear and nonlinear level in Chap. 5 of this thesis. An analytical analysis of the modes of a lossless metallic dimer in the electrostatic limit in Chap. 3 revealed the four categories of modes. Due to hybridization, there were two classes of modes above and two below the surface plasmon frequencies and these pairs of modes were found to be degenerate in frequency. The fact that the degeneracy is lifted in the non-static case of a lossy Drude metal can in some cases be seen in the the DGTD calculations. For instance in Fig. 5.12 **1b**), there are two overlapping but distinct peaks, with very different Q -values and slightly shifted frequencies in the vicinity of the low-frequency $k = 1$ -line. Clearly, this does not paint a full picture, and inherently, none of the plots in Fig. 5.12 could reveal the presence of the dark modes above the surface plasmon frequency. The quasinormal mode-plots in Fig. 5.13, in combination with the spectra, reveal everything that is going on in such a dimer structure. While the surface plots show the complex frequencies of all modes, the scattering and absorption spectra reveal how (and if at all) they are selected, due to the symmetries of the incoming field. This information can even be carried over to a hydrodynamic material. While the modes do experience a blueshift when going from a local to a nonlocal material, which can even lead to interchanged positions of the modes, the Q -factors are not significantly altered. Furthermore, all $k = 1$ -modes exhibited a comparable shift, as did all $k = 2$ -modes and so forth (Sec. 5.2.2). Thus, if it is known from the local quasinormal mode calculations that there is a dark $k = 1$ -mode with high Q -factor, slightly to the blue of a bright $k = 1$ -mode, then this is also going to be true in the nonlocal case. This is confirmed in the numerical simulations in Sec. 5.2.3.

BIBLIOGRAPHY

1. T. Bernhard, *Das Kalkwerk* (Suhrkamp, 2014).
2. M. L. Brongersma and P. G. Kik, *Surface plasmon nanophotonics* (Springer, 2007).
3. P. Drude, “Zur Iontentheorie der Metalle”, *Physikalische Zeitschrift* **1**, 161 (1900).
4. S. A. Maier, *Plasmonics: fundamentals and applications* (Springer Science & Business Media, 2007).
5. J. Maxwell Garnett, “Colours in Metal Glasses and Metallic Films”, *Phil. Trans. R. Soc. London* **203**, 385 (1904).
6. G. Mie, “Beiträge zur Optik trüber Medien, speziell kolloidaler Metallösungen”, *Annalen der Physik* **4**, 377 (1908).
7. R. Wood, “On a remarkable case of uneven distribution of light in a diffraction grating spectrum”, *The London, Edinburgh, and Dublin Philosophical Magazine and Journal of Science* **4**, 396 (1902).
8. M. Fleischmann, P. J. Hendra and A. McQuillan, “Raman spectra of pyridine adsorbed at a silver electrode”, *Chemical Physics Letters* **26**, 163 (1974).
9. D. L. Jeanmaire and R. P. Van Duyne, “Surface Raman spectroelectrochemistry: Part I. Heterocyclic, aromatic, and aliphatic amines adsorbed on the anodized silver electrode”, *Journal of Electroanalytical Chemistry and Interfacial Electrochemistry* **84**, 1 (1977).
10. M. G. Albrecht and J. A. Creighton, “Anomalously intense Raman spectra of pyridine at a silver electrode”, *Journal of the American Chemical Society* **99**, 5215 (1977).
11. S. Ben-Jaber *et al.*, “Photo-induced enhanced Raman spectroscopy for universal ultra-trace detection of explosives, pollutants and biomolecules”, *Nature Communications* **7** (2016).
12. K. Kneipp, M. Moskovits and H. Kneipp, *Surface-enhanced Raman scattering: physics and applications* (Springer Science & Business Media, 2006).
13. M. Kauranen and A. V. Zayats, “Nonlinear plasmonics”, *Nature Photonics* **6**, 737 (2012).
14. P. Reichenbach *et al.*, “Nonlinear optical point light sources through field enhancement at metallic nanocones”, *Optics express* **22**, 15484 (2014).
15. J. D. Jackson, *Classical electrodynamics* (Wiley, 1999).
16. M. Dressel and G. Grüner, *Electrodynamics of Solids: Optical Properties of Electrons in Matter* (Cambridge University Press, 2002).
17. L. Novotny and B. Hecht, *Principles of Nano-Optics* (Cambridge University Press, 2006).
18. S. Enoch and N. Bonod, *Plasmonics: from basics to advanced topics* (Springer, 2012).

19. J. Pitarke, V. Silkin, E. Chulkov and P. Echenique, "Theory of surface plasmons and surface-plasmon polaritons", *Reports on progress in physics* **70**, 1 (2007).
20. A. Campion, J. Ivanecy III, C. Child and M. Foster, "On the mechanism of chemical enhancement in surface-enhanced Raman scattering", *Journal of the American Chemical Society* **117**, 11807 (1995).
21. M. Moskovits, "Surface-enhanced spectroscopy", *Reviews of modern physics* **57**, 783 (1985).
22. P. G. Etchegoin and E. Le Ru, "A perspective on single molecule SERS: current status and future challenges", *Physical Chemistry Chemical Physics* **10**, 6079 (2008).
23. H. Xu, E. J. Bjerneld, M. Käll and L. Börjesson, "Spectroscopy of single hemoglobin molecules by surface enhanced Raman scattering", *Physical review letters* **83**, 4357 (1999).
24. M Moskovits, "Surface roughness and the enhanced intensity of Raman scattering by molecules adsorbed on metals", *The Journal of Chemical Physics* **69**, 4159 (1978).
25. M. R. Philpott, "Effect of surface plasmons on transitions in molecules", *The Journal of Chemical Physics* **62**, 1812 (1975).
26. H. Xu, J. Aizpurua, M. Käll and P. Apell, "Electromagnetic contributions to single-molecule sensitivity in surface-enhanced Raman scattering", *Physical Review E* **62**, 4318 (2000).
27. E. J. Blackie, E. C. L. Ru and P. G. Etchegoin, "Single-molecule surface-enhanced Raman spectroscopy of nonresonant molecules", *Journal of the American Chemical Society* **131**, 14466 (2009).
28. S. Marqués-González, R. Matsushita and M. Kiguchi, "Surface enhanced Raman scattering of molecules in metallic nanogaps", *Journal of Optics* **17**, 114001 (2015).
29. Y.-T. Kim, J. Schilling, S. L. Schweizer and R. B. Wehrspohn, "Morphology Dependence on Surface-Enhanced Raman Scattering Using Gold Nanorod Arrays Consisting of Agglomerated Nanoparticles", *Plasmonics*, 1 (2016).
30. J. W. Jarrett, M. Chandra and K. L. Knappenberger Jr, "Optimization of nonlinear optical localization using electromagnetic surface fields (NOLES) imaging", *The Journal of chemical physics* **138**, 214202 (2013).
31. G. Bautista, M. J. Huttunen, J. M. Kontio, J. Simonen and M. Kauranen, "Third- and second-harmonic generation microscopy of individual metal nanocones using cylindrical vector beams", *Opt. Express* **21**, 21918 (2013).
32. P. Reichenbach, L. M. Eng, U. Georgi and B. Voit, "3D-steering and superfocusing of second-harmonic radiation through plasmonic nano antenna arrays", *J. Laser Appl.* **24**, – (2012).
33. P. N. Melentiev *et al.*, "Split Hole Resonator: A nanoscale UV light source", *Nano letters* **16**, 1138 (2016).
34. I. Razdolski *et al.*, "Resonant enhancement of second harmonic generation in the mid-infrared using localized surface phonon polaritons in sub-diffractive nanostructures", *arXiv preprint arXiv:1607.05158* (2016).
35. R. W. Boyd, *Nonlinear optics* (Academic press, 2003).

36. S. S. Jha, “Nonlinear response theory—I”, *Pramana* **22**, 173 (1984).
37. L. D. Landau and E. M. Lifšic, *Lehrbuch der theoretischen Physik*, 5., von E. M. Lifschitz u. L. P. Pitajewski erg. u. berichtigte Aufl. (Akademie-Verlag, Berlin, 1990).
38. J. M. Ziman and P. Rennert, *Prinzipien der Festkörpertheorie* (Akad.-Verlag, 1974).
39. L. Landau and E. Lifschitz, “Lehrbuch der Theoretischen Physik Band VI: Hydrodynamik”, Akademie Verlag, Berlin (1991).
40. R. E. Wyatt, *Quantum dynamics with trajectories: introduction to quantum hydrodynamics* (Springer Science & Business Media, 2006).
41. S. Raza, S. I. Bozhevolnyi, M. Wubs and N. A. Mortensen, “Nonlocal optical response in metallic nanostructures”, *Journal of Physics: Condensed Matter* **27**, 183204 (2015).
42. S. Raza, G. Toscano, A.-P. Jauho, M. Wubs and N. A. Mortensen, “Unusual resonances in nanoplasmonic structures due to nonlocal response”, *Phys. Rev. B* **84**, 121412 (2011).
43. R. Rupp, “Extinction properties of thin metallic nanowires”, *Opt. Commun.* **190**, 205 (2001).
44. I. Tokatly and O. Pankratov, “Hydrodynamics beyond local equilibrium: Application to electron gas”, *Physical Review B* **62**, 2759 (2000).
45. G. Toscano *et al.*, “Resonance shifts and spill-out effects in self-consistent hydrodynamic nanoplas-monics”, *Nature communications* **6** (2015).
46. G. Toscano, S. Raza, A.-P. Jauho, N. A. Mortensen and M. Wubs, “Modified field enhancement and extinction by plasmonic nanowire dimers due to nonlocal response”, *Opt. Express* **20**, 4176 (2012).
47. G. Giuliani and G. Vignale, *Quantum theory of the electron liquid* (Cambridge university press, 2005).
48. S. Lundqvist and N. H. March, *Theory of the inhomogeneous electron gas* (Springer Science & Business Media, 2013).
49. A. Sommerfeld, “Zur Elektronentheorie der Metalle auf Grund der Fermischen Statistik”, *Zeitschrift für Physik* **47**, 1 (1928).
50. F. Bloch, “Bremsvermögen von Atomen mit mehreren Elektronen”, *Zeitschrift für Physik A Hadrons and Nuclei* **81**, 363 (1933).
51. L. H. Thomas, “The calculation of atomic fields”, **23**, 542 (1927).
52. E. Fermi, “Eine statistische Methode zur Bestimmung einiger Eigenschaften des Atoms und ihre Anwendung auf die Theorie des periodischen Systems der Elemente”, *Zeitschrift für Physik* **48**, 73 (1928).
53. N. H. March, *Electron density theory of atoms and molecules* (Academic Press, 1992).
54. P. Hohenberg and W. Kohn, “Inhomogeneous electron gas”, *Physical review* **136**, B864 (1964).
55. R. M. Martin, *Electronic Structure: Basic Theory and Practical Methods* (Cambridge University Press, 2004).
56. A. Eguiluz and J. Quinn, “Hydrodynamic model for surface plasmons in metals and degenerate semiconductors”, *Physical Review B* **14**, 1347 (1976).

57. G. Toscano *et al.*, “Resonance shifts and spill-out effects in self-consistent hydrodynamic nanoplas-monics - SUPPLEMENTARY MATERIAL”, *Nature communications* **6** (2015).
58. U. Mizutani, *Introduction to the electron theory of metals* (Cambridge University Press, 2001).
59. M. Brack, “The physics of simple metal clusters: self-consistent jellium model and semiclassical approaches”, *Reviews of modern physics* **65**, 677 (1993).
60. E. K. Gross and E. Runge, “Many-particle theory”, (1986).
61. P. J. Morrison and J. M. Greene, “Noncanonical Hamiltonian density formulation of hydrody-namics and ideal magnetohydrodynamics”, *Physical Review Letters* **45**, 790 (1980).
62. P. J. Morrison, “Hamiltonian description of the ideal fluid”, *Reviews of modern physics* **70**, 467 (1998).
63. P. Lynch, “Hamiltonian methods for geophysical fluid dynamics: An introduction”, Retrieved from the University of Minnesota Digital Conservancy on March 24, 2016, <http://purl.umn.edu/3742>, 2002.
64. P. Ginzburg, A. V. Krasavin, G. A. Wurtz and A. V. Zayats, “Nonperturbative hydrodynamic model for multiple harmonics generation in metallic nanostructures”, *ACS Photonics* **2**, 8 (2014).
65. A. Krasavin, P. Ginzburg, G. Wurtz and A. Zayats, “Nonlocality-driven supercontinuum white light generation in plasmonic nanostructures”, *Nature communications* **7** (2016).
66. Y. Grynko, T. Zentgraf, T. Meier and J. Förstner, “Simulations of high harmonic generation from plasmonic nanoparticles in the terahertz region”, *Applied Physics B* **122**, 242 (2016).
67. I. Villó-Pérez and N. R. Arista, “Hydrodynamical model for bulk and surface plasmons in cylin-drical wires”, *Surface Science* **603**, 1 (2009).
68. J. Armstrong, N. Bloembergen, J. Ducuing and P. Pershan, “Interactions between light waves in a nonlinear dielectric”, *Physical Review* **127**, 1918 (1962).
69. C. Ciraci, J. B. Pendry and D. R. Smith, “Hydrodynamic model for plasmonics: a macroscopic approach to a microscopic problem”, *ChemPhysChem* **14**, 1109 (2013).
70. A. R. Melnyk and M. J. Harrison, “Theory of optical excitation of plasmons in metals”, *Physical Review B* **2**, 835 (1970).
71. N. Bloembergen, R. K. Chang, S. Jha and C. Lee, “Optical second-harmonic generation in re-flection from media with inversion symmetry”, *Physical Review* **174**, 813 (1968).
72. S. S. Jha, “Theory of optical harmonic generation at a metal surface”, *Physical Review* **140**, A2020 (1965).
73. A. Hille, PhD Thesis (Technische Universität Dresden, 2012).
74. J. E. Sipe, V. C. Y. So, M. Fukui and G. I. Stegeman, “Analysis of second-harmonic generation at metal surfaces”, *Phys. Rev. B* **21**, 4389 (1980).
75. R Ruppin, “Optical properties of a plasma sphere”, *Physical Review Letters* **31**, 1434 (1973).
76. M Anderegg, B Feuerbacher and B Fitton, “Optically excited longitudinal plasmons in potas-sium”, *Physical Review Letters* **27**, 1565 (1971).

77. L. Stella, P. Zhang, F. García-Vidal, A. Rubio and P. García-González, “Performance of nonlocal optics when applied to plasmonic nanostructures”, *The Journal of Physical Chemistry C* **117**, 8941 (2013).
78. C. Ciraci and F. Della Sala, “Quantum Hydrodynamic Theory for Plasmonics: The Impact of the Electron Density Tail”, arXiv preprint arXiv:1601.01584 (2016).
79. P. Halevi, “Hydrodynamic model for the degenerate free-electron gas: Generalization to arbitrary frequencies”, *Phys. Rev. B* **51**, 7497 (1995).
80. J. D. Jackson, *Classical electrodynamics*, 2. ed. (Wiley, New York [u.a.], 1975).
81. N. D. Mermin, “Lindhard dielectric function in the relaxation-time approximation”, *Physical Review B* **1**, 2362 (1970).
82. J. Dawson, “On Landau damping”, *Physics of Fluids* (1958-1988) **4**, 869 (1961).
83. N. A. Mortensen, S. Raza, M. Wubs, T. Søndergaard and S. I. Bozhevolnyi, “A generalized non-local optical response theory for plasmonic nanostructures”, *Nature communications* **5** (2014).
84. A. Liebsch, “Surface-plasmon dispersion and size dependence of Mie resonance: Silver versus simple metals”, *Phys. Rev. B* **48**, 11317 (1993).
85. W. Yang, “Gradient correction in Thomas-Fermi theory”, *Physical Review A* **34**, 4575 (1986).
86. R. Parr and W. Yang, *Density-Functional Theory of Atoms and Molecules* (Oxford University Press, USA, 1994).
87. R. Esteban, A. G. Borisov, P. Nordlander and J. Aizpurua, “Bridging quantum and classical plasmonics with a quantum-corrected model”, *Nature communications* **3**, 825 (2012).
88. J. Zuloaga, E. Prodan and P. Nordlander, “Quantum description of the plasmon resonances of a nanoparticle dimer”, *Nano letters* **9**, 887 (2009).
89. P. B. Johnson and R. W. Christy, “Optical Constants of the Noble Metals”, *Phys. Rev. B* **6**, 4370 (1972).
90. N. W. Ashcroft and D. N. Mermin, *Festkörperphysik* (Oldenbourg Verlag, 2012).
91. Y. Zeng, W. Hoyer, J. Liu, S. W. Koch and J. V. Moloney, “Classical theory for second-harmonic generation from metallic nanoparticles”, *Phys. Rev. B* **79**, 1 (2009).
92. P. Ginzburg, A. V. Krasavin, G. A. Wurtz and A. V. Zayats, “Nonperturbative Hydrodynamic Model for Multiple Harmonics Generation in Metallic Nanostructures”, *ACS Photonics* **2**, 8 (2015).
93. T. Christensen *et al.*, “Nonlocal Response of Metallic Nanospheres Probed by Light, Electrons, and Atoms”, *ACS Nano* **8**, 1745 (2014).
94. K. R. Hiremath, L. Zschiedrich and F. Schmidt, “Numerical solution of nonlocal hydrodynamic Drude model for arbitrary shaped nano-plasmonic structures using Nédélec finite elements”, *J. Comput. Phys.* **231**, 5890 (2012).
95. H. C. Hulst and H. Van De Hulst, *Light scattering by small particles* (Courier Corporation, 1957).
96. P. T. Kristensen, R.-C. Ge and S. Hughes, “Normalization of quasinormal modes in leaky optical cavities and plasmonic resonators”, *Phys. Rev. A* **92**, 053810 (2015).

97. Wolfram Research, “Mathematica”, <http://wolfram.com/products/mathematica>, Version 10.0.1.0.
98. The MathWorks, “MATLAB”, <http://mathworks.com/products/matlab>, Version R2014a.
99. D. J. Bergman and M. I. Stockman, “Surface plasmon amplification by stimulated emission of radiation: quantum generation of coherent surface plasmons in nanosystems”, *Physical review letters* **90**, 027402 (2003).
100. M. Noginov *et al.*, “Demonstration of a spaser-based nanolaser”, *Nature* **460**, 1110 (2009).
101. G. Kewes *et al.*, “Threshold Limitations of the SPASER”, arXiv preprint arXiv:1408.7054 (2014).
102. R. Koch, Bachelor Thesis (Humboldt-Universität zu Berlin, 2016).
103. M. Abramowitz and I. A. Stegun, “Handbook of mathematical functions, US Department of Commerce”, National Bureau of Standards, Applied Mathematics Series **55**, 948 (1964, Tenth Printing, 1972).
104. G. Berendt and E. Weimar, *Mathematik für Physiker (2): Funktionentheorie, Gewöhnliche und partielle Differentialgleichungen* (Akademie, 1983).
105. B. B. Dasgupta and R. Fuchs, “Polarizability of a small sphere including nonlocal effects”, *Phys. Rev. B* **24**, 554 (1981).
106. R. Fuchs and F. Claro, “Multipolar response of small metallic spheres: Nonlocal theory”, *Phys. Rev. B* **35**, 3722 (1987).
107. C. D. Cantrell, *Modern mathematical methods for physicists and engineers* (Cambridge University Press, 2000).
108. G. N. Watson, *A treatise on the theory of Bessel functions* (Cambridge University Press, 1995).
109. W. Neutsch, *Koordinaten: Theorie und Anwendungen* (Spektrum, Akad. Verlag, 1995).
110. P. Lucht, “Bipolar Coordinates and the Two-Cylinder Capacitor”, Retrieved from Rimrock Digital Technology on September 22, 2015, <http://user.xmission.com/~rimrock/>, 2015.
111. R. Rupp, “Optical absorption of two spheres”, *Journal of the Physical Society of Japan* **58**, 1446 (1989).
112. M. Nakahara, *Geometry, Topology and Physics, (Graduate Student Series in Physics)* (Taylor & Francis, 2003).
113. H. Georgi, *Lie Algebras in Particle Physics* (Westview Press, 1999).
114. P. Y. Yu and M. Cardona, *Fundamentals of Semiconductors* (Springer, 1996).
115. K.-H. Gericke, “Charakterentabelle für chemisch wichtige Punktgruppen”, Retrieved from Physical and Theoretical Chemistry Braunschweig, TU Braunschweig, on September 20, 2016, <http://www.pci.tu-bs.de/aggericke/PC2/Punktgruppen/Punktgruppen.htm>, 2016.
116. J. Niegemann, PhD Thesis (Universität Karlsruhe (TH), 2009).
117. M. C. König, PhD Thesis (Karlsruher Institut für Technologie (KIT), 2011).
118. K. Busch, M. König and J. Niegemann, “Discontinuous Galerkin methods in nanophotonics”, *Laser Photonics Rev.* **5**, 773 (2011).

119. C. Ciraci, E. Poutrina, M. Scalora and D. R. Smith, “Second-harmonic generation in metallic nanoparticles: Clarification of the role of the surface”, *Phys. Rev. B* **86**, 115451 (2012).
120. C. Ciraci, E. Poutrina, M. Scalora and D. R. Smith, “Origin of second-harmonic generation enhancement in optical split-ring resonators”, *Phys. Rev. B* **85**, 201403 (2012).
121. J. M. McMahon, S. K. Gray and G. C. Schatz, “Calculating nonlocal optical properties of structures with arbitrary shape”, *Phys. Rev. B* **82**, 035423 (2010).
122. J. Hesthaven and T. Warburton, “Discontinuous Galerkin methods for the time-domain Maxwell’s equations”, *ACES Newsletter* **19**, 10 (2004).
123. R. Diehl, K. Busch and J. Niegemann, “Comparison of low-storage Runge-Kutta schemes for discontinuous Galerkin time-domain simulations of Maxwell’s equations”, *J. Comput. Theor. Nanosci.* **7**, 1572 (2010).
124. M. Hazewinkel, *Encyclopaedia of Mathematics* (Springer, 1989).
125. E. F. Toro, *Riemann solvers and numerical methods for fluid dynamics* (Springer, 2009).
126. J. S. Hesthaven and T. Warburton, *Nodal discontinuous Galerkin methods: algorithms, analysis, and applications* (Springer, 2007).
127. L. Fezoui, S. Lanteri, S. Lohrengel and S. Piperno, “Convergence and stability of a discontinuous Galerkin time-domain method for the 3D heterogeneous Maxwell equations on unstructured meshes”, *ESAIM: Mathematical Modelling and Numerical Analysis* **39**, 1149 (2005).
128. N. Schmitt, C. Scheid, S. Lanteri, A. Moreau and J. Viquerat, “A DGTD method for the numerical modeling of the interaction of light with nanometer scale metallic structures taking into account non-local dispersion effects”, *Journal of Computational Physics* **316**, 396 (2016).
129. J. Viquerat, Theses (Université Nice Sophia Antipolis, 2015).
130. A. Taflov, *Computational Electrodynamics: The Finite-Difference Time-Domain Method* (Artech House, Boston, 2000).
131. J. F. M. Werra, PhD Thesis (Humboldt-Universität zu Berlin, 2016).
132. J. S. Hesthaven and T. Warburton, “Nodal high-order methods on unstructured grids: I. Time-domain solution of Maxwell’s equations”, *Journal of Computational Physics* **181**, 186 (2002).
133. J. Schöberl, “Netgen”, Software available at <http://www.hpfem.jku.at/netgen> (2001).
134. csimsoft, “TRELIS”, <http://www.csimsoft.com/trelis>,
135. T. V. Teperik, P. Nordlander, J. Aizpurua and A. G. Borisov, “Quantum effects and nonlocality in strongly coupled plasmonic nanowire dimers”, *Optics express* **21**, 27306 (2013).
136. G. Toscano *et al.*, “Surface-enhanced Raman spectroscopy: nonlocal limitations”, *Opt. Lett.* **37**, 2538 (2012).
137. F. J. García de Abajo, “Nonlocal effects in the plasmons of strongly interacting nanoparticles, dimers, and waveguides”, *The Journal of Physical Chemistry C* **112**, 17983 (2008).
138. I. Romero, J. Aizpurua, G. W. Bryant and F. J. G. De Abajo, “Plasmons in nearly touching metallic nanoparticles: singular response in the limit of touching dimers”, *Optics express* **14**, 9988 (2006).

139. W. Sigle, J. Nelayah, C. T. Koch and P. A. van Aken, “Electron energy losses in Ag nanoholes—from localized surface plasmon resonances to rings of fire”, *Optics letters* **34**, 2150 (2009).
140. E. Ching *et al.*, “Quasinormal-mode expansion for waves in open systems”, *Reviews of Modern Physics* **70**, 1545 (1998).
141. P. T. Kristensen, P. Lodahl and J. Mørk, “Light propagation in finite-sized photonic crystals: multiple scattering using an electric field integral equation”, *JOSA B* **27**, 228 (2010).
142. P. T. Kristensen, C. Van Vlack and S. Hughes, “Generalized effective mode volume for leaky optical cavities”, *Optics letters* **37**, 1649 (2012).
143. J. R. de Lasson, J. Mørk and P. T. Kristensen, “Three-dimensional integral equation approach to light scattering, extinction cross sections, local density of states, and quasi-normal modes”, *JOSA B* **30**, 1996 (2013).

Publication List

- M1. M. Moeferd, P. Schmitteckert and K. Busch, “Correlated photons in one-dimensional waveguides”, *Opt. Lett.* **38**, 3693 (2013).
- M2. A. Hille *et al.*, “Second Harmonic Generation from Metal Nano-Particle Resonators: Numerical Analysis On the Basis of the Hydrodynamic Drude Model”, *The Journal of Physical Chemistry C* **120**, 1163 (2016).
- M3. D.-N. Huynh, M. Moeferd, C. Matyssek, C. Wolff and K. Busch, “Ultrafast three-wave-mixing in plasmonic nanostructures”, *Applied Physics B* **122**, 139 (2016).
- M4. M. Moeferd, T. Kiel, T. Sproll and K. Busch, “Plasmonic modes in nanowire dimers: A comprehensive study based on the hydrodynamic Drude model including nonlocal and nonlinear effects”, in preparation.

LIST OF FIGURES

1.1	Schematic of a propagating and a localized surface plasmon	3
1.2	Stokes- and anti-Stokes processes	5
1.3	Periodic nanorod array	6
1.4	Schematic of the movement of the charges in a dimer under static illumination for different polarizations	7
2.1	Real and imaginary part of the permittivity for a Drude metal	12
2.2	Plasmon dispersion relations for the plasma model and the Drude model	13
2.3	Bulk Plasmon	14
2.4	Initial density at time $t = 0$	23
3.1	Permittivity of the Drude silver used in the thesis	35
3.2	Local and nonlocal spectra of a single cylinder of 10 nm radius	37
3.3	Positions of the maxima of the local and the nonlocal Mie coefficients	39
3.4	Positions of the maxima of the local and the nonlocal Mie coefficients for a 10 nm cylinder	42
3.5	Nonlocal spectra for a 2 nm cylinder	43
3.6	Positions of the maxima of the local and the nonlocal Mie coefficients for a 2 nm cylinder	44
3.7	Influence of the nonlocal parameter β on the Cross Sections	45
3.8	Linear regressions studying the influence of the degree of nonlocality on the spectra	47
3.9	Bulk plasmons in the absorption spectrum and the derivative of the Bessel functions	48
3.10	Potentials and field distributions for a single cylinder from electrostatic theory	51
3.11	Graphical solution of the equation for the modes of a electrostatic nonlocal cylinder	53
3.12	Conformal map between a plane and a dimer and the solutions to the Laplace equation	55
3.13	The bicylindrical coordinates	56
3.14	The conformal map and the solutions to the Laplace equation	59
3.15	classes of potentials which can be constructed for a cylindrical dimer	60
3.16	The electric field components corresponding to the four different classes of potentials	61
3.17	Graphical solution for the modes of a cylindrical dimer	62
3.18	Potentials of the modes of a cylindrical dimer and their symmetries	64
3.19	Electric field components of the modes of a cylindrical dimer and their symmetries	65
3.20	Schematic describing the symmetries of an incoming light pulse	66
3.21	Geometry of the V-Groove	73
4.1	Cylinder Geometry	83
4.2	Electric field component for a high order mode surface mode	88
4.3	Convergence plots for the surface plasmon resonances for uniform refinement of the bulk	90
4.4	Field Images for a bulk plasmon resonance	91

List of Figures

4.5	Absorption spectra showing bulk plasmons for different polynomial orders and mesh refinements	92
4.6	Convergence plots for the bulk plasmon resonances for uniform refinement of the bulk	93
4.7	Convergence plots for the second harmonic spectrum	94
5.1	Cylinder Geometry	98
5.2	Nonlocal spectra for a single cylinder	98
5.3	Electric field distributions at the dipole and quadrupole frequency for a single cylinder	99
5.4	Density fluctuations for a single cylinder	99
5.5	Spectrum including the second harmonic	100
5.6	Cylinder Mesh	101
5.7	Second harmonic fields and density fluctuations for a single cylinder at twice the plasmon frequency	102
5.8	Second harmonic fields and density fluctuations for a single cylinder at the quadrupole frequency	103
5.10	Graphical solution for the modes of a cylindrical dimer	107
5.11	Dimer mesh	107
5.12	Local spectra for a dimer with 10nm radius and 2nm separation and electrostatic calculation	108
5.13	Local spectra for a dimer and the spectral location of the quasinormal modes	109
5.14	Field images for a dimer for $k=1$, orthogonal incidence	110
5.15	Field images for a dimer for $k=1$, parallel incidence	111
5.16	Local and Nonlocal spectra for a dimer with 10nm radius and 2nm separation	112
5.17	Electrostatic Limit: Spectra for a very small dimer, radius 10 nm, 1 nm separation	114
5.18	Semilogarithmic Plot of the absorption spectra for a very small dimer	116
5.19	Nonlinear scatterin spectra for a cylindrical dimer	117
5.20	Field distributions for the second harmonic signal at the highest frequency peaks of a dimer	117
5.21	Zoom on the low-frequency peak of the SHG spectrum of a dimer	118
5.22	Density fluctuations for the modes of a dimer	119
5.23	Schematic of the movement of the charges in a dimer corresponding to the four classes of modes for a dimer	119
5.24	Field enhancement spectra for a cylindrical dimer, local and nonlocal	121
5.25	SERS-active area of a dimer, perpendicular incidence	122
5.26	SERS-active area of a dimer, incidence along the dimer axis	123
5.27	Sketch of the V-groove structure	125
5.28	V-groove mesh	125
5.29	Linear V-groove spectra	126
5.30	SHG frequency scan for a double resonant V-groove	127
5.31	Bowtie mesh	128
5.32	Scattering and absorption spectra for a bow-tie	129
5.33	Sum-frequency generation from a bow-tie	130
5.34	Analytically and numerically calculated nonlocal extinction spectrum for a 3d sphere	132

ACKNOWLEDGMENTS

I am deeply indebted to Professor Kurt Busch for giving me the opportunity to write this thesis as a member of his group.

Furthermore, I would like to thank Professor Stephen Hughes and Professor Oliver Benson for agreeing to invest their time to read and grade this thesis, as well as Professor Christoph T. Koch and Professor Heinz-Wilhelm Hübers for being part of the examination committee.

The group Theoretical Optics & Photonics has been a wonderful and inspirational environment over the course of the past four years. I am grateful for insightful discussions with all members of this group, with Dan-Nha Huynh, who is an expert in nonlinearities, with Tobias Sproll and Francesco Intravaia, who are not only living encyclopedia of solid state physics but also possess a vast mathematical knowledge, and with Philip Kristensen and Rogelio Rodríguez-Oliveros who made sure I would not forget the physics over all the numerics. I am also thankful to Thomas Kiel who shared with me his knowledge on group theory. This work would not have been possible without Christian Matyssek, and Julia Werra, who were important partners in physical and numerical questions.

Special thanks go out to those who have proof-read this work, namely Dan-Nha Huynh, Tobias Sproll, Julia Werra, Thomas Kiel, Philip Kristensen, Paraschos Varytis and Christian Gryzik.

I thank Andreas Hille who was a great ally during some of the more challenging days, and Giuseppe Toscano for very interesting discussions.